Noise Dynamics in Stimulated Brillouin Scattering

by Oscar Andres Nieves

Thesis submitted in fulfillment of the requirements for the degree of

Doctor of Philosophy

under the supervision of Prof. Christopher G. Poulton and A. Prof. Matthew D. Arnold.

University of Technology Sydney
Faculty of Science
School of Mathematical and Physical Sciences

January 2022

Certificate of Original Authorship

I, Oscar Andres Nieves declare that this thesis, is submitted in fulfilment of the requirements for the award of Doctor of Philosophy in the School of Mathematical and Physical Sciences at the University of Technology Sydney.

This thesis is wholly my own work unless otherwise referenced or acknowledged. In addition, I certify that all information sources and literature used are indicated in the thesis.

This document has not been submitted for qualifications at any other academic institution.

This research is supported by the Australian Government Research Training Program.

Production Note:
Signature removed
prior to publication.

January 10, 2022

UNIVERSITY OF TECHNOLOGY SYDNEY

Abstract

Faculty of Science
School of Mathematical and Physical Sciences

Doctor of Philosophy

Noise Dynamics in Stimulated Brillouin Scattering

by Oscar Andres NIEVES

Interactions between light and sound in optical waveguides are of great interest in the photonics and quantum computation communities, due to the potential for information storage and transmission via acoustic and optical pulses. Such interactions are made possible via nonlinear optical processes such as Raman scattering and stimulated Brillouin scattering (SBS). SBS has been used in the past three decades for multiple applications, including optical and acoustic sensing, novel microscopy and endoscopy applications, microwave and optical filtering, and more recently information storage via acoustic waves. However, noise arising from the thermal acoustic background has been shown to also be amplified by the SBS process. Although previous studies have investigated the noise properties of the SBS process in the steady-state regime, our understanding of these processes is still limited. This research intends to fill this gap by developing new mathematical and numerical models that capture these noise dynamics in more detail, and how they impact applications such as opto-acoustic storage.

In this Thesis, we extend the theoretical analysis of SBS to short pulses by deriving a set of coupled SBS equations with thermal and laser noise, and investigate the noise properties within the undepleted pump regime. We show that in the case of a constant energy pump field and lossy media, the optical signal-to-noise ratio (OSNR) has a minimum in the region where the interaction time of the pulses matches their transit time in the waveguide. Then, we develop a numerical method for solving the coupled stochastic partial differential equations beyond the undepleted pump approximation. We find that the noise properties of the fields rely on the length of the optical pulses involved as well as on the net SBS gain in the waveguide. Furthermore, for short-pump, low gain regimes, the spontaneous Stokes field is found to be incoherently amplified, thus exhibiting large spatial and temporal fluctuations, whereas for the long-pump, high gain regime the field is amplified coherently, resulting in a smooth field but with large variations in peak power between independent realizations. Similar observations were made for the stimulated scattering case using a Stokes seed. Finally, we perform numerical simulations of Brillouin storage under different modulation schemes, namely amplitude storage and phase storage, and find that phase storage offers longer storage times as a result of phase encoding being more robust to noise than amplitude encoding, in accordance with the additive-white-Gaussian-noise (AWGN) model of discrete communication theory.

Acknowledgements

I would like to acknowledge, first and foremost, my wife, who has been of immense support to me in all these years, and for always believing in me. I would like to thank my parents, who were very supportive of my pursuits since I was a kid. I would like to acknowledge my supervisor Prof. Christopher G. Poulton, and co-supervisor A/Prof. Matthew D. Arnold, for providing expert guidance throughout my degree, and helping me troubleshoot non-compliant Matlab code. Finally, I would like to show appreciation and gratitude for Prof. Michael J. Steel and Dr. Mikołaj K. Schmidt from Macquarie University, my main research collaborators, for providing a lot of support and mentoring throughout these long years, and actively contributing to my research pursuits.

List of Publications

Journal Papers

1. Nieves, O.A., Arnold, M.D., Steel, M.J., Schmidt, M.K. and Poulton, C.G., 2021. Noise and pulse dynamics in backward stimulated Brillouin scattering. Optics express, 29(3), pp.3132-3146.

2. Nieves, O.A., Arnold, M.D., Steel, M.J., Schmidt, M.K. and Poulton, C.G., 2021. Numerical simulation of noise in pulsed Brillouin scattering. JOSA B, 38(8), pp.2343-2352.

3. Nieves, O.A., Arnold, M.D., Schmidt, M.K., Steel, M.J. and Poulton, C.G., 2021. Noise in Brillouin based information storage. Optics Express, 29(24), pp.39486-39497.

We note that Chapters 4, 5 and 6 are written according to papers 1, 2 and 3 respectively, and that the author performed all the mathematical derivations and numerical simulations, Figures, results and analysis, with contributions to the text, analysis and Figure editing from the other authors: Michael J. Steel, Mikołaj K. Schmidt, Matthew D. Arnold and Christopher G. Poulton.

Contents

Chapter 1

Background Theory of Stimulated Brillouin Scattering

1.1 Introduction

Light is at the center of multiple modern technologies and applications. From electrical energy generation through photovoltaics, light-emitting diodes and displays, to the transmission of data at the speed of light in optical fibers; light has played a crucial role in driving forward many technologies that were inconceivable before the invention of the laser in the 1960s [1, 2]. In the past few decades, the growth of these technologies has been considerably enhanced by the field of nanophotonics — in which light is investigated in micro or nano-scale structures where the spatial confinement can considerably change the way in which the light waves propagate — owing to new advancements in nanofabrication technologies.

To understand the importance of nanophotonics in the modern era, we must first look back in time to the early 20th century when the true nature of light began to be understood. The discovery of photons began with the first experimental observations of the so-called photoelectric effect — the emission of electrons when electromagnetic radiation is incident on a material — by Heinrich Hertz in 1887 [3], although the phenomenon was not well understood at the time due to the lack of an atomic theory to explain the interactions between light and matter. In later years, following the discovery of the electron by J. J. Thompson in 1897 [4], Phillip Lenard expanded Hertz's experimental work on the photoelectric effect in which he demonstrated that for a given frequency of ultraviolet radiation, the maximum kinetic energy of the emitted electrons depends on the metal used, rather than on the intensity of the ultraviolet light. He also demonstrated that for each metal there is a minimum light frequency necessary to induce the emission of electrons, regardless of the intensity [5].

In 1905, Albert Einstein published his paper "On a heuristic viewpoint concerning the production and transformation of light", in which he proposed the idea of *light quanta* or photons, and qualitatively showed how this could be used to explain the photoelectric effect [6]. In this paper, he postulated that light is a beam of particles whose energies E are related to their frequencies ν according to the formula $E = h\nu$, where h is Planck's constant. When that beam is directed at a metal, the photons collide with the atoms and if the frequency is sufficient to scatter an electron, this leads to the photoelectric effect. His work, along with that of Max Planck and many others, presented a major breakthrough in the physics of light, ultimately leading to the development of photonics as its own field of study. In later decades, new discoveries regarding the interaction between light and matter were made, leading to new insights into the field of nonlinear optical processes, which Brillouin scattering is a part of.

Brillouin scattering is a nonlinear optical process in which light and sound waves interact inside a propagation medium, which can be in a solid, liquid or gaseous

state [7, 8]. In this process, photons interact with acoustic phonons; a quasi-particle characterized by the collective excitation of the atomic lattice. Photons can either absorb or emit acoustic phonons, and in the process also scattering either frequency down-shifted photons (Stokes) or frequency up-shifted photons (anti-Stokes) [9]. When the process is driven by a laser at a high enough intensity, the interaction between optical waves of the same wavelength results in the formation of a coherent interference pattern — which propagates at the speed of sound in that particular medium — as a result of two physical mechanisms: electrostriction and photoelasticity. When a feedback loop is created between the interacting light and sound waves, we refer to the process as stimulated Brillouin scattering (SBS). One can compare the SBS process to a moving Bragg grating [10], where the regions of compression or rarefaction introduced by the interference pattern between the optical waves generate variations in the refractive index, as shown in Fig. 1.1.

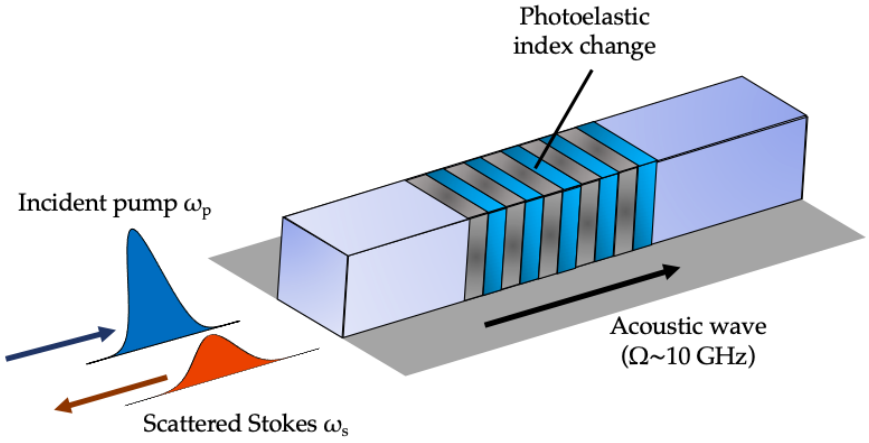

FIGURE 1.1: Illustration of the Brillouin scattering process, with an acoustic wave acting as a moving Bragg grating that reflects some of the pump energy (with frequency ω_1 back in the form of a Stokes field (with frequency ω_2).

Brillouin scattering was first theorized by the French physicist Léon Brillouin in 1922, in the context of electromagnetic wave scattering of X-rays from acoustic vibrations in a dielectric medium [11], at around the same time in which Raman scattering was being investigated for the first time [12]. The same phenomenon was also investigated independently by Mandelstam [13], so the phenomenon is sometimes referred to as Brillouin-Mandelstam scattering. In this theoretical work on X-ray scattering from acoustic vibrations, Brillouin explored the following ideas:

1. Presume that a light ray with wavevector $\mathbf{S}_i$ is incident upon a transparent medium which gives rise to a scattered light ray $\mathbf{S}_s$. In this scenario, only acoustic waves that travel in the direction of the vector $\mathbf{S}_{s-i} = \mathbf{S}_s - \mathbf{S}_i$ will contribute to the scattering process.

2. The acoustic waves travelling in this direction must also possess a wavelength which is close to the wavelength of the incident and scattered light rays. Mathematically, this means that the regions of maximum density in the acoustic waves must be separated by a distance $\Lambda = \lambda/||\mathbf{S}_{s-i}||$, where λ is the optical wavelength of the scattered light and $||\mathbf{S}_{s-i}||$ is the length of the vector $\mathbf{S}_{s-i}$. This condition is also known as the Bragg condition [14].

It was proposed by Brillouin then that a reflected light ray would arise due to the presence of the elastic waves in the medium, and that according to the Doppler effect,

the scattered light frequency f_s would occur at two frequencies around the incident frequency f_i described by the equation

$$f_s = f_i \left[1 \pm 2n \frac{v_a}{c} \sin\left(\frac{\theta}{2}\right) \right], \tag{1.1}$$

where c is the speed of light in a vacuum, v_a is the group velocity of the acoustic wave, n is the refractive index of the medium, and θ is the scattering angle. Brillouin also proposed a way to test this theory experimentally by using artificially excited elastic waves in a liquid by a quartz crystal driven by a high-frequency oscillator (i.e. in the radio-frequency regime), and in the following years between 1925−1938 the first experimental observations of this phenomenon were achieved by different researchers including Gross, Debye and Raman [15, 16, 17, 18, 19]. The experiments confirmed Brillouin's predictions of the scattered light frequency shifts, but also observed that multiple orders of diffraction were present. Later investigations found that the diffraction orders arising from the Brillouin scattering process depended not only on the material used, but also on the orientation of the crystals inside the structure [20].

Up until the 1960s, the investigation of Brillouin scattering was limited to what is known as *spontaneous* Brillouin scattering (see Section 1.2), arising from the thermal fluctuations in the propagation medium. With the invention of the laser in the 1960s, and the first experimental demonstration of a Ruby laser by Maiman [21], it was now possible to induce *stimulated* Brillouin scattering, a feedback process first demonstrated experimentally in quartz and sapphire crystals in 1964 by Chiao *et al* [22]. Following these results, Kroll developed a theoretical framework for describing the mechanisms giving rise to SBS via the process of electrostriction [23]. This was followed by the work of Shen and Bloembergen [24] who proposed a solution for the coupling of infinite plane Stokes and anti-Stokes waves satisfying appropriate boundary conditions on a plane-parallel Raman cell, finding qualitative explanations for the earlier experimental observations of SBS. Further theoretical models of SBS were extended shortly afterwards by Tang, who looked at saturation and pump depletion effects [25], and investigations on the phonon lifetime and its impact on SBS by Pohl *et al* [26]. Later in 1972, a landmark paper by Ippen and Stolen experimentally demonstrated how backward SBS was induced in glass optical fibers even at low pump powers, not only limiting the amount of narrow-band power that is transmissible in the fiber, but also causing damage to the fiber when the peak power of the amplified back-scattered pulse greatly exceeded the input power [27]. These initial investigations led to further research on the suppression of SBS, as at the time it was only seen as a hindrance for optical communications and other applications. At the same time, SBS was found to have various useful applications, as demonstrated with the first Brillouin lasers [28, 29]. Other works also looked at different waveguide structures and the role of moving boundaries on SBS [30, 31, 32], such as the effect light scattering by surface ripples in thin films.

Over the course of the next four decades, SBS found new applications in photonics, with new growth spurred in this field by the development of compact-sized waveguide structures and photonic chips [7, 33, 34, 35, 36, 37]. These micron-sized structures allowed for for better control of the electromagnetic and acoustic modes, which led to discoveries in which SBS was now a useful process instead of just a nuisance. Some notable recent applications of SBS include: narrow-band RF and optical signal filtering and processing [38, 39, 40, 41], phase conjugation and precision spectroscopy and sensing [42, 43, 44, 45], novel laser sources and resonators [46, 47, 48, 49, 50], Brillouin microscopy and micro-mechanic measurements [51, 52], pulse compression [53, 54, 55], Brillouin scattering in photonic crystal fibers and bandgap filters [56, 57, 58], and in

recent developments of opto-acoustic pulse storage and memory [59, 60, 61, 62, 63]. However, one of the key challenges limiting the application of SBS is the coupling of thermal noise (at room temperature or higher) to the optical and acoustic fields. Thermal noise has been known to significantly hinder the performance of SBS-based devices [64, 65, 66, 67], and a general theoretical framework for describing and simulating this noise is still needed for improving existing technologies.

In this thesis we study the noise mechanisms in Brillouin scattering, particularly in what is known as backward stimulated Brillouin scattering (BSBS). We numerically simulate optical and acoustic waves in the presence of this noise, and investigate its impact on performance and information retrieval accuracy in opto-acoustic memory storage. In the remainder of this Chapter, we focus on the physics of Brillouin scattering, outlining the main areas of research which are yet to be expanded, including the noise dynamics arising from the SBS interaction.

1.2 Physics of Brillouin scattering

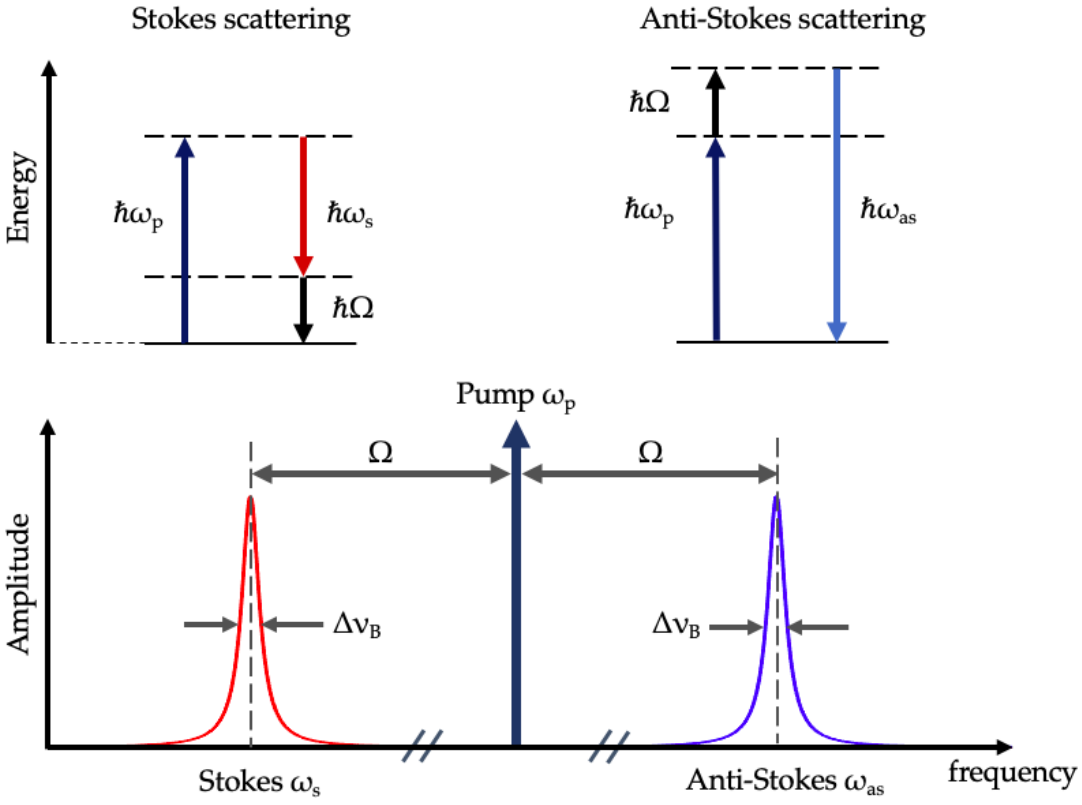

FIGURE 1.2: Frequency spectra for the Stokes and Anti-Stokes transitions in Brillouin scattering, and energy transition diagrams for Stokes and anti-Stokes processes. The Brillouin process shifts the optical frequencies of the scattered fields with respect to the pump frequency ω_p by the Brillouin frequency Ω, with Stokes frequency $\omega_s < \omega_p$ and Anti-Stokes frequency $\omega_{as} > \omega_p$. The scattered spectra also become broadened, with Brillouin linewidth $\Delta\nu_B$ associated with the acoustic phonon lifetime of the medium.

Brillouin scattering originates from the interaction of electromagnetic waves with propagating acoustic waves. In a quantum mechanical picture [8], incident photons (often referred to as pump photons) are annihilated and photons with a shifted frequency are

created. This shifted frequency is determined by one of two possible Brillouin transitions [68, 8, 69] (see Fig. 1.2):

1. In the Stokes transition, a high-frequency photon is annihilated and both a lower-frequency Stokes photon and an acoustic phonon are created.

2. In the anti-Stokes transition, a lower-frequency photon absorbs a phonon and creates a higher-frequency photon.

In a semi-classical picture, the Brillouin scattering process is defined as follows: an optical wave induces changes to the density of the propagation medium in the form of an acoustic wave, which is mediated by the process of electrostriction [55, 70, 71, 72], while the changes in density modifies the permittivity (and therefore refractive index) of the material via a process called photoelasticity [73, 74]. Electrostriction is a property of all dielectric materials that arises from the application of an external electromagnetic field, in which the electromagnetic field causes a atomic displacements in the propagation medium. The accumulation of these small displacements across the bulk of the material then leads to strains in the direction of the applied field [75]. When two electromagnetic waves interfere and form a beat-pattern in the medium, regions of high and low light intensity are generated. Then, electrostriction generates a force towards the high-intensity region, leading to a periodic compression of the material, and a density wave is formed. At the same time, the reverse process takes place: material compression causes the dielectric permittivity — and consequently the refractive index — to change, through photoelasticity [76, 77]. The density variations propagate at a speed — which is dictated by the difference in frequencies between the two optical waves — relative to the frame of reference of the pump. When the induced wave speed matches the acoustic wave speed, a resonance is induced and consequently some of the pump's energy is scattered into the Stokes field according to the Bragg condition [14], with its frequency Doppler-shifted by an amount Ω (known as the Brillouin shift) [11].

Electrostriction and photoelasticity are not the only processes that can lead to Brillouin scattering. For instance, when Brillouin scattering occurs in a solid medium, the radiation pressure arising from internal reflection of the optical fields at the waveguide boundaries can lead to a moving-boundary effect, in which transverse elastic waves propagate across the surface of the solid. This effect is enhanced when the solid material is free-standing or surrounded by a gaseous medium, but can in some cases be suppressed by embedding the guiding medium (also referred to as the core) inside of a solid cladding [69]. By contrast, Brillouin scattering in liquids does not lead to a moving-boundary effect, as the radiation pressure arising from the boundary reflections is not strong enough to induce it [78].

To understand the interaction between optical and acoustic fields, or conversely between optical photons and acoustic phonons; it is useful to start with an *ansatz* for the fields in a three-dimensional space with position vector $\mathbf{r}$ and time t, namely:

$$\mathbf{E_p}(\mathbf{r},t) = \mathbf{A_p}(\mathbf{r},t)e^{i(\mathbf{k_p}\cdot\mathbf{r}-\omega_p t)} + \text{c.c.} \quad \text{(pump)}, \tag{1.2}$$

$$\mathbf{E_{s,as}}(\mathbf{r},t) = \mathbf{A_{s,as}}(\mathbf{r},t)e^{i(\mathbf{k_{s,as}}\cdot\mathbf{r}-\omega_s t)} + \text{c.c.} \quad \text{(Stokes/anti-Stokes)}, \tag{1.3}$$

$$\mathbf{U}(\mathbf{r},t) = \mathbf{B}(\mathbf{r},t)e^{i(\mathbf{q}\cdot\mathbf{r}-\omega_p t)} + \text{c.c.} \quad \text{(acoustic)}, \tag{1.4}$$

where $\mathbf{E_{p,s,as}}$ represent the pump, Stokes or anti-Stokes electric fields respectively, $\mathbf{U}$ is the displacement field of the medium, $\mathbf{A_{p,s,as}}$ and $\mathbf{B}$ are functions describing the envelope and modal fields of the optical and acoustic waves respectively, and c.c. is the complex conjugate. In order to fulfill the conservation of momentum in the Stokes

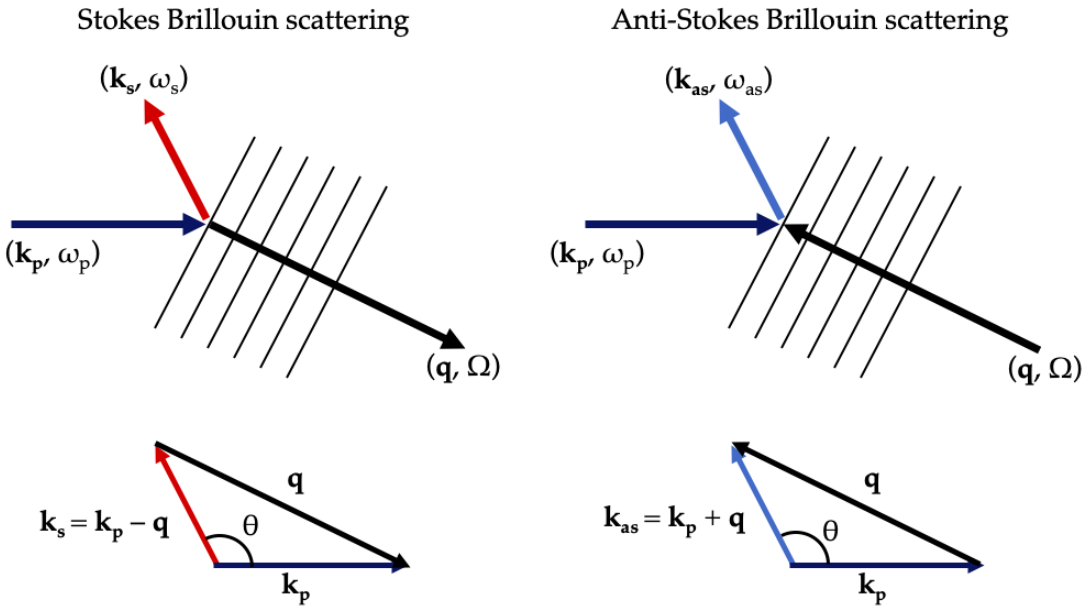

FIGURE 1.3: Illustration of the Stokes scattering process (left) and anti-Stokes scattering process (right). Stokes scattering: the incident pump photon with wavevector $\mathbf{k_p}$ and frequency ω_p interacts with a forward moving acoustic phonon with wavevector $\mathbf{q}$ and frequency Ω and creates a Stokes photon with wavevector $\mathbf{k_s}$ and frequency $\omega_s = \omega_p - \Omega$. Anti-Stokes scattering: the pump interacts with an acoustic phonon propagating in the opposite direction and generates an anti-Stokes photon with wavevector $\mathbf{k_{as}}$ and frequency $\omega_{as} = \omega_p + \Omega$. The scattering angle in both cases is denoted by θ.

case, the scattered Stokes photon must have a wavevector $\mathbf{k_s} = \mathbf{k}_p - \mathbf{q}$, where $\mathbf{k_s}$ corresponds to the Stokes optical field, $\mathbf{k}_p$ corresponds to the pump (incident optical field) and $\mathbf{q}$ correspond to the acoustic phonons or sound waves in the medium. In this interaction, the incident pump photon is annihilated in the medium and creates one Stokes photon and one acoustic phonon. From conservation of energy we require that the pump frequency satisfy $\omega_p = \omega_s + \Omega$, where ω_s is the Stokes frequency and Ω is the acoustic frequency. Consequently, the Stokes photon is down-shifted (red-shifted) in frequency. In a similar manner for anti-Stokes scattering, the incident pump photon absorbs an incoming acoustic phonon, and creates an anti-Stokes photon. From conservation of momentum, we require that the anti-Stokes wavevector satisfy $\mathbf{k_{as}} = \mathbf{k_p} + \mathbf{q}$, and from conservation of energy the anti-Stokes frequency is given by $\omega_{as} = \omega_p + \Omega$. In this latter case, the anti-Stokes photon is up-shifted (blue-shifted) in frequency, as illustrated in Fig. 1.2. The frequency profile of the scattered Stokes or anti-Stokes has a linewidth $\Delta\nu_B$, and the Brillouin frequency shift with respect to the pump's center frequency (ω_p) is given by Ω [79]. In general Brillouin scattering experimental setups, the Brillouin linewidth $\Delta\nu_B$ is of the order of < 100 MHz, while the Brillouin shift is of the order of < 20 GHz (with the exception of diamond, which is of the order of ~ 70 GHz) [68, 80].

Depending on the mode of initiation, Brillouin scattering can be classified into two main types: spontaneous and stimulated. In this Section, we will describe the physical mechanisms giving rise to each type, and their consequences on certain applications.

1.2.1 Spontaneous Brillouin scattering

Spontaneous Brillouin scattering arises from the interaction between incident light and thermally excited acoustic waves in the propagation medium. By thermally excited

acoustic waves, we are referring to incoherent acoustic fluctuations in the propagation medium that are present at any temperature above absolute zero. These thermal fluctuations lead to small changes in the optical properties of the medium, such as the dielectric permittivity ε, which may arise from fluctuations in thermodynamic quantities such as the pressure, entropy, density, or temperature of the material [68].

In a lot of Brillouin scattering experiments however, spontaneous Brillouin scattering is used for describing the process in which only a pump laser field is present in the interaction, but there is no input optical seed or signal [44], and this means that any measured output Stokes (or anti-Stokes) signal is a result of the scattering of pump photons by thermally excited phonons in the medium. For the remainder of this Thesis, we will use this latter definition of spontaneous scattering, but will make the necessary distinctions where appropriate.

1.2.2 Stimulated Brillouin scattering

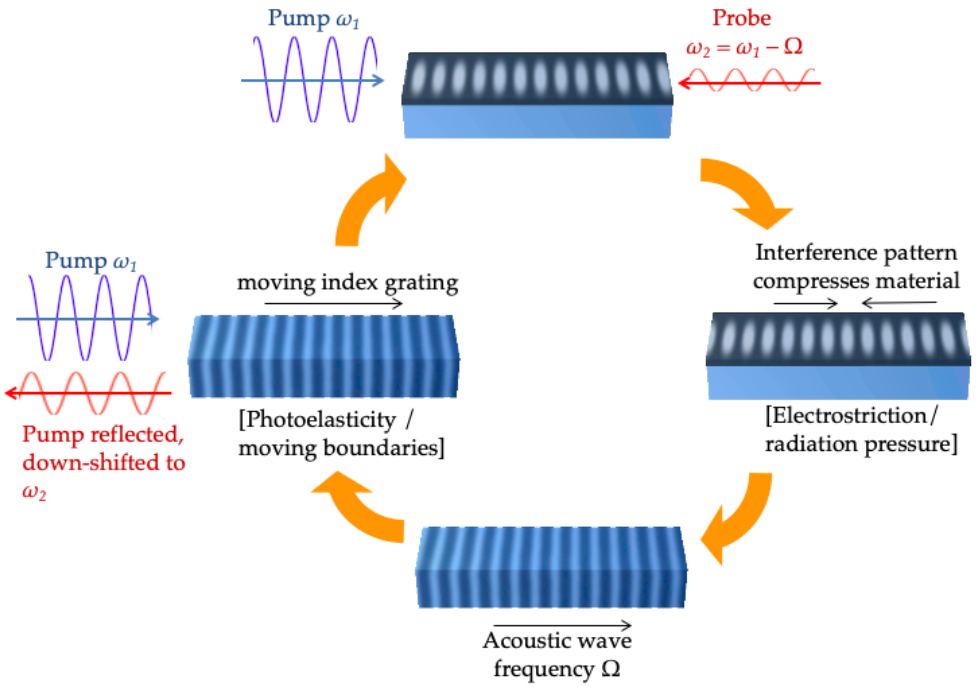

FIGURE 1.4: Illustration of the SBS process inside a solid material (Fig. from [81]). Starting from the top figure then going clockwise: a pump and probe are introduced at opposite ends of the waveguide with similar frequencies. Their interference compresses the material via electrostriction, exciting an acoustic wave in the material. This acoustic wave reflects some of the pump energy backwards.

In contrast with spontaneous Brillouin scattering, stimulated Brillouin scattering (SBS) is characterized by a feedback process between the pump and the Stokes (or anti-Stokes) optical fields. For example, when an incident optical pump field interferes with an input optical seed (at the Stokes or anti-Stokes frequency), an interference pattern between the two waves is generated [68]. This interference induces strains in the material by coherently displacing the atoms in the lattice through electrostriction. It should be noted that SBS can be initiated not just by an optical seed field, but also by the scattering of pump photons by a thermal acoustic background, which is often referred to as spontaneous SBS [64, 68]. However, this is not to be confused with regular spontaneous Brillouin scattering. The key difference between the two is that in

SBS, the pump interacts with the acoustic field as well as the scattered Stokes/anti-Stokes field, whereas in spontaneous Brillouin scattering the pump interacts with the thermally excited acoustic field only. A summary of the SBS process is illustrated in Fig. 1.4.

An important feature of SBS is that it is possible to control the amount of interference between pump and signal fields by tuning the input pump power into the propagation medium, with more pump power leading to greater amplification of the signal field (e.g. Stokes or anti-Stokes) [70].

Brillouin scattering is also classified into two types based on the direction of propagation of the two optical fields with respect to each other, namely forward Brillouin scattering (FBS) and backward stimulated Brillouin scattering (BSBS), as shown in Fig. 1.5. In BSBS, two counter-propagating optical waves exchange energy via an acoustic wave whose wavevector is oriented along the propagation direction of the pump (Stokes process), and in the opposite direction to the pump (anti-Stokes process). This coupling requires a large acoustic wavevector $\mathbf{q}$ in the waveguide direction, and as a result the acoustic waves inside the core are usually very close to pure longitudinal plane waves [69]. Since the optical wavevectors are very close in magnitude and the scattering angle is close to 180°, the acoustic frequency in the backward SBS case can be approximated by the frequency-wavenumber relation $\Omega \approx 2k_0 v_a$, where $k_0 = 2\pi/\lambda$ as the maximum optical wavenumber and v_a is the acoustic group velocity. By contrast, in forward Brillouin scattering, two co-propagating optical waves couple to an acoustic wave that has a finite frequency but a very small wavevector $\mathbf{q}$. Another important difference between the two types of scattering is that in BSBS, the pump can provide exponential gain to the Stokes field, whereas in FBS the interaction between pump and Stokes generates an interference pattern that results in an acoustic wave, but the energy is exchanged periodically between the three without providing any amplification [69].

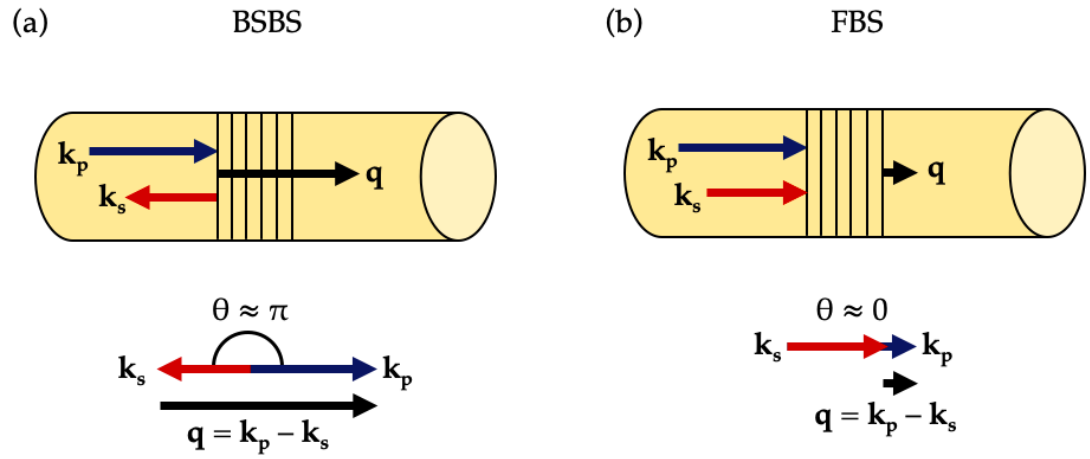

FIGURE 1.5: Illustration of (a) backward stimulated Brillouin scattering (BSBS) and (b) forward Brillouin scattering (FBS) in an arbitrary medium in the Stokes process configuration (i.e. acoustic wave propagates in the direction of the pump).

To avoid confusion between Stokes and anti-Stokes processes, we will for the remainder of this thesis refer to the pump wavevector and frequency as $(\mathbf{k}_1, \omega_1)$, and the Stokes wavevector and frequency as $(\mathbf{k}_2, \omega_2)$.

1.2.3 Guided modes in SBS

So far we have described the behaviour of SBS in a general context and how it is initiated. However, in order to achieve specific guided modes in both the electromagnetic and elastic cases in a particular waveguide — and therefore ensure that the feedback loop between the optical and acoustic fields is achieved — it is important to choose appropriate materials. For optical modes, it generally suffices that the refractive index of the waveguide (also referred to as the waveguide core) be greater than the surrounding material (referred to as the cladding) [69]. Confined acoustic modes can also be supported in a waveguide depending on the material composition. Acoustic waves have stricter conditions for propagation than electromagnetic waves, due to the presence of shear waves, pressure (or longitudinal) waves and Rayleigh or surface waves. This means that there are more mechanisms in acoustic waves in which energy can be exchanged or lost. One way to achieve acoustic wave confinement in a material is by total internal reflection (TIR), for which the acoustic wave speed within the core must be less than the speed in the cladding [69]. When this condition is satisfied, no energy is transferred from the core to the cladding. However, if this condition is not satisfied, longitudinal waves in the core can lose energy to the cladding in the form of shear waves. TIR can be achieved by using a strong mechanical contrast between the two materials, i.e. choosing core and cladding materials with significantly different densities or stiffness. Under these conditions it is possible to excite backward SBS in the waveguide. In the case of FBS, however; it is necessary to ensure that very little energy is lost to the cladding. This can be achieved by isolating the waveguide from its surroundings as much as possible, such as suspending the waveguide in air; thereby creating a large acoustic impedance mismatch (defined as the resistance of a medium to applied pressure or density waves) between the core and its surroundings. These conditions are important for tailoring SBS for integrated photonic chip applications, as we shall see in Section 1.3.

1.2.4 Brillouin gain in the SBS process

A common measure of the efficiency of the SBS process is the Brillouin gain G, which is dependent upon the waveguide geometry and material parameters (such as acoustic phonon decay rate) [70, 76]. This is a dimensionless factor that relates the input Stokes seed power $P_2(L)$ (assuming it propagates from $z = L$ to $z = 0$) to the output Stokes seed power $P_2(0)$ via the equation

$$P_2(0) = P_2(L)e^G. \tag{1.5}$$

The Brillouin gain is generally measured in continuous-wave (CW) setups, in which the optical fields (both pump and Stokes seed) have a constant input power while the lasers are operating. For this reason, we can consider the system to be in a steady-state. Within this regime, the SBS coupled equations for the counter-propagating pump and Stokes powers, namely P_1 and P_2, are [66]

$$\frac{\mathrm{d}P_1}{\mathrm{d}z} = -g(\Delta)P_1P_2 - \alpha P_1, \tag{1.6}$$

$$\frac{\mathrm{d}P_2}{\mathrm{d}z} = -g(\Delta)P_1P_2 + \alpha P_2, \tag{1.7}$$

where α is the optical attenuation of the waveguide (in m^{-1}) and $g(\Delta)$ is the SBS gain parameter (in $\mathrm{m}^{-1}\mathrm{W}^{-1}$), which is a function of the frequency detuning $\Delta = \omega_2 - \omega_1 +$

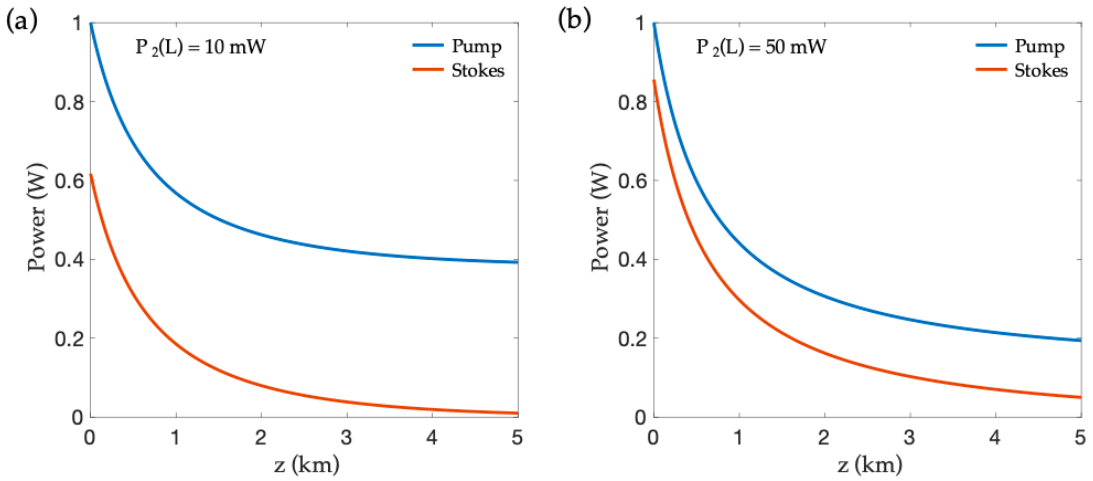

FIGURE 1.6: Stokes power $P_2(z)$ and pump power $P_1(z)$ along a 5 km optical fiber, using $g_0 = 0.83$ m^{-1}W^{-1}, $\Delta = 0$, $P_1(0) = 1$ and $\alpha = 0.2$ dB/km, produced with the analytic solutions to (1.6) and (1.7) in [66]. (a) shows the steady-state powers for a Stokes seed of 10 mW, while (b) uses a Stokes seed of 50 mW.

Ω from the Brillouin center line [76]. This function can be shown to be Lorentzian [82]

$$g(\Delta) = g_0 \frac{\Gamma^2}{\Gamma^2 + \Delta^2}, \tag{1.8}$$

where g_0 is the maximum SBS gain parameter for the waveguide, and is sometimes written in the literature as g_B / A_{eff} where A_{eff} is the effective area of the waveguide core and g_B is the Brillouin gain coefficient (m/W). The parameter Γ is the decay rate of the phonons, related to the acoustic lifetime via $\tau_a = 1/\Gamma$, which occurs due to the loss of energy of the acoustic wave via irreversible scattering into numerous other phonon states. The Brillouin spectral linewidth is generally in the order of magnitude of a few tens of MHz, corresponding to acoustic lifetimes of a few nanoseconds [70, 44, 69]; meaning that the gain profile of $g(\Delta)$ is highly localized at the phase matched Stokes frequency $\omega_2 = \omega_1 - \Omega$. Analytic solutions to the equations (1.6) and (1.7) have been found [66], and some examples are shown in Fig. 1.6. The dimensionless SBS gain G is then defined as a combination of the length L, peak pump power $P_1(0)$ and SBS gain parameter g_0 as $G = g_0 P_1(0) L$. However, this relation only holds true when we are operating in the steady-state regime and when the input seed Stokes is not strong enough to deplete the pump, as we shall see next.

1.2.5 Undepleted pump regime

Because the SBS process involves an energy exchange between pump and Stokes, where the pump loses energy and the Stokes gains energy; it is often useful to make an approximation when the Stokes seed power is much lower than the pump [70]. This approximation is called the undepleted pump approximation (UPA), and consists of assuming that the energy depleted from the pump is negligible. Under such assumption, the nonlinear interaction in (1.6) is neglected, leading to the analytic solution for the forward-propagating pump in the steady-state:

$$P_1(z) = P_1(0) e^{-\alpha z}. \tag{1.9}$$

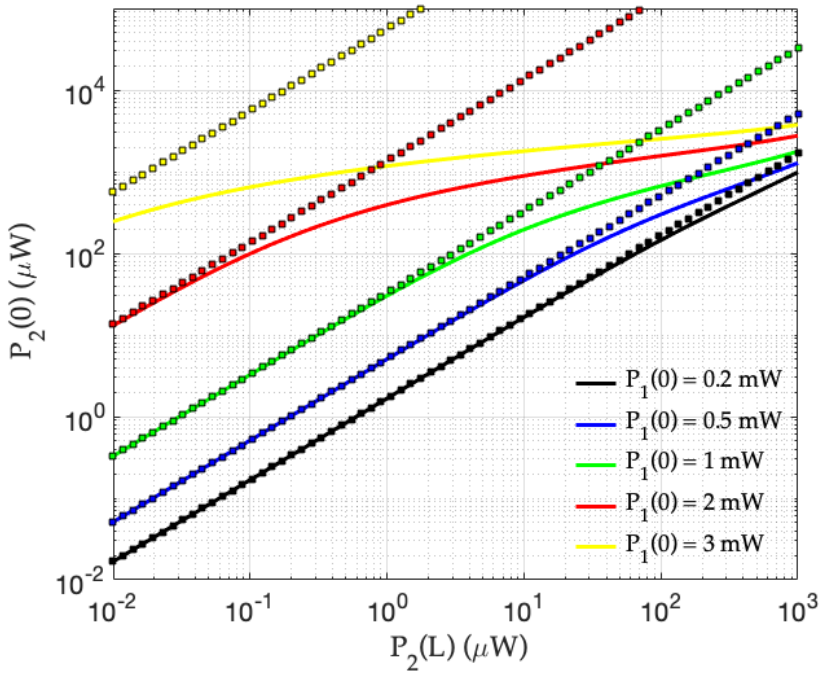

FIGURE 1.7: Analytic solutions of the output Stokes power $P_2(0)$ for different input Stokes powers $P_2(L)$ and input pump powers $P_1(0)$, using $g_0 = 0.83\ \mathrm{m^{-1}W^{-1}}$, $\Delta = 0$ and $\alpha = 0.2$ dB/km on a 5 km optical fiber. Solid curves include pump depletion while the dotted curves use the UPA in (1.10).

Using this result, the solution for the Stokes power in (1.7) is written as

$$P_2(z) = P_2(L) \exp\left\{g_0 P_1(0) L_{\mathrm{eff}}(L-z) - \alpha(L-z)\right\}, \tag{1.10}$$

where the effective length function $L_{\mathrm{eff}}(\xi)$ is defined as

$$L_{\mathrm{eff}}(\xi) = \frac{1}{\alpha}\left(1 - e^{-\alpha\xi}\right). \tag{1.11}$$

A comparison of output Stokes power as a function of input Stokes power for different pump inputs is shown in Fig. 1.7. Here we see the points at which the UPA solution deviates from the real solution with pump depletion, which depends on the input pump power. This is because the amplification provided by the pump is nonlinear, which means there is a certain threshold in which the Stokes field becomes large enough to deplete the pump, as shown in Fig. 1.6, and the UPA is no longer valid. This threshold varies with the waveguide parameters as well as the input pump energy [70]. Nevertheless, the UPA is still very useful for understanding the SBS process when the Stokes seed powers are low, as we shall see in Chapter 4.

1.3 On-chip SBS

SBS for photonic applications is used predominantly in two types of structures: optical fibers and integrated photonic chips. Optical fibers range anywhere between a few meters to a few kilometers in length, whereas photonic chips are generally a few centimeters in length, and the waveguide core cross-section dimensions are in the sub-micron range. Up until the 1990s, SBS applications were limited to optical fibers, mainly due

to the unavailability of more advanced fabrication methods that could be used for producing micrometer-scale photonic waveguides on chips. However, with improving technologies in recent decades, SBS found new applications in short-scale photonic chips, only a few tens of centimeters in size [83]. The theoretical framework for on-chip SBS was laid out by [34], and predictions for a giant enhancement of the Brillouin gain were made through numerical simulations of a suspended silicon nanophotonic waveguide. In this research, computations of the SBS gain in both backward and FBS (see Fig. 1.8) demonstrated that at the nanoscale, the radiation pressure becomes so high that it introduces new types of SBS nonlinearities, and that the backward and forward Brillouin processes are enhanced by several orders of magnitude when there is a coherent combination of radiation pressure and electrostrictive forces in the medium. In addition, the researchers also demonstrated a 10−100 fold increase in SBS gain by cooling the nanoscale silicon waveguides to low temperatures.

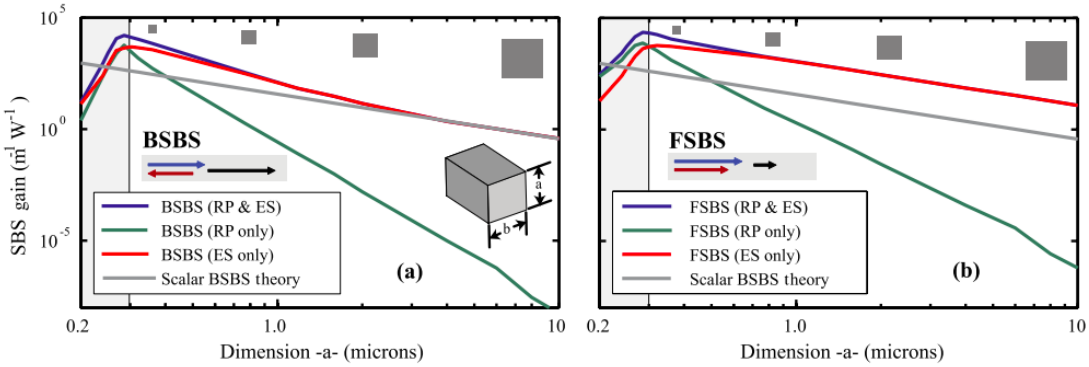

FIGURE 1.8: Computed SBS contributions from electrostriction (ES) and radiation pressure (RP) as the waveguide dimension a is varied from 0.2−10 microns (for $b = 0.93a$). (a) Backward SBS gain resulting from ES (red), RP (green), and the coherent combination of both ES and RP (blue). (b) An identical set of curves for forward Brillouin scattering. The conventional microscope SBS theory (gray curves) underestimates the BSBS gain by up to 2 orders of magnitude. Image and caption from [34].

The first experimental demonstration of such a large enhancement of SBS gain in photonic chips was performed by [33] in a 7-cm long chalcogenide waveguide with cross-section 4 µm × 850 nm, and a measured Brillouin shift and linewidth of 7.72 GHz and 34 MHz respectively. This followed from earlier measurements of SBS in chalcogenide fibers [85] where very large Brillouin gain coefficients in the range of $g_B \approx 10^{-10} - 10^{-9}$ m/W were achieved due to its high refractive index ($n = 2.44 - 2.81$). In this work, the recorded Brillouin gain coefficient was $g_B \approx 0.715 \times 10^{-9}$ m/W, at least 100 times larger than the corresponding gain coefficients in silicon single-mode fibers [66]. Furthermore, they achieved a 16 dB probe gain for a 300 mW continuous-wave (CW) pump, as shown in Fig. 1.9.

Similar experiments on a silicon waveguide [86] also demonstrated the predictions in [34]. Here, researchers made the first demonstration of Brillouin nonlinearities and Brillouin gain in silicon waveguides, using a novel class of hybrid photonic–phononic waveguides. The forward Brillouin scattering nonlinear susceptibilities were measured to be more than 1,000 times stronger than any previous waveguide system. Later experiments in a 2.9 cm long continuously suspended Brillouin-active silicon waveguide [35] demonstrated a net amplification of over 5 dB for 60 mW pump powers (see Fig. 1.10), which represented a 30-fold improvement in net amplification over previous systems.

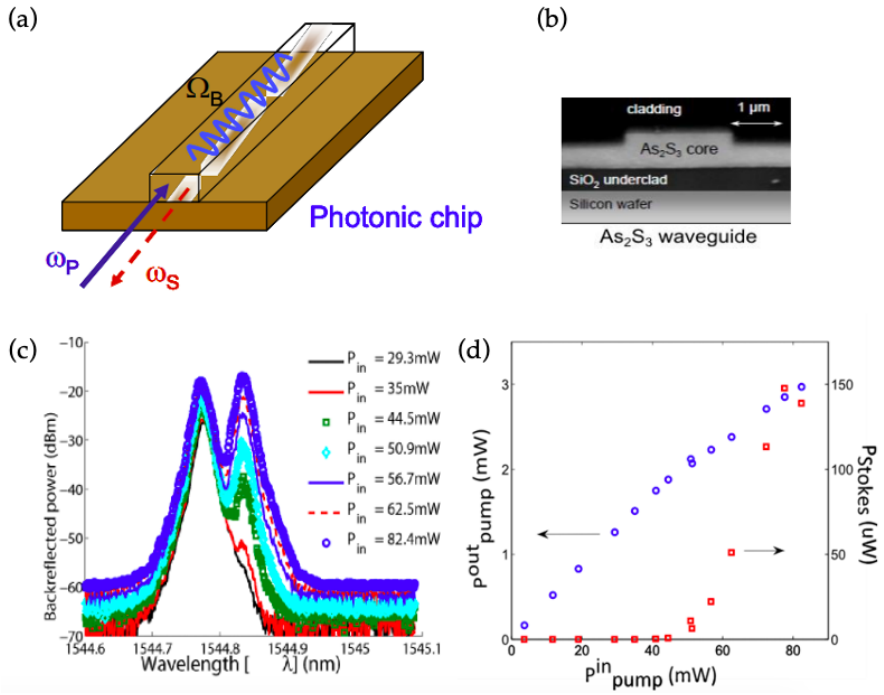

FIGURE 1.9: (a) Concept diagram of on-chip SBS showing the interaction of the pump (solid) with frequency ω_p with an acoustic wave of frequency Ω_B, resulting in the generation of a backscattered signal at $\omega_s = \omega_p - \Omega_B$. (b) Scanning Electron Microscope (SEM) image of a typical rib chalcogenide waveguide. (c) Characterisation of SBS using the backscattered signal and (d) output pump power and filtered Stokes power as a function of the average input pump power. Image and caption from [33].

Later computations [87] found that strong gradient forces improve the efficiency of Brillouin scattering in narrow silicon slot waveguides. SBS was found to be very efficient because the fundamental mechanical flexural mode could be excited. The researchers predicted that a 20 dB gain was feasible with 50 mW on-chip pump power over 1 mm propagation length, with gain coefficient of 10^5 $m^{-1}W^{-1}$. These predictions were later confirmed experimentally [84] through a novel opto-acoustic nanodevice, consisting of a series of suspended silicon wires with suspension length of 25.4 μm, as shown in Fig. 1.11. In these experiments, researchers demonstrated a modest (0.5 dB) net Brillouin gain with high efficiencies of up to 10^4 $m^{-1}W^{-1}$, consistent with earlier theoretical predictions. In addition, they found that fabrication disorder of the waveguide (such as in the waveguide width), broadens and splits the phonon resonances in some cases. Furthermore, it was found that the acoustic quality factor (i.e. a dimensionless parameter that describes how underdamped an oscillator/resonator is, or how resistant it is to energy losses due to damping) strongly decreases as the number of suspended silicon beams increases.

However, despite all of these advancements in chip-based SBS, noise still remains a challenge in nanoscale devices. Furthermore, the role of noise in pulsed SBS is not yet well understood [67, 88], and is important for applications such as opto-acoustic memory storage in which short pulses of a few hundreds of picoseconds in duration must be used.

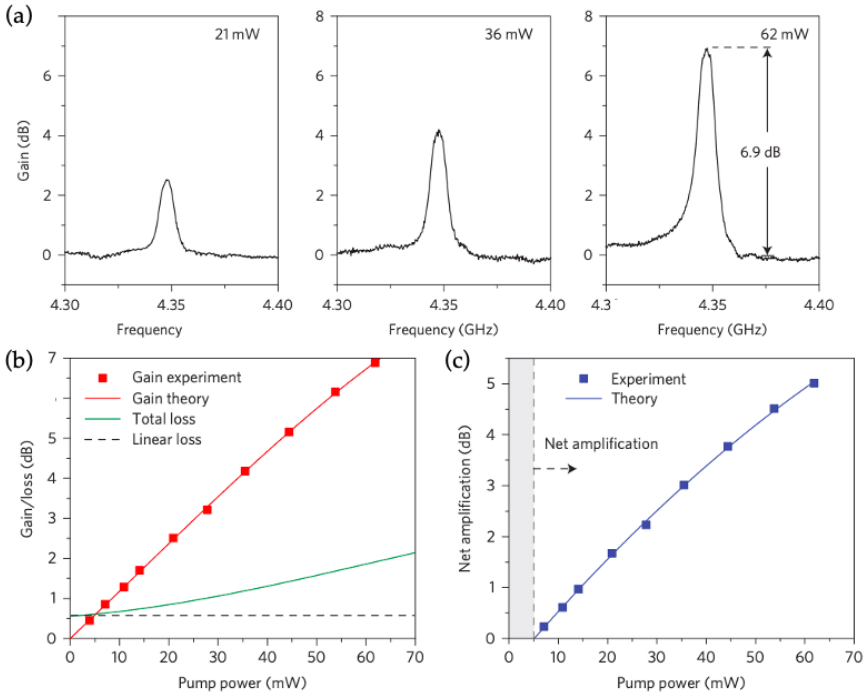

FIGURE 1.10: (a) Brillouin gain spectra obtained for different pump powers. (b) Plots of the peak gain (red), linear loss (dash) and total loss (green) versus on-chip pump power at 1550 nm. (c) Net amplification as a function of pump power (threshold for amplification is 5 mW). Image and caption from [35].

1.4 Applications of SBS

In this Section, we discuss some of the main applications of SBS which are relevant to this Thesis. In particular, we focus on applications such as signal filtering, narrow-linewidth sources and opto-acoustic storage, in which noise has a large impact on performance and scalability.

1.4.1 Optical signal filtering and amplification

Due to the narrow linewidth of the SBS process [44], it has been used in a variety of microwave photonic (MWP) filters. The first application of on-chip SBS for MWP filters was done by Marpaung *et al* [89]. In this research, the first chip-based MWP bandstop filter with ultrahigh suppression was achieved, also with resolution in the megahertz range, 0−30 GHz frequency tuning and high stopband rejection of more than 55 dB, using an ultra-low Brillouin gain (1−4 dB) from a compact centimeter-scale chalcogenide chip as described in Fig. 1.12. This application demonstrated that it is possible to create compact high-performance signal filters without the usual trade-offs between key parameters, such as tuning range, resolution and suppression, thereby leading the way towards energy-efficient and reconfigurable MWP signal processors for wireless communications. Similar filtering capabilities were testes in the RF regime [90], where they demonstrated a photonic-phononic emitter-receiver (PPER) in a silicon/silicon-nitride hybrid structure, and studied the frequency response of coherent information, showing a high dynamic range (70 dB), high Q-factor, wide rejection bandwidth (1.9 GHz) and high selectivity (bandwidth of 3 MHz, low shape factor of 5 and slope of 20/3 dB/MHz).

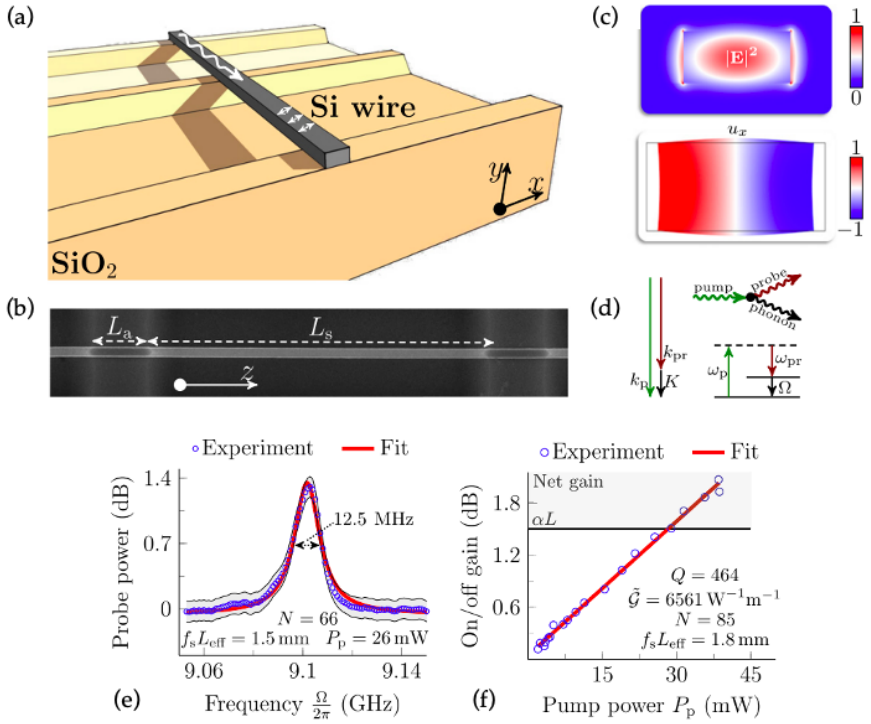

FIGURE 1.11: (a) Impression of a silicon-on-insulator waveguide with a series of suspensions and anchors. (b) SEM micrograph of an actual suspension of length $L_s = 25.4$ µm held by $L_a = 4.6$ µm long anchors. (c) Photonic (top) and phononinc (bottom) travelling modes. (d) Brillouin process converts pump photons with energy-momentum $(\hbar\omega_p, \hbar k_p)$ into redshifted probe (Stokes) photons $(\hbar\omega_{pr}, \hbar k_{pr})$ and phonons $(\hbar\Omega, \hbar K)$. (e) An example of a Brillouin gain resonance with on/off gain of 1.4 dB and quality factor $Q_m = 728$ and an on-chip input power of 26 mW. (f) Scan of on/off gain with pump power, with a Brillouin gain coefficient $\tilde{\mathcal{G}} = 6561$ W^{-1}m^{-1}. Image and caption from [84].

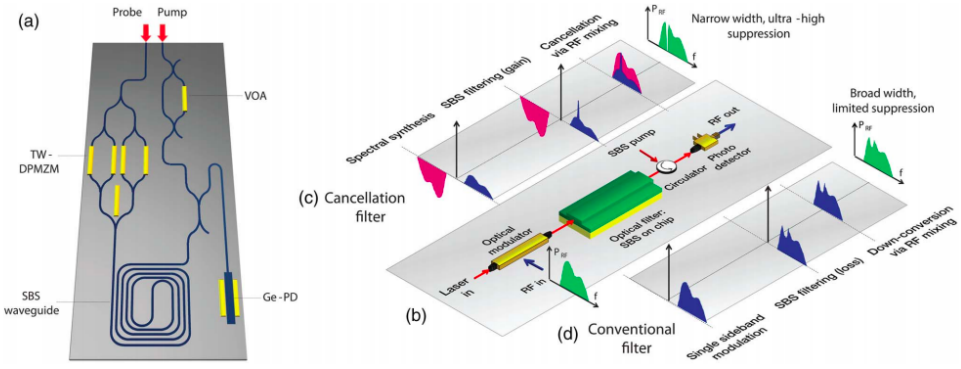

FIGURE 1.12: SBS-based integrated microwave photonic filter. (a) Artist's impression of a future monolithic-integrated high-suppression and reconfigurable SBS MWP filter in a silicon chip. VOA, variable optical attenuator; TW-DPMZM, traveling wave dual-parallel Mach–Zehnder modulator; Ge-PD, germanium high-speed photodetector. (b) Topology of the filter. (c) Near-phase modulation signals (opposite-phase, unequal-amplitude sidebands) were generated and processed using SBS gain spectrum, leading to a highly selective filter. (d) In the conventional filter, a single-sideband spectrum was generated and processed using the SBS loss/absorption spectrum, resulting in a filter with low selectivity. Image and caption from [89].

SBS has been used to build a variety of photonic amplification devices [91] by using

a large pump power acting on a small seed (Stokes) signal. Notably, recent experiments [92] showed that it is possible to enhance the Brillouin amplification process by harnessing an intermodal Brillouin interaction within a multi-spatial-mode silicon racetrack resonator. The researchers achieved upwards of 20 dB net Brillouin amplification in silicon, enhancing performance in silicon waveguides by a factor of 30 with modest (∼15 mW) continuous-wave (CW) pump powers. Additionally, they showed that the same system can behave as a unidirectional amplifier providing more than 28 dB of optical non-reciprocity without insertion loss.

1.4.2 Narrow-linewidth sources

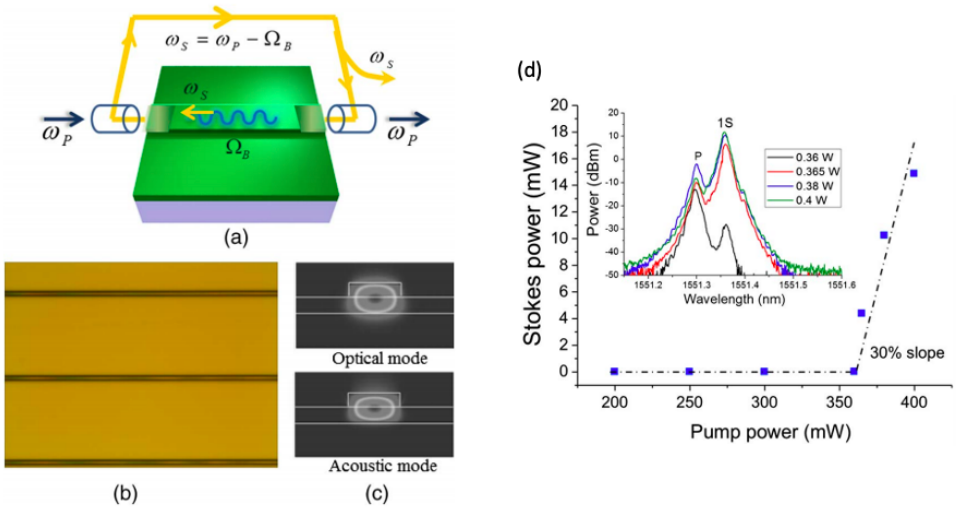

FIGURE 1.13: (a) Schematic of a Brillouin laser based on photonic chip, (b) micrograph of the As_2S_3 (chalcogenide) waveguides (top view) with vertical tapers, (c) numerically calculated acoustic and optical modes in the waveguide. Plot (d) shows the Stokes power versus input pump power (markers), with the inset showing the back-scattered optical-spectrum analyzer (OSA) spectra. Image and caption from [93].

The development of on-chip SBS allowed for a large enhancement in the SBS gain, making it now possible to create narrow-linewidth optical sources by exploiting this nonlinear process. For instance, a small-scale Brillouin laser using a chalcogenide waveguide was first demonstrated experimentally by [93] as shown in Fig. 1.13. In this experiment, the Stokes signal was generated in a 7 cm-long, 4 µm-wide As_2S_3 rib waveguide with an effective area of 2.3 μm^2, and circulated in a ring fiber cavity containing the chip. Through this, they achieved a 100 kHz linewidth laser, with a reduced lasing threshold of 360 mW (five times lower than the calculated single-pass Brillouin threshold), and a slope efficiency of 30%.

Another notable advancement in Brillouin laser technologies was achieved by [94], in which the authors demonstrated a sub-Hertz (∼0.7 Hz) fundamental linewidth Brillouin laser in a Si_3N_4 waveguide platform (as shown in Fig. 1.14), bringing laser designs to the integrated chip scale. In addition, their design supported low losses between 405−2350 nm wavelengths and low-phase-noise.

1.4.3 Brillouin sensing and microscopy

Stimulated Brillouin scattering has found numerous applications in sensing. This is because SBS is strongly dependent on the physical properties of the guiding medium:

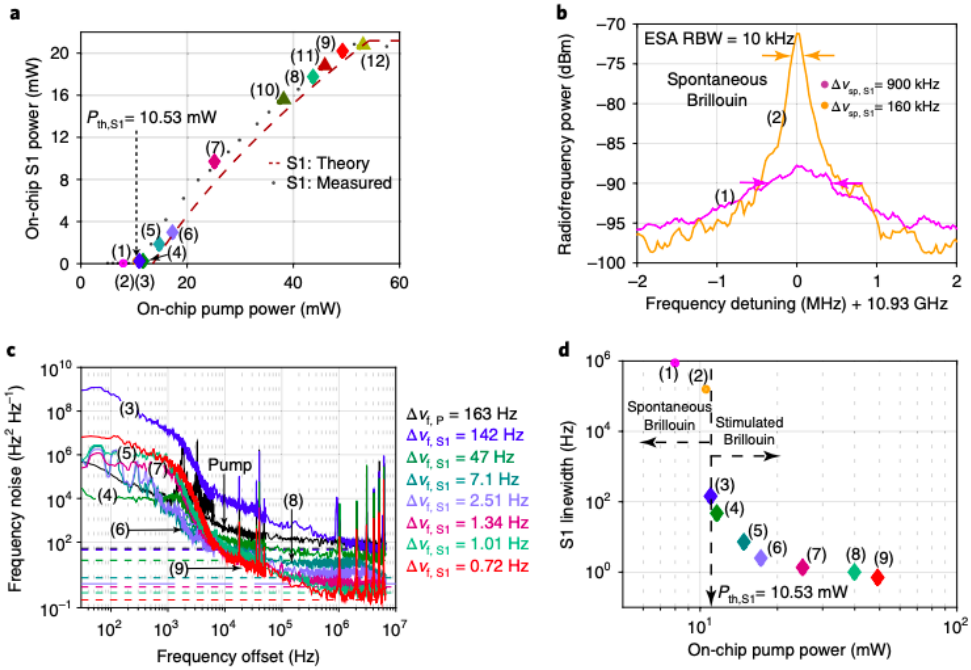

FIGURE 1.14: (a) Measured S1 (1st Stokes order) power as a function of pump power. (b) Sub-threshold spontaneous emission spectrum. (c) Measurement of the S1 single-sided frequency noise and (d) linewidth evolution of S1 from ∼1 MHz spontaneous linewidth below threshold to ∼0.7 Hz fundamental linewidth above threshold at the onset of S2 (2nd Stokes order) lasing. Image and caption from [94].

the scattered light experiences a frequency shift $\Delta\nu_B$ proportional to the acoustic velocity within the medium, which is proportional to properties such as temperature and strain [95]. One such application is Brillouin optical-fiber time domain analysis (BOTDA), in which the temperature and strain distribution across an optical fiber can be measured by accessing only one end of the fiber [96, 97, 98, 99, 100]. In a similar way, Brillouin optical-fiber frequency-domain (BOFDA) was used to make temperature and strain measurements with a spatial resolution of 3 m over a 1 km fiber, finding strong correlations with the Brillouin frequency shift [101], as shown in Fig. 1.15. Further improvements to these techniques were performed over the next decade, with higher spatial and spectral resolution achieved by [102]. Here, fully resolved measurements of the Brillouin frequency shift of a 5 cm spot perturbation at the far end of a 5 km fiber were performed, achieving a frequency resolution of 3 MHz, and using a 500 ps (5 cm) π phase shift pulse.

SBS has also been used in the characterization of optical microfibers and nanofibers as a non-destructive method, offering sensitivites as high as a few nanometers in fiber diameters ranging from 500 nm to 1.2 µm, valid for all optical wavelengths and arbitrary glass materials [42]. These characterization techniques have also been extended to small silicon-chalcogenide photonic waveguides, in which the localized Brillouin response of the structure is highly sensitive to geometrical variations [43, 103], with experimentally demonstrated spatial resolutions of 500 µm which are able to detect feature sizes down to 200 µm, by using the Brillouin optical correlation domain analysis technique (BOCDA) [104].

The same principles used for Brillouin sensing have also been applied in the field of microscopy and endoscopy, enabling much higher resolution microscopy [51, 105]. Because SBS provides a non-invasive way of probing the acoustic response of a material,

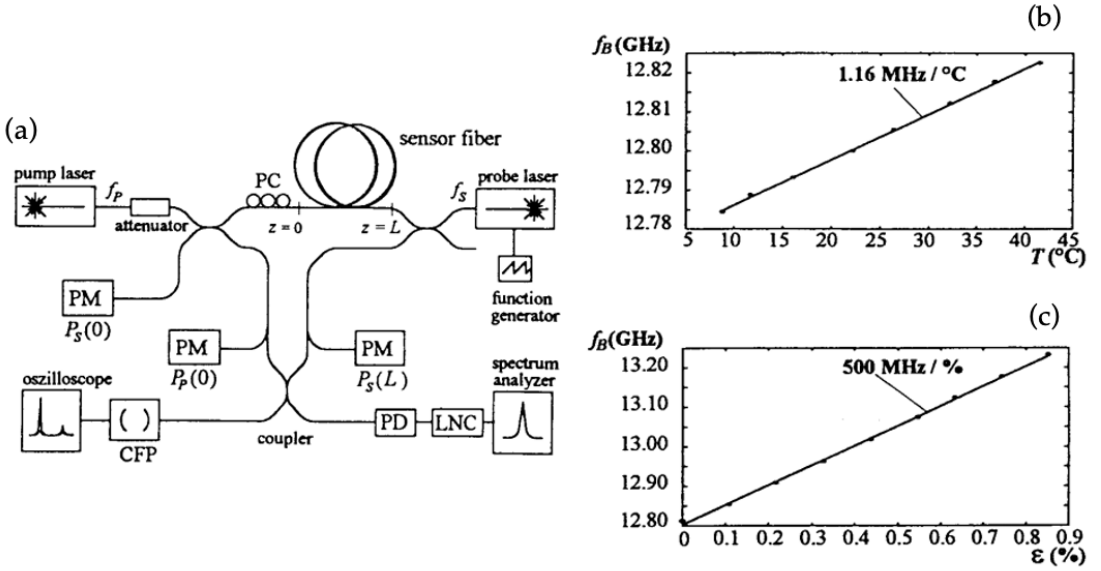

FIGURE 1.15: (a) Pump-probe-laser configuration for the measurement of the Stokes linewidth in a BOFDA experiment. Measured temperature (b) and strain (c) dependence of the Brillouin frequency shift. Image and caption from [101]. ©1997 IEEE.

it is possible to extract elastic properties of delicate biological materials which would be impossible otherwise [106]. One such example was the probing of a human eye in vivo [107]. In this experiment, the authors constructed a Brillouin optical scanner safe for human use, by employing CW laser light at 780 nm and at a low power of 0.7 mW. Using a single scan along the optical axis of the eye, the axial profile of Brillouin frequency shift was obtained with a pixel acquisition time of 0.4 s and axial resolution of about 60 µm, showing the depth-dependent biomechanical properties in the cornea and lens. Another example was the application of SBS for the measurement of the elastic properties of multiple types of spider silk [108], which allowed the authors to obtain the entire stiffness tensors, refractive indices, and longitudinal and transverse sound velocities.

1.4.4 Opto-acoustic memory storage

Because acoustic waves propagate at a speed at least 6 orders of magnitude lower than electromagnetic waves in a medium, the acoustic field can be considered to be stationary in the space during the interaction of optical pulses [69]. The acoustic lifetime in the nanophotonic waveguides used for SBS is generally in the range of nanoseconds [44], which is a long time on optical scales. This effect makes it possible to build opto-acoustic memory storage devices based on SBS, where an optical data pulse interacts with an optical write-pulse, creating an acoustic hologram in which the original data is temporarily stored [59, 109, 110]. Then, an optical read-pulse interacts with the acoustic pulse to generate another optical pulse, thus retrieving the original data, as illustrated in Fig. 1.16.

Opto-acoustic storage via SBS was first investigated experimentally by [59] in a room-temperature optical fiber, in which 2-nanosecond-long data pulses were effectively stored in an acoustic wave for up to 12 ns, using 1.5-nanosecond long read-/write pulses. In this experiment, up to 29% readout efficiency (defined as the ratio of the retrieved data power to the input data power) was achieved at 4 ns storage

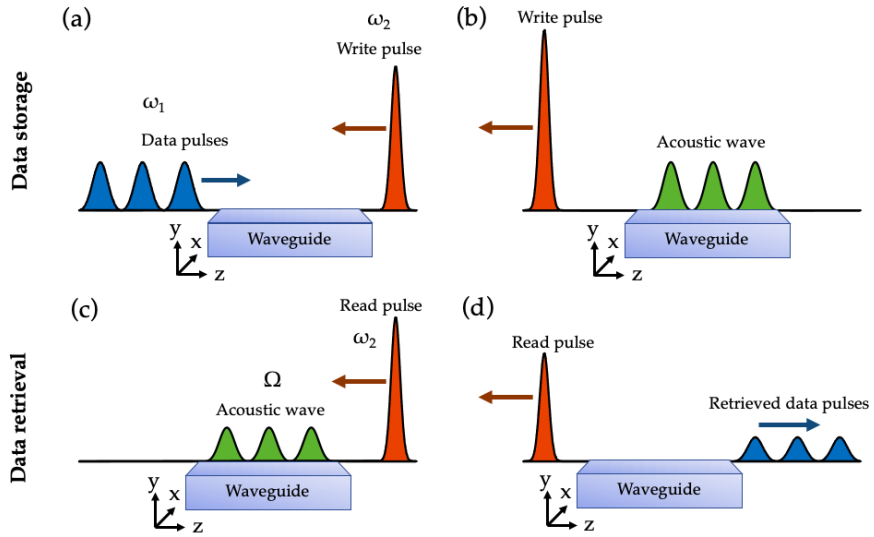

FIGURE 1.16: (a) An optical data pulse (pump) gets depleted by a strong counter-propagating write pulse (Stokes), storing the data pulse as an acoustic wave (b). (c) In the retrieval process, a read pulse depletes the acoustic wave, converting the data pulse back into the optical domain (d).

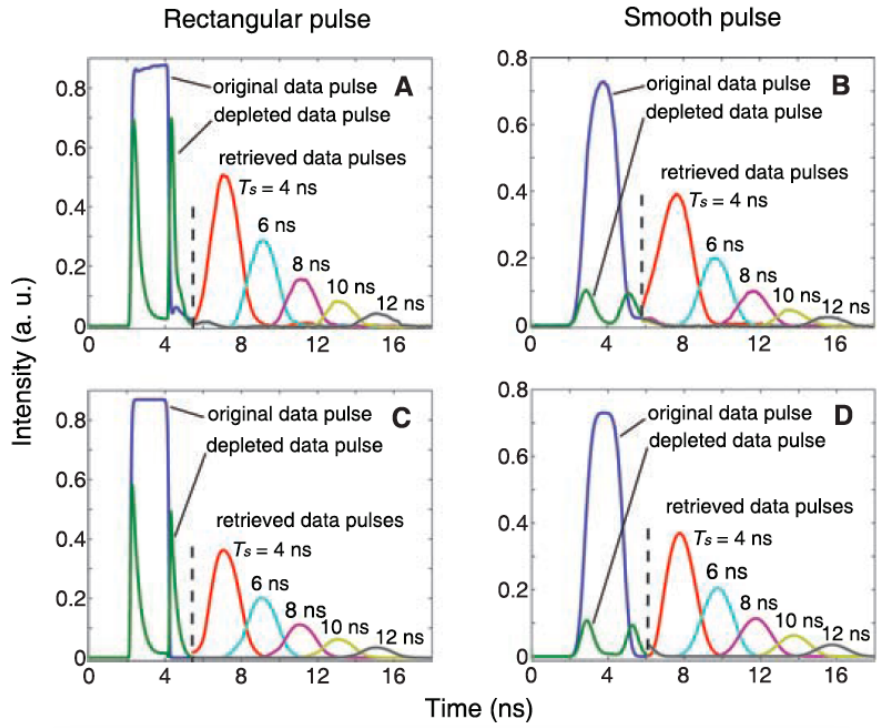

FIGURE 1.17: Measurements and numerical simulations of stored light via SBS. (**A**) shows experimental results for a 2-ns-long rectangular-shaped data pulse, and (**C**) shows the corresponding theoretical simulations. (**B**) shows the case of a 2-ns-long smooth data pulse, with the corresponding simulations shown in (**D**). The retrieved pulses are shown with a multiplication factor of 2 to the right of the dashed vertical line. Image and caption from [59].

times as shown in Fig. 1.17, and noting that higher storage efficiency might be possible in materials with longer acoustic lifetimes. It was also found that optimal storage is achieved when the read/write pulses are shorter than the shortest data pulse, and

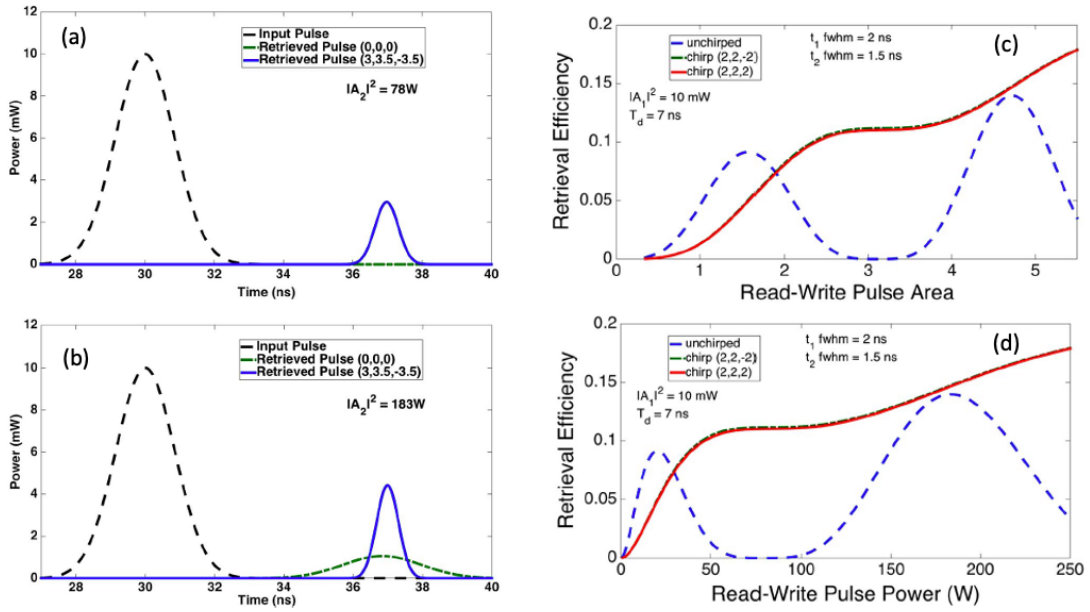

FIGURE 1.18: Data and retrieved pulses for two values of control pulse power. (a) Control pulse power = 78 W. For unchirped pulses the retrieved pulse amplitude is negligible. With chirped pulses the output is significant. (b) Control pulse power = 183 W. The retrieved pulse in the case of chirped input is stronger and narrower than for the unchirped case. The read pulse delay is 7 ns. Pulse retrieval efficiency versus (c) read and write pulse area and (d) power for chirped and unchirped Gaussian pulses. Adapted with permission from [61] ©The Optical Society.

that the pulse area for the read/write must obey certain conditions [59] based on the waveguide properties. Similar experiments [109] achieved 13% readout efficiency for 8−25 ns storage times.

Later theoretical investigations found that the storage efficiency could be further enhanced through the use of chirped pulses [60, 61], which relaxed the conditions for maximum retrieval efficiency outlined in earlier work [59], in which the read/write pulse area must be equal to an odd integer multiple of $\pi/2$ (see Fig. 1.18). In this work, approximate analytic solutions to the three-wave interaction in the steady-state were found, and the results demonstrated that the use of chirped pulses in SBS based storage improves retrieval efficiency just as it improves population transfer in the adiabatic rapid passage in two-level atom systems.

Building on the previous work in opto-mechanical resonator storage [111, 112]; investigations on non-reciprocal storage in micro-ring resonators were performed, achieving light storage in an circulating acoustic wave with a lifetime up to 10 µs [113]. More recently, successful opto-acoustic storage in higher-gain chalcogenide waveguides between 9−24 cm in length was experimentally demonstrated, with readout efficiencies of 15−32% after 3.5 ns [62]. Finally, more recent experiments used the coherent refreshing of acoustic phonons [63], as shown in Fig. 1.19. This technique achieved on-chip storage times of up to 40 ns, or four times the acoustic lifetime, with potential extensions up to the µs regime.

1.5 The role of noise in SBS

Despite the multiple applications of SBS in modern photonics, recent advances in the development of a general theory of SBS dating back to the 1990s have demonstrated

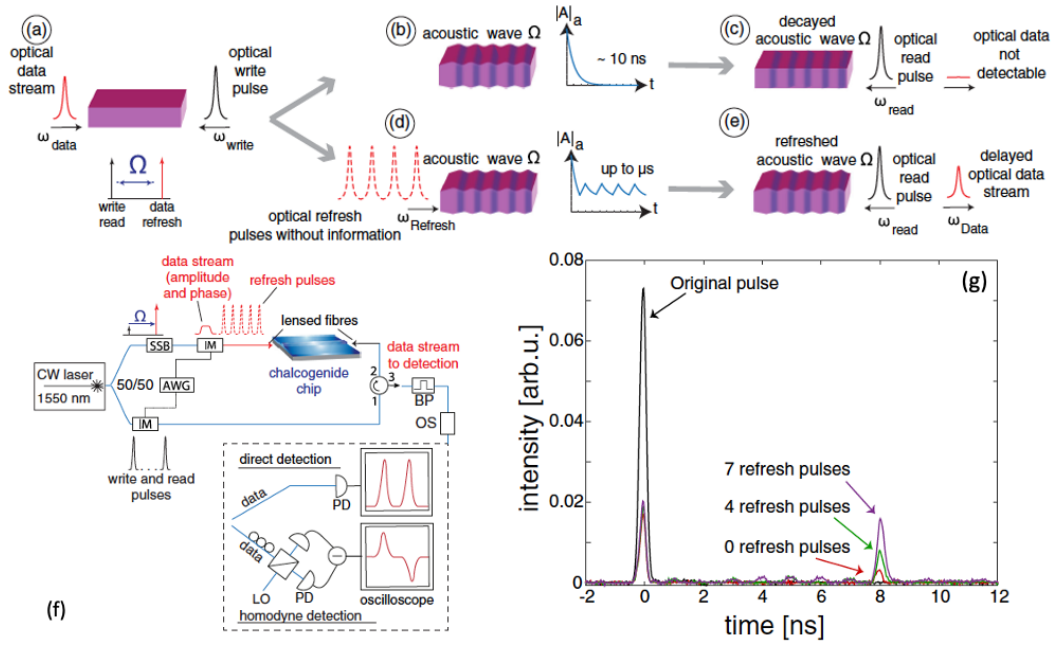

FIGURE 1.19: (a) An optical write pulse converts the information of an optical data stream to an acoustic wave. (b) Acoustic wave propagates and decays with the acoustic lifetime. (c) Acoustic wave dissipates leading to information loss. (d) Optical refresh pulses at $\omega_{\text{refresh}} = \omega_{\text{data}}$ transfer energy to the acoustic phonons. (e) Optical read pulse converts the information back to the optical domain, and the delayed optical information exits the waveguide. (f) Experimental setup and (g) experimental results for increasing retrieval efficiency using phonon refreshing. Images and captions from [63].

that background noise due to thermal fluctuations in the waveguide can negatively impact signal integrity in optical communication systems [64, 65, 66, 70, 114, 115]. This is due to background thermal phonons contributing to the amplified spontaneous emission of Stokes photons when a pump field propagates through the waveguide. This noise then combines with the input signal or Stokes seed, and generates a noisy output signal.

The first work on SBS noise was published by Boyd *et al.* [64], in which they presented a theoretical framework for modelling thermal fluctuations in SBS, by incorporating an additive white noise term into the acoustic equation, finding solutions to the Stokes field in the CW undepleted pump regime, and also performing numerical integrations for depleted pumps. They specifically looked at the relation between two quantities: the product ΓT_t in which Γ is the phonon damping rate, and T_t is the transit time of the optical fields in the waveguide, as well as the single-pass gain $G = gI_L L$ with g is the SBS gain coefficient, I_L is the pump intensity and L is the fiber length, with numerical simulations shown in Fig. 1.20. They found that the fluctuations in the Stokes output are more prominent for small ΓT_t, in which the transit time is much shorter than the time scale $1/\Gamma$ on which the Stokes intensity fluctuations occur. In this research, they concluded that since the degree of pump depletion can change considerably during the time duration of a fluctuation, this tends to smooth out the fluctuations in the output Stokes intensity.

Later experiments in [65] confirmed these observations, and also found that large Stokes fluctuations would be observed whenever $\Gamma T_t > G$, since this regime would be limited by gain saturation and thus the fluctuations in the Stokes field cannot be suppressed. However, if $\Gamma T_t < G$ then the fluctuations are diminished.

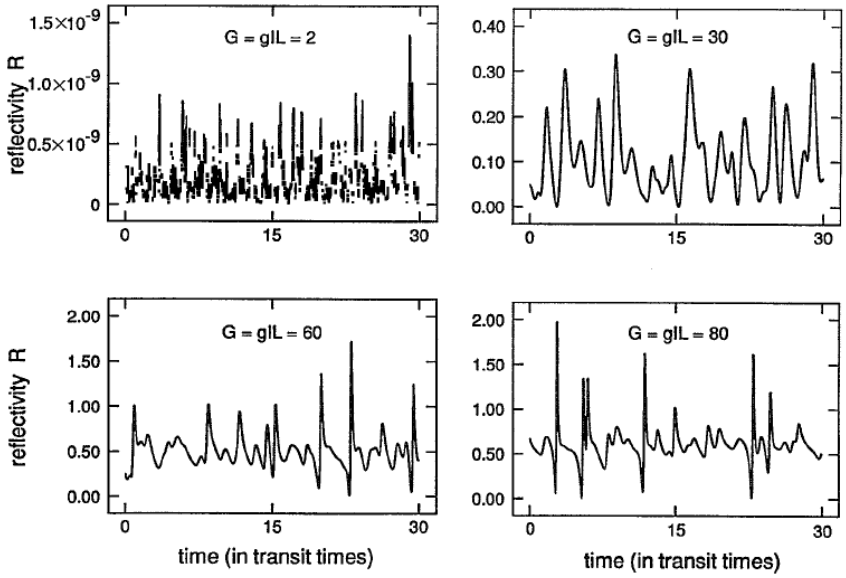

FIGURE 1.20: Fluctuations in the Stokes output intensity for the case $\Gamma T_t = 20$, as predicted by the numerical integration of the equations described in the paper. As the single-pass gain $G = gI_L(0)L$ is increased, the mean reflectivity increases and the fluctuations become suppressed due to pump depletion effects [64].

A few years later, Ferreira *et al.* [66] expanded the original theoretical model in [64] by including the effect of optical loss into the underlying equations, which was previously neglected, as well as taking into account the signal detuning from the Brillouin line center and the depletion of the pump. In these computations, it was shown that the amplified spontaneous emission noise is reduced at higher signal (Stokes seed) levels and that detuning the signal reduces the amplifier gain in the linear regime and increases the spontaneous noise power in the saturation regime. Additionally, it was found that the analytical approximation commonly used to describe the effective bandwidth of the amplified spontaneous emission spectrum was inadequate both for low and for high values of the pump power and of the amplifier length.

Despite shedding some light on the dynamics of noise in SBS, these initial theoretical models assumed that the optical and acoustic fields are weakly guided, such as in optical fibers, and that the pump operates under the quasi-continuous or CW wave regime, which at the time was very common in experimental setups. However, with the advent of more compact waveguides over the next decade, the noise models would need to be updated in order to account for different geometries and operating conditions. The theoretical work of Kobyakov *et al.* [116] extended the distributed fluctuating source model from [64] with the addition of an opto-acoustic effective area using scalar modal fields, allowing for the analysis of noise in structures beyond optical fibers. In this work, an exact formula for the back-reflected power generated by the stimulated Brillouin scattering in media with loss was derived, focusing on quasi-CW pulses and weak guidance, and provided a more accurate prediction of the back-scattered SBS signal which was shown to be $2-3$ dB higher than the level calculated with the previous models.

The study of SBS noise then focused on applications such as SBS lasers and micro-ring resonators in the following years [117, 67, 49, 50]. For instance, Loh *et al.* [117] developed a theoretical model, consisting of a set of coupled-mode equations that accurately describe the steady-state behavior and noise dynamics of an SBS micro-ring laser. They found that the coupling between the forward, backward, and density

waves results in a complex noise response to amplitude or phase perturbation, with the intrinsic limits of SBS laser noise degraded by a noisy pump due to the transfer of pump noise into the SBS wave. Nevertheless, it was also demonstrated in this study that these effects are mitigated with the use of micro-cavities with higher Q factors.

Noise and dynamics in forward Brillouin interactions have also been studied [67]. In this study, the authors looked at the spatio-temporal dynamics of spontaneous and stimulated forward Brillouin scattering (FBS), by incorporating the optomechanical coupling produced from boundary effects and photoelastic effects, using a general Hamiltonian framework. The authors established a connection between the power spectral density of spontaneously scattered light in FBS and the nonlinear coupling strength, showing that noise-initiated FBS is forbidden in the majority of experimental systems, due to the single-pass gain G being negative for a large class of devices. Similarly, noise and dynamics in cascaded order Brillouin lasers was investigated by Behunin et al. [49]. Here, the authors formulated a theoretical model based on the coupled mode dynamics governed by electrostriction and the fluctuation-dissipation theorem, from which they obtained analytical formulas describing the steady-state power evolution and accompanying noise properties such as: phase noise, relative-intensity noise, and power spectra for beat notes of cascaded laser orders. In this study, it was found that cascading can enhance laser noise, resulting in a broader emission linewidth and larger intensity fluctuations with increased power, and that higher-coherence laser emission can be achieved if indefinite cascading can be prevented.

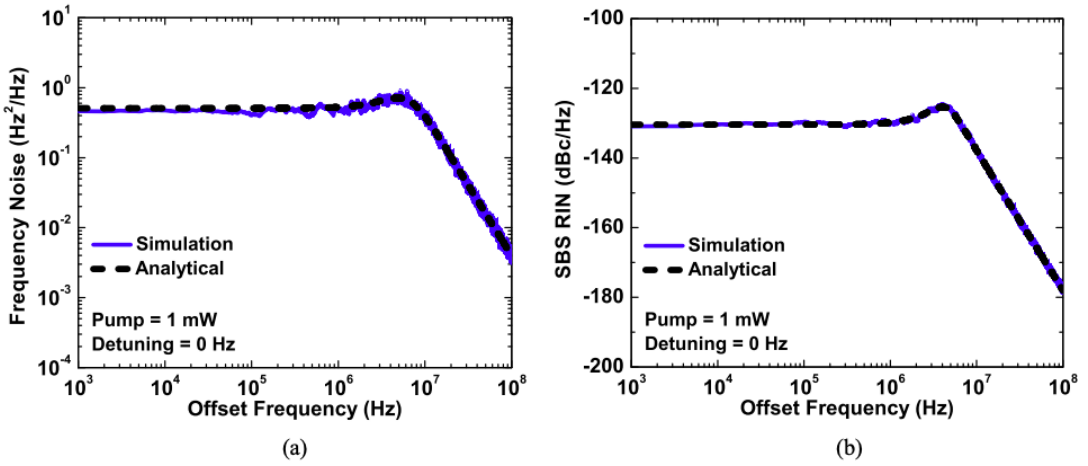

FIGURE 1.21: Simulated (blue solid line) and analytical (black dashed line) SBS laser (a) frequency noise and (b) RIN for a pump power of 1 mW and pump detuning of 0 Hz [117].

So far, theoretical frameworks have been established for backward and forward Brillouin scattering in the steady-state regime, with useful analytical formulas for computing noise properties associated with the SBS process. However, the models have focused on steady-state regimes of operation or quasi-CW pulses, either in the context of SBS amplification in fibers or in the context of lasers and micro-ring resonators. Thus far, a general theoretical framework for SBS noise in the case of optical pulses of arbitrary shape and size has not been formulated, and is still of importance for accurately predicting and characterizing the noise in modern integrated SBS waveguide experiments [118, 119, 62].

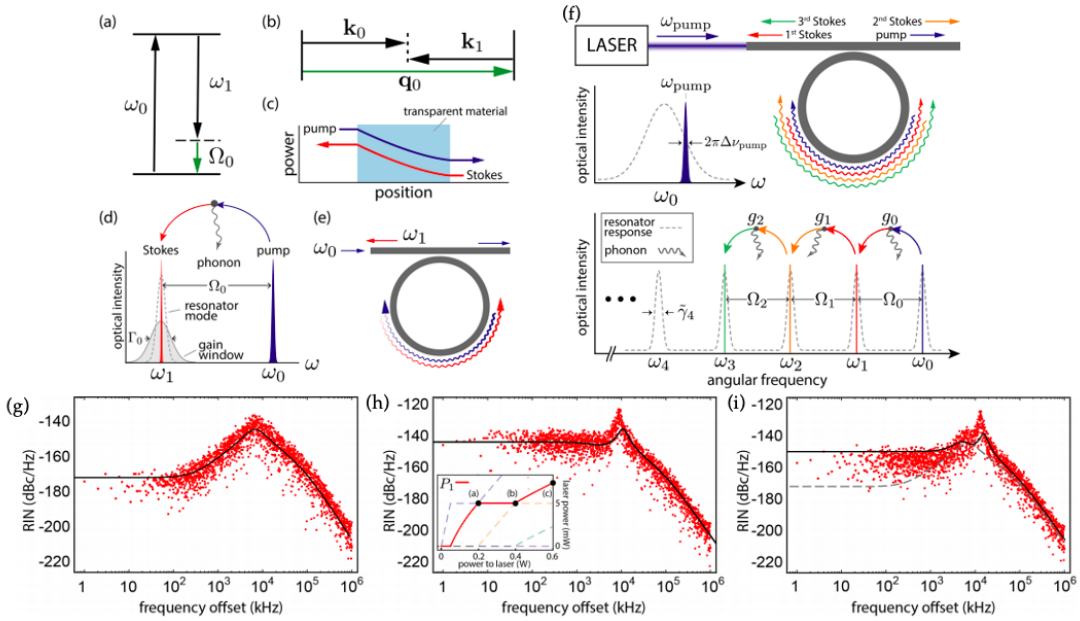

FIGURE 1.22: Fundamentals of Brillouin lasing: (a) Energy conservation and (b) wave vector phase matching requirements. Brillouin coupling mediated (c) optical amplifier and (d) energy transfer, (e) Ring resonator-based Brillouin laser. (f) Illustration of a cascaded Brillouin laser. A laser of frequency ω_{pump} and linewidth $\Delta\nu_{\text{pump}}$ pumps an optical resonator. Light in the ω_0 mode (blue) can scatter to ω_1 (red) by emitting a phonon. When lasing, the ω_1 optical mode can act as a pump for higher Stokes orders. Relative-intensity noise of the first Stokes order (g) prior to cascaded lasing, (h) cascaded lasing to two Stokes orders, and (i) cascaded lasing to three Stokes orders. Gray dashed line (i) is the theory curve from (g) included for comparison. Images and captions from [49].

1.6 The main problems addressed in this thesis

The work on SBS noise thus far has primarily focused on steady-state systems or CW regimes, and has been investigated in the context of specific devices such as lasers, micro-ring resonators and amplifiers. In order to further understand the dynamics of noise and how it interacts with the SBS process, we need to look at the case of short optical pulses and how the noise couples to the optical and acoustic fields in nanoscale photonic waveguides where the SBS gain is significantly higher than in fibers but so are the optical losses. In particular, we are interested in investigating what the physical mechanisms behind thermal noise in nanophotonic waveguides are, how this noise is amplified through the SBS interaction and how it manifests in the output optical pulses, namely in terms of amplitude and phase noise, signal-to-noise ratio (SNR) and other measures of signal integrity. Furthermore, we would also like to develop numerical methods for simulating thermal and laser noises, as well as solving the transient SBS equations for pulses of arbitrary shape and size as they interact with different noise sources. These numerical methods can then be applied to the simulation of realistic SBS devices and systems, such as Brillouin-based opto-acoustic storage, in order to predict the impact noise will have in them.

In this thesis we present both a theoretical framework for noise dynamics in backward SBS, as well as numerical methods for solving the transient SBS equations with a variety of noise sources, with particular focus on thermal noise and laser phase noise. We concentrate on the noise dynamics in pulsed SBS interactions, which have so far

not been investigated in depth, and study how the noise impacts the integrity of information retention in Brillouin-based storage.

The Thesis is broken down as follows: in Chapter 2, we derive the coupled-mode SBS equations from Maxwell's equations and the elastodynamic equations, and discuss the parameters associated with the modal fields and how they may be computed numerically. We also demonstrate how the well-known steady-state SBS equations for the pump and Stokes powers can be recovered from the general transient SBS equations derived here. This Chapter is also supplemented by background material in Appendix B, which gives an overview of elasticity theory.

In Chapter 3, we develop a mathematical theory of thermal noise in SBS by computing the energy of the acoustic field in the long-time limit, and using the equipartition theorem and fluctuation-dissipation theorem to relate the noise strength to the acoustic loss in the medium. We then develop a model for laser phase noise which simulates phase fluctuations as a Brownian motion, with variance proportional to the intrinsic laser linewidth. This Chapter is supplemented by Appendices A and C, which present an overview of random variables, a rigorous derivation of Brownian motion, and an overview of white noise and stochastic differential equations.

Chapter 4 develops a general theory of stochastic dynamics in pulsed backward SBS, and finds analytic solutions to the Stokes power in the undepleted pump regime, including thermal noise. These analytic expressions are then used for investigating the effect of pulse width and optical loss on the optical signal to noise ratio (OSNR) in a chalcogenide waveguide. We find that the OSNR has a minimum peak near the region in which the interaction time between the optical pulses matches their transit time across the waveguide, as a result of longer pump pulses compensating for the linear optical losses of the medium.

Chapter 5 expands on the theoretical work from Chapter 4 and develops a numerical method for solving the three coupled mode SBS equations with both thermal noise and input laser phase noise. The method is used for simulating pulses in a high SBS gain waveguide, and we find that for short pump regimes, the spontaneous Stokes field is incoherently amplified with large spatio-temporal fluctuations, whereas for the long-pump regime the Stokes field is amplified coherently, resulting in a smooth field with large variations in peak power. Furthermore, Appendix D described a MATLAB code that implements the numerical method derived in Chapter 5.

Chapter 6 applies the numerical methods developed to simulating Brillouin based storage with short pulses in the $100-150$ ps range, by using a set of low-power pump data pulses, and high-power Stokes read/write pulses, which deplete energy from the pump field and transfer it to an acoustic wave which temporarily stores the amplitude and phase information of the original optical field. We compare the performance of information encoding of two schemes: phase storage and amplitude storage. In this investigation, we find that phase storage allows for longer storage times than amplitude storage as it is more robust to thermal noise. We also find that increasing the read/write pulse energy also increases the maximum storage time attainable, and that the error rate in the retrieved data increases when the retrieval efficiency of the setup decreases.

Chapter 7 presents a summary and outlook of the current research, and discusses some future directions that can add to the work presented in this Thesis.

Chapter 2

Mathematical Theory of Stimulated Brillouin Scattering

2.1 Overview

The SBS interaction is mathematically described by a set of three coupled partial differential equations, two for the optical envelope fields and one for the acoustic envelope field. To derive these equations we need to combine the effects of electromagnetic waves in a continuous dielectric medium as well as elastic waves arising from two sources: thermal fluctuations in the medium, micro-strains and refractive index variations induced by electrostriction, photoelasticity and radiation pressure from the optical fields. Derivations of these coupled equations in the noiseless case have been made elsewhere [76, 8, 68, 120]. Here, we adopt a similar procedure as in [76] but use a matrix notation method to simplify the computations, before adding the noise functions at the end.

2.2 Electromagnetic equations

We describe the classical propagation of light using Maxwell's equations in a continuous medium, which are covered in detail elsewhere [121, 122, 123, 124, 125]. We will use the following form of Maxwell's equations throughout this Thesis:

$$\nabla \times \mathbf{E} = -\frac{\partial \mathbf{B}}{\partial t}, \tag{2.1}$$

$$\nabla \times \mathbf{H} = \frac{\partial \mathbf{D}}{\partial t} + \mathbf{J}, \tag{2.2}$$

$$\nabla \cdot \mathbf{D} = \rho_{\text{free}}, \tag{2.3}$$

$$\nabla \cdot \mathbf{B} = 0, \tag{2.4}$$

with electric field $\mathbf{E}$, displacement field $\mathbf{D}$, magnetising field $\mathbf{H}$, current density $\mathbf{J}$ and free charge density ρ_{free}, along with the constitutive relations for the displacement and magnetic fields respectively

$$\mathbf{D} = \varepsilon \mathbf{E} + \mathbf{P}_{\text{nl}}, \tag{2.5a}$$

$$\mathbf{B} = \mu \mathbf{H} + \mathbf{M}, \tag{2.5b}$$

where $\mathbf{P}_{\text{nl}}$ is the nonlinear polarisation term, $\varepsilon = \varepsilon_0 \varepsilon_r$ is the permittivity of the medium, μ is the permeability and $\mathbf{M}$ is the magnetic moment. In the case of non-magnetic materials, we set $\mathbf{M} = 0$. In addition, we assume free charges and free currents in the medium such that $\mathbf{J} = 0$ and $\rho_{\text{free}} = 0$ [120]. This reduces Maxwell's equations, along

with their constitutive relations, to only two: one for $\mathbf{E}$ and one for $\mathbf{H}$

$$\nabla \times \mathbf{E} = -\mu \frac{\partial \mathbf{H}}{\partial t}, \tag{2.6}$$

$$\nabla \times \mathbf{H} = \frac{\partial (\varepsilon \mathbf{E})}{\partial t} + \frac{\partial \mathbf{P}_{\text{nl}}}{\partial t}. \tag{2.7}$$

We now assume $\mathbf{P}_{\text{nl}} = \Delta\varepsilon \mathbf{E}$ under a non-dispersive treatment, given that the variation in frequency $\Delta\omega$ is small; where $\Delta\varepsilon$ is a change in the permittivity [76]. Orienting the longitudinal axis of the guiding medium along the z-axis allows us to separate the curl operator into two terms

$$\nabla \times = \nabla_{\perp} \times + \hat{\mathbf{z}} \times \partial_z, \tag{2.8}$$

where $\nabla_{\perp} \times$ is the curl with respect to only x and y. This then leads to the coupled equations

$$\partial_t (\varepsilon \mathbf{E}) - \hat{\mathbf{z}} \times \partial_z \mathbf{H} - \nabla_{\perp} \times \mathbf{H} = -\partial_t \mathbf{P}, \tag{2.9}$$

$$\partial_t (\mu \mathbf{H}) + \hat{\mathbf{z}} \times \partial_z \mathbf{E} + \nabla_{\perp} \times \mathbf{E} = 0. \tag{2.10}$$

In a manner analogous to the derivation of the electromagnetic reciprocity relations in [126], we write our system of equations in matrix form as

$$\partial_t \begin{pmatrix} \varepsilon & 0 \\ 0 & \mu \end{pmatrix} \begin{bmatrix} \mathbf{E} \\ \mathbf{H} \end{bmatrix} + \partial_z \begin{bmatrix} 0 & -\hat{\mathbf{z}}\times \\ \hat{\mathbf{z}}\times & 0 \end{bmatrix} \begin{bmatrix} \mathbf{E} \\ \mathbf{H} \end{bmatrix} + \begin{bmatrix} 0 & -\nabla_{\perp}\times \\ \nabla_{\perp}\times & 0 \end{bmatrix} \begin{bmatrix} \mathbf{E} \\ \mathbf{H} \end{bmatrix} = -\partial_t \begin{bmatrix} \Delta\varepsilon & 0 \\ 0 & 0 \end{bmatrix} \begin{bmatrix} \mathbf{E} \\ \mathbf{H} \end{bmatrix}. \tag{2.11}$$

To simplify the equations, we borrow notation from quantum mechanics and write

$$\partial_t \boldsymbol{\mathcal{E}} |\Psi\rangle + \partial_z \boldsymbol{\mathcal{P}} |\Psi\rangle + \boldsymbol{\mathcal{D}} |\Psi\rangle = -\partial_t \Delta\varepsilon |\Psi\rangle, \tag{2.12}$$

with

$$\boldsymbol{\mathcal{E}} = \begin{pmatrix} \varepsilon & 0 \\ 0 & \mu \end{pmatrix}; \quad \boldsymbol{\mathcal{P}} = \begin{bmatrix} 0 & -\hat{\mathbf{z}}\times \\ \hat{\mathbf{z}}\times & 0 \end{bmatrix}; \quad \boldsymbol{\mathcal{D}} = \begin{bmatrix} 0 & -\nabla_{\perp}\times \\ \nabla_{\perp}\times & 0 \end{bmatrix}, \tag{2.13}$$

and $|\Psi\rangle = \begin{bmatrix} \mathbf{E} & \mathbf{H} \end{bmatrix}^T$. Next, we expand

$$|\Psi(x,y,z,t)\rangle = A_1(z,t)|\Psi_1(x,y)\rangle e^{i(\beta_1 z - \omega_1 t)} + A_2(z,t)|\Psi_2(x,y)\rangle e^{i(\beta_2 z - \omega_2 t)} + \text{c.c.}, \tag{2.14}$$

where the modal fields $|\Psi_k(x,y)\rangle = \begin{bmatrix} \mathbf{e}_k(x,y), & \mathbf{h}_k(x,y) \end{bmatrix}^T$ must satisfy the modal wave equation

$$-i\omega_k \boldsymbol{\mathcal{E}} |\Psi_k\rangle + i\beta_k \boldsymbol{\mathcal{P}} |\Psi_k\rangle + \boldsymbol{\mathcal{D}} |\Psi_k\rangle = 0, \tag{2.15}$$

Next, we perform an integral over the entire cross-sectional plane with infinitesimal area element $\mathrm{d}A$, using the following definition:

$$\langle \psi | \mathcal{O} | \psi \rangle = \int \mathrm{d}A \; \psi^*(x,y) \mathcal{O} \psi(x,y), \tag{2.16}$$

for some mathematical operator $\mathcal{O}$. This is similar to computing the expected value of an observable quantity in quantum mechanics whose associated operator is $\mathcal{O}$ [127]. Applying this formula to Ψ_k using the operators $\boldsymbol{\mathcal{E}}$ and $\boldsymbol{\mathcal{P}}$ yields

$$\langle \Psi_k | \boldsymbol{\mathcal{E}} | \Psi_k \rangle = \int \mathrm{d}A \begin{bmatrix} \mathbf{e}_k^* & \mathbf{h}_k^* \end{bmatrix} \cdot \begin{pmatrix} \varepsilon & 0 \\ 0 & \mu \end{pmatrix} \begin{bmatrix} \mathbf{e}_k \\ \mathbf{h}_k \end{bmatrix} = \int \mathrm{d}A \mathbf{e}_k^* \cdot (\varepsilon \mathbf{e}_k) + \mathbf{h}_k^* \cdot (\mu \mathbf{h}_k) = E_k,$$

$$\begin{aligned}\langle\Psi_k|\boldsymbol{\mathcal{P}}|\Psi_k\rangle &= \int \mathrm{d}A \begin{bmatrix}\mathbf{e}_k^* & \mathbf{h}_k^*\end{bmatrix} \cdot \begin{bmatrix}0 & -\hat{\mathbf{z}}\times \\ \hat{\mathbf{z}}\times & 0\end{bmatrix} \begin{bmatrix}\mathbf{e}_k \\ \mathbf{h}_k\end{bmatrix} \\ &= \int \mathrm{d}A \mathbf{e}_k^* \cdot (-\hat{\mathbf{z}} \times \mathbf{h}_k) + \mathbf{h}_k^* \cdot (\hat{\mathbf{z}} \times \mathbf{e}_k) \\ &= \int \mathrm{d}A \left[-\hat{\mathbf{z}} \cdot (\mathbf{h}_k \times \mathbf{e}_k^*) + \hat{\mathbf{z}} \cdot (\mathbf{e}_k \times \mathbf{h}_k)\right] \\ &= 2\Re\left(\int \mathrm{d}A (\mathbf{e}_k \times \mathbf{h}_k^*)_z\right) = \mathcal{P}_k.\end{aligned}$$

In other words, E_k is the electromagnetic modal energy and $\mathcal{P}_k$ is the modal power:

$$E_k = \langle\Psi_k|\boldsymbol{\mathcal{E}}|\Psi_k\rangle, \tag{2.17a}$$
$$\mathcal{P}_k = \langle\Psi_k|\boldsymbol{\mathcal{P}}|\Psi_k\rangle. \tag{2.17b}$$

Next, we substitute

$$|\Psi\rangle = A_1 e^{i\phi_1(z,t)}|\Psi_1\rangle + A_2 e^{i\phi_2(z,t)}|\Psi_2\rangle + \text{c.c.},$$

where $\phi_{1,2}(z,t) = \beta_{1,2}z - \omega_{1,2}t$; into equation (2.12), and using the relations

$$\partial_t(A_1 e^{i\phi_1}) = (\partial_t A_1 - i\omega_1 A_1)e^{i\phi_1} = e^{i\phi_1}(\partial_t - i\omega_1)A_1,$$

$$\partial_z(A_1 e^{i\phi_1}) = (\partial_z A_1 + i\beta_1 A_1)e^{i\phi_1} = e^{i\phi_1}(\partial_z + i\beta_1)A_1,$$

and $\boldsymbol{\mathcal{D}}|\Psi_k\rangle = i\omega_k\boldsymbol{\mathcal{E}}|\Psi_k\rangle - i\beta_k\boldsymbol{\mathcal{P}}|\Psi_k\rangle$, we obtain

$$\begin{aligned}&\partial_t\boldsymbol{\mathcal{E}}\left(A_1 e^{i\phi_1}|\Psi_1\rangle + A_2 e^{i\phi_2}|\Psi_2\rangle + \text{c.c.}\right) + \partial_z\boldsymbol{\mathcal{P}}\left(A_1 e^{i\phi_1}|\Psi_1\rangle + A_2 e^{i\phi_2}|\Psi_2\rangle + \text{c.c.}\right) \\ &+ \boldsymbol{\mathcal{D}}\left(A_1 e^{i\phi_1}|\Psi_1\rangle + A_2 e^{i\phi_2}|\Psi_2\rangle + \text{c.c.}\right) = -\partial_t\Delta\boldsymbol{\varepsilon}\left(A_1 e^{i\phi_1}|\Psi_1\rangle + A_2 e^{i\phi_2}|\Psi_2\rangle + \text{c.c.}\right),\end{aligned}$$

which simplifies to

$$\begin{aligned}&e^{i\phi_1}\left(\boldsymbol{\mathcal{E}}\partial_t + \boldsymbol{\mathcal{P}}\partial_z\right)A_1|\Psi_1\rangle + e^{i\phi_2}\left(\boldsymbol{\mathcal{E}}\partial_t + \boldsymbol{\mathcal{P}}\partial_z\right)A_2|\Psi_2\rangle + \text{c.c.} \\ &\qquad = -\partial_t\left[\Delta\boldsymbol{\varepsilon}e^{i\phi_1}A_1|\Psi_1\rangle + \Delta\boldsymbol{\varepsilon}e^{i\phi_2}A_2|\Psi_2\rangle + \text{c.c.}\right],\end{aligned} \tag{2.18}$$

Next, we make an *ansatz* for the elastic field in a manner similar to the method in Appendix B.2:

$$\mathbf{U}(x,y,z,t) = B(z,t)\mathbf{u}(x,y)e^{i(qz-\Omega t)} + \text{c.c.} \tag{2.19}$$

where $\mathbf{u}(x,y)$ is the modal displacement field and $B(z,t)$ is the envelope field in the direction of propagation. For SBS, we assume that the variation in permittivity for the medium $\Delta\varepsilon(x,y,z,t)$ is then linearly related to the displacement field $\mathbf{U}$, and is defined as

$$\Delta\varepsilon(x,y,z,t) = B(z,t)e^{i(qz-\Omega t)}\Delta\varepsilon_\perp(x,y) + \text{c.c.}, \tag{2.20}$$

where the function $\Delta\varepsilon_\perp(x,y)$ gives the change in permittivity of the medium along the cross-section on the $xy-$plane. Here, we set $q = \beta_2 - \beta_1$ and $\Omega = \omega_2 - \omega_1$, and this simplifies the expression to

$$\Delta\varepsilon(x,y,z,t) = B(z,t)e^{i(\phi_2-\phi_1)}\Delta\varepsilon_\perp(x,y) + \text{c.c.} \tag{2.21}$$

Next, we write

$$\partial_t \Delta\varepsilon \left(A_1 e^{i\phi_1}|\Psi_1\rangle + A_2 e^{i\phi_2}|\Psi_2\rangle + \text{c.c.} \right) = \partial_t \Big[\left(B e^{i(\phi_2-\phi_1)} \Delta\varepsilon_\perp + B^* e^{i(\phi_1-\phi_2)} \Delta\varepsilon_\perp^* \right) \times \left(A_1|\Psi_1\rangle e^{i\phi_1} + A_1^*|\Psi_1\rangle^* e^{-i\phi_1} + A_2|\Psi_2\rangle e^{i\phi_2} + A_2^*|\Psi_2\rangle^* e^{-i\phi_2} \right) \Big]$$

The right-hand side of (2.18) then becomes

$$\begin{aligned} \text{RHS} &= -\partial_t \left[e^{i\phi_1} B^* \Delta\varepsilon_\perp^* A_2|\Psi_2\rangle + e^{i\phi_2} B \Delta\varepsilon_\perp A_1|\Psi_1\rangle \right] \\ &= -e^{i\phi_1} \left(\partial_t B^* A_2 \Delta\varepsilon_\perp^*|\Psi_2\rangle + B^* \partial_t A_2 \Delta\varepsilon_\perp^*|\Psi_2\rangle - i\omega_1 B^* \Delta\varepsilon_\perp^* A_2|\Psi_2\rangle \right) \\ &\quad - e^{i\phi_2} \left(\partial_t B A_1 \Delta\varepsilon_\perp|\Psi_1\rangle + B \partial_t A_1 \Delta\varepsilon_\perp|\Psi_1\rangle - i\omega_2 B \Delta\varepsilon_\perp A_1|\Psi_1\rangle \right), \end{aligned}$$

In SBS experiments, the width of the field's envelope is generally a few orders of magnitude longer than the optical carrier frequencies [44]. This means that only those terms in Eq. (2.18) which are multiples of these carrier frequencies will contribute significantly to this expression. In other words, we apply what is known as the slowly-varying envelope approximation (SVEA) [128]:

$$\begin{aligned} \partial_t B^* A_2 \Delta\varepsilon_\perp^*|\Psi_2\rangle + B^* \partial_t A_2 \Delta\varepsilon_\perp^*|\Psi_2\rangle &\ll i\omega_1 B^* \Delta\varepsilon_\perp^* A_2|\Psi_2\rangle, \\ \partial_t B A_1 \Delta\varepsilon_\perp|\Psi_1\rangle + B \partial_t A_1 \Delta\varepsilon_\perp|\Psi_2\rangle &\ll i\omega_2 B \Delta\varepsilon_\perp A_1|\Psi_1\rangle, \end{aligned}$$

which in turn allows us to write the approximate expression

$$\text{RHS} \approx i\omega_1 e^{i\phi_1} B^* \Delta\varepsilon_\perp^* A_2|\Psi_2\rangle + i\omega_2 e^{i\phi_2} B \Delta\varepsilon_\perp A_1|\Psi_1\rangle. \tag{2.22}$$

At this stage, we can now equate terms containing the same phase on the left-hand side and right-hand sides of (2.18), namely $e^{i\phi_1}$ or $e^{i\phi_2}$, which leads to

$$\begin{aligned} e^{i\phi_1} \left(\boldsymbol{\mathcal{E}} \partial_t + \boldsymbol{\mathcal{P}} \partial_z \right) A_1|\Psi_1\rangle + \text{c.c.} &= i\omega_1 e^{i\phi_1} B^* \Delta\varepsilon_\perp^* A_2|\Psi_2\rangle + \text{c.c.}, \\ e^{i\phi_2} \left(\boldsymbol{\mathcal{E}} \partial_t + \boldsymbol{\mathcal{P}} \partial_z \right) A_2|\Psi_2\rangle + \text{c.c.} &= i\omega_2 e^{i\phi_2} B \Delta\varepsilon_\perp A_1|\Psi_1\rangle + \text{c.c.} \end{aligned}$$

Multiplying each equation by either $e^{-i\phi_1}$ or $e^{-i\phi_2}$ respectively, we can now neglect the complex conjugate terms by using the rotating-wave approximation (RWA) [129]: effectively, oscillatory terms such as $e^{-2\phi_{1,2}}$ vary considerably faster than $e^{i(0)}$, so we write:

$$e^{i\phi_1} \left(\boldsymbol{\mathcal{E}} \partial_t + \boldsymbol{\mathcal{P}} \partial_z \right) A_1|\Psi_1\rangle = i\omega_1 e^{i\phi_1} B^* \Delta\varepsilon_\perp^* A_2|\Psi_2\rangle \tag{2.23}$$

$$e^{i\phi_2} \left(\boldsymbol{\mathcal{E}} \partial_t + \boldsymbol{\mathcal{P}} \partial_z \right) A_2|\Psi_2\rangle = i\omega_2 e^{i\phi_2} B \Delta\varepsilon_\perp A_1|\Psi_1\rangle. \tag{2.24}$$

The next step in our derivation consists of multiplying (2.23) by $\langle\Psi_1|$ and (2.24) by $\langle\Psi_2|$, and applying the results from earlier $\langle\Psi_k|\boldsymbol{\mathcal{E}}|\Psi_k\rangle = E_k$ and $\langle\Psi_k|\boldsymbol{\mathcal{P}}|\Psi_k\rangle = \mathcal{P}_k$ we obtain the following pair of equations:

$$\left(E_1 \partial_t + \mathcal{P}_1 \partial_z \right) A_1 = i\omega_1 \langle\Psi_1|\Delta\varepsilon_\perp^*|\Psi_2\rangle B^* A_2, \tag{2.25}$$

$$\left(E_2 \partial_t + \mathcal{P}_2 \partial_z \right) A_2 = i\omega_2 \langle\Psi_2|\Delta\varepsilon_\perp|\Psi_1\rangle B A_1. \tag{2.26}$$

Finally, we can define the inner product terms on the right as coupling constants $\tilde{Q}_1$ and $\tilde{Q}_2$:

$$\langle \Psi_1 | \Delta\varepsilon_\perp^* | \Psi_2 \rangle = \int \mathrm{d}A \begin{bmatrix} \mathbf{e}_1^* & \mathbf{h}_1^* \end{bmatrix} \cdot \begin{bmatrix} \Delta\varepsilon_\perp^* : & 0 \\ 0 & 0 \end{bmatrix} \begin{bmatrix} \mathbf{e}_2 \\ \mathbf{h}_2 \end{bmatrix} = \int \mathrm{d}A \mathbf{e}_1^* \cdot (\Delta\varepsilon_\perp^* : \mathbf{e}_2) = \tilde{Q}_1, \tag{2.27a}$$

$$\langle \Psi_2 | \Delta\varepsilon_\perp | \Psi_1 \rangle = \int \mathrm{d}A \begin{bmatrix} \mathbf{e}_2^* & \mathbf{h}_2^* \end{bmatrix} \cdot \begin{bmatrix} \Delta\varepsilon_\perp : & 0 \\ 0 & 0 \end{bmatrix} \begin{bmatrix} \mathbf{e}_1 \\ \mathbf{h}_1 \end{bmatrix} = \int \mathrm{d}A \mathbf{e}_2^* \cdot (\Delta\varepsilon_\perp : \mathbf{e}_1) = \tilde{Q}_2, \tag{2.27b}$$

where : denotes the double-contraction operator (also known as the double dot-product) of two tensors $\mathbf{T} : \mathbf{U} = T_{ij}U_{ji}$. This then leads to the coupled optical equations in SBS

$$\frac{\partial A_1}{\partial z} + \frac{E_1}{\mathcal{P}_1}\frac{\partial A_1}{\partial t} = \frac{i\omega_1 \tilde{Q}_1}{\mathcal{P}_1} B^* A_2, \tag{2.28a}$$

$$\frac{\partial A_2}{\partial z} + \frac{E_2}{\mathcal{P}_2}\frac{\partial A_2}{\partial t} = \frac{i\omega_2 \tilde{Q}_2}{\mathcal{P}_2} B A_1. \tag{2.28b}$$

2.3 Elastodynamic equation

Having derived (2.28a) and (2.28b) for the optical envelope fields A_1 and A_2 respectively, we are now required to find an equation for the acoustic envelope field B so we can solve for the other two. This can be done by establishing a relation between the displacement field $\mathbf{U}(x,y,z,t)$ (or alternatively the velocity field $\mathbf{V}(x,y,z,t) = \partial_t \mathbf{U}(x,y,z,t)$) and the coupling of the two optical fields $\mathbf{E}_1$ and $\mathbf{E}_2$ via electrostriction. We shall begin with the general elastodynamic equation:

$$\rho \frac{\partial \mathbf{V}}{\partial t} = \nabla \cdot \mathbf{T} + \mathbf{f}, \tag{2.29}$$

where ρ is the medium's density, $\mathbf{V}$ is the velocity field of the continuous medium, $\mathbf{T}$ is the stress tensor and is the sum of all external applied force densities. This equation is complemented by the constitutive relation:

$$\mathbf{S} : \frac{\partial \mathbf{T}}{\partial t} = \nabla_s \mathbf{V} + \mathbf{S} : \boldsymbol{\eta} : \frac{\partial}{\partial t} \nabla_s \mathbf{V}. \tag{2.30}$$

where $\mathbf{S}$ is the compliance tensor and $\boldsymbol{\eta}$ is the viscosity tensor (see Appendix B for derivation and details). Here the Nabla operator follows the Voigt convention outlined in (B.10)

$$\nabla \cdot = \nabla_\perp \cdot + \partial_z \hat{\mathbf{z}} \cdot = \begin{bmatrix} \partial_x & 0 & 0 & 0 & 0 & \partial_y \\ 0 & \partial_y & 0 & 0 & 0 & \partial_x \\ 0 & 0 & 0 & \partial_y & \partial_x & 0 \end{bmatrix} + \begin{bmatrix} 0 & 0 & 0 & 0 & \partial_z & 0 \\ 0 & 0 & 0 & \partial_z & 0 & 0 \\ 0 & 0 & \partial_z & 0 & 0 & 0 \end{bmatrix}, \tag{2.31}$$

$$\nabla_s = \nabla_{s,\perp} + \partial_z \hat{\mathbf{z}} = \begin{bmatrix} \partial_x & 0 & 0 \\ 0 & \partial_y & 0 \\ 0 & 0 & 0 \\ 0 & 0 & \partial_y \\ 0 & 0 & \partial_x \\ \partial_y & \partial_x & 0 \end{bmatrix} + \begin{bmatrix} 0 & 0 & 0 \\ 0 & 0 & 0 \\ 0 & 0 & \partial_z \\ 0 & \partial_z & 0 \\ \partial_z & 0 & 0 \\ 0 & 0 & 0 \end{bmatrix}. \tag{2.32}$$

Next, we assume that the compliance tensor $\mathbf{S}$ and viscosity tensor $\boldsymbol{\eta}$ are constant in time, which leads to the matrix equation

$$\frac{\partial}{\partial t}\begin{bmatrix}\mathbf{S}: & 0\\ 0 & \rho\end{bmatrix}\begin{bmatrix}\mathbf{T}\\ \mathbf{V}\end{bmatrix}+\frac{\partial}{\partial z}\begin{bmatrix}0 & -\hat{\mathbf{z}}\\ -\hat{\mathbf{z}}\cdot & 0\end{bmatrix}\begin{bmatrix}\mathbf{T}\\ \mathbf{V}\end{bmatrix}+\begin{bmatrix}0 & -\nabla_{s,\perp}\\ \nabla_{s,\perp}\cdot & 0\end{bmatrix}\begin{bmatrix}\mathbf{T}\\ \mathbf{V}\end{bmatrix} + \begin{bmatrix}0 & -\mathbf{S}:\boldsymbol{\eta}:\frac{\partial}{\partial t}\nabla_s\\ 0 & 0\end{bmatrix}\begin{bmatrix}\mathbf{T}\\ \mathbf{V}\end{bmatrix}=\begin{bmatrix}0\\ \mathbf{f}\end{bmatrix}. \tag{2.33}$$

We can further simplify the equation by making use of the following notation

$$\partial_t\boldsymbol{\mathcal{E}}|\boldsymbol{\Phi}\rangle+\partial_z\boldsymbol{\mathcal{P}}|\boldsymbol{\Phi}\rangle+\boldsymbol{\mathcal{D}}|\boldsymbol{\Phi}\rangle+\mathbf{Y}|\boldsymbol{\Phi}\rangle=|\mathbf{F}\rangle, \tag{2.34}$$

with

$$\boldsymbol{\mathcal{E}}=\begin{bmatrix}\mathbf{S}: & 0\\ 0 & \rho\end{bmatrix};\quad \boldsymbol{\mathcal{P}}=\begin{bmatrix}0 & -\hat{\mathbf{z}}\\ -\hat{\mathbf{z}}\cdot & 0\end{bmatrix};\quad \boldsymbol{\mathcal{D}}=\begin{bmatrix}0 & -\nabla_{s,\perp}\\ \nabla_{s,\perp}\cdot & 0\end{bmatrix};\quad \mathbf{Y}=\begin{bmatrix}0 & -\mathbf{S}:\boldsymbol{\eta}:\frac{\partial}{\partial t}\nabla_s\\ 0 & 0\end{bmatrix}, \tag{2.35}$$

$$|\boldsymbol{\Phi}\rangle=\begin{bmatrix}\mathbf{T}\\ \mathbf{V}\end{bmatrix};\quad |\mathbf{F}\rangle=\begin{bmatrix}0\\ \mathbf{f}\end{bmatrix}. \tag{2.36}$$

We now introduce the ansatz

$$|\boldsymbol{\Phi}\rangle=B(z,t)|\boldsymbol{\phi}(x,y)\rangle e^{i(qz-\Omega t)}+\text{c.c.}, \tag{2.37}$$

where $|\boldsymbol{\phi}(x,y)\rangle=\left[\mathbf{t}(x,y),\ \mathbf{v}(x,y)\right]^T$, leading to the equation

$$\left(\partial_t B-i\Omega B\right)e^{i\theta}\boldsymbol{\mathcal{E}}|\boldsymbol{\phi}\rangle+\left(\partial_z+iq\right)Be^{i\theta}\boldsymbol{\mathcal{P}}|\boldsymbol{\phi}\rangle+Be^{i\theta}\boldsymbol{\mathcal{D}}|\boldsymbol{\phi}\rangle+Be^{i\theta}\mathbf{Y}|\boldsymbol{\phi}\rangle+\text{c.c.}=|\mathbf{F}\rangle, \tag{2.38}$$

where $\theta=qz-\Omega t$. In the absence of sources and damping forces, the modal field $|\boldsymbol{\phi}(x,y)\rangle$ must satisfy the modal wave equation

$$-i\Omega\boldsymbol{\mathcal{E}}|\boldsymbol{\phi}\rangle+iq\boldsymbol{\mathcal{P}}|\boldsymbol{\phi}\rangle+\boldsymbol{\mathcal{D}}|\boldsymbol{\phi}\rangle=0, \tag{2.39}$$

so making use of this in equation (2.38) yields

$$e^{i\theta}\left(\partial_t\boldsymbol{\mathcal{E}}B|\boldsymbol{\phi}\rangle+\partial_z B\boldsymbol{\mathcal{P}}|\boldsymbol{\phi}\rangle\right)+\mathbf{Y}\left(B|\boldsymbol{\phi}\rangle e^{i\theta}\right)=|\mathbf{F}\rangle. \tag{2.40}$$

We will now use this equation to find values for $\langle\boldsymbol{\phi}|\boldsymbol{\mathcal{E}}|\boldsymbol{\phi}\rangle$ and $\langle\boldsymbol{\phi}|\boldsymbol{\mathcal{P}}|\boldsymbol{\phi}\rangle$, in a similar way to the electromagnetic case. First, we take

$$\begin{aligned}\langle\boldsymbol{\phi}|\boldsymbol{\mathcal{E}}|\boldsymbol{\phi}\rangle&=\int\begin{bmatrix}\mathbf{t}^* & \mathbf{v}^*\end{bmatrix}:\begin{bmatrix}\mathbf{S}: & 0\\ 0 & 0\end{bmatrix}\begin{bmatrix}\mathbf{t}\\ \mathbf{v}\end{bmatrix}\mathrm{d}A=\int\begin{bmatrix}\mathbf{t}^* & \mathbf{v}^*\end{bmatrix}:\begin{bmatrix}\mathbf{S}:\mathbf{t}\\ \rho\mathbf{v}\end{bmatrix}\mathrm{d}A\\ &=\int\left[\mathbf{t}^*\cdot(\mathbf{S}:\mathbf{t})+\rho||\mathbf{v}||^2\right]\mathrm{d}A=\int\left(\epsilon:\mathbf{t}^*+\rho||\mathbf{v}||^2\right)\mathrm{d}A=E_a,\end{aligned}$$

where $\rho(x,y)$ denotes the density of the medium across the transverse plane and E_a is the acoustic mode energy:

$$E_a=\langle\boldsymbol{\phi}|\boldsymbol{\mathcal{E}}|\boldsymbol{\phi}\rangle. \tag{2.41}$$

Similarly

$$\begin{aligned}\langle\phi|\boldsymbol{\mathcal{P}}|\phi\rangle &= \int \begin{bmatrix}\mathbf{t}^* & \mathbf{v}^*\end{bmatrix} : \begin{bmatrix}0 & -\hat{\mathbf{z}} \\ -\hat{\mathbf{z}}\cdot & 0\end{bmatrix}\begin{bmatrix}\mathbf{t} \\ \mathbf{v}\end{bmatrix} \mathrm{d}A = \int \begin{bmatrix}\mathbf{t}^* & \mathbf{v}^*\end{bmatrix} : \begin{bmatrix}-\hat{\mathbf{z}}\mathbf{v} \\ -\hat{\mathbf{z}}\cdot\mathbf{t}\end{bmatrix} \mathrm{d}A \\ &= \int \left[\mathbf{t}^* : (-\hat{\mathbf{z}}\mathbf{v}) + \mathbf{v}^*\cdot(-\hat{\mathbf{z}}\cdot\mathbf{t})\right]\mathrm{d}A = \int \left((-\mathbf{v}\cdot\mathbf{t}^*)\cdot\hat{\mathbf{z}} + \hat{\mathbf{z}}\cdot(-\mathbf{t}\cdot\mathbf{v}^*)\right)\mathrm{d}A \\ &= 2\Re\left(-\int \mathbf{v}\cdot\mathbf{t}^*\mathrm{d}A\right) = \mathcal{P}_a,\end{aligned}$$

which is the average power per acoustic cycle:

$$\mathcal{P}_a = \langle\phi|\boldsymbol{\mathcal{P}}|\phi\rangle. \tag{2.42}$$

Now, expanding the $\mathbf{Y}$ matrix as

$$\mathbf{Y} = \partial_t\left(\mathbf{Y}_\perp + \partial_z\mathbf{Y}_z\right) = \frac{\partial}{\partial t}\left(\begin{bmatrix}0 & \mathbf{S}:\boldsymbol{\eta}:\nabla_\perp \\ 0 & 0\end{bmatrix} + \partial_z\begin{bmatrix}0 & \mathbf{S}:\boldsymbol{\eta}:\hat{\mathbf{z}} \\ 0 & 0\end{bmatrix}\right), \tag{2.43}$$

results in

$$\begin{aligned}\mathbf{Y}Be^{i\theta}|\phi\rangle &= \partial_t\left(\mathbf{Y}_\perp + \partial_z\mathbf{Y}_z\right)Be^{i\theta}|\phi\rangle \\ &= \partial_t(Be^{i\theta})\mathbf{Y}_\perp|\phi\rangle + \partial_t\partial_z(Be^{i\phi})\mathbf{Y}_z|\phi\rangle \\ &= e^{i\theta}\left[(\partial_t - i\Omega)B\mathbf{Y}_\perp|\phi\rangle + \partial_z\left(\partial_t - i\Omega\right)\mathbf{Y}_z|\phi\rangle\right],\end{aligned}$$

and using the fact that Ω is generally very large in the context of the optical time-scales (e.g. Ω^{-1} is of the order of nanoseconds while ω^{-1} is of the order of picoseconds) [44, 69], we neglect the time-derivatives such that

$$\mathbf{Y}Be^{i\theta}|\phi\rangle = -i\Omega Be^{i\theta}\mathbf{Y}_\perp|\phi\rangle - i\Omega\left(\partial_z + iq\right)Be^{i\theta}\mathbf{Y}_z|\phi\rangle.$$

Using a similar argument for q, we neglect ∂_z to obtain

$$\mathbf{Y}Be^{i\theta}|\phi\rangle = -i\Omega\left(\mathbf{Y}_\perp + iq\mathbf{Y}_z\right)|\phi\rangle Be^{i\theta}. \tag{2.44}$$

It follows that

$$\langle\phi|\mathbf{Y}Be^{i\theta}|\phi\rangle = -i\Omega B\langle\phi|\mathbf{Y}_\perp + iq\mathbf{Y}_z|\phi\rangle = \mathcal{A}B, \tag{2.45}$$

where the constant $\mathcal{A}$ is an acoustic power loss quantity that arises from the material's viscosity and stiffness (e.g. it is proportional to the damping of the medium), and is defined in terms of the modal fields $\mathrm{t}(x,y)$ and $\mathbf{v}(x,y)$ as

$$\mathcal{A} = -i\Omega\langle\phi|\mathbf{Y}_\perp + iq\mathbf{Y}_z|\phi\rangle = -i\Omega\int \mathrm{d}A\begin{bmatrix}\mathbf{t}^* & \mathbf{v}^*\end{bmatrix}\left(\mathbf{Y}_\perp + iq\mathbf{Y}_z\right)\begin{bmatrix}\mathbf{t} \\ \mathbf{v}\end{bmatrix}. \tag{2.46}$$

Combining all the above results, and using a rotating-wave approximation to eliminate complex conjugate terms, we obtain

$$E_a\partial_t B + \mathcal{P}_a\partial_z B + \mathcal{A}B = \langle\phi|\mathbf{F}\rangle e^{-i\theta}. \tag{2.47}$$

2.3.1 External forces and noise

Now, we must specify the force $|\mathbf{F}\rangle$ explicitly. First, we shall define a force density in the form of a linear multiplicative coupling between the optical fields as

$$\mathbf{f} = \mathbf{f}_{\text{electrostriction}} + \mathbf{f}_{\text{thermal}}, \tag{2.48}$$

where $\mathbf{f}_{\text{electrostriction}}$ comes from the electrostrictive force coupling between the two optical fields, namely

$$\mathbf{f}_{\text{electrostriction}} = \mathbf{c}(x,y)A_1^*(z,t)A_2(z,t)e^{i(qz-\Omega t)} + \text{c.c.}, \tag{2.49}$$

for an arbitrary modal function $\mathbf{c}(x,y)$, and $\mathbf{f}_{\text{thermal}}$ comes from the background thermal noise in the waveguide,

$$\mathbf{f}_{\text{thermal}} = \rho\sqrt{\tilde{\sigma}}R(z,t)e^{i(qz-\Omega t)}\mathbf{v}(x,y) + \text{c.c.}, \tag{2.50}$$

where $R(z,t)$ is a complex-valued stochastic field that describes the fluctuations in space-time of the thermal acoustic background and has units of $\text{m}^{-1/2}\text{s}^{-1/2}$, while $\rho(x,y)$ is the equilibrium density of the medium with respect to the $xy-$plane. The parameter $\tilde{\sigma}$ is related to the strength of the noise. Next, we write

$$\begin{aligned}\langle\phi|\mathbf{F}\rangle e^{-i\theta} &= \int \begin{bmatrix}\mathbf{t}^* & \mathbf{v}^*\end{bmatrix}\begin{bmatrix}0\\ \mathbf{f}\end{bmatrix} e^{-i\theta}\mathrm{d}A \\ &= A_1^*(z,t)A_2(z,t)\int \mathbf{v}^*(x,y)\cdot\mathbf{c}(x,y)\mathrm{d}A + \rho\sqrt{\tilde{\sigma}}R(z,t)\int|\mathbf{v}(x,y)|^2\mathrm{d}A \\ &= i\Omega\tilde{Q}_a A_1^* A_2 + i\Omega\tilde{Q}_R\sqrt{\tilde{\sigma}}R,\end{aligned}$$

with

$$\tilde{Q}_a = -\frac{i}{\Omega}\int \mathbf{v}^*(x,y)\cdot\mathbf{c}(x,y)\mathrm{d}A; \quad \tilde{Q}_R = -\frac{i}{\Omega}\int\rho|\mathbf{v}(x,y)|^2\mathrm{d}A. \tag{2.51}$$

In backwards SBS, we can set

$$\tilde{Q}_a = \frac{\tilde{Q}_1 + \tilde{Q}_2^*}{2}, \tag{2.52}$$

by using a thermodynamic argument [76]. The factor $\tilde{Q}_R$ has been chosen to match the modal energy of the acoustic field via

$$\tilde{Q}_R = -\frac{i}{\Omega}\int\rho|\mathbf{v}(x,y)|^2\mathrm{d}A = -i\frac{E_a}{\Omega}. \tag{2.53}$$

Therefore, the elastodynamic equation now yields the slowly-varying envelope acoustic wave equation

$$\frac{\partial B}{\partial z} + \frac{E_a}{\mathcal{P}_a}\frac{\partial B}{\partial t} + \frac{\mathcal{A}}{\mathcal{P}_a}B = \frac{i\Omega\tilde{Q}_a}{\mathcal{P}_a}A_1^*A_2 + \frac{i\Omega\tilde{Q}_R\sqrt{\tilde{\sigma}}}{\mathcal{P}_a}R(z,t). \tag{2.54}$$

Therefore, we arrive at the coupled SBS equations for the three-wave interaction

$$\frac{\partial A_1}{\partial z} + \frac{E_1}{\mathcal{P}_1}\frac{\partial A_1}{\partial t} = \frac{i\omega_1 \tilde{Q}_1}{\mathcal{P}_1} B^* A_2, \tag{2.55a}$$

$$\frac{\partial A_2}{\partial z} + \frac{E_2}{\mathcal{P}_2}\frac{\partial A_2}{\partial t} = \frac{i\omega_2 \tilde{Q}_2}{\mathcal{P}_2} B A_1, \tag{2.55b}$$

$$\frac{\partial B}{\partial z} + \frac{E_a}{\mathcal{P}_a}\frac{\partial B}{\partial t} + \frac{\mathcal{A}}{\mathcal{P}_a} B = \frac{i\Omega \tilde{Q}_a}{\mathcal{P}_a} A_1^* A_2 + \frac{i\Omega \tilde{Q}_R \sqrt{\tilde{\sigma}}}{\mathcal{P}_a} R(z,t). \tag{2.55c}$$

However, it is important to note that the relationship $\mathcal{P}_i = E_i v_i$ holds for all three waves, which leads to the simplified equations

$$\frac{\partial A_1}{\partial z} + \frac{1}{v_1}\frac{\partial A_1}{\partial t} = \frac{i\omega_1 \tilde{Q}_1}{\mathcal{P}_1} B^* A_2, \tag{2.56a}$$

$$\frac{\partial A_2}{\partial z} + \frac{1}{v_2}\frac{\partial A_2}{\partial t} = \frac{i\omega_2 \tilde{Q}_2}{\mathcal{P}_2} B A_1, \tag{2.56b}$$

$$\frac{\partial B}{\partial z} + \frac{1}{v_a}\frac{\partial B}{\partial t} + \frac{1}{2}\alpha_{\mathrm{ac}} B = \frac{i\Omega \tilde{Q}_a}{\mathcal{P}_a} A_1^* A_2 + \frac{i\Omega \tilde{Q}_R \sqrt{\tilde{\sigma}}}{\mathcal{P}_a} R(z,t), \tag{2.56c}$$

where $\alpha_{\mathrm{ac}} = 2\mathcal{A}/\mathcal{P}_a$ is the acoustic loss coefficient (in units of m^{-1}). This is related to the acoustic decay rate $\Gamma = v_a \alpha_{\mathrm{ac}} = 2\pi\Delta\nu_B$, where $\Delta\nu_B$ is the Brillouin linewidth and $\tau_a = 1/\Gamma$ is the acoustic lifetime of the phonons. The SBS equations presented above can be extended to include the effect of optical loss $\alpha_{1,2}$ by adding a linear term to the optical envelope field equations, such that

$$\frac{\partial A_1}{\partial z} + \frac{1}{v_1}\frac{\partial A_1}{\partial t} + \frac{1}{2}\alpha_1 A_1 = \frac{i\omega_1 \tilde{Q}_1}{\mathcal{P}_1} B^* A_2, \tag{2.57a}$$

$$\frac{\partial A_2}{\partial z} + \frac{1}{v_2}\frac{\partial A_2}{\partial t} + \frac{1}{2}\alpha_2 A_2 = \frac{i\omega_2 \tilde{Q}_2}{\mathcal{P}_2} B A_1, \tag{2.57b}$$

$$\frac{\partial B}{\partial z} + \frac{1}{v_a}\frac{\partial B}{\partial t} + \frac{1}{2}\alpha_{\mathrm{ac}} B = \frac{i\Omega \tilde{Q}_a}{\mathcal{P}_a} A_1^* A_2 + \frac{i\Omega \tilde{Q}_R \sqrt{\tilde{\sigma}}}{\mathcal{P}_a} R(z,t). \tag{2.57c}$$

It should be noted that these SBS coupled equations are valid for single-mode cases, since it is possible to select the acoustic mode by tuning the input laser frequencies [130]. This model can further be extended by including additional acoustic fields with their own opto-acoustic coupling constants and potentially different noise properties [131].

2.4 Backward SBS equations

In the case of backward SBS, we can make further simplifications to the underlying equations by noting that $v_2 = -v_1$ and $\alpha_2 = -\alpha_1$, and letting $v_1 = v$ and $\alpha_1 = \alpha$ we write

$$\frac{\partial A_1}{\partial z} + \frac{1}{v}\frac{\partial A_1}{\partial t} + \frac{1}{2}\alpha A_1 = \frac{i\omega_1 \tilde{Q}_1}{\mathcal{P}_1} B^* A_2, \tag{2.58a}$$

$$\frac{\partial A_2}{\partial z} - \frac{1}{v}\frac{\partial A_2}{\partial t} - \frac{1}{2}\alpha A_2 = \frac{i\omega_2 \tilde{Q}_2}{\mathcal{P}_2} B A_1, \tag{2.58b}$$

$$\frac{\partial B}{\partial z} + \frac{1}{v_a}\frac{\partial B}{\partial t} + \frac{1}{2}\alpha_{\mathrm{ac}} B = \frac{i\Omega \tilde{Q}_a}{\mathcal{P}_a} A_1^* A_2 + \frac{i\Omega \tilde{Q}_R \sqrt{\tilde{\sigma}}}{\mathcal{P}_a} R(z,t). \tag{2.58c}$$

A further simplification to eliminate the modal powers $\mathcal{P}_{1,2,a}$ consists of defining a new set of envelope fields $a_{1,2} = \sqrt{\mathcal{P}_{1,2}}A_{1,2}$ and $b = \sqrt{\mathcal{P}_a}B$, all of which have units of $\sqrt{\text{Watts}}$ such that the total field powers are given by $P_{1,2}(z,t) = |a_1(z,t)|^2$ and $P_a(z,t) = |b(z,t)|^2$. This leads to the new set of coupled SBS equations

$$\begin{aligned}
\frac{\partial a_1}{\partial z} + \frac{1}{v}\frac{\partial a_1}{\partial t} + \frac{1}{2}\alpha a_1 &= \frac{i\omega_1\tilde{Q}_1}{\sqrt{\mathcal{P}_1\mathcal{P}_2\mathcal{P}_a}}a_2 b^*, \\
\frac{\partial a_2}{\partial z} - \frac{1}{v}\frac{\partial a_2}{\partial t} - \frac{1}{2}\alpha a_2 &= \frac{i\omega_2\tilde{Q}_2}{\sqrt{\mathcal{P}_1\mathcal{P}_2\mathcal{P}_a}}a_1 b, \\
\frac{\partial b}{\partial z} + \frac{1}{v_a}\frac{\partial b}{\partial t} + \frac{1}{2}\alpha_{\text{ac}} b &= \frac{i\Omega\tilde{Q}_a}{\sqrt{\mathcal{P}_1\mathcal{P}_2\mathcal{P}_a}}a_1^* a_2 + \frac{i\Omega\tilde{Q}_R\sqrt{\tilde{\sigma}}}{\sqrt{\mathcal{P}_a}}R(z,t),
\end{aligned}$$

and making the substitutions $Q_j = \tilde{Q}_j/\sqrt{\mathcal{P}_1\mathcal{P}_2\mathcal{P}_a}$ and introducing the new constant $\sqrt{\sigma} = i\Omega\tilde{Q}_R\sqrt{\tilde{\sigma}}/\sqrt{\mathcal{P}_a}$ (with units of $\sqrt{\text{J/m}}$) we get

$$\frac{\partial a_1}{\partial z} + \frac{1}{v}\frac{\partial a_1}{\partial t} + \frac{1}{2}\alpha a_1 = i\omega_1 Q_1 a_2 b^*, \tag{2.59a}$$

$$\frac{\partial a_2}{\partial z} - \frac{1}{v}\frac{\partial a_2}{\partial t} - \frac{1}{2}\alpha a_2 = i\omega_2 Q_2 a_1 b, \tag{2.59b}$$

$$\frac{\partial b}{\partial z} + \frac{1}{v_a}\frac{\partial b}{\partial t} + \frac{1}{2}\alpha_{\text{ac}} b = i\Omega Q_a a_1^* a_2 + \sqrt{\sigma}R(z,t). \tag{2.59c}$$

The coupling constants $Q_{1,2,a}$ are computed by finding the EM and acoustic modal fields for the desired waveguide geometry and material. The norm squared of these complex-valued quantities is defined as

$$|Q_j|^2 = \frac{1}{2v^2 v_a \rho_0 \Omega^2}\frac{1}{\left(A_{\text{eff}}^{\text{oa}}\right)^2}, \tag{2.60}$$

where $A_{\text{eff}}^{\text{oa}}$ is the opto-acoustic effective area, expressed as

$$\frac{1}{\left(A_{\text{eff}}^{\text{oa}}\right)^2} = \frac{\left|\int \mathbf{e}_1 \cdot (\Delta\varepsilon(x,y)\mathbf{e}_2)\,\mathrm{d}A\right|^2}{\int \varepsilon||\mathbf{e}_1||^2\mathrm{d}A \int \varepsilon||\mathbf{e}_2||^2\mathrm{d}A \int \frac{\rho}{\rho_0}||\mathbf{u}||^2\mathrm{d}A}, \tag{2.61}$$

where $\rho(x,y)$ is the density deviation of the medium in the transverse plane from its equilibrium density ρ_0, $\Delta\varepsilon(x,y)$ is the change in permittivity tensor and ε is the equilibrium permittivity of the medium. The integration here is done across all of the transverse space in (x,y). From conservation of energy [76], we can relate the three constants as follows: $Q_1 = -Q_2^*$ and $Q_a = Q_2^*$. The quantity $\Delta\varepsilon(x,y)$ is defined implicitly in terms of the displacement mode $\mathbf{u}(x,y)$ (which may be computed from $\mathbf{v}(x,y)$) as

$$\Delta(\varepsilon(x,y)^{-1}) = \mathbf{p} : \nabla_s \mathbf{u}. \tag{2.62}$$

where $\mathbf{p}$ is the photoelasticity tensor. Under symmetric permittivity tensor assumptions, it is possible to write a direct relationship for a relative background permittivity ε_r [76]

$$\Delta(\varepsilon(x,y)) = -\varepsilon_r^2 \mathbf{p} : \nabla_s \mathbf{u}. \tag{2.63}$$

The computation of the modes can be done analytically only in the simplest of cases, such as a linear isotropic dielectric cylindrical waveguide, and in practice these modes must be computed numerically. There exist different numerical methods for this purpose, for instance in the electromagnetic case one can use a finite difference method

such as [132]. For the acoustic case, one can use an eigenmode equation method as in [133]. The method used in this thesis for computing these field quantities is the finite element method described in [134], which makes use of the open source program NumBAT [135].

2.4.1 Steady-state equations

Although the coupling constants $Q_{1,2,a}$ can be computed explicitly by using a numerical solver for the modal fields as described previously, it is often useful to relate these quantities to a parameter which can be computed directly from experimental measurements, such as the SBS gain parameter g_0 (in $\mathrm{m}^{-1}\mathrm{W}^{-1}$) that we introduced in Chapter 1. This can be done by looking at the steady-state form of equations (2.59a)−(2.59c) and neglecting the thermal noise term ($R(z,t) = 0$), so that we can focus purely on the nonlinear interaction between the envelope fields $a_{1,2}$ and b.

To simplify these equations, we first recognize that in nanophotonic waveguides of length in the range of 5−50 cm, the time-scale of the SBS interaction is of the order of a few nanoseconds up to a few hundreds of nanoseconds [44]. Within this time window, the acoustic field only propagates along the waveguide by a few tens or hundreds of microns. This means that the spatial drift of b is negligible in the time-scale of interest, so we can use the approximation $\partial_z b \to 0$ [64, 68]. Then, we eliminate the transient nature of the envelop fields by setting $\partial_t \to 0$ in all three equations, implying we are now operating in the steady-state. This leads to the following approximation for the acoustic field:

$$b(z) \approx \frac{2i\Omega Q_2^*}{\alpha_{\mathrm{ac}}} a_1^*(z) a_2(z), \tag{2.64}$$

which in turn leads to the two optical field equations:

$$\begin{aligned}
\frac{\partial a_1}{\partial z} &= -\frac{1}{2}\alpha a_1 - \frac{2\omega_1 \Omega |Q_2|^2}{\alpha_{\mathrm{ac}}} P_2 a_1, \\
\frac{\partial a_2}{\partial z} &= \frac{1}{2}\alpha a_2 - \frac{2\omega_2 \Omega |Q_2|^2}{\alpha_{\mathrm{ac}}} P_1 a_2.
\end{aligned}$$

The next step is to express the two equations entirely in terms of the field powers $P_1(z) = |a_1(z)|^2$ and $P_2(z) = |a_2(z)|^2$. This is achieved by exploiting the property of complex-valued functions

$$\frac{\partial |f|^2}{\partial z} = \frac{\partial}{\partial z}\left[f f^*\right] = f\frac{\partial f^*}{\partial z} + f^*\frac{\partial f}{\partial z}, \tag{2.65}$$

leading to

$$\begin{aligned}
\frac{\partial P_1}{\partial z} &= -\alpha P_1 - \frac{4\omega_1 \Omega |Q_2|^2}{\alpha_{\mathrm{ac}}} P_1 P_2, \\
\frac{\partial P_2}{\partial z} &= \alpha P_2 - \frac{4\omega_2 \Omega |Q_2|^2}{\alpha_{\mathrm{ac}}} P_1 P_2.
\end{aligned}$$

Finally, we would like to relate these expressions to the SBS gain parameter g_0 in units of $\mathrm{m}^{-1}\mathrm{W}^{-1}$. By using the expression

$$g_0 = \frac{4 v_a \omega_2 \Omega |Q_2|^2}{\Gamma}, \tag{2.66}$$

where $\Gamma = v_a \alpha_{\text{ac}}$ is the acoustic decay rate, and $\omega_1 \approx \omega_2$; we arrive at the steady-state equations in Section 1.2.3

$$\frac{\partial P_1}{\partial z} = -\alpha P_1 - g_0 P_1 P_2,$$
$$\frac{\partial P_2}{\partial z} = \alpha P_2 - g_0 P_1 P_2.$$

The main advantage of expressing $Q_{1,2,a}$ in terms of g_0 as we have done here is that we can now focus on the impact of the overall SBS gain on the optical and acoustic fields, as opposed to having to compute the modal fields explicitly for a particular waveguide. These expressions involving g_0 can in fact be extended to the transient case, as we shall see later in Chapters 4 and 5.

Chapter 3

Noise Mechanisms in Stimulated Brillouin Scattering

3.1 Overview

In the previous Chapter, we discussed how to derive the coupled SBS equations for the pump, Stokes and acoustic envelope fields, or $a_1(z,t)$, $a_2(z,t)$ and $b(z,t)$ respectively. We also introduced a random thermal force density in the form of a complex-valued stochastic process $R(z,t)$, scaled by a thermal noise parameter σ. In this Chapter, we present a mathematical framework for simulating this thermal noise, and relate its strength to the temperature and acoustic losses in the waveguide via the fluctuation-dissipation theorem. We then present a mathematical model for laser phase noise which can be incorporated into the boundary conditions of Eq. (2.59a)−(2.59c), and how it is related to the laser's intrinsic linewidth. The bulk of this work will be used later in Chapters 4−6 to analyse the impact of noise on SBS within different scenarios.

It should be noted that from this Chapter onwards we use the definition of the expectation operator $\langle\cdot\rangle$ as described in Appendix A, where $\langle X(t)\rangle$ represents the ensemble average of a stochastic process $X(t)$ at each point in t over an infinite number of independent realizations, and is related to the probability density function $p(x,t)$ of the random variable $X(t)$ as

$$\langle X(t)\rangle = \int_{-\infty}^{\infty} x(t)p(x,t)\mathrm{d}x. \tag{3.1}$$

3.2 Thermal noise

Thermal fluctuations in an optical waveguide can give rise to small changes in the permittivity of the medium [64, 65, 68], thereby impacting the optical fields that propagate through it by scattering photons spontaneously. We begin our model by defining $R(z,t)$ as a complex-valued normally distributed process with zero mean $\langle R(z,t)\rangle = 0$ and auto-correlation function [64]

$$\langle R(z,t)R^*(z',t')\rangle = \delta(z-z')\delta(t-t'), \tag{3.2}$$

where $\delta(\cdot)$ denotes the Dirac-delta function. This is what is known as white noise, which has a constant spectral density (for more details on white noise and stochastic processes, see Appendix C on Brownian motion). $R(z,t)$ becomes a Brownian motion when integrated with respect to z or t. Next, we note that in Eq. (2.59c):

$$\frac{\partial b}{\partial z} + \frac{1}{v_a}\frac{\partial b}{\partial t} + \frac{1}{2}\alpha_{\mathrm{ac}} b = i\Omega Q_a a_1^* a_2 + \sqrt{\sigma}R(z,t), \tag{3.3}$$

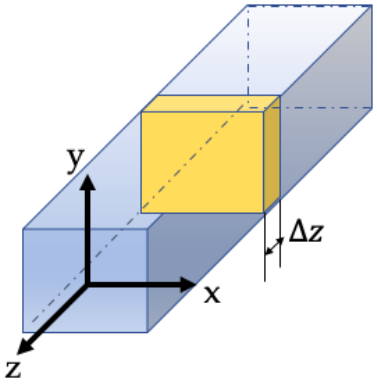

FIGURE 3.1: Illustration of an arbitrary waveguide with a cross-sectional slice of thickness Δz.

the constant parameter σ represents the noise strength of the thermal fluctuations in the waveguide. It is essential that this quantity be related to the waveguide properties, such as temperature and acoustic loss. To derive such a relationship, we first take $\partial_z b \to 0$ as the propagation of the acoustic wave over the optical time-scales is negligible [68] (i.e. in the scale of a few nanoseconds, the acoustic field only propagates over a few micrometers, which is a very small portion of any waveguide longer than a few centimeters). With this simplification, we then consider the acoustic envelope field b_j at a set of discrete positions along the waveguide z_j, separated by a small uniform width Δz, such that $b_j = b(z_j)$ as shown in Fig. 3.1. Then, we define the thermal noise field in each waveguide slice as $\tilde{R}_j$, and we assume it to be statistically independent between any two distinct slices due to the fact that white noise contains the same statistical properties across the waveguide (e.g. zero mean and constant variance). Additionally, we neglect the opto-acoustic coupling (i.e. setting the input laser fields to zero) so that the b_j field is only impacted by the thermal noise.

These simplifications lead to the following equation for the acoustic envelope field in the jth slice in the waveguide:

$$\frac{\mathrm{d}b_j}{\mathrm{d}t} + \frac{1}{2}\Gamma b_j = v_a\sqrt{\sigma_j}\tilde{R}_j(t), \tag{3.4}$$

where $\sigma_j = \sigma/\Delta z$ and $\Gamma = v_a\alpha_{\mathrm{ac}}$. We choose $\tilde{R}_j(t)$ to be complex-valued so that thermal noise introduces both amplitude and phase fluctuations into the acoustic field, which is also complex-valued. In that sense, $\tilde{R}_j(t)$ can be written as a linear combination of two statistically independent real-valued processes $\tilde{R}_j^{(1,2)}(t)$:

$$\tilde{R}_j(t) = \frac{\tilde{R}_j^{(1)}(t) + i\tilde{R}_j^{(2)}(t)}{\sqrt{2}}, \tag{3.5}$$

with the properties

$$\langle\tilde{R}_j(t)\rangle = 0, \quad \langle\tilde{R}_j^{(1)}(t)\tilde{R}_j^{(2)}(t)\rangle = 0, \quad \langle\tilde{R}_j(t)\tilde{R}_j^{*}(t')\rangle = \delta(t-t'). \tag{3.6}$$

It should be noted here that since $\tilde{R}_j(t)$ is only delta-correlated in time, it has units of $s^{-1/2}$, and σ_j has units of J/m^2. Equation (3.4) then has the solution

$$b_j(t) = b_j(0)e^{-\frac{1}{2}\Gamma t} + v_a\sqrt{\sigma_j}\int_0^t e^{-\frac{1}{2}\Gamma(t-t')}\tilde{R}_j(t')\,dt', \tag{3.7}$$

and thus the mean squared amplitude can be found via

$$\langle|b_j(t)|^2\rangle = |b_j(0)|^2e^{-\Gamma t} + v_a^2\sigma_j\int_0^t\int_0^{t'} e^{-\frac{1}{2}\Gamma(2t-t'-t'')}\langle\tilde{R}_j(t')\tilde{R}_j^*(t'')\rangle\,dt''dt', \tag{3.8}$$

and using $\langle\tilde{R}_j(t)\tilde{R}_j^*(t')\rangle = \delta(t-t')$ one finds

$$\begin{aligned}\langle|b_j(t)|^2\rangle &= |b_j(0)|^2e^{-\Gamma t} + v_a^2\sigma_j\int_0^t\int_0^{t'} e^{-\frac{1}{2}\Gamma(2t-t'-t'')}\delta(t'-t'')\,dt''dt' \\ &= |b_j(0)|^2e^{-\Gamma t} + v_a^2\sigma_j\int_0^t e^{-\Gamma(t-t')}\,dt' \\ &= |b_j(0)|^2e^{-\Gamma t} + \frac{v_a\sigma_j}{\alpha_{ac}}\left(1-e^{-\Gamma t}\right),\end{aligned}$$

which in the limit $t\to\infty$ yields the steady-state expression

$$\langle|b_j(t)|^2\rangle_\infty = \frac{v_a\sigma_j}{\alpha_{ac}}. \tag{3.9}$$

This quantity represents the average acoustic power of the noise field. Using the equipartition theorem [136], we note that the total energy of the system can be defined in terms of the quantity k_BT, where k_B is the Boltzmann constant and T is the temperature of the propagation medium. We can then relate the quantity $\langle|b_j(t)|^2\rangle_\infty/v_a$ to the thermal energy per slice Δz as:

$$\frac{1}{v_a}\langle|b_j(t)|^2\rangle_\infty = \frac{\sigma_j}{\alpha_{ac}} = \frac{k_BT}{\Delta z}, \tag{3.10}$$

which then yields

$$\sigma_j = \frac{k_BT\alpha_{ac}}{\Delta z}. \tag{3.11}$$

Then, we obtain the value for σ based on the slice thickness Δz

$$\sigma = \sigma_j\Delta z = k_BT\alpha_{ac}. \tag{3.12}$$

This expression implies that the noise strength is directly proportional to both the temperature and the acoustic loss of the medium, which is consistent with the fluctuation-dissipation theorem [137]. Here, σ plays a similar role to the noise strength defined in the Boyd paper [64] denoted as Q, which is linearly proportional to the waveguide temperature and acoustic phonon decay rate.

3.3 Properties of the thermal acoustic background

Now, we will derive the statistical properties of the thermal acoustic background. Starting with Eq. (3.4), we now turn to $b(z,t)$ in a continuum picture and include the effect

of optical fields (i.e. input laser fields are now back on). This allows us to write

$$\frac{1}{v_a}\frac{\partial b}{\partial t} + \frac{1}{2}\alpha_{\text{ac}} b = i\Omega Q_a a_1^* a_2 + \sqrt{\sigma} R(z,t). \tag{3.13}$$

This equation is then formally integrated in time by using the integrating factor method (or simply using the Green's function associated with the left-hand side operator), which yields the solution

$$b(z,t) = i v_a \Omega Q_a \int_{-\infty}^{t} e^{\frac{1}{2}\Gamma(s-t)} a_1^*(z,s) a_2(z,s) \mathrm{d}s + D(z,t), \tag{3.14}$$

where $D(z,t)$ is

$$D(z,t) = v_a \sqrt{\sigma} \int_{-\infty}^{t} e^{\frac{1}{2}\Gamma(s-t)} R(z,s) \mathrm{d}s. \tag{3.15}$$

Function $D(z,t)$ represents the acoustic field in the absence of optical waves, and thus contains all the statistical properties of the background thermal field. To derive its statistical properties we first note that $R(z,t)$ was previously defined as a normally distributed random process, and since the integrand in (3.15) is deterministic; this means $D(z,t)$ will also be a normally distributed process [138]. The mean value of $D(z,t)$ is found by applying the expectation operator to (3.15). Since $R(z,t)$ has zero mean and the integral is a linear operator, we arrive at the result

$$\langle D(z,t) \rangle = v_a \sqrt{\sigma} \int_{-\infty}^{t} e^{\frac{1}{2}\Gamma(s-t)} \langle R(z,s) \rangle \, \mathrm{d}s = 0. \tag{3.16}$$

The next statistical property of interest is the auto-correlation function at two points in space (z, z') and two points in time (t, t'). To do this, we will make use of the following property of Dirac-delta functions:

$$\int_0^a \int_0^b f(s,s') \delta(s-s') \mathrm{d}s' \mathrm{d}s = \int_0^{\min\{a,b\}} f(s,s) \mathrm{d}s. \tag{3.17}$$

Then, we take the expectation of $D(z,t) D^*(z',t')$:

$$\begin{aligned}
\langle D(z,t) D^*(z',t') \rangle &= v_a^2 \sigma \left\langle \int_{-\infty}^{t} e^{\frac{1}{2}\Gamma(s-t)} R(z,s) \mathrm{d}s \int_{-\infty}^{t'} e^{\frac{1}{2}\Gamma(s-t')} R^*(z',s) \mathrm{d}s \right\rangle \\
&= v_a^2 \sigma \left\langle e^{-\frac{1}{2}\Gamma(t+t')} \int_{-\infty}^{t} e^{\frac{1}{2}\Gamma s} R(z,s) \mathrm{d}s \int_{-\infty}^{t'} e^{\frac{1}{2}\Gamma s} R^*(z',s) \mathrm{d}s \right\rangle \\
&= v_a^2 \sigma e^{-\frac{1}{2}\Gamma(t+t')} \int_{-\infty}^{t} \int_{-\infty}^{t'} e^{\frac{1}{2}\Gamma(s+s')} \langle R(z,s) R(z',s') \rangle \, \mathrm{d}s' \mathrm{d}s \\
&= v_a^2 \sigma e^{-\frac{1}{2}\Gamma(t+t')} \int_{-\infty}^{t} \int_{-\infty}^{t'} e^{\frac{1}{2}\Gamma(s+s')} \delta(z-z') \delta(s-s') \mathrm{d}s' \mathrm{d}s \\
&= v_a^2 \sigma \delta(z-z') e^{-\frac{1}{2}\Gamma(t+t')} \int_{-\infty}^{\min\{t,t'\}} e^{\Gamma s} \mathrm{d}s \\
&= \frac{v_a \sigma}{\alpha_{\text{ac}}} \delta(z-z') e^{-\frac{1}{2}\Gamma(t+t')} \left[e^{\Gamma s} \right]_{-\infty}^{\min\{t,t'\}} \\
&= \frac{v_a \sigma}{\alpha_{\text{ac}}} \delta(z-z') e^{-\frac{1}{2}\Gamma(t+t') + \Gamma \min\{t,t'\}}.
\end{aligned}$$

Here we used the stochastic Fubini theorem [139, 140] to combine the product of the two integrals $D(z,t)$ into a double integral. The expression in the exponent can be

further simplified by taking $t < t'$, which yields

$$\left\langle D(z,t)D(z',t')\right\rangle = \frac{v_a\sigma}{\alpha_{\text{ac}}}\delta(z-z')e^{-\frac{1}{2}\Gamma|t-t'|}. \tag{3.18}$$

This expression shows that the noise term $D(z,t)$ is δ-correlated in space as expected, but behaves as a random walk in time, so its temporal evolution at each point z depends on the past history of $D(z,t)$. Furthermore, this process is classified as an Ornstein-Uhlenbeck process [141], which means that as time increases, the function $D(z,t)$ eventually reaches a point of thermal equilibrium. We can further investigate the properties of $D(z,t)$ by looking at its power spectral density (PSD). Following the definition of stochastic processes in Appendix A, we can classify $D(z,t)$ as a stationary process in time because its auto-correlation function in (3.18) depends only on the difference of two times $t-t'$. Therefore, we can compute the PSD of D by applying the Wiener-Khinchin theorem [142, 143]

$$\begin{aligned} S_D(z,z',\omega) &= \frac{1}{2\pi}\int_{-\infty}^{\infty} e^{i\omega(t-t')}\left\langle D(z,t)D(z',t')\right\rangle \mathrm{d}(t-t') \\ &= \frac{1}{2\pi}\frac{v_a\sigma}{\alpha_{\text{ac}}}\delta(z-z')\int_{-\infty}^{\infty} e^{-\frac{1}{2}\Gamma|t-t'|}e^{i\omega(t-t')}\mathrm{d}(t-t') \\ &= \frac{1}{\pi}\frac{v_a\sigma}{\alpha_{\text{ac}}}\delta(z-z')\frac{\Gamma/2}{(\Gamma/2)^2+\omega^2}. \end{aligned}$$

This means that the spectral density of $D(z,t)$ at each point z is a Lorentzian with linewidth Γ, corresponding to the acoustic phonon lifetime $\tau_a = 1/\Gamma$ in the propagation medium.

3.4 Laser phase noise

Another important source of noise in SBS systems is the noise introduced by the lasers at the ends of the waveguide. Phase noise in the input optical fields a_1 and a_2 originate from the spontaneous emission events within the laser system. Models for laser noise can vary drastically depending on the type of laser, but many mathematical models assume a random phase that behaves as a random walk in time and is related to the laser's intrinsic linewidth [144, 145, 146, 147]. To understand how this works, let us begin with a fully monochromatic laser with central frequency ω_0. If such a theoretical laser could exist, we would represent its power-spectral density (PSD) as

$$S(\omega) = \frac{1}{2}\left[\delta(\omega+\omega_0)+\delta(\omega-\omega_0)\right], \tag{3.19}$$

such that no other oscillating components are present in the frequency spectrum. In this sense, the laser would output an optical field $\cos(\omega_0 t)$ that consists of a single continuous wave of frequency ω_0. For mathematical simplicity and without loss of generality, we shall consider only the positive frequencies of $S(\omega)$, by defining a complex-valued quantity $x(t) = e^{-i\omega_0 t}$. In reality, lasers will possess a spectrum with more than one frequency due to spontaneous emission, which makes this $S(\omega)$ not appropriate for physical simulations. Therefore, we must think of a more realistic model containing a non-zero linewidth: the full-width at half-maximum (FWHM) of the spectral density $S(\omega)$. We shall denote this as $\Delta\Omega$ (rad/s), or equivalently $\Delta\nu = \Delta\Omega/2\pi$ (Hz). The PSD

may therefore be expressed in terms of the Lorentzian function

$$S(\omega) = \frac{1}{\pi} \frac{\Delta\Omega/2}{(\Delta\Omega/2)^2 + (\omega - \omega_0)^2}. \tag{3.20}$$

where $\Delta\Omega$ is the FWHM in frequency space. Using the Wiener-Khinchin theorem (see Appendix A for details), which entails taking the inverse Fourier transform of $S(\omega)$, one finds the two-time auto-correlation function

$$r_x(\tau) = \langle x(t)x^*(t-\tau)\rangle = e^{-i\omega_0\tau} e^{-\frac{1}{2}\Delta\Omega|\tau|}, \tag{3.21}$$

where τ is the lag-time between $x(t)$ and its complex-conjugate. By letting $\tau = t - t'$, one finds that the exponential term $e^{-\frac{1}{2}\Delta\Omega|t-t'|}$ must correspond to the auto-correlation of some stochastic process $z(t)$, namely $\langle z(t)z^*(t')\rangle = e^{-\frac{1}{2}\Delta\Omega|t-t'|}$. We may equivalently express this process in terms of a stochastic phase function $\phi(t)$, such that

$$\left\langle e^{i[\phi(t)-\phi(t')]} \right\rangle = e^{-\frac{1}{2}\Delta\Omega|t-t'|}. \tag{3.22}$$

One possible candidate for $\phi(t)$ is the Brownian motion

$$\phi(t) = \sqrt{\Delta\Omega} W(t), \tag{3.23}$$

where $W(t)$ is a standard Wiener process with zero mean and variance t. It also has the property $W(t) - W(s) \sim \mathcal{N}(0, |t-s|)$, where $\mathcal{N}(\mu, \sigma^2)$ is a normally distributed random variable with mean μ and variance σ^2. To test if this process satisfies the condition $\left\langle e^{i[\phi(t)-\phi(t')]} \right\rangle = e^{-\frac{1}{2}\Delta\Omega|t-t'|}$, we use the following property of Wiener processes (see Appendix A):

$$\phi(t) - \phi(t') = \sqrt{\Delta\Omega}\left(W(t) - W(t')\right) \sim \sqrt{\Delta\Omega}\,\mathcal{N}(0, |t-t'|), \tag{3.24}$$

where the expression $X(t,t') \sim \mathcal{N}(0, |t-t'|)$ indicates that the random process $X(t,t')$ has a normal probability distribution with zero mean and variance $|t-t'|$. This then leads to the quantity

$$\left\langle e^{i[\phi(t)-\phi(t')]} \right\rangle = \left\langle e^{i\sqrt{\Delta\Omega}\mathcal{N}(0,|t-t'|)} \right\rangle,$$

and making the substitution $\zeta = i\sqrt{\Delta\Omega}$, this becomes the Moment-Generating Function (MGF) of the variable $\mathcal{N}(0, |t-t'|)$ with respect to the parameter ζ. Using the properties of normal random variables outlined in Appendix A.3.1, we compute the MGF as

$$\left\langle e^{i\sqrt{\Delta\Omega}\mathcal{N}(0,|t-t'|)} \right\rangle = e^{-\frac{1}{2}\Delta\Omega|t-t'|}, \tag{3.25}$$

which satisfies the condition in Eq. (3.22). We can simulate this phase noise numerically by using the following approximation of the Wiener process:

$$W(t) = \int_0^t \mathrm{d}W(t) \approx \sum_{n=1}^{N} \Delta W_n, \tag{3.26}$$

where $\Delta W_n \sim \sqrt{\Delta t}\mathcal{N}_n(0,1)$. In this sense $\phi(t)$ is a random walk that can be computed using the Euler-Mayurama scheme [148]

$$\phi(t_{n+1}) = \phi(t_n) + \sqrt{\Delta\Omega}\Delta W_n. \tag{3.27}$$

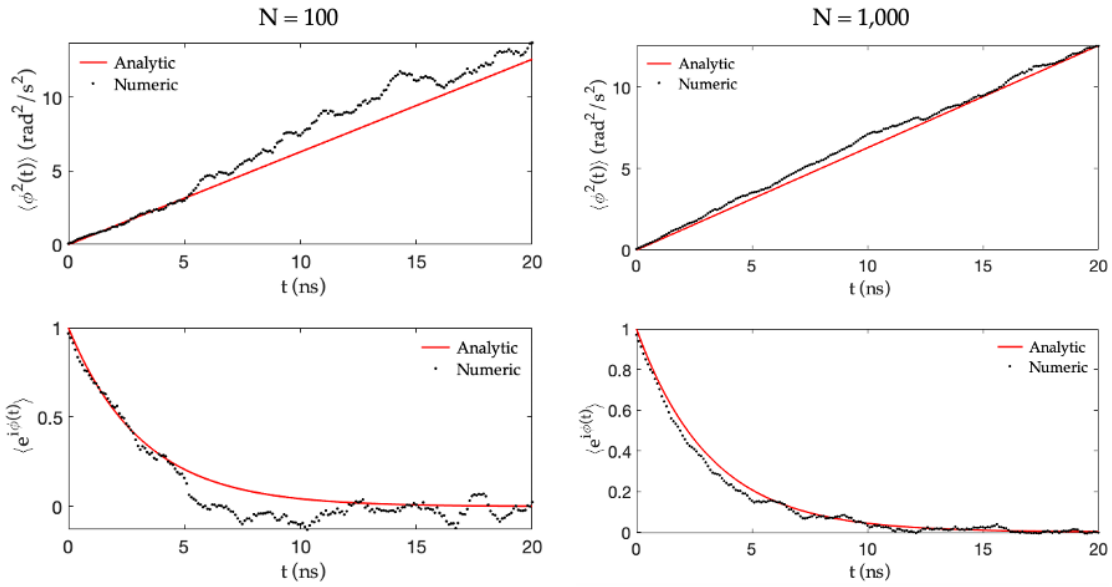

FIGURE 3.2: Variance (top) and $\langle e^{i\phi(t)} \rangle$ (bottom) for multiple independent realizations of $\phi(t)$. On the left hand side: ensemble average over 100 realizations, right hand side: ensemble average over 1,000 realizations.

The analytic mean and variance of $\phi(t)$ are

$$\langle \phi(t) \rangle = 0, \tag{3.28}$$

$$\langle \phi^2(t) \rangle = \Delta\Omega t. \tag{3.29}$$

A comparison of the numeric and analytic statistical properties of $\phi(t)$ for 10,000 independent samples is shown in Fig. 3.2.

Chapter 4

Noise and Pulse Dynamics in Backward Stimulated Brillouin Scattering

4.1 Overview

This Chapter is based on the contents of the research paper

> Oscar A. Nieves, Matthew D. Arnold, M. J. Steel, Mikołaj K. Schmidt, and Christopher G. Poulton, "Noise and pulse dynamics in backward stimulated Brillouin scattering," Opt. Express 29, 3132-3146 (2021).

Here derive a theoretical model for SBS noise for pulses in integrated optical waveguides with high-contrast materials. We focus on amplitude noise arising from the thermal phonon field, because in backwards SBS experiments this process has been observed to be significantly stronger than phase noise [149, 150]. Furthermore, we explore the dependence of the noise on the waveguide and pulse properties. We find that in the regime where the pump is undepleted by the SBS process, it is possible to derive analytic results for the absolute level of noise, as well as for the signal-to-noise ratio, even for time-varying pulses of arbitrary shape. Since numerical computation of ensemble averages are expensive, an analytic model that computes the SBS noise properties of pulses is extremely useful for the design of SBS-active devices. We use this analytic model to explore the impact of pulse and waveguide properties on the noise and optical signal-to-noise ratio (OSNR), and discuss the implications of these results in SBS experiments, where it is often advantageous to minimize the Stokes noise.

4.2 Theory and formalism

We consider backward SBS interactions in a waveguide of finite length L oriented along the z-axis (see Fig. 4.1): a pump pulse with angular frequency ω_1 is injected into the waveguide at $z = 0$ and propagates in the positive z-direction, while a signal pulse is injected at $z = L$ and propagates in the negative z-direction. The signal pulse has frequency centred around the Brillouin Stokes frequency $\omega_2 = \omega_1 - \Omega$, which is downshifted from the pump by the Brillouin shift Ω, and has a spectral width that lies entirely within the Brillouin linewidth. When these two pulses meet, the pump transfers energy to the signal field, resulting in coherent amplification of the signal around the Brillouin frequency. At the same time, as the pump moves through the waveguide, it interacts with the thermal phonon field and generates spontaneous Stokes photons

which also propagate in the negative z-direction. This spontaneous Stokes field combines with the coherent signal to form a noisy amplified output field centered around the Stokes frequency.

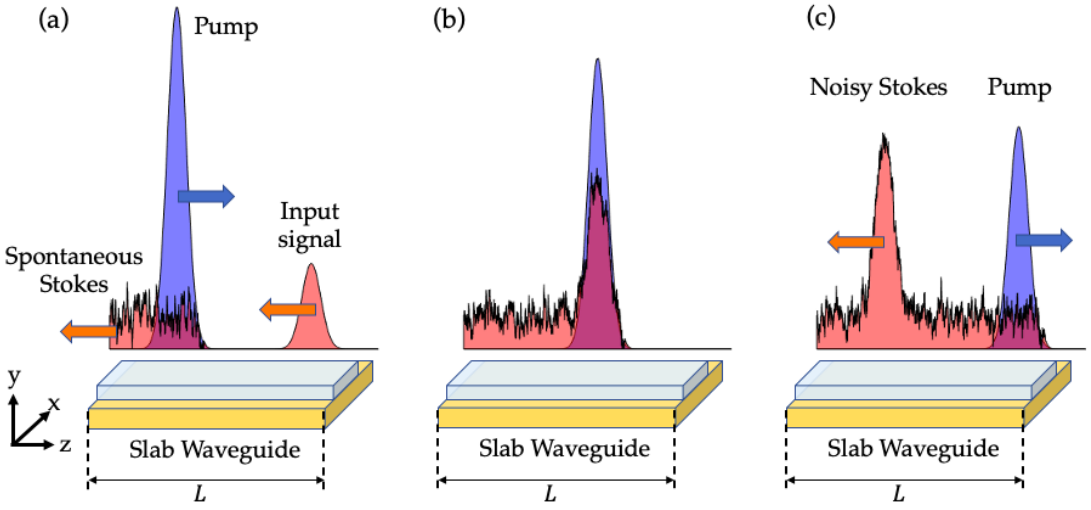

FIGURE 4.1: Propagation of two Gaussian pulses along a waveguide consisting of substrate (yellow) and core (light blue) dielectrics. L denotes the total length of the waveguide medium. The input fields in (a) overlap in (b), resulting in an exchange of energy between the pump and Stokes through the acoustic field, whereby the pump's energy is depleted by the Stokes. The spontaneous Stokes noise generated by the pump interacting with the thermal phonon field combines with the coherent signal in (b), leading to a noisy output field at the Stokes frequency in (c).

The noise transferred to the signal from the thermal field is computed by solving for the optical envelope fields $a_{1,2}$ and acoustic envelope field b (all in units of $\sqrt{\text{Watts}}$) in Eq. (2.59a)−(2.59c), namely:

$$\frac{\partial a_1}{\partial z} + \frac{1}{v}\frac{\partial a_1}{\partial t} + \frac{1}{2}\alpha a_1 = i\omega_1 Q_1 a_2 b^*, \tag{4.1a}$$

$$\frac{\partial a_2}{\partial z} - \frac{1}{v}\frac{\partial a_2}{\partial t} - \frac{1}{2}\alpha a_2 = i\omega_2 Q_2 a_1 b, \tag{4.1b}$$

$$\frac{\partial b}{\partial z} + \frac{1}{v_a}\frac{\partial b}{\partial t} + \frac{1}{2}\alpha_{\text{ac}} b = i\Omega Q_a a_1^* a_2 + \sqrt{\sigma} R(z,t). \tag{4.1c}$$

The boundary conditions for the pump and signal fields are applied by specifying the input values $a_1(0,t)$ and $a_2(L,t)$ respectively. These boundary conditions can be deterministic, as is the case in our calculations, or stochastic if laser noise is incorporated into the model. The analytic results presented in this Chapter are valid for both cases.

4.2.1 Noise under the undepleted pump approximation

An analytic solution to equations (2.59a)−(2.59c) exists under the undepleted pump approximation, which is valid for the case in which the signal power P_2 remains much smaller than the pump power P_1. We also assume that the depletion of the pump by the thermal field is negligible compared to optical loss [66]. The equation for the pump envelope is therefore

$$\frac{\partial a_1}{\partial z} + \frac{1}{v}\frac{\partial a_1}{\partial t} + \frac{\alpha}{2} a_1 = 0, \tag{4.2}$$

which, for an input field $a_p(t) = \sqrt{P^{\text{in}}_{\text{pump}}(t)}$ at $z = 0$ has the solution

$$a_1(z,t) = a_p\left(t - \frac{z}{v}\right) \mathrm{e}^{-\alpha z/2}, \tag{4.3}$$

by the method of characteristics. Next, we simplify (3.14) further by using a separation of time-scales in the integral: since $\tau_a = 1/\Gamma$ is large compared to the characteristic timescales of the optical envelope fields; this allows us to use the following Markov approximation [50]:

$$a_1^*(z,s)a_2(z,s) \approx a_1^*(z,t)a_2(z,t)\mathrm{e}^{-i\Delta(s-t)}, \tag{4.4}$$

where Δ is a detuning parameter relative to the center of the Brillouin gain profile written as $\Delta = \omega_2 - \omega_1 + \Omega$. This approximation is valid in the regime where the optical pulse widths $\tau_{p,s} < \tau_a$, where the phonon decay rate is slow compared to the propagation of the photons in the waveguide, and provided that the pump is undepleted. Taking $a_1^*(z,t)a_2(z,t)$ out of the integral in (3.14) yields the approximate expression for the acoustic envelope field

$$b(z,t) \approx i\frac{v_a \Omega Q_a}{\Gamma/2 - i\Delta} a_1^*(z,t)a_2(z,t) + D(z,t). \tag{4.5}$$

Now we can eliminate the elastic field by substituting (4.5) into (4.1b), which yields

$$\frac{\partial a_2}{\partial z} - \frac{1}{v}\frac{\partial a_2}{\partial t} + \frac{1}{2}\left[g(\Delta)P_1(z,t) - \alpha\right] a_2 = i\omega_2 Q_2 a_1(z,t)D(z,t), \tag{4.6}$$

where $g(\Delta)$ is the usual SBS gain parameter in ($\mathrm{m}^{-1}\mathrm{W}^{-1}$)

$$g(\Delta) = \frac{2v_a\omega_2\Omega|Q_2|^2}{\Gamma/2 - i\Delta} = g_0\frac{\Gamma/2}{\Gamma/2 - i\Delta}, \tag{4.7}$$

with $g_0 = g(0)$. Equation (4.6) is then solved by making a variable transformation to the frame of reference that is co-propagating with the Stokes field [151], namely $\xi = z$ and $\tau = t + z/v$. The partial derivatives in the new coordinate system (ξ, τ) are

$$\frac{\partial}{\partial t} = \frac{\partial \xi}{\partial t}\frac{\partial}{\partial \xi} + \frac{\partial \tau}{\partial t}\frac{\partial}{\partial \tau} = \frac{\partial}{\partial \tau}, \tag{4.8}$$

$$\frac{\partial}{\partial z} = \frac{\partial \xi}{\partial z}\frac{\partial}{\partial \xi} + \frac{\partial \tau}{\partial z}\frac{\partial}{\partial \tau} = \frac{\partial}{\partial \xi} + \frac{1}{v}\frac{\partial}{\partial \tau}. \tag{4.9}$$

Upon substituting these derivatives into Eq. (4.1b) we obtain

$$\frac{\partial a_2}{\partial \xi} + \frac{1}{2}\left[g(\Delta)P_1(\xi, \tau - \xi/v) - \alpha\right] a_2 = i\omega_2 Q_2 a_1(\xi, \tau - \xi/v)D(\xi\tau - \xi/v), \tag{4.10}$$

Identifying the integrating factor

$$I(\xi,\tau) = \exp\left\{-\frac{1}{2}\int_\xi^L \left[g(\Delta)P_1\left(\xi', \tau - \frac{\xi'}{v}\right) - \alpha\right] \mathrm{d}\xi'\right\}, \tag{4.11}$$

leads to the equation

$$\int_{\xi}^{L} \frac{\partial}{\partial \xi'} \left[a_2(\xi', \tau) I(\xi', \tau) \right] \mathrm{d}\xi' = i\omega_2 Q_2 \int_{\xi}^{L} I(\xi', \tau) a_1 \left(\xi', \ \tau - \frac{\xi'}{v} \right) D \left(\xi', \ \tau - \frac{\xi'}{v} \right) \mathrm{d}\xi', \tag{4.12}$$

The left-hand side of Eq. (4.10) is $a_2(L, \tau) I(L, \tau) - a_2(\xi, \tau) I(\xi, \tau)$. Then, using $a_2(L, \tau)$ as the input boundary condition for the Stokes field, and introducing the cumulative net gain function

$$\tilde{G}_N(\xi, \xi', \tau) = \exp \left\{ \frac{1}{2} \int_{\xi}^{\xi'} \left[g(\Delta) P_1 \left(\xi'', \tau - \frac{\xi''}{v} \right) - \alpha \right] \mathrm{d}\xi'' \right\}. \tag{4.13}$$

we write the solution for the Stokes envelope field at the point ξ as

$$\begin{aligned} a_2(\xi, \tau) = a_2(L, \tau) \tilde{G}_N(\xi, L, \tau) \\ - i\omega_2 Q_2 \int_{\xi}^{L} \tilde{G}_N(\xi, \xi', \tau) a_1 \left(\xi', \ \tau - \frac{\xi'}{v} \right) D \left(\xi', \ \tau - \frac{\xi'}{v} \right) \mathrm{d}\xi'. \end{aligned} \tag{4.14}$$

Finally, we switch back to the coordinate system (z, t) by replacing τ in the above equation by $\tau = t + z/v$, which yields the solution for the Stokes envelope field

$$\begin{aligned} a_2(z, t) = a_2(L, t) G_N(z, L, t) \\ - i\omega_2 Q_2 \int_{z}^{L} G_N(z, z', t) a_1 \left(z', \ t + \frac{z - z'}{v} \right) D \left(z', \ t + \frac{z - z'}{v} \right) \mathrm{d}z', \end{aligned} \tag{4.15}$$

where the *net gain function* is expressed as

$$G_N(z, z', t) = \exp \left\{ \frac{1}{2} \int_{z}^{z'} \left[g(\Delta) P_1 \left(\eta, \ t + \frac{z - \eta}{v} \right) - \alpha \right] \mathrm{d}\eta \right\}, \tag{4.16}$$

for $z < z'$. The modulus squared $|G_N(z, z', t)|^2$ of this function gives the net cumulative gain in the Stokes power between z and z', taking into account the effect of optical losses. As the distance between z and z' increases, both the amplification from the pump and the optical loss increase. However, for any time t in which the pump pulse $P_1(z, t)$ lies outside the domain $[z, z']$, optical loss dominates over the SBS amplification.

We compute the total, noisy, Stokes power by considering the Stokes envelope as a sum of two contributions: a coherent signal field, which is the Stokes in the absence of any thermal noise, and a spontaneous Stokes field which contains all the contributions from the background thermal noise. This is expressed by separating the two terms in Eq. (4.15) as $a_2(z, t) = a_2^{\mathrm{sig}}(z, t) + a_2^{\mathrm{spo}}(z, t)$ where

$$a_2^{\mathrm{sig}}(z, t) = a_2(L, t) G_N(z, L, t), \tag{4.17}$$

$$a_2^{\mathrm{spo}}(z, t) = -i\omega_2 Q_2 \int_{z}^{L} G_N(z, z', t) a_1 \left(z', \ t + \frac{z - z'}{v} \right) D \left(z', \ t + \frac{z - z'}{v} \right) \mathrm{d}z'. \tag{4.18}$$

The ensemble-average of the total Stokes power is then

$$\langle P_2(z, t) \rangle = \left\langle P_2^{\mathrm{sig}}(z, t) \right\rangle + \langle P_2^{\mathrm{spo}}(z, t) \rangle = \left\langle \left| a_2^{\mathrm{sig}}(z, t) \right|^2 \right\rangle + \left\langle \left| a_2^{\mathrm{spo}}(z, t) \right|^2 \right\rangle, \tag{4.19}$$

where the relation $\left\langle a_2^{\mathrm{sig}} a_2^{\mathrm{spo}} \right\rangle = 0$ holds since the input laser noise in a_2^{sig} and thermal

noise in a_2^{spo} are statistically independent from each other. The average signal power is computed by taking the ensemble average of the input field defined by the noisy boundary condition $a_2(L,t)$

$$\left\langle P_2^{\text{sig}}(z,t)\right\rangle = \left\langle |a_2(L,t)|^2\,|G_N(z,L,t)|^2\right\rangle. \tag{4.20}$$

Here G_N is taken inside the ensemble average because it is dependent on the pump P_1, which may contain input laser noise. The spontaneous Stokes power is

$$\begin{aligned} P_2^{\text{spo}}(z,t) = \frac{\alpha_{\text{ac}}}{4}\frac{\omega_2}{\Omega}g_0\int_z^L G_N(z,z',t)\,a_1\left(z',\,t+\frac{z-z'}{v}\right)D\left(z',\,t+\frac{z-z'}{v}\right)\mathrm{d}z' \\ \times\int_z^L G_N^*(z,z'',t)\,a_1^*\left(z'',\,t+\frac{z-z''}{v}\right)D^*\left(z'',\,t+\frac{z-z''}{v}\right)\mathrm{d}z''. \end{aligned} \tag{4.21}$$

This product of integrals can be cast as a double-integral by applying the stochastic Fubini theorem [139]. A sufficient condition for this to hold is that the integrand in (4.18) be square-integrable and finite [140]. This condition holds since $D(z,t)$ reaches a steady-state after a short time t [137] and both a_1 and G_N are bounded functions [152]. The spontaneous power becomes

$$\begin{aligned} P_2^{\text{spo}}(z,t) = \frac{\alpha_{\text{ac}}}{4}\frac{\omega_2}{\Omega}g_0\int_z^L\int_z^L G_N(z,z',t)G_N^*(z,z'',t)a_1\left(z',\,t+\frac{z-z'}{v}\right)\times \\ a_1^*\left(z'',\,t+\frac{z-z''}{v}\right)D\left(z',\,t+\frac{z-z'}{v}\right)D^*\left(z'',\,t+\frac{z-z''}{v}\right)\mathrm{d}z''\mathrm{d}z'. \end{aligned} \tag{4.22}$$

The relation $\langle a_1(z,t)D(z,t)\rangle = \langle a_1(z,t)\rangle\langle D(z,t)\rangle = 0$ holds since the laser noise in a_1 and the thermal noise in D are not coupled to each other, so they are statistically independent. Taking the ensemble average of both sides of (4.22) yields

$$\begin{aligned} \langle P_2^{\text{spo}}(z,t)\rangle &= \left\langle \frac{\alpha_{\text{ac}}}{4}\frac{\omega_2}{\Omega}g_0\int_z^L\int_z^L G_N(z,z',t)G_N^*(z,z'',t)a_1\left(z',\,t+\frac{z-z'}{v}\right)\times\right. \\ &\quad \left. a_1^*\left(z'',\,t+\frac{z-z''}{v}\right)D\left(z',\,t+\frac{z-z'}{v}\right)D^*\left(z'',\,t+\frac{z-z''}{v}\right)\mathrm{d}z''\mathrm{d}z'\right\rangle \\ &= \frac{\alpha_{\text{ac}}}{4}\frac{\omega_2}{\Omega}g_0\int_z^L\int_z^L\left\langle G_N(z,z',t)G_N^*(z,z'',t)a_1\left(z',\,t+\frac{z-z'}{v}\right)\times\right. \\ &\quad \left. a_1^*\left(z'',\,t+\frac{z-z''}{v}\right)\right\rangle\left\langle D\left(z',\,t+\frac{z-z'}{v}\right)D^*\left(z'',\,t+\frac{z-z''}{v}\right)\right\rangle\mathrm{d}z''\mathrm{d}z' \\ &= \frac{\alpha_{\text{ac}}}{4}\frac{\omega_2}{\Omega}g_0\int_z^L\int_z^L\left\langle G_N(z,z',t)G_N^*(z,z'',t)a_1\left(z',\,t+\frac{z-z'}{v}\right)\times\right. \\ &\quad \left. a_1^*\left(z'',\,t+\frac{z-z''}{v}\right)\right\rangle\frac{v_a\sigma}{\alpha_{\text{ac}}}\delta\left(z'-z''\right)\exp\left\{-\frac{\Gamma}{2}\left|\frac{z'-z''}{v}\right|\right\}\mathrm{d}z''\mathrm{d}z' \\ &= \frac{v_a\sigma}{4}\frac{\omega_2}{\Omega}g_0\int_z^L\left\langle P_1\left(z',\,t+\frac{z-z'}{v}\right)|G_N(z,z',t)|^2\right\rangle\mathrm{d}z'. \end{aligned}$$

Finally, using $\sigma = k_BT\alpha_{\text{ac}}$ and $\Gamma = v_a\alpha_{\text{ac}}$ we obtain the ensemble averaged spontaneous Stokes power:

$$\left\langle P_2^{\text{spo}}(z,t)\right\rangle = \frac{k_BT\Gamma}{4}\frac{\omega_2}{\Omega}g_0\int_z^L\left\langle P_1\left(z',\,t+\frac{z-z'}{v}\right)|G_N(z,z',t)|^2\right\rangle\mathrm{d}z'. \tag{4.23}$$

Equation (4.23) is one of the main results in this Chapter. It gives the ensemble-averaged spontaneous Stokes power, which is proportional to the pump power $P_1(z,t)$ multiplied by the net gain over the length of the waveguide. As the temperature increases, more spontaneous phonons are generated, leading to more collisions of phonons with pump photons. The annihilation of these photons then creates spontaneous Stokes photons, which amplifies the Stokes noise in the medium. The integration from z to L indicates that as the pump propagates through the medium, there is an accumulation of spontaneous Stokes photons propagating in the opposite direction.

Once this spontaneous power has been calculated, a useful measure to quantify the integrity of the Stokes signal detected at the waveguide output is the OSNR. This is computed by taking the ratio of the average coherent signal power to spontaneous noise power over a specified bandwidth [153]. In time-domain, the OSNR may be calculated over an arbitrary but suitably long time period T_0 using the time averaged powers

$$\mathrm{OSNR} = \frac{\int_0^{T_0} \left\langle P_2^{\mathrm{sig}}(0,t) \right\rangle \mathrm{d}t}{\int_0^{T_0} \left\langle P_2^{\mathrm{spo}}(0,t) \right\rangle \mathrm{d}t}. \tag{4.24}$$

In the following calculations, using a Gaussian pulse we choose T_0 as four times the intensity full width at half maximum (FWHM).

4.3 Results for a chalcogenide SBS chip

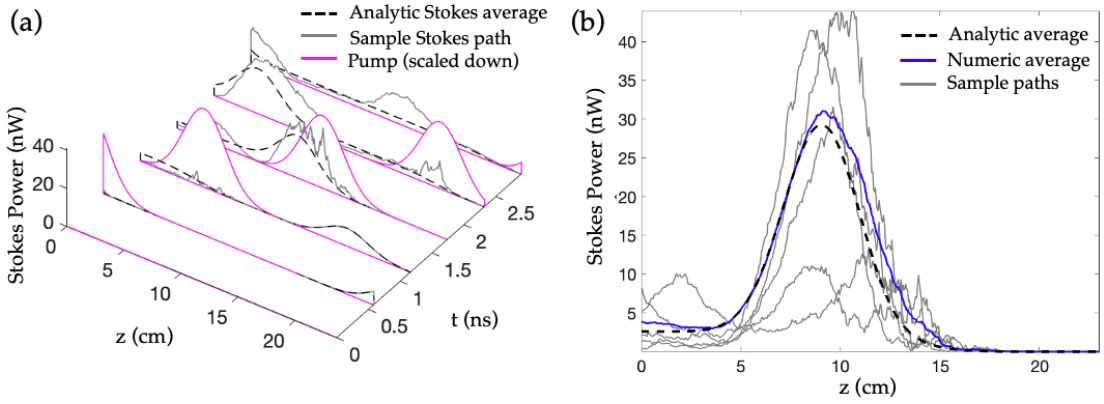

FIGURE 4.2: Numerical simulation of the Stokes noise inside a 23.7 cm long waveguide. (a) Temporal evolution of the total Stokes power across the waveguide for a single run of the numerical method (gray). The dashed black line represents the ensemble-averaged expression for the total Stokes power being the sum of Eqs. (4.20) and (4.23), while the solid magenta line is the pump pulse, scaled down from its original peak power of 110 mW. (b) Several independent runs of the Stokes field (gray), with the numerical ensemble average (blue) and the analytic ensemble average (dashed black), at $t = 1.8$ ns.

Figure 4.2 shows the ensemble-averaged signal power and spontaneous Stokes power computed using Eqs (4.20) and (4.23). These calculations assume a dielectric waveguide at temperature 300 K of length 23.7 cm and SBS gain coefficient $g_0 = 423\ \mathrm{m^{-1}W^{-1}}$, which corresponds to the SBS chip structure used in [154] at zero detuning ($\Delta = 0$). We consider a Gaussian pump pulse with peak power 110 mW and FWHM of 200 ps, and a Gaussian signal pulse with peak power 10 nW and FWHM of 200 ps. The optical pump frequency is fixed at 200 THz, while the acoustic frequency is set to 7.6 GHz, with a Brillouin linewidth of $\Delta\nu_B = 30$ MHz. The linear optical loss is 0.05 dB/cm.

Equations (4.1a)–(4.1c) are solved numerically using the method described in detail in Chapter 5.

For these simulations, the numerical grid consists of 600 points in z and 900 points in t. These values were chosen, using convergence tests in the absence of noise, to ensure an error in the gain of under 1%. We see in Fig. 4.2(a) that as the pump propagates through the waveguide, a noisy Stokes field is generated that trails the leading edge of the pump pulse. This field combines with the input signal, with the resulting noisy Stokes field further amplified by the pump. Figure 4.2(b) shows the total Stokes power as a function of z at $t = 1.8$ ns, where the dashed black line represents the analytic solution to (4.23) added to the coherent Stokes power in (4.20), and the blue line is a numerical ensemble average over 20 independent runs of the numerical method. Eq. (4.23) contributes approximately 3 nW of Stokes power across the length of the waveguide, while Eq. (4.20) contributes 10 nW at $z = 23.7$ cm which is amplified as it moves towards $z = 0$.

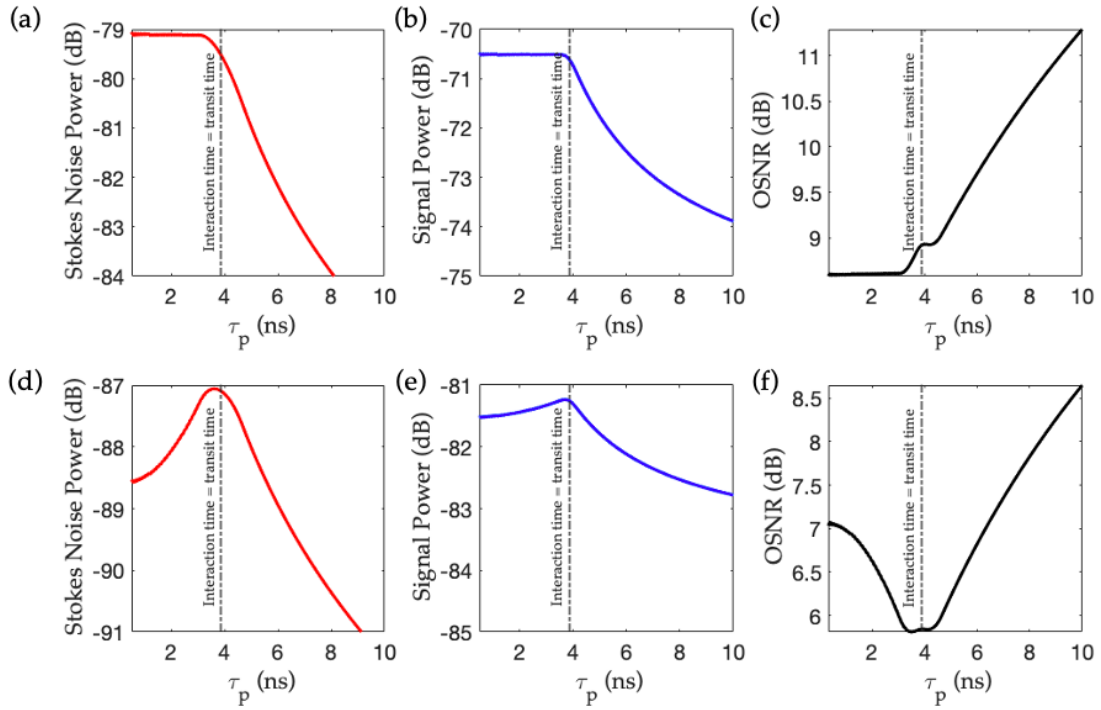

FIGURE 4.3: Time-averaged Stokes noise power, coherent signal power and OSNR for a dielectric waveguide of length $L = 23.7$ cm. Plots (a)−(c) are for $\alpha = 0.01$ dB/cm, while plots (d)−(f) are for $\alpha = 1.0$ dB/cm. The signal pulse is a Gaussian with FWHM of 200 ps and peak power of 100 nW. The pump consists of a rectangular pulse with constant energy, ranging from $P_{p0} = 5$ mW ($\tau_p = 10$ ns) to $P_{p0} = 5$ W ($\tau_p = 10$ ps). The vertical dashed lines mark the point at which the interaction time between pump and signal becomes equal to the transit time of the signal pulse.

We now use (4.23) to study the effect on the noise of the tunable properties of the pump such as peak power and pulse duration, and how this may interact with fixed parameters such as waveguide length and optical loss. We consider a Gaussian signal pulse with FWHM of 200 ps, and a rectangular pump pulse of width τ_p that varies between 10 ps−10 ns. The total pulse energy of the input pump field is kept constant, while the peak power P_{p0} varies with the pulse width, ranging from $P_{p0} = 5$ mW ($\tau_p = 10$ ns) to $P_{p0} = 5$ W ($\tau_p = 10$ ps). In all the calculations, the output Stokes field at $z = 0$ is averaged over a time period of 800 ps, which is four times the signal FWHM and contains more than 99.7% of the pulse's energy. The results for the spontaneous Stokes

power, signal power and OSNR are shown in Fig. 4.3. We observe in Fig. 4.3(a) and (b) that the Stokes noise and signal powers remain constant for pump widths $\tau_p \lesssim 3$ ns before decreasing. In this low optical loss case, the near-constant values of the Stokes noise and signal power can be attributed to the constant energy in the pump pulse, as shown in Fig. 4.4: for short pulse-lengths, the signal and the pump interact entirely within the waveguide. As the pump pulse becomes longer than the waveguide and its peak power decreases, the Stokes field is able to interact with less of its energy inside the medium, resulting in less amplification of the Stokes. The signal and spontaneous fields fall off at different rates with respect to τ_p because the signal is proportional to the net gain squared $|G_N|^2$ via (4.20), while the spontaneous Stokes power is proportional to the pump power P_1 multiplied by $|G_N|^2$ via (4.23). The gain $|G_N|^2$ decreases with larger τ_p because more of the pump pulse lies outside of the interaction region, and at the same time P_1 decreases while its peak power is lowered for longer τ_p, causing the spontaneous Stokes to decrease more rapidly than the signal. This results in an OSNR figure which increases with τ_p, as shown in Fig. 4.3(c).

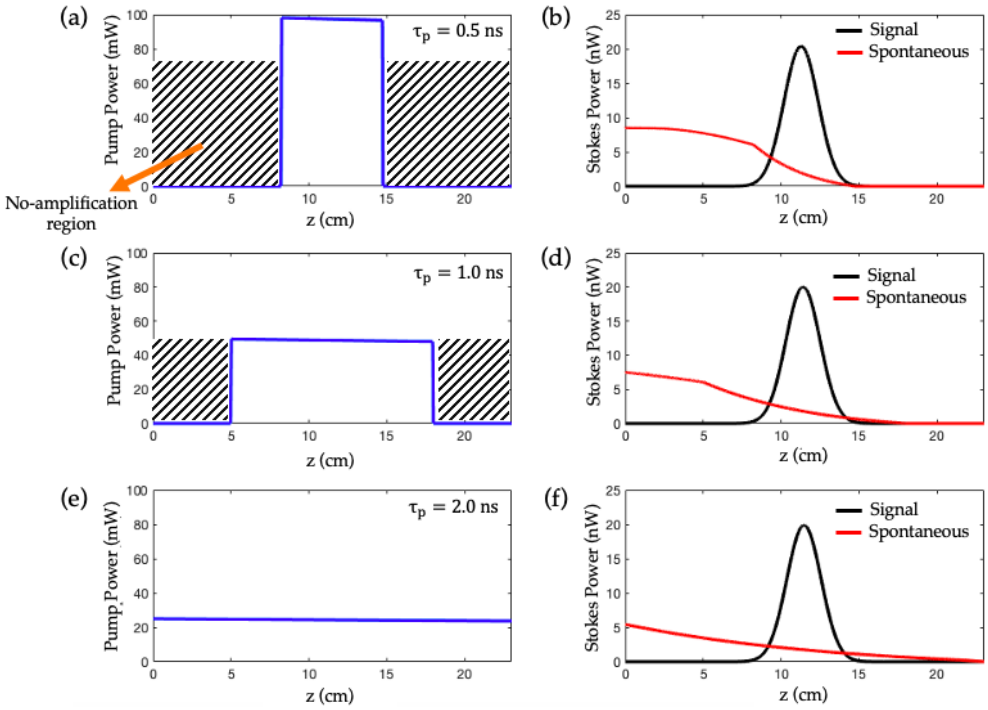

FIGURE 4.4: Snapshots of the pump and Stokes powers with varying pump width and peak power at a fixed time t, with optical loss $\alpha = 0.01$ dB/cm. The powers in (b), (d) and (f) are calculated using Eq. (4.20) and (4.23). The input pump energy is kept constant.

For the high optical loss case shown in Fig. 4.3(d)−(f), we observe a maximum in both the Stokes noise and signal powers for a critical value of τ_p, before decreasing with longer pump lengths as in the lower loss case. This results in a minimum in the OSNR; this minimum occurs because the optical loss is dominant in the regions inside the waveguide that are not covered by the pump (see Fig. 4.5). As the pump becomes wider, the pump coverage inside the waveguide increases, compensating for the losses incurred at the uncovered regions. This results in higher amplification of the Stokes despite the peak pump power decreasing with larger τ_p. However, this increased amplification vanishes once the pump pulse becomes longer than the waveguide, in which case the Stokes power decreases in a similar manner to the low-loss case.

The emergence of the OSNR minimum in Fig. 4.3(f) is a function of the optical loss

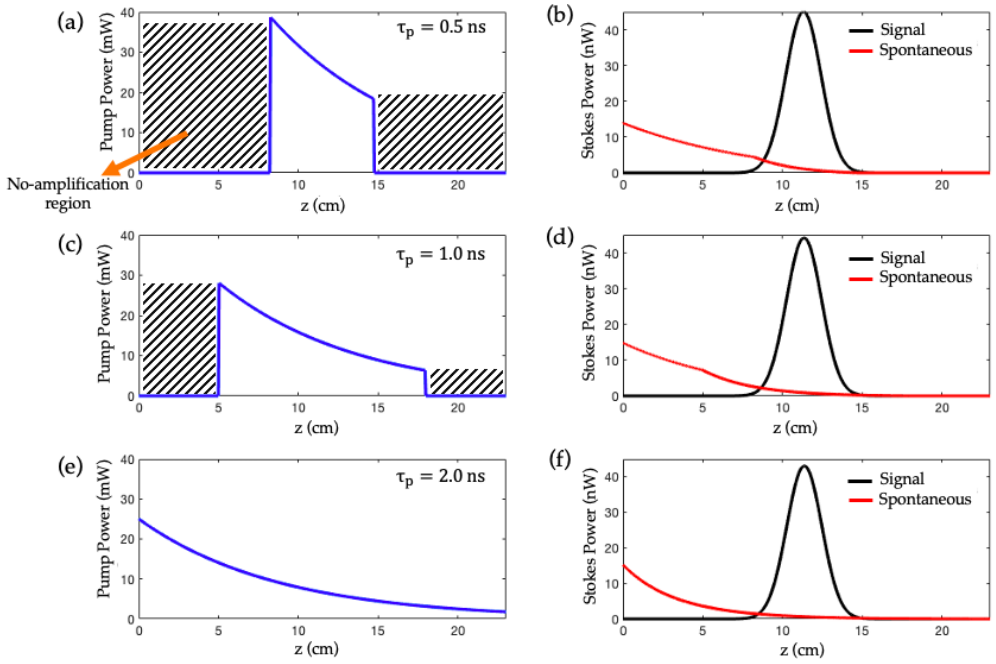

FIGURE 4.5: Snapshots of the pump and Stokes powers with varying pump width and peak power at a fixed time t, with optical loss $\alpha = 0.5$ dB/cm. The powers in (b), (d) and (f) are calculated using Eq. (4.20) and (4.23). The input pump energy is kept constant.

α, the pump pulse width τ_p and the waveguide length L. This is shown as a contour plot in Fig. 4.6; we see that for smaller losses there is no maximum peak in the spontaneous noise power, and therefore no minimum in the OSNR. Below this value the Stokes power and OSNR follow the behavior of Fig. 4.3(a)−(c), staying approximately constant for short pump pulses, then decreasing and increasing respectively for higher values of τ_p. However, once the loss reaches a critical value, the noise power develops a maximum at approximately the point in which the interaction time τ_i between pump and signal is equal to the transit time L/v. This corresponds to a minimum in the OSNR, because making τ_p longer than the transit time results in a reduced level of noise, since the spontaneous Stokes decreases more rapidly than the amplified signal. The value τ_{max} that maximizes the noise corresponds to the pump-length when the interaction time τ_i satisfies $\tau_i = L/v$ and can be computed as follows: first, we compute an effective pulse-width τ_{eff} using the equation

$$\int_0^{\tau_{\text{eff}}/2} P_1(0,t)\mathrm{d}t = \frac{1}{2}\tilde{f}\int_{-\infty}^{\infty} P_1(0,t)\mathrm{d}t, \tag{4.25}$$

where $0 \leq \tilde{f} \leq 1$ represents the fraction of the total energy in the pump that is contained within τ_{eff}. In our calculations, we set $\tilde{f} = 0.95$. The interaction time between the pulses is $\tau_i = \tau_{\text{eff}}/2$ because the signal and pump counter-propagate at the same speed, so the time of overlap is halved. This gives an approximation of the value τ_p for which the maximum amount of pump energy is able to interact with the signal, before it no longer fits inside the structure.

This noise behavior is not restricted to rectangular pump pulses. In Fig. 4.6(c) and (d), we observe the same behavior when using a Gaussian pump pulse, and again the same maximum in the Stokes noise can be observed. Here, some of the pump's energy is more localized near the central peak, while the long tails of the pulse contain a very small portion of the energy. This limits the region inside the waveguide in which the

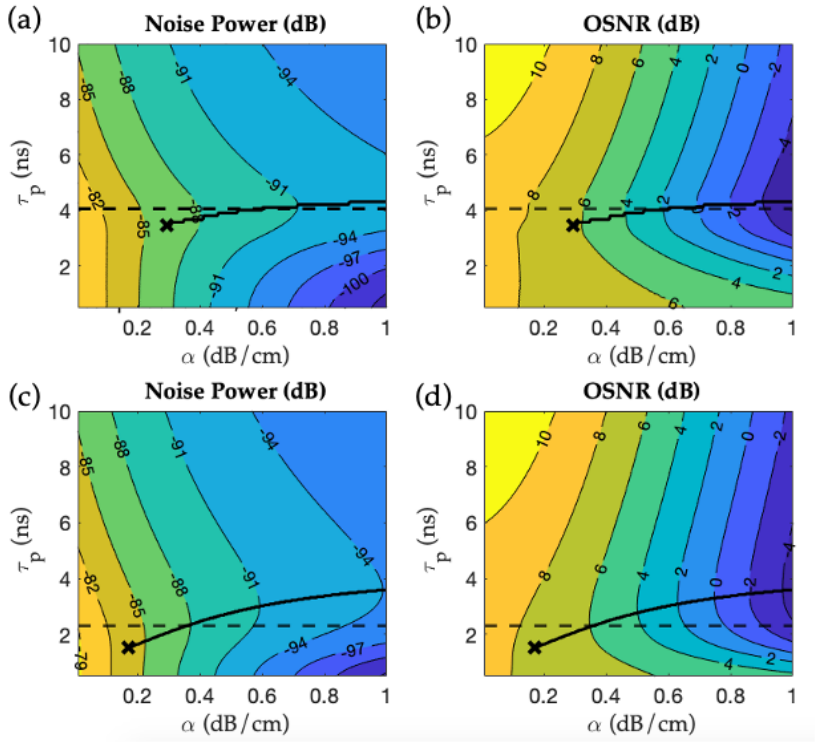

FIGURE 4.6: Contour plot of the Stokes noise power (a) and the OSNR (b) as functions of the rectangular pump width τ_p and optical loss α, for constant energy pump pulses. Plots (c) and (d) are for Gassuan pump pulses of varying FWHM τ_p. The black curve denotes where the maximum in the noise power occurs for each loss α. The horizontal dashed line denotes when the interaction time of the pump and Stokes is equal to the transit time of the signal pulse. The cross indicates the value of α below which the maximum peak in the noise power vanishes.

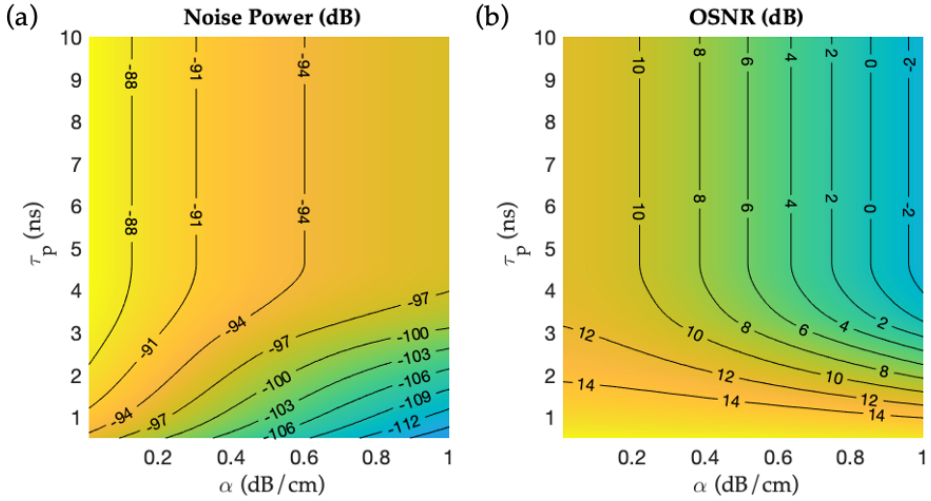

FIGURE 4.7: Stokes noise power (a) and OSNR (b) for a rectangular pump pulse using a constant peak pump power.

amplification from the pump is able to compensate for the optical losses, and results in a maximum Stokes noise peak that occurs at a smaller τ_p compared to the rectangular pump case.

Finally, we compute the effects of the noise and OSNR in the case where the pump

pulse has a fixed peak power. Both the spontaneous Stokes noise and signal power increase with τ_p, reaching a steady state for τ_p longer than the transit time of the waveguide. This results in the OSNR decreasing until reaching a constant value for larger τ_p, as shown in Fig. 4.7(b). This occurs due to the pump pulse covering more of the waveguide as τ_p gets larger: initially there is more energy injected into the SBS medium, but as soon as the pump pulse becomes comparable in size to the waveguide; the amount of pump energy that interacts with the Stokes field reaches a constant value. This then leads to a steady-state for both the signal and spontaneous Stokes powers.

4.4 Validity of the analytic model

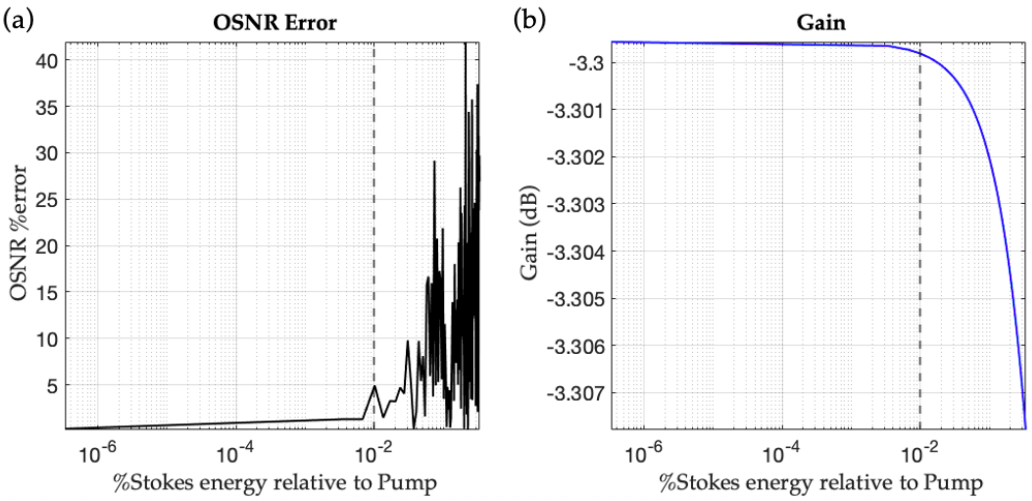

FIGURE 4.8: Plots for the signal percentage error in the OSNR (a) and signal gain (b). All the plots are represented as functions of the input signal energy as a percentage of the input pump energy, over a range of signal powers between 1 nW$-$1 mW relative to a 300 mW input pump at a fixed optical attenuation of 0.3 dB/cm. The dashed vertical lines represent the point at which the near-constant gain begins to decrease, indicating that the pump is being depleted by the Stokes field.

We now estimate the region of validity of our analytic model, by considering an SBS chalcogenide chip with length 23.7 cm, with a Gaussian pump pulse of $P_{\text{p0}} = 300$ mW and fixed optical loss of $\alpha = 0.3$ dB/cm. The energy in both the pump and signal input fields is given by the expressions $E_1 = \int_{-\infty}^{\infty} P_1(0,t)\mathrm{d}t$ and $E_2 = \int_{-\infty}^{\infty} P_2(L,t)\mathrm{d}t$ respectively. For each ratio of energies E_2/E_1 where $E_2 \leq E_1$ we compute the relative error in the OSNR using both the analytic model in (4.23) and the numerical solver for Eqs (4.1a)$-$(4.1c).

In Fig. 4.8(a) we see that the ONSR error remains below 2% when the signal energy relative to the pump is small, but increases suddenly for larger signal powers. This occurs because of pump depletion, which was neglected in Eq. (4.23) in deriving the analytic model: as the pump becomes depleted, some of its energy gets transferred to the spontaneous Stokes as well as to the signal, enhancing the coupling between the fields. This results in some of the spontaneous Stokes energy feeding back into the pump, making the multiplicative noise more dominant than the additive noise in Eq. (4.23). This means that as the pump becomes depleted, there is less spontaneous Stokes generated from the thermal background than coherent Stokes amplified from the input signal, even though both fields increase as the pump power increases. This is in line with previous studies [155, 156] which considered variance in the reflected

Stokes beam in the absence of an input signal (i.e. for purely spontaneous SBS): these studies found that the relative strength of the spontaneous Stokes field was reduced compared to the coherent field once the pump power began to be depleted. For the analytic model, the departure from the undepleted regime results in an error in the OSNR, as shown in Fig. 4.8(a). The analytic model is therefore expected to yield accurate results provided the pump remains undepleted. To extend the study of the noise dynamics of SBS interactions beyond the undepleted pump regime, and to study other features such as phase noise, it is necessary to solve Eqs. (4.1a)−(4.1c) numerically, following the procedure shown in Chapter 5.

4.5 Conclusion

In this Chapter, we have developed a general mathematical model for solving the dynamical SBS equations in the presence of thermal noise. We present a simple analytic model in the undepleted pump regime whereby the amplitude noise in the Stokes field can be computed for pulses of arbitrary shape and size, which is useful in Brillouin signal processing. The analytic results show that in the case of a constant energy pump field and lossy media, the OSNR has a minimum peak near the region in which the interaction time of the pulses matches the transit time of the signal in the waveguide. This occurs as the spontaneous Stokes noise increases towards a maximum value, which results from longer pump pulses compensating for the linear optical losses in the medium. Once the pump pulse becomes longer than the waveguide, the loss dominates again as less pump energy fits inside the SBS medium. This behaviour of the OSNR is mediated by the pump energy, pump shape, waveguide length and optical loss, making it important to choose the right parameter combination to maximize the OSNR in a specific device.

Chapter 5

Numerical Simulation of Noise in Pulsed Brillouin Scattering

5.1 Overview

This Chapter is based on the contents of the research paper

> Oscar A. Nieves, Matthew D. Arnold, Michael J. Steel, Mikołaj K. Schmidt, and Christopher G. Poulton, "Numerical simulation of noise in pulsed Brillouin scattering," J. Opt. Soc. Am. B 38, 2343-2352 (2021)

Here we present a numerical method by which the transient SBS equations with thermal noise can be solved for pulses of arbitrary shape and size, in arbitrary waveguide geometries, which allows us to extend the noise analysis in Chapter 4 beyond the undepleted pump approximation (UPA). We apply this method to the case of a short chalcogenide waveguide and use the model to compute the statistics of the output envelope fields. We examine the dynamics of the noise when the Stokes arises spontaneously from the thermal field, and for the case when it is seeded with an input pulse at the far end of the waveguide. We demonstrate the transition from the low-gain, short pulse case, in which noise is amplified by the pump, to the high gain, long pulse regime in which coherent amplification occurs. In this latter situation, we show that while the output pulses remain smooth, significant fluctuations in the peak powers arising from the thermal field can persist. We also show that, within the framework of this model, phase noise from the pump only has a significant impact on Stokes noise when the laser coherence time matches the time scales of the pulses involved in the interaction. Finally, we investigate the convergence of this numerical method, and find that it yields linear convergence in both the average power and variance of the power for three fields in the SBS interaction, which is in agreement with the Euler-Mayurama scheme for solving stochastic ordinary differential equations.

5.2 Numerical method

5.2.1 The SBS equations

We consider backward SBS interactions in a waveguide of finite length L along the z-axis as shown in Fig. 5.1. The spectrum of the signal pulse is centered around the Brillouin Stokes frequency $\omega_2 = \omega_1 - \Omega$, which is down-shifted from the pump by the Brillouin shift Ω, and its spectral extent lies entirely within the Brillouin linewidth $\Delta\nu_B$. The interaction can be modelled using three envelope fields for the pump ($a_1(z,t)$), Stokes ($a_2(z,t)$) and acoustic field $b(z,t)$, according to the equations (4.1a)−(4.1c) we also saw in Chapter 4, with stochastic boundary conditions $a_1(0,t)$ and $a_2(L,t)$. As

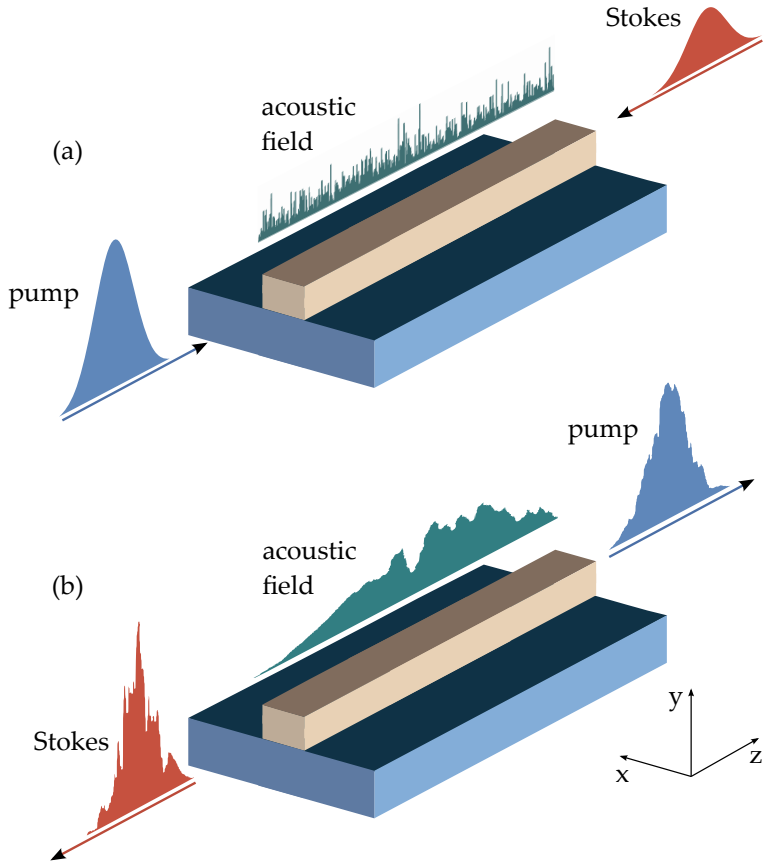

FIGURE 5.1: Illustration of the SBS interaction, showing the pump, Stokes and acoustic powers on a photonic chip waveguide. In (a), the pump and Stokes pulses are injected into opposite ends of the waveguide, and the acoustic field is made up of random thermal fluctuations. In (b), the optical fields have interacted inside the waveguide, the Stokes depletes the pump to gain some energy, and the rest of the energy goes to the acoustic field.

before, we apply apply the limit $\partial_z b \to 0$ to (4.1c), which simplifies into (3.14). Upon substituting (3.14) into (4.1a) and (4.1b), and assuming that the fields $a_{1,2}$ are everywhere zero for $t < 0$, we obtain the pair of equations

$$\frac{\partial a_1}{\partial z} + \frac{1}{v}\frac{\partial a_1}{\partial t} + \frac{1}{2}\alpha a_1 = i\omega_1 Q_1 a_2(z,t)D^*(z,t) - \frac{1}{4}g_1\Gamma a_2(z,t)\int_0^t e^{-\frac{\Gamma}{2}(t-s)}a_1(z,s)a_2^*(z,s)\mathrm{d}s, \quad (5.1)$$

$$\frac{\partial a_2}{\partial z} - \frac{1}{v}\frac{\partial a_2}{\partial t} - \frac{1}{2}\alpha a_2 = i\omega_2 Q_2 a_1(z,t)D(z,t) - \frac{1}{4}g_2\Gamma a_1(z,t)\int_0^t e^{-\frac{\Gamma}{2}(t-s)}a_1^*(z,s)a_2(z,s)\mathrm{d}s, \quad (5.2)$$

where $g_1 = g_0\omega_1/\omega_2$, $g_2 = g_0$, and the SBS gain parameter $g_0 = 4v_a\omega_2\Omega|Q_2|^2/\Gamma$ (with units of $\mathrm{m}^{-1}\mathrm{W}^{-1}$) as defined in Chapter 4.

The approach of the numerical method is to solve (5.1) and (5.2) in a step-wise

manner to find the optical fields; the optical fields at each time step are then substituted into (3.14) to obtain the acoustic envelope field, and the process is repeated. At each time step the solution requires calculation of the thermal noise function $D(z,t)$ which behaves as a random walk in time while remaining white in space. The optical equations are solved with the input boundary conditions $a(0,t) = a_p(t)$ and $a(L,t) = a_s(t)$; in general, these boundary conditions may be stochastic to account for noise in the input lasers. In the following we first describe the approach taken to compute the thermal noise function, then discuss the inclusion of noise into the boundary conditions, before describing the iterative algorithm itself.

It should be noted that it is also possible to solve (4.1a)−(4.1c) directly without integrating the acoustic envelope field in time first (as in (3.14)), and this procedure would yield the same results. However, since the thermal background field is assumed to be in an equilibrium state by $t = 0$, this alternative method would require simulating the acoustic envelope field for a very long time $t < 0$. This is computationally less efficient and poses no advantages over the present method.

5.2.2 Computing the thermal noise function

The function $D(z,t)$ contains all the thermal noise information about the system. To model $D(z,t)$ numerically, we note that its evolution in time corresponds to an Ornstein-Uhlenbeck process [157]. Equation (3.15) can be written in Itô differential form [158] as

$$\mathrm{d}D(z_j,t) = -\frac{1}{2}\Gamma D(z_j,t)\mathrm{d}t + v_a\sqrt{\sigma}R(z_j,t)\mathrm{d}t, \tag{5.3}$$

where the z axis is discretized on the equally spaced grid z_j with spacing Δz. We know that $R(z_j,t_n)\mathrm{d}t = \frac{1}{\sqrt{\Delta z}}\mathrm{d}W_j(t_n)$ where $\mathrm{d}W_j(t_n)$ is the standard complex-valued Wiener increment in time, and the scaling factor arises from the Dirac-delta nature of the continuous-space auto-correlation function of $D(z,t)$. The complex increment $\mathrm{d}W_j(t)$ is a linear combination of two independent real Wiener processes

$$\mathrm{d}W_j(t) = \frac{1}{\sqrt{2}}\left[\mathrm{d}W_j^{(1)}(t) + i\mathrm{d}W_j^{(2)}(t)\right], \tag{5.4}$$

where $\left\langle \mathrm{d}W_j^{(p)}(t)\mathrm{d}W_j^{(q)}(t)\right\rangle = \delta_{pq}\mathrm{d}t$, where δ_{pq} is the Kronecker delta. Integrating (5.3) from 0 to t yields the analytic solution

$$D(z_j,t) = e^{-\frac{1}{2}\Gamma t}D_0(z_j) + v_a\sqrt{\frac{\sigma}{\Delta z}}\int_0^t e^{-\frac{\Gamma}{2}(t-s)}\mathrm{d}W_j(s), \tag{5.5}$$

where $D_0(z_j)$ is the cumulative random walk from $t = -\infty$ up to $t = 0$. This quantity is calculated using

$$D_0(z_j) = \frac{1}{\sqrt{2}}\left[\mathcal{N}_{z_j}^{(1)}\left(0, \frac{v_a\sigma}{\alpha_{\mathrm{ac}}\Delta z}\right) + i\mathcal{N}_{z_j}^{(2)}\left(0, \frac{v_a\sigma}{\alpha_{\mathrm{ac}}\Delta z}\right)\right], \tag{5.6}$$

where $\mathcal{N}_{z_j}^{(1,2)}\left(0, v_a\sigma/\alpha_{\mathrm{ac}}\Delta z\right)$ are normal random variables with zero mean and variance $v_a\sigma/(\alpha_{\mathrm{ac}}\Delta z)$, independently sampled at each z_j. Numerically, we can compute the integral in (5.5) as follows: first, we note that since the integrand is a deterministic function of time, and $\mathrm{d}W_j(s)$ is a normally distributed stochastic process, the integral is also a normally distributed stochastic process. Secondly, $\mathrm{d}W_j(s)$ is a complex-valued process,

so the integral can be split into two statistically independent real-valued integrals

$$\int_0^t e^{-\frac{\Gamma}{2}(t-s)}\mathrm{d}W_j(s) = \frac{1}{\sqrt{2}}\int_0^t e^{-\frac{\Gamma}{2}(t-s)}\mathrm{d}W_j^{(1)}(s) + i\frac{1}{\sqrt{2}}\int_0^t e^{-\frac{\Gamma}{2}(t-s)}\mathrm{d}W_j^{(2)}(s), \tag{5.7}$$

each of these real integrals will have the same statistical properties, namely

$$\left\langle \int_0^t e^{-\frac{\Gamma}{2}(t-s)}\mathrm{d}W_j^{(q)}(s) \right\rangle = 0. \tag{5.8}$$

The variance is derived using the Itô isometry property [159]

$$\left\langle \left(\int_0^t X(s)\mathrm{d}W(s) \right)^2 \right\rangle = \left\langle \int_0^t X^2(s)\mathrm{d}s \right\rangle. \tag{5.9}$$

The proof of this identity is as follows: let the Itô integral be approximated by a discrete sum such as

$$\int_0^t X(s)\mathrm{d}W(s) \approx \sum_k X(s_k)\Delta W_k$$

where all the discrete Wiener steps ΔW_k are statistically independent from one another, namely $\langle \Delta W_j \Delta W_k \rangle = \delta_{jk}\Delta t$ where δ_{jk} is the Kronecker-delta. Here the assumption is that $X(t)$ and $W(t)$ are statistically independent. The expected value of the square of this integral can then be written as

$$\begin{aligned}
\left\langle \left(\int_0^t X(s)\mathrm{d}W(s) \right)^2 \right\rangle &\approx \left\langle \left(\sum_k X(s_k)\Delta W_k \right)^2 \right\rangle \\
&= \Big\langle (X(s_1)\Delta W_1)^2 + (X(s_2)\Delta W_2)^2 + (X(s_3)\Delta W_3)^2 + \cdots \\
&\qquad + X(s_1)X(s_2)\Delta W_1\Delta W_2 + X(s_1)X(s_3)\Delta W_1\Delta W_3 + \cdots \Big\rangle \\
&= \left\langle \sum_k X^2(s_k)\,(\Delta W_k)^2 + \sum_{j\neq k} X(s_j)X(s_k)\Delta W_j\Delta W_k \right\rangle \\
&= \sum_k \langle X^2(s_k)\rangle \langle (\Delta W_k)^2\rangle + \sum_{j\neq k}\langle X(s_j)X(s_k)\rangle\langle \Delta W_j\Delta W_k\rangle \\
&= \sum_k \langle X^2(s_k)\rangle \Delta t \\
&\approx \int_0^t \langle X^2(s)\rangle \mathrm{d}s = \left\langle \int_0^t X^2(s)\mathrm{d}s \right\rangle,
\end{aligned}$$

which concludes the proof. Using this isometry property of Itô integrals, we then write

$$\left\langle \left(\int_0^t e^{-\frac{\Gamma}{2}(t-s)}\mathrm{d}W_j^{(q)}(s) \right)^2 \right\rangle = \frac{1}{\Gamma}\left(1 - e^{-\Gamma t}\right), \tag{5.10}$$

which leads to the result for the variance

$$\mathrm{Var}\left[\int_0^t e^{-\frac{\Gamma}{2}(t-s)}\mathrm{d}W_j^{(q)}(s) \right] = \frac{1}{\Gamma}\left(1 - e^{-\Gamma t}\right). \tag{5.11}$$

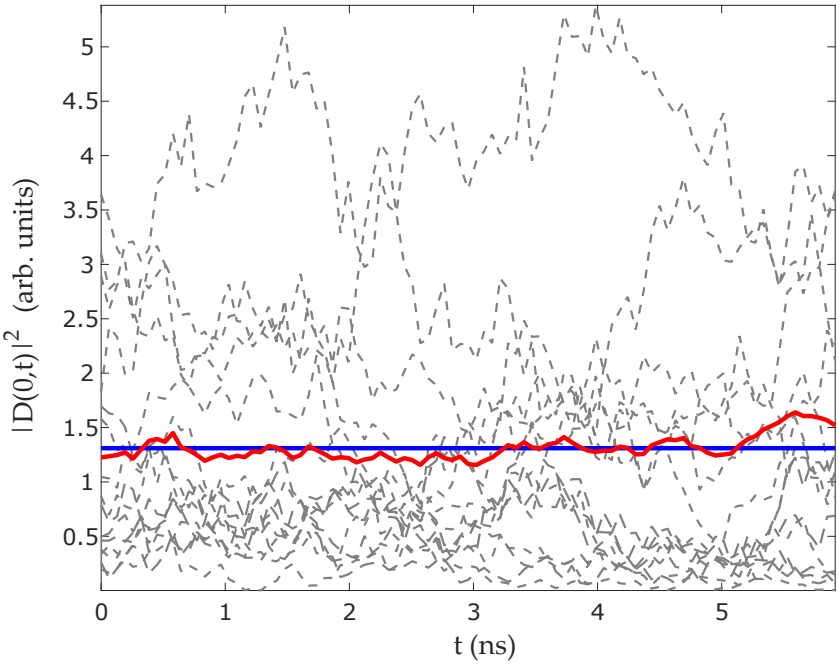

FIGURE 5.2: Multiple independent realizations (dashed grey) of the modulus squared of the thermal function $|D(z_j,t)|^2$ at an arbitrary position z_j, the numerical ensemble average over 20 realizations (red) and the analytic ensemble average (blue). We use a temperature of $T = 300$ K, $v_a = 2500$ m/s, $\tau_a = 5.3$ ns, $\Delta z = 0.79$ mm and $\Delta t = 6.43$ ps.

This means the integral can be computed as a normal random variable as

$$\int_0^t e^{-\frac{\Gamma}{2}(t-s)} \mathrm{d}W_j(s) \sim \sqrt{\frac{1-e^{-\Gamma t}}{2\Gamma}} \left[\mathcal{N}^{(1)}_{z_j,t}(0,1) + i\mathcal{N}^{(1)}_{z_j,t}(0,1)\right], \tag{5.12}$$

where $\mathcal{N}^{(1,2)}_{z_j,t_n}(0,1)$ is a standard normal random number sampled independently at each point (z_j, t_n). Thus, we simulate (5.5) as a random walk using discrete increments in time Δt

$$D(z_j,t_{n+1}) = e^{-\frac{1}{2}\Gamma\Delta t} D(z_j,t_n) + \gamma(\Delta t)\left[\mathcal{N}^{(1)}_{z_j,t_n}(0,1) + i\mathcal{N}^{(2)}_{z_j,t_n}(0,1)\right], \tag{5.13}$$

where

$$\gamma(\Delta t) = v_a \sqrt{\frac{\sigma\left(1-e^{-\Gamma\Delta t}\right)}{2\Delta z\Gamma}}, \tag{5.14}$$

and setting the initial value as $D(z_j,t_0) = D_0(z_j)$. Fig. 5.2 shows multiple realizations of $D(z_j,t)$ at an arbitrary point z_j and its ensemble average.

5.2.3 Noisy boundary conditions

Input laser noise can be an important feature in SBS experiments. In the context of the SBS envelope equations, it enters in the form of random phase fluctuations at the inputs of the waveguide, namely $z = 0$ for the pump field and $z = L$ for the Stokes field. We simulate this laser phase noise in the input fields by modeling the boundary

conditions as

$$a_1(0,t_n) = a_p(t_n) = \sqrt{P_1^{\text{in}}(t_n)}e^{i\phi_1(t_n)}, \tag{5.15}$$

$$a_2(L,t_n) = a_s(t_n) = \sqrt{P_2^{\text{in}}(t_n)}e^{i\phi_2(t_n)}, \tag{5.16}$$

where $P_1^{\text{in}}(t)$ and $P_2^{\text{in}}(t)$ are deterministic envelope shape functions for the pump and Stokes fields respectively representing input power from the lasers. The variables $\phi_1(t)$ and $\phi_2(t)$ are stochastic phase functions modeled as zero-mean independent Brownian motions. The variation in the phase $\phi(t)$ is related to the laser's intrinsic linewidth $\Delta\nu_L$, or conversely the coherence time $\tau_{\text{coh}} = 1/(\pi\Delta\nu_L)$, via the expression $\left\langle [\phi(t+\tau)-\phi(t)]^2 \right\rangle = 2\pi\Delta\nu_L|\tau|$, where $\tau = t' - t$ for the two times t' and t [144, 145, 146]. Following a similar numerical procedure to [147], we compute $\phi_j(t)$ as

$$\phi_j(t) = \sqrt{2\pi\Delta\nu_L}\int_0^t \mathrm{d}W_j(s), \tag{5.17}$$

where $\mathrm{d}W(s)$ is a real-valued Wiener process increment in time. To generate the random walk numerically, we cast this integral as an Itô differential equation $\mathrm{d}\phi_j(t) = \sqrt{2\pi\Delta\nu_L}\mathrm{d}W_j(t)$, which is discretized using an Euler-Mayurama [148] scheme as

$$\phi_j(t_{n+1}) = \phi_j(t_n) + \sqrt{2\pi\Delta\nu_L}\sqrt{\Delta t}\,\mathcal{N}_{t_n}(0,1), \tag{5.18}$$

where $\mathcal{N}_{t_n}(0,1)$ is a standard normally distributed random number sampled at each t_n. A simulation of a single realization of the noisy boundary conditions is shown in Figure 5.3.

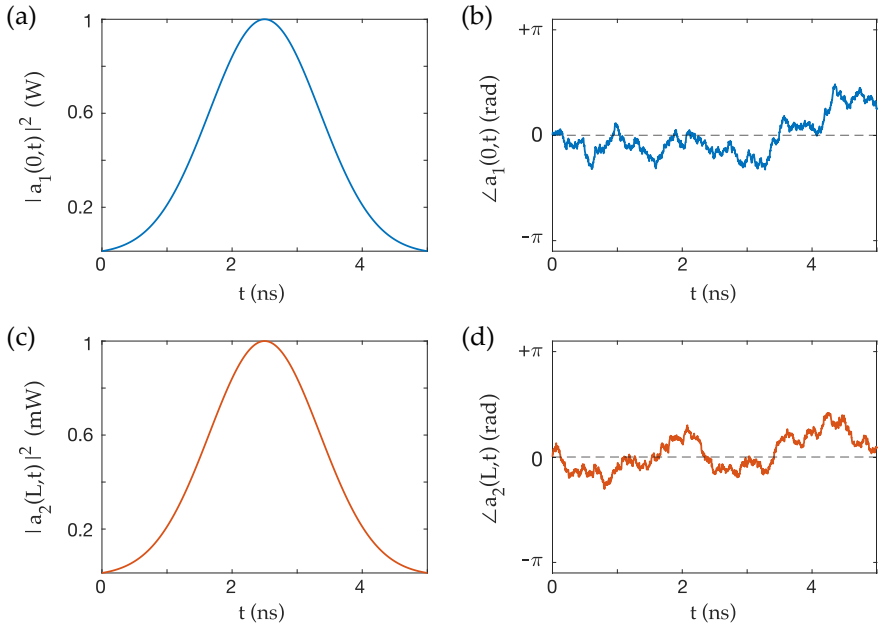

FIGURE 5.3: Single realization of the noisy boundary conditions. The plots show (a) pump power, (b) pump phase, (c) Stokes power and (d) Stokes phase. Both pulses are Gaussian with FWHM of 2 ns. The laser linewidth used here is $\Delta\nu_L = 100$ MHz.

5.2.4 The numerical algorithm

We now present the main numerical algorithm of this paper. The algorithm consists of two consecutive steps: first, we solve Eqs. (4.1a) and (4.1b) in the absence of optical loss or nonlinear interactions. In other words, we solve the following pair of advection equations

$$\frac{\partial a_1}{\partial z} + \frac{1}{v}\frac{\partial a_1}{\partial t} = 0, \tag{5.19}$$

$$\frac{\partial a_2}{\partial z} - \frac{1}{v}\frac{\partial a_2}{\partial t} = 0. \tag{5.20}$$

With the boundary conditions $a_1(0,t) = a_p(t)$ and $a_2(L,t) = a_s(t)$, these have the elementary solutions

$$a_1(z,t) = a_p\left(t - \frac{z}{v}\right), \tag{5.21}$$

$$a_2(z,t) = a_s\left(t - \frac{L-z}{v}\right). \tag{5.22}$$

Setting the numerical grid parameter $\Delta z = v\Delta t$ further simplifies (5.21) and 5.22 to

$$a_1(z_j,t_n) \leftarrow a_1(z_{j-1},t_{n-1}), \tag{5.23}$$

$$a_2(z_j,t_n) \leftarrow a_2(z_{j+1},t_{n-1}), \tag{5.24}$$

such that the optical fields are shifted in space by exactly Δz during each time iteration. The envelope field $b(z,t)$ is assumed to remain stationary in space during each time step, as is typical in the context of SBS experiments involving pulses [82]. After the fields are shifted across the waveguide, we solve the time evolution equations at each point z_j independently; i.e. we solve

$$\frac{1}{v}\frac{\partial a_1(z_j,t)}{\partial t} = -\frac{1}{2}\alpha a_1(z_j,t) - \frac{1}{4}g_1\Gamma a_2(z_j,t)I^*_{1,2}(z_j,t) + i\omega_1 Q_1 a_2(z_j,t)D^*(z_j,t), \tag{5.25}$$

$$\frac{1}{v}\frac{\partial a_2(z_j,t)}{\partial t} = -\frac{1}{2}\alpha a_2(z_j,t) + \frac{1}{4}g_2\Gamma a_1(z_j,t)I_{1,2}(z_j,t) - i\omega_2 Q_2 a_1(z_j,t)D(z_j,t), \tag{5.26}$$

where the interaction integral $I_{1,2}(z_j,t)$ is computed as

$$I_{1,2}(z_j,t_n) = \frac{\Delta t}{2}e^{-\frac{\Gamma}{2}n\Delta t}\Big[I_{1,2}(z_j,t_{n-1}) + a_1^*(z_j,t_{n-1})a_2(z_j,t_{n-1})e^{\frac{\Gamma}{2}(n-1)\Delta t} + a_1^*(z_j,t_n)a_2(z_j,t_n)e^{\frac{\Gamma}{2}n\Delta t}\Big]. \tag{5.27}$$

To integrate the envelope fields a_1 and a_2 in time, we use an Euler-Mayurama scheme [160], which yields the following finite-difference equations

$$a_1(z_j,t_{n+1}) = \left[1 - \frac{v\alpha\Delta t}{2}\right]a_1(z_j,t_n) - v\Delta t\left[\frac{g_1\Gamma I^*_{1,2}(z_j,t_n)}{4} - i\omega_1 Q_1 D^*(z_j,t_n)\right]a_2(z_j,t_n), \tag{5.28}$$

$$a_2(z_j,t_{n+1}) = \left[1 - \frac{v\alpha\Delta t}{2}\right]a_2(z_j,t_n) + v\Delta t\left[\frac{g_2\Gamma I_{1,2}(z_j,t_n)}{4} - i\omega_2 Q_2 D(z_j,t_n)\right]a_1(z_j,t_n). \tag{5.29}$$

The acoustic field is computed at each z_j and t_{n+1} after computing $a_{1,2}$, via the equation

$$b(z_j, t_{n+1}) = iv_a \Omega Q_a I_{12}(z_j, t_{n+1}) + \sqrt{\Delta z} D(z_j, t_{n+1}). \tag{5.30}$$

The factor $\sqrt{\Delta z}$ in front of the thermal noise function D is used so that the acoustic noise scales only with respect to the physical parameters such as v_a, σ and α_{ac}, and not with respect to the numerical grid parameters (Δz) which would otherwise lead to non-physical results. Once all the fields are computed at t_{n+1}, we repeat the drift steps in (5.23) and (5.24) and the entire process is iterated until the optical fields have propagated across the waveguide. The steps of this numerical method are given in Algorithm 1.

Algorithm 1 Numerical algorithm

```
Compute D(z_j, t_n) for all t_n
Compute φ_{1,2}(t_n) for all t_n
Set a_{1,2} = 0 inside z ∈ [0, L]
for n = 1 to N_t − 1 do                    ▷ N_t = size of time grid
    Insert noisy boundary conditions in a_{1,2} at t_n
    Shift optical fields a_{1,2} in space by Δz
    Compute interaction integral I_{1,2}(z_j, t_n)
    Compute a_{1,2}(z_j, t_{n+1}) from a_{1,2}(z_j, t_n)
    Compute b(z_j, t_{n+1})
end for
```

5.2.5 Statistical properties of the fields

The iterative scheme in Algorithm 1 computes a single realization of the SBS interaction given a specific set of input parameters. We must repeat this process M times with the same input parameters to build an ensemble of M independent simulations, from which statistical properties may be calculated. For instance, the true average of the power for all three fields ($P_{1,2}$ for the optical fields and P_a for the acoustic field) may be calculated as

$$\left\langle P_{1,2}(z_j, t_n) \right\rangle = \left\langle \left| a_{1,2}(z_j, t_n) \right|^2 \right\rangle \approx \frac{1}{M} \sum_{m=1}^{M} \left| a_{1,2}^{(m)}(z_j, t_n) \right|^2, \tag{5.31}$$

$$\left\langle P_a(z_j, t_n) \right\rangle = \left\langle \left| b(z_j, t_n) \right|^2 \right\rangle \approx \frac{1}{M} \sum_{m=1}^{M} \left| b^{(m)}(z_j, t_n) \right|^2, \tag{5.32}$$

where m refers to a specific realization of each process. Similarly, we compute the standard deviation in the power at each point (z_j, t_n) as

$$\text{std}\left[P_{1,2}(z_j, t_n) \right] = \sqrt{\left\langle \left[P_{1,2}(z_j, t_n) \right]^2 \right\rangle - \left\langle P_{1,2}(z_j, t_n) \right\rangle^2}, \tag{5.33}$$

$$\text{std}\left[P_a(z_j, t_n) \right] = \sqrt{\left\langle \left[P_a(z_j, t_n) \right]^2 \right\rangle - \left\langle P_a(z_j, t_n) \right\rangle^2}. \tag{5.34}$$

The standard deviation is useful when comparing with experiments, since it gives a quantitative measure of the size of the power fluctuations in the measured optical fields.

5.3 Results and Discussion

We demonstrate the numerical method by simulating the SBS interaction of the three fields with both thermal noise ($T = 300$ K, $\Delta\nu_B = 30$ MHz) and laser noise ($\Delta\nu_L = 100$ kHz), using a chalcogenide waveguide of length 50 cm, with the properties in Table 5.1. Although our formalism includes optical loss through the factor α, we have chosen $\alpha = 0$ in the simulations to focus on the effect of net SBS gain and pulse properties on the noise. Here we study the noisy SBS interaction in two different cases: spontaneous scattering and stimulated scattering, and investigate the effects of pump width and SBS gain on the noise properties of the Stokes field.

Parameter	Value	Paramter	Value
Waveguide length L	50 cm	Peak pump power	1 W
Waveguide temperature T	300 K	Peak Stokes power	0−1 mW
Refractive index n	2.44	Laser linewidth $\Delta\nu_L$	100 kHz
Acoustic velocity v_a	2500 m/s	Pump pulse FWHM	0.5−5 ns
Brillouin linewidth $\Delta\nu_B$	30 MHz	Stokes pulse FWHM	1 ns
Brillouin shift $\Omega/2\pi$	7.7 GHz	Grid size (space) N_z	1001
Brillouin gain parameter g_0	423 $\mathrm{m^{-1}W^{-1}}$	Grid size (time) N_t	2601
Optical wavelength λ	1550 nm	Step-size Δt	4.07 p

TABLE 5.1: Simulation parameters using a chalcogenide waveguide of the type shown in [154].

5.3.1 The spontaneous Brillouin scattering case

We first consider the situation in which there is no input Stokes field from an external laser source, and the Stokes arises purely from the interaction between the pump and the thermal field — this situation is customarily referred to as *spontaneous* or *spontaneously-seeded* Brillouin scattering. We specify a Gaussian pump pulse of varying widths and constant peak power, with input phase noise ($\Delta\nu_L = 100$ kHz). Setting the waveguide temperature at 300 K and the pump FWHM of 2 ns, in Fig. 5.4(a)−(c) we see that the thermal acoustic field interacts with the pump to generate an output Stokes signal. At the same time, the Stokes field depletes some of the pump and amplifies the acoustic field, which leads to more Stokes energy being generated. The noisy character of the Stokes field in Fig. 5.4(b) is due to the incoherent thermal acoustic background, which generates multiple random Stokes frequencies. In this short-pump regime, the SBS amplification is small, and the generated Stokes field remains incoherent.

As we increase the width of the pump to 5 ns, the net SBS gain in the waveguide also increases. In this long-pump regime, the (spontaneously-generated) Stokes field is amplified coherently, as shown in Fig. 5.5(b). However, it should be noted that, although the Stokes output becomes smooth, there is significant variation in the peak Stokes power from one independent realization to the next, as illustrated in Fig. 5.6(a) and (b). The standard deviation of the Stokes power over multiple independent realizations increases with longer pump pulses, as shown in Fig. 5.5(e).

As the pump becomes very long we approach the CW regime, in which the pump power ramps up quickly at $z = 0$ and is kept at a constant value. If the waveguide is sufficiently long, the spontaneously generated Stokes field is amplified coherently until pump depletion begins to take effect, initially at $z = 0$ and then throughout the length

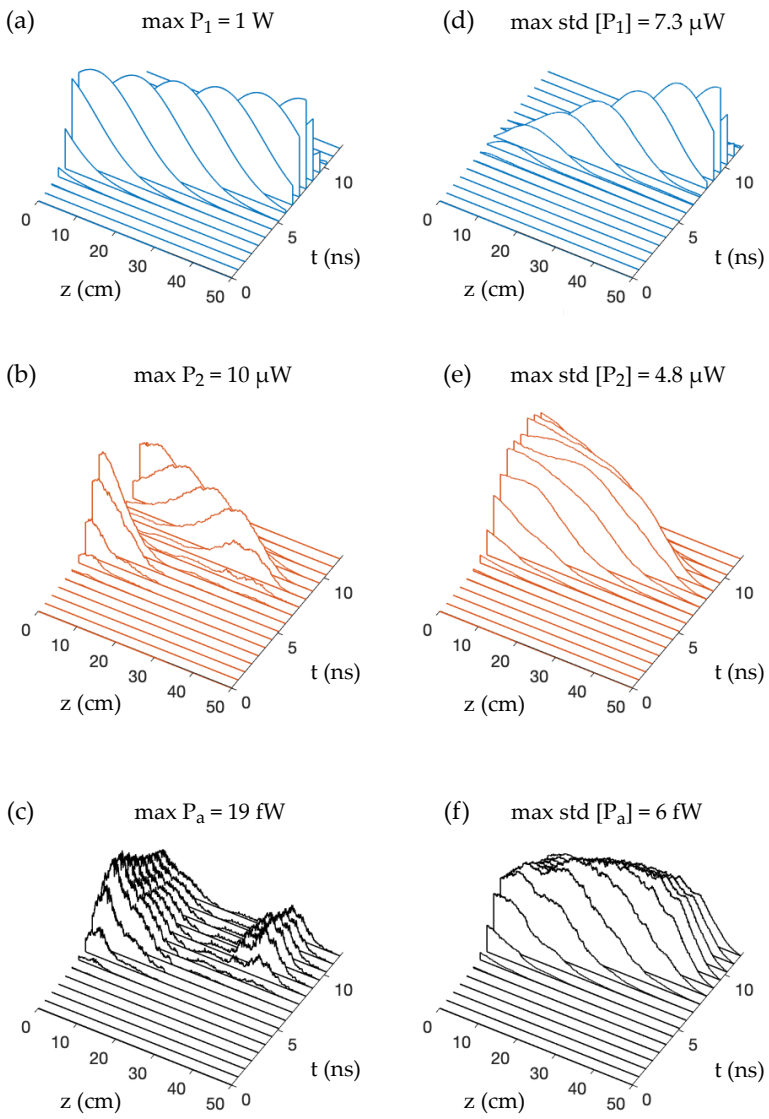

FIGURE 5.4: Waterfall plots for a single numerical realization of (a) pump power, (b) Stokes power and (c) acoustic power in the spontaneous scattering case, using a Gaussian pump of FWHM 2 ns and peak power of 1 W. Plots (d)−(f) show the standard deviation of the field powers at each point (z, t), calculated from 100 independent realizations of the SBS interaction.

of the waveguide, until both Stokes and pump fields relax into the steady-state configuration in which the pump decreases exponentially, as shown in Fig. 5.8(a)−(b). When such a steady state is reached, the depletion induced by the spontaneously-seeded Stokes may inhibit Brillouin scattering from an input Stokes pulse injected at $z = L$.

Returning to the pulsed case, we investigate the effect of increasing the peak pump power, and therefore the overall SBS gain, on the amplification of the spontaneous Stokes field. Figure 5.7 shows how the Stokes spectral linewidth increases for input pump powers between 0.1−2 W for a Gaussian pump pulse with fixed FWHM of 5 ns. The increase in linewidth occurs due to the transition from linear to nonlinear SBS amplification: in the linear amplification regime, the spontaneously generated Stokes field retains a constant temporal width while its peak power increases with input pump power. In the nonlinear amplification regime, the Stokes field undergoes

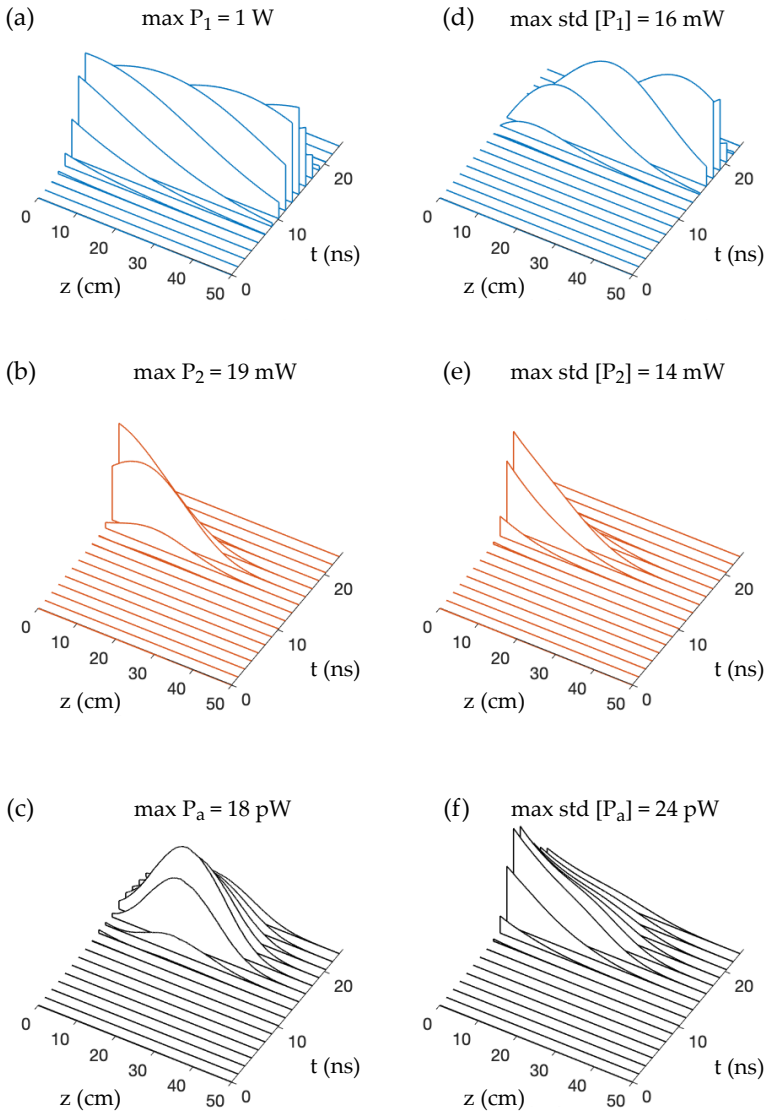

FIGURE 5.5: Waterfall plots for a single numerical realization of (a) pump power, (b) Stokes power and (c) acoustic power in the spontaneous scattering case, using a Gaussian pump of FWHM 5 ns and peak power of 1 W. Plots (d)−(f) show the standard deviation of the field powers at each point (z, t), calculated from 100 independent realizations of the SBS interaction.

temporal compression as a result of the central peak of the pulse being amplified faster than the tails. Beyond 2 W of peak pump power, the spectral linewidth of the Stokes field narrows as pump depletion becomes significant, because the Stokes field is prevented from uniformly experiencing exponential gain throughout the waveguide, an effect which is also observed in the CW pump case [161].

5.3.2 The effect of laser phase noise

Our previous simulations included laser phase noise corresponding to a laser linewidth of 100 kHz in the pump. This is equivalent to a coherence time of $\tau_{\text{coh}} = 3.2\ \mu$s, which is at least 100 times larger than the characteristic time of the SBS interaction in Fig. 5.4−5.8. For this reason it is understandable that no contribution from the laser

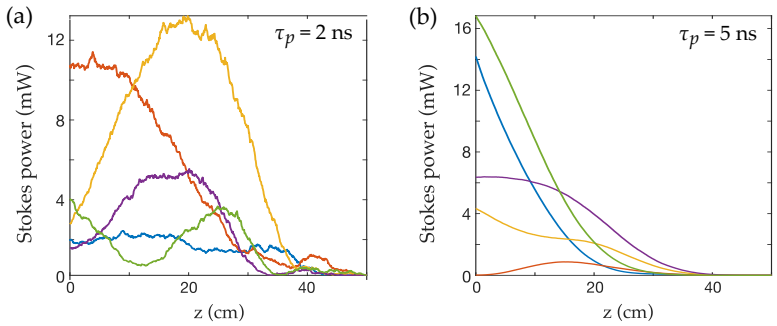

FIGURE 5.6: Multiple independent realizations of the spontaneously generated Stokes power across the waveguide for (a) 2 ns wide pump and (b) 5 ns wide pump. These snapshots are taken at the time when the peak of the pump pulse reaches $z = 50$ cm.

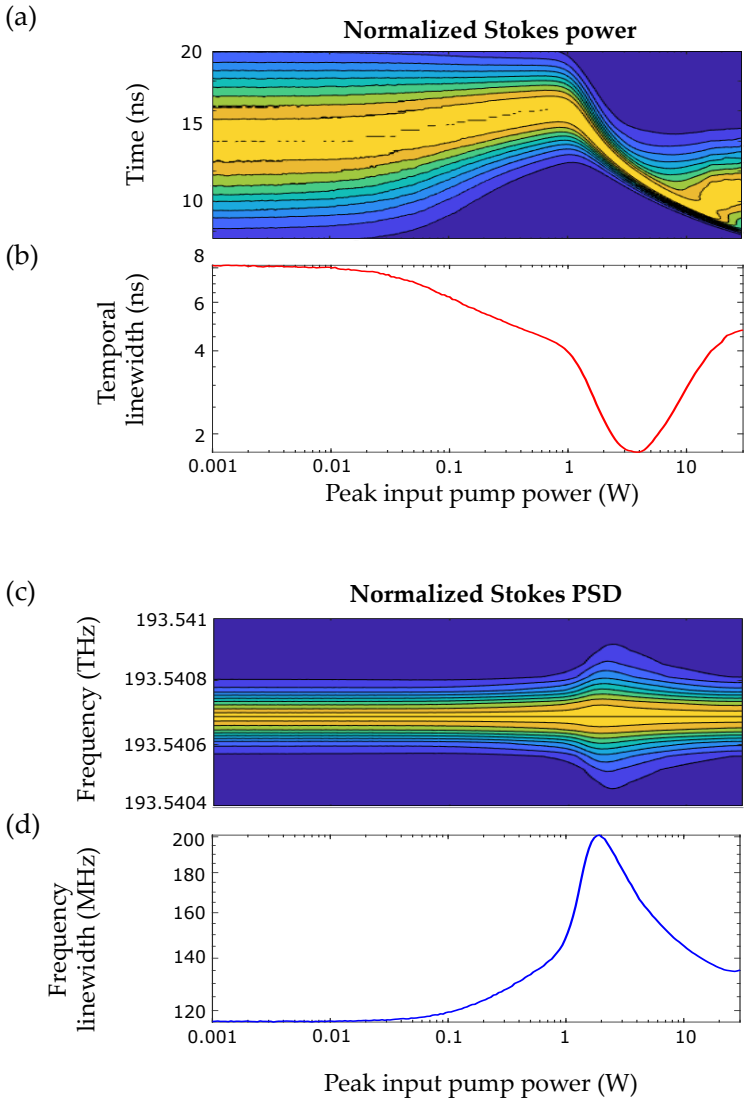

FIGURE 5.7: Spontaneously generated Stokes field (at $z = 0$) over 500 independent realizations, using a 5 ns Gaussian pump pulse and varying input peak pump power. (a) ensemble averaged Stokes power normalized by the maximum power at each input pump power, (b) FWHM of the Stokes in time domain. (c) normalized power spectral density (PSD) of the Stokes field, and (d) Stokes FWHM in frequency domain.

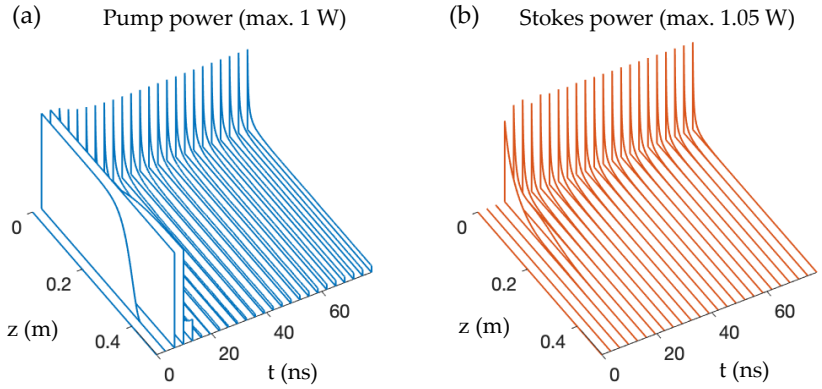

FIGURE 5.8: Waterfall plots for a single numerical realization of (a) pump power and (b) Stokes power in the spontaneous scattering case, using a CW pump with 1 W peak power and a laser linewidth of 100 kHz.

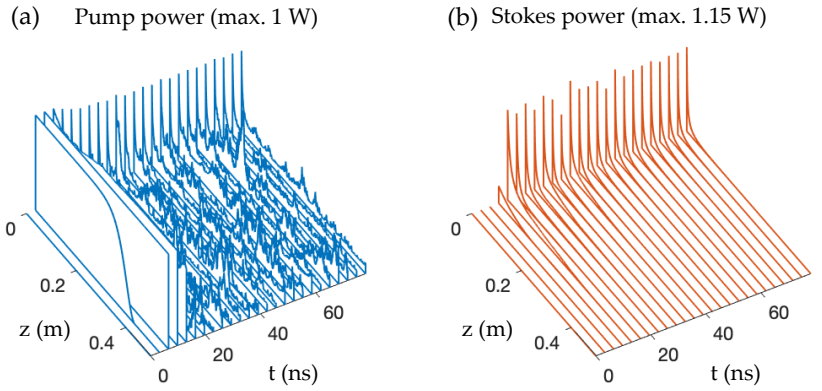

FIGURE 5.9: Waterfall plots for a single numerical realization of (a) pump power and (b) Stokes power in the spontaneous scattering case, using a CW pump with 1 W peak power and a laser linewidth of 100 MHz.

phase noise to the optical or acoustic fields was observed. The contribution of laser phase noise can however be observed if the linewidth of the pump is suffiently broad. We therefore consider the CW-pump regime with zero Stokes input power, with a laser linewidth of 100 MHz, which corresponds to a coherence time of 3.2 ns (Fig. 5.9). We see a significant contribution from the laser phase noise in the form of amplitude fluctuations, which are completely absent in the 100 kHz linewidth case (Fig. 5.8). From this we infer that when the laser coherence time τ_{coh} is comparable to the pulse widths $\tau_{p,s}$, the fluctuations in the phase are fast enough to be transferred to the envelope of the pulse. However, when $\tau_{\text{coh}} \gg \tau_{p,s}$, the noisy character of the envelope fields will vanish. This has important implications for the case of pulsed SBS: phase noise can only play a significant role in the interaction if $\tau_{\text{coh}} \leq \tau_{p,s}$. For lasers with a relatively small linewidth, such as in the kHz range, phase noise will only become a significant effect when operating in the long-pulse or CW regime.

5.3.3 The stimulated Brillouin scattering case

We now examine the case of *seeded* Brillouin scattering, in which a Stokes signal is injected at $z = L$. We first consider a 1 mW peak power Stokes pulse of FWHM 1 ns in

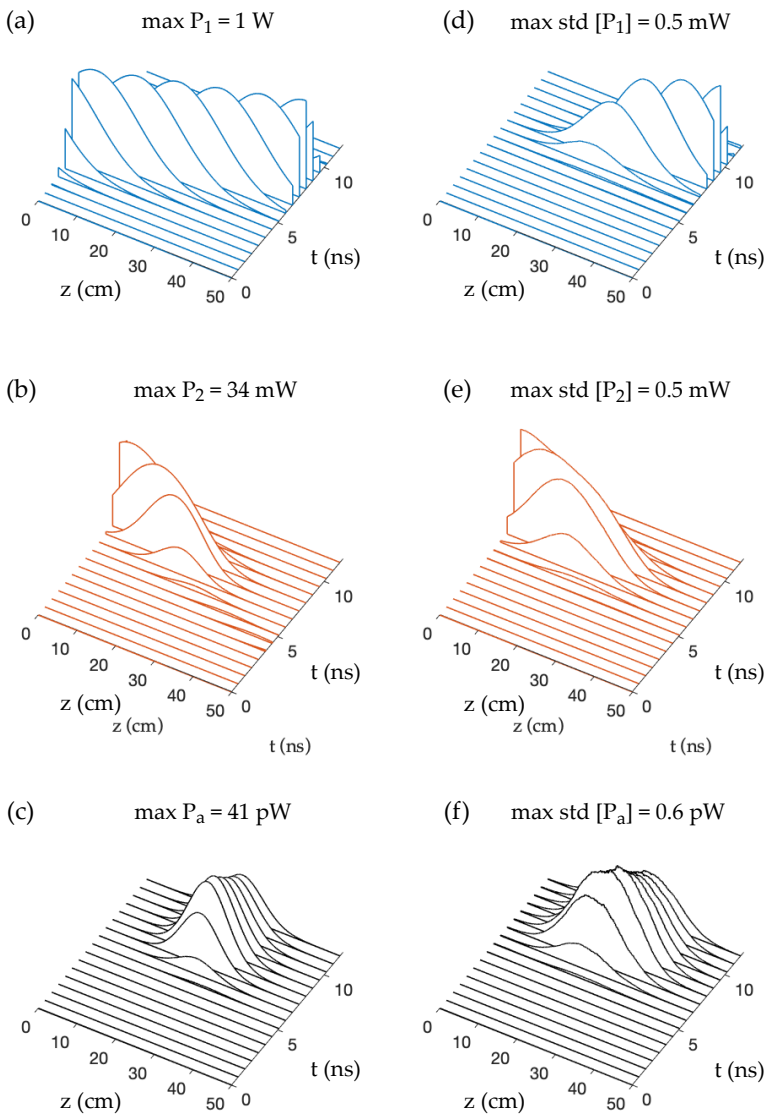

FIGURE 5.10: Waterfall plots for a single numerical realization of (a) pump power, (b) Stokes power and (c) acoustic power in the stimulated scattering case, using a Gaussian pump pulse of width 2 ns and peak power 1 W. The input Stokes pulse has width 1 ns and peak power 1 mW. Plots (d)−(f) show the standard deviation in the fields at each point (z, t) for 100 independent realizations of the SBS interaction.

the same chalcogenide waveguide as before. The pump is a Gaussian pulse of constant peak power of 1 W, with a width of 2 ns. As can be seen in Fig. 5.10, the Stokes pulse remains smooth throughout the interaction, and although the standard deviation over 100 independent realizations is approximately 1.4% of the peak value, there are no visible fluctuations in the power across space or time in Fig. 5.10(b). A closer look at multiple individual realizations in Fig. 5.11(a) reveals that there is a measurable level of variation in the Stokes power, although each individual realization of the Stokes field is smooth. By increasing the pump width to 5 ns as shown in Fig. 5.11(b), we also increase the standard deviation in the Stokes, however each independent realization appears smoother compared to Fig. 5.11(a). This further demonstrates how in the longer pump, high SBS gain regime, the amplification of the Stokes is sufficient to cancel random phase differences in the Stokes field, as we observed in the spontaneous scattering

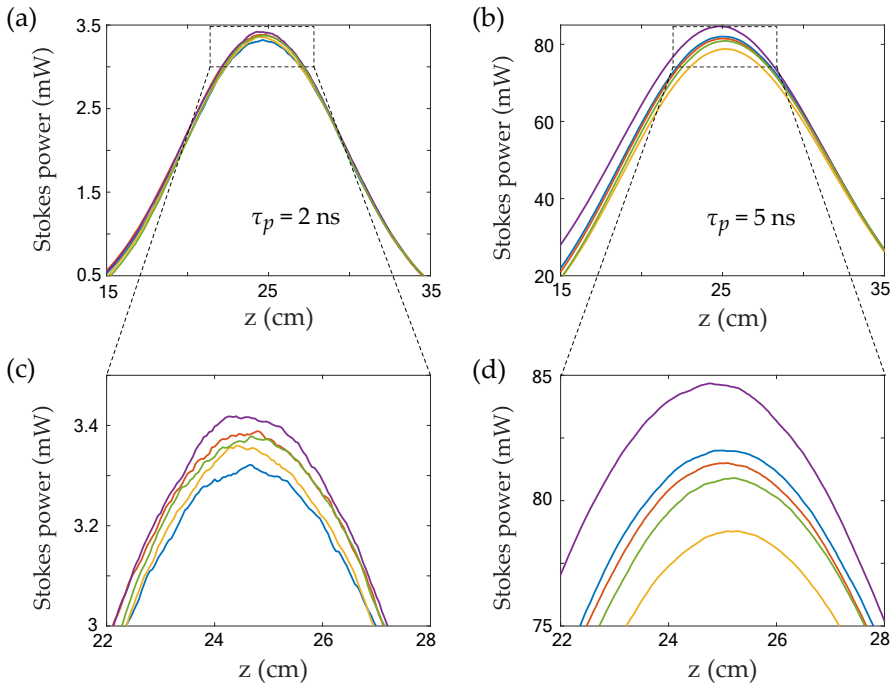

FIGURE 5.11: Multiple independent realizations of the Stokes power across the waveguide for (a) 2 ns wide pump and (b) 5 ns wide pump, shown at the time where the pump pulse peak reaches $z = 50$ cm.

case in Fig. 5.5.

5.3.4 Convergence of the method

Convergence in the noiseless case

We first test our numerical method against a known analytic solution for steady-state optical fields, as outlined in [66]. To achieve this, we set all the noise sources in our algorithm to zero, including thermal and input phase noise, and simulate constant power envelope fields a_1 and a_2 in the same chalcogenide waveguide using a 100 mW pump and 1 mW Stokes, with $\alpha = 0.01$ dB/cm optical attenuation. The fields are simulated for a sufficiently long time so that they reach a steady-state, in this case 650 ns. The overlaid plots between the analytic solutions from [66] and our numerical solutions are shown in Fig. 5.12 for a step-size $\Delta t = 4.07$ ps.

The convergence plots are shown in Fig. 5.13. As it can be seen, the convergence rate for the pump and Stokes powers is linear with the step size Δt, which is expected from the Euler-Mayurama scheme reducing to a simple Euler method in the noiseless case [148].

Convergence with noise

We now study the convergence of the numerical method by looking at the statistical properties of the power in each field at fixed points on (z, t). We use a default minimum step-size in time $\Delta t_{\text{min}} = 40.7$ fs against which we compare the results for larger step-sizes Δt. We compute the relative error in the power and variance of the power, taken over 1,000 independent realizations. These results correspond to what is known as weak convergence in stochastic differential equations [148], where the mean value of a

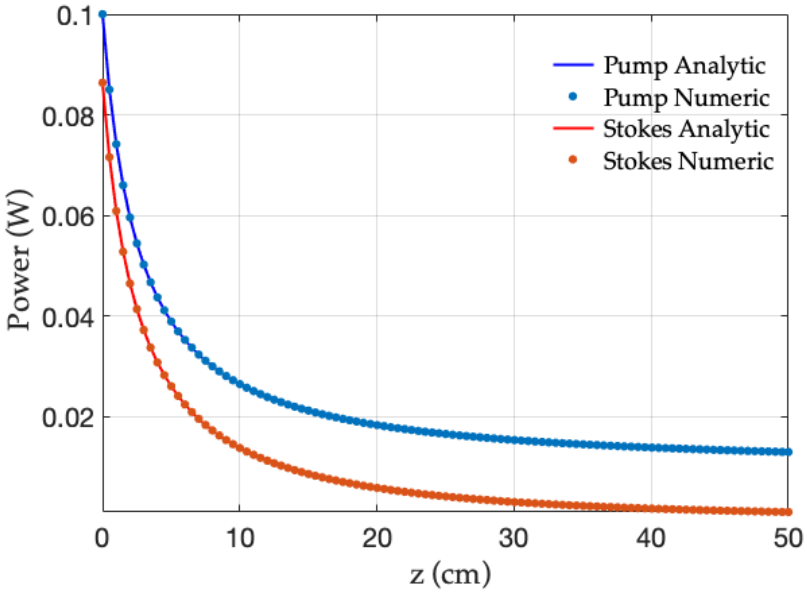

FIGURE 5.12: Comparison of the analytic solutions to the pump and Stokes power from [66] and the numerical solutions computed using the method presented in this Chapter.

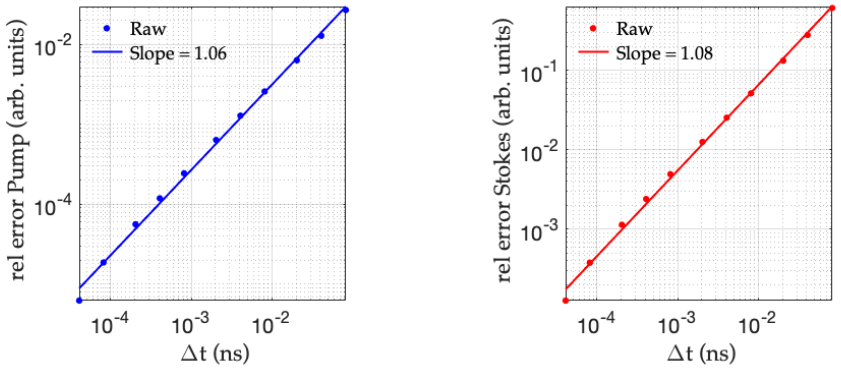

FIGURE 5.13: Noiseless SBS convergence plots for the pump and Stokes power. The relative error in the powers are calculated at the waveguide outputs, namely $z = 0$ for P_2 and $z = L$ for P_1, using the analytic values calculated from [66] as the reference.

random quantity, in our case the power, converges at a specific rate with respect to the step-size used.

The results for the convergence computations are shown in Fig. 5.14. As expected from the Euler-Mayurama scheme [148], the convergence rate is at most linear for the mean power of all three fields. A similar rate of convergence is recorded for the variance in each power, showing a one-to-one error reduction with step-size. Although some higher order methods exist which implement higher order Taylor expansions and Runge-Kutta schemes [148, 162, 163, 164], these methods only work with ordinary stochastic differential equations; numerical methods for partial stochastic differential equations are an active area of research in applied mathematics [165].

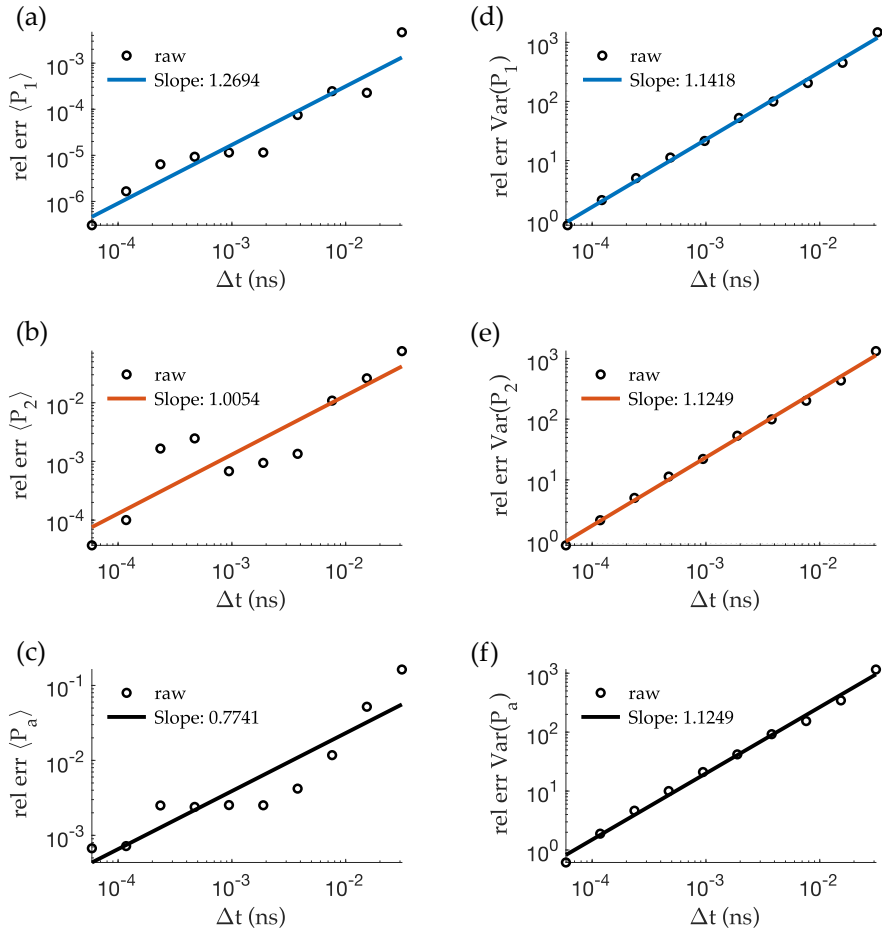

FIGURE 5.14: Convergence plots showing the relative error in the ensemble averaged powers (a)−(c) and in the variance of the powers (d)−(f), as a function of the step-size Δt used in the numerical grid. The reference step-size used is $\Delta t_{\min} = 40.7$ fs. The calculations are based on a sample size of 1,000 independent simulations of the fields. The test problem consists of two optical Gaussian pulses for the pump and Stokes of width 1 ns, with peak powers pump 100 mW (pump) and 10 μW (Stokes). The statistical properties of P_1, P_2 and P_a are calculated from $P_1(L, t_{\max})$, $P_2(0, t_{\max})$ and $P_a(L/2, t_{\max})$ respectively, where $t_{\max}$ is the time at which the peaks of the optical pulses reach the opposite ends of the waveguide. The computations include thermal noise in the waveguide at temperature 300 K, and input laser phase noise with linewidth 100 kHz. The waveguide properties are given in Table 5.1.

5.4 Conclusion

We have presented a numerical method by which the fully-dynamic coupled SBS equations in both CW and pulsed scenarios with thermal and laser noise can be solved. The method offers linear convergence in both the average power and variance of the power of the optical and acoustic fields, with variances that do not depend on step-size. From our simulations, we find that the noise properties of the fields rely on the length of the optical pulses involved as well as on the net SBS gain in the waveguide. For short-pump, low gain regimes, the spontaneous Stokes field is incoherently amplified and exhibits large spatial and temporal fluctuations, whereas for the long-pump, high gain regime the field is amplified coherently, resulting in a smooth field but with large variations in peak power between independent realizations. Similar observations are made for the stimulated scattering case using a Stokes signal. We also find that laser phase

noise does not play a significant role in the SBS interaction unless the laser coherence time is comparable to the characteristic time-scales of the SBS interaction.

Chapter 6

Noise in Brillouin Based Storage

6.1 Overview

This Chapter is based on the contents of the research paper:

> Oscar A. Nieves, Matthew D. Arnold, M. J. Steel, Mikołaj K. Schmidt, and Christopher G. Poulton, "Noise in Brillouin based information storage", Opt. Express 29, 39486-39497 (2021)

In this Chapter, we apply the theoretical and numerical models from Chapters 4 and 5 to simulate Brillouin based storage, accounting for the effects of thermal noise and laser phase noise. We compare the impact of noise on both amplitude and phase encoded storage of information, by using a small pump power and a large Stokes seed power. We quantify the retrieval efficiency and accuracy in the form of the packet error rate (PER) of 8-bit sequences. We find that phase storage offers a significant improvement in the duration with which information can be stored without degradation due to thermal noise. We examine this effect in more detail by computing the effect of thermal noise on the amplitude and phase of a phase-encoded signal, and find that although the variance in amplitude and phase increases at the same rates, the phase information is more robust to noise in accordance with the additive-white-Gaussian-noise (AWGN) model of discrete communication theory.

6.2 Introduction

Opto-acoustic memory storage consists of temporarily storing information encoded from an optical wave into an acoustic wave inside some propagation medium. This process is facilitated by SBS as follows (see Fig. 6.1): an optical data pulse at the pump frequency interacts with an optical "write" pulse (at the Stokes frequency), creating an acoustic hologram where the original data is temporarily stored [59, 109, 166]; an optical "read" pulse at the Stokes frequency can then be used to regenerate the original data pulse. Brillouin-based opto-acoustic information storage has been demonstrated experimentally in fibres [59] as well as more recently in on-chip experiments [109, 113, 62, 166, 110, 63], with storage times ranging up to 40 ns [63]. Opto-acoustic storage, however, will inevitably be limited by noise, which exists because of the presence of thermal phonons in the waveguide, as well as being an inherent feature of the lasers used in the data and read/write pulses. At room temperatures, it is known that thermal noise significantly degrades the quality of Brillouin processes [64, 65, 66, 67, 49, 82], and it can be expected that it will also place limits on information *retrieval efficiency* in Brillouin storage experiments, measured as the amount of power that can be retrieved from the acoustic field after a certain time. This has been experimentally measured [110, 59], however while noise has been observed as a feature of these experiments, it is not yet

clear how noise impacts the accuracy of the information retrieval. Furthermore, most studies (except, notably, [62]) have focused on amplitude encoded storage, in which bits of information are stored in individual pulses. Alternatively, phase encoded storage may offer higher storage efficiency and be less sensitive to noise. A quantitative understanding of the impact of noise on the storage of both amplitude and phase information is needed for the further development of practical Brillouin-based storage devices.

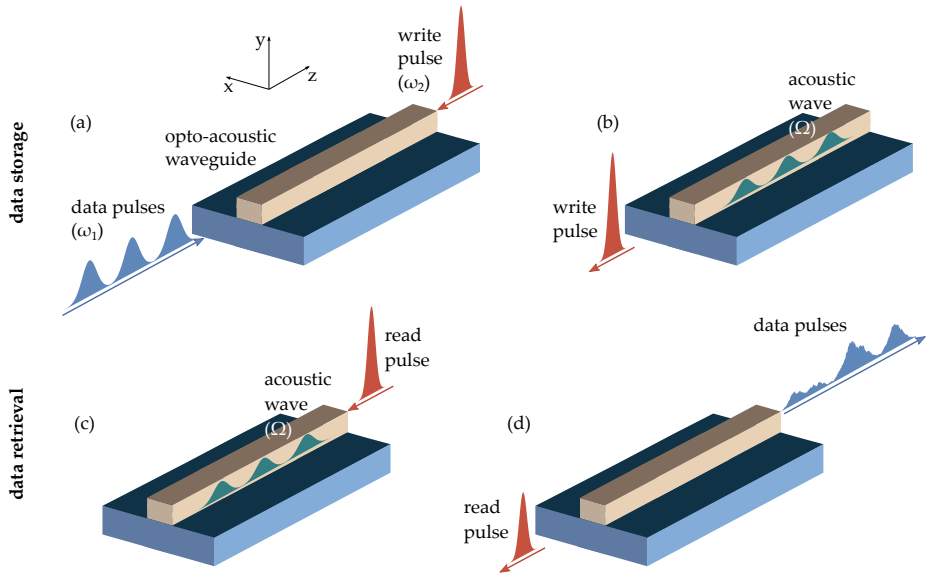

FIGURE 6.1: Illustration of the opto-acoustic storage achieved via SBS, neglecting the effects of noise, and using amplitude shift-keying (amplitude storage). Storage process in (a) and (b): data pulses are depleted by the write-pulse, exciting an acoustic wave inside the waveguide, with some energy gained by the write-pulse. Retrieval process in (c) and (d): a read-pulse interacts with the acoustic wave, both become depleted and the energy is used to regenerate the original sequence of data pulses. The retrieval efficiency is limited by the acoustic lifetime of the phonons.

6.3 Methods

Following the formalism in Chapters 4 and 5 for solving the SBS equations (4.1a)−(4.1c) numerically, we define the input optical fields at the ends of the waveguide by stochastic boundary conditions, namely $a_1(0,t) = a_{\text{data}}(t)e^{i\phi_1(t)}$ for the data pulse, and the read/write pulses combined into $a_2(L,t) = [a_{\text{read}}(t) + a_{\text{write}}(t)]\, e^{i\phi_2(t)}$, where $\phi_{1,2}(t)$ are random phase terms modelled as Brownian motions. We also set the pump frequency ω_1 larger than the Stokes frequency ω_2, so that the pump transfers energy to the Stokes field. In non-storage SBS setups [82, 131] the pump has higher input power P_{p0} than the Stokes P_{s0} and thus behaves as an amplifier. However, in the case of Brillouin storage, we require $P_{\text{p0}} \ll P_{\text{s0}}$ so that the read/write pulse can completely deplete the pump, which contains the data to be stored. Optimum storage requires two conditions on the read/write pulse. First, the read/write pulses must be at least as short in duration as the shortest data pulse. Second, the pulse area for the read/write pulse, defined as [59, 61]

$$\Theta_w = \sqrt{\frac{g_0 v}{8\tau_a}} \int_{-\infty}^{\infty} a_{\text{read/write}}(t)\mathrm{d}t, \tag{6.1}$$

must obey the condition $\Theta_w = (m + 1/2)\pi$ where $m = 0, 1, 2, ...$ This is because once the data pulse is depleted completely, the transfer of energy reverses and the data pulse is regenerated [60, 61, 167]. The dependence of the pulse-area on τ_a may seem deceptive at first, but since g_0 is also dependent on τ_a these two effects cancel out.

The storage efficiency thus tells us how effective the storage system is, and may be defined as the ratio of the total output data power $|a_{\text{out}}(t)|^2$ to the total input data power $|a_{\text{data}}(t)|^2$ [62]:

$$\eta_{\text{sto}} = \frac{\int_0^{\tau_{\text{data}}} \left\langle |a_{\text{out}}(t)|^2 \right\rangle \mathrm{d}t}{\int_0^{\tau_{\text{data}}} \left\langle |a_{\text{data}}(t)|^2 \right\rangle \mathrm{d}t}, \tag{6.2}$$

where $\langle X(t) \rangle = \frac{1}{N} \sum_{n=1}^{N} X_n(t)$ is the ensemble average of a function $X(t)$ over N independent runs, and τ_{data} is the duration of the data train. Because the acoustic wave decays in time at a rate $1/\tau_a$, η_{sto} decreases with longer storage times, reducing the efficiency in addition to the effects of noise. We define the storage time τ_{sto} as the temporal delay between the write and read pulses.

Parameter	Value	Parameter	Value
Waveguide length L	30 cm	Peak read/write power	0.5−10.5 W
Waveguide temperature T	300 K	Data packets	256
Refractive index n	2.44	Data stream duration τ_{data}	2.44 ns
Acoustic velocity v_a	2500 m/s	Bit duration τ_{bit}	300 ps
Acoustic lifetime τ_a	10.2 ns	Data pulse width τ_1	150 ps
Brillouin shift $\Omega/2\pi$	7.8 GHz	Read pulse width τ_2	100 ps
Brillouin gain parameter g_0	411 $\text{m}^{-1}\text{W}^{-1}$	Grid size (space) N_z	800
Optical wavelength λ	1550 nm	Grid size (time) N_t	2797
Laser linewidth $\Delta\nu_L$	100 kHz	Step-size Δz	375 μm
Peak data power	10 mW	Step-size Δt	3.05 ps
Optical loss α	0.1 dB/cm		

TABLE 6.1: Parameters used in this study. Physical parameters correspond to a chalcogenide waveguide [154].

For our simulations we use the parameters summarized in Table 6.1. We assume a high gain chalcogenide waveguide, of the type used in previous SBS experiments [154]. We store individual 8-bit packets one at a time, consisting of all 256 possible unique 8-bit sequences. Each packet corresponds to 8 individual pulses in the amplitude storage case, and 4 phases in the phase storage case, as shown in Fig. 6.2.

It should be noted that the model used here (Eq. (4.1a)−(4.1c)) makes the assumption of the slowly-varying envelope approximation (SVEA) and rotating-wave approximation (RWA) [82, 76]. Because the acoustic frequencies used in SBS experiments are typically in the range of a few GHz [44, 69], the optical pulses simulated must be longer than a few hundred picoseconds in duration so that these approximations remain valid [168]. Therefore, we limit our simulations to pulses no shorter than 100 ps, for both for the data and read/write cases. We have chosen to focus on the storage of 8-bit sequences because they can fit inside a 30 cm chalcogenide waveguide without being too short for a 7.8 GHz Brillouin frequency shift, since the acoustic pulses generated from 300 ps optical bits are approximately 3.7 cm in length.

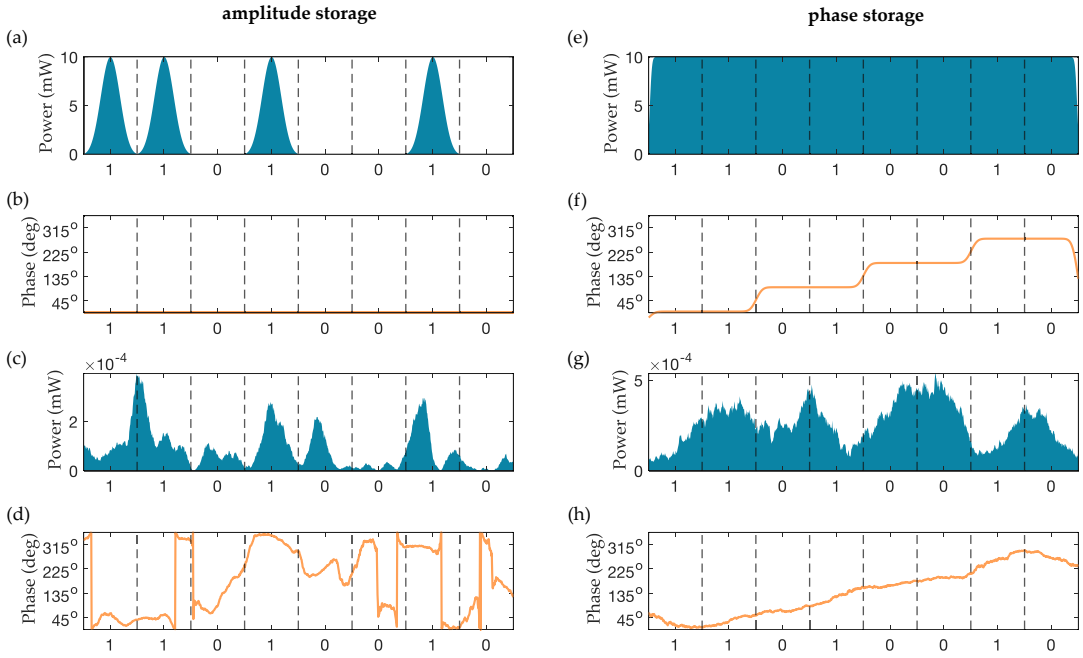

FIGURE 6.2: Illustration of how the 8-bit sequence $\mathbf{x} = 11010010$ is encoded in the numerical simulation. Amplitude storage: (a)−(b) input power and phase, (c)−(d) output power and phase after some storage time. Phase storage: (e)−(f) input power and phase, (g)−(h) output power and phase after some storage time. Here we use thermal noise at $T = 300$ K.

6.3.1 Data encoding

The two storage schemes used in this paper — amplitude and phase storage — are summarized in Fig. 6.2. Each bit is defined as having a duration τ_{bit}. For amplitude storage, we encode ones into Gaussian pulses of the same peak power P_{p0}, while zeros are represented by gaps of duration τ_{bit}. For phase storage, we use the same scheme as in quadrature phase-shift keying (QPSK) with gray coding [169], where bit pairs are assigned a unique phase, namely $11 = 45^{\text{o}}$, $01 = 135^{\text{o}}$, $00 = 225^{\text{o}}$and $10 = 315^{\text{o}}$. For a given input information packet, we quantify the retrieval accuracy in both storage schemes via the packet error rate (PER). This is similar to the bit error rate (BER) of a binary stream, except that we count correct 8-bit packets as opposed to counting individual correct bits. Therefore, the PER is the ratio of correctly retrieved packets with respect to the input data, and has a value $0 \leq \text{PER} \leq 1$.

In the amplitude storage case, we encode bits=1 into Gaussian pulses of full-width at half-maximum (FWHM) τ_1, while bits=0 are represented by gaps of duration τ_{bit} in the data sequence. Mathematically, we represent this by the formula

$$a_{\text{data}}(t) = \sqrt{P_{\text{p0}} \sum_{n=1}^{N} \tilde{\beta}_n(t) \cos\left(\frac{\pi}{\tau_{\text{bit}}}(t - \Delta\tau_n)\right) \exp\left\{-4\ln(2)\frac{(t-\Delta\tau_n)^2}{\tau_1^2}\right\}}, \tag{6.3}$$

where P_{p0} is the peak power of the pulses, $\Delta\tau_n$ is the delay of the nth pulse in the sequence and τ_1 is the full-width at half-maximum (FWHM) of each pulse representing a 1. The cosine function is used here in order to prevent individual pulses from overlapping with one another. For a data-stream starting at $t = 0$, the successive pulse delays are calculated as $\Delta\tau_n = (2n-1)\tau_{\text{bit}}/2$ for $n = 1, 2, 3, ..., N$. By default, we choose all

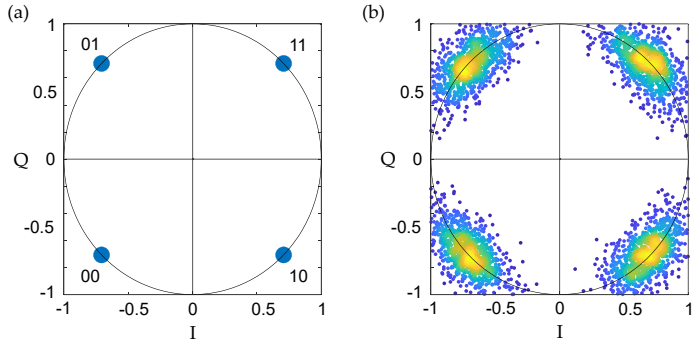

FIGURE 6.3: Constellation diagrams used in phase storage. These plots are done on the complex plane, where the modulus of each point corresponds to the normalized power of the signal, and the argument corresponds to the phase of the signal. (a) ideal system: each point lies at exactly 45°from the horizontal line in either direction, and on the circle of radius 1. (b) Effect of noise in the detected signal: amplitude noise shifts the points in the radial direction, while phase noise shifts the points in the angular direction, and the color scheme shows the regions of higher or lower density of points.

pulses to have a phase of 0°. In the retrieval stage, the output data power $|a_{\text{out}}(t)|^2$ is separated into equal intervals of length τ_{bit}. We use a dynamic threshold technique: initially, a threshold power P_{thresh} is set. Then, we record the output power at the center of the bit period, and a single bit is read as 0 if $|a^{(n)}_{\text{out}}(t)|^2 < P_{\text{thresh}}$ and as 1 if $|a^{(n)}_{\text{out}}(t)|^2 \geq P_{\text{thresh}}$ [170], for all 256 data packets. This process is repeated for different values of P_{thresh} until the total PER has been minimized, which is then selected as the PER for that particular simulation.

In the phase storage case, we encode bit-pairs into 4 different phases, as shown in Fig. 6.3(a). The phase itself is described mathematically as

$$\varphi_{\text{data}}(t) = \frac{\pi}{4}\left[1 + 2\sum_{m=1}^{N/2}\theta_m \text{rect}\left(\frac{t-(2m-1)\tau_{\text{bit}}}{2\tau_{\text{bit}}}\right)\right], \tag{6.4}$$

where $\theta_m = \{0,1,2,3\}$, and each value corresponds to the bit pairs $\{11,01,00,10\}$, which correspond to increments of 90°starting at 45°. For instance, in a bit sequence 11001100, the corresponding values are $\theta = \{0,2,0,2\}$. Therefore, the duration of each unique phase in $\varphi_{\text{data}}(t)$ is $2\tau_{\text{bit}}$, which means PS has twice the information bandwidth of AS [169]. To make the model more realistic without phase discontinuities from symbol to symbol, we pass $\varphi_{\text{data}}(t)$ through a Gaussian filter of temporal full-width half-maximum τ_{filter}, so the actual phase in the data pulse becomes

$$\phi_{\text{data}}(t) = \int_0^t \varphi_{\text{data}}(t')\exp\left\{-4\ln(2)\frac{(t-t')^2}{\tau^2_{\text{filter}}}\right\}\text{d}t'. \tag{6.5}$$

To emulate the effect of the modulators used in SBS experiments, we set the filter to have a frequency FWHM of 5 GHz, or equivalently $\tau_{\text{filter}} = 88$ ps. The envelope of the data pulse in the phase storage case consists of an analytical smooth rectangular (ASR) pulse as described in [171]. Therefore, the pulse is described mathematically as

$$a_{\text{data}}(t) = \frac{\sqrt{P_{\text{p0}}}}{2}\left[\text{erfc}\left(\frac{\tilde{\gamma}(t-\delta_{\text{data}})-\tau_1/2}{\Delta_0}\right) - \text{erfc}\left(\frac{\tilde{\gamma}(t-\delta_{\text{data}})+\tau_1/2}{\Delta_0}\right)\right]e^{i\phi_{\text{data}}(t)}, \tag{6.6}$$

where δ_{data} is the delay of the center of the data pulse, $\tilde{\gamma} = 1^{0.81\tau_1/\Delta_0}$ is a chirp-dependent parameter and $\Delta_0 = 0.0067\tau_1$ controls how quickly the pulse ramps up from 0.

In the retrieval stage, $|a_{\text{out}}(t)|^2$ is separated into equal intervals of length $2\tau_{\text{bit}}$. We extract the phase from the amplified output signal as:

$$\phi_{\text{out}}(t) = \tan^{-1}\left(\text{Im}\left[a_{\text{out}}(t)\right]/\text{Re}\left[a_{\text{out}}(t)\right]\right) \tag{6.7}$$

As with the case of amplitude storage, we assume ideal detector conditions and record the phase at the center of the $2\tau_{\text{bit}}$ period, such that if $0^{\text{o}} < \phi_{\text{out}}(t) < 90^{\text{o}}$, we read the output bit-pair as 11, if $90^{\text{o}} < \phi_{\text{out}}(t) < 180^{\text{o}}$we read the bit-pair as 01 and so on. In phase storage, we use another measure of signal integrity based on the constellation diagram data: let $z_{\text{out}}^{(m)}$ represent a single point on the constellation diagram corresponding to the mth bit-pair in the binary sequence (such as 00), with magnitude $\left|z_{\text{out}}^{(m)}\right|$ and phase ϕ_z^{m}. The relative variances in each point can be found via

$$\text{Var}\left[\left|z_{\text{out}}^{(m)}\right|\right] = \left\langle\left|z_{\text{out}}^{(m)}\right|^2\right\rangle - \left\langle\left|z_{\text{out}}^{(m)}\right|\right\rangle^2, \quad \text{Var}\left[\phi_{\text{out}}^{(m)}\right] = \left\langle\left(\phi_{\text{out}}^{(m)}\right)^2\right\rangle - \left\langle\phi_{\text{out}}^{(m)}\right\rangle^2. \tag{6.8}$$

6.4 Results and Discussion

6.4.1 Effect of thermal noise

We investigate the effect of varying the read/write pulse peak power between 0.5−10.5 W, while maintaining a read/write pulse width of 100 ps. We include thermal noise into the waveguide at 300 K, but neglect the input laser phase noise by setting the laser linewidth $\Delta\nu_L$ to zero. In the amplitude storage case, we use Gaussian data pulses with 10 mW peak power and pulse width 150 ps, while in the phase storage case we use a rectangular pulse of duration 2.44 ns, and phase intervals of duration 600 ps. Each bit of optical information is 300 ps in length for both amplitude and phase storage. The results of the simulations are shown in Fig. 6.4. First, we observe in Fig. 6.4(a) and (b) that the storage efficiency in both storage schemes is higher as we increase the peak write pulse power, as the pulse area is lower than the optimum value given by Eq. (6.1). Second, we see in Fig. 6.4(c) and (d) that lower peak write powers lead to increased PER, thus reducing the maximum storage time achievable in both encoding schemes. This occurs because at lower peak read/write powers — which also corresponds to the lower storage efficiency regime — the coherent output data field is less distinguishable from the amplified spontaneous noise arising from the interaction between the read/write pulse and the thermal background fluctuations in the waveguide [82, 131]. Consequently, this increases the probability of retrieving the wrong data sequence at the waveguide output ($z = L$).

Similarly, we see an increase in PER in both AS and PS schemes with increasing τ_{sto}, as shown in Fig. 6.4(c) and (d). This occurs because in the time between the write and read-process, the acoustic wave containing the stored information decays at a rate $1/\tau_a$. As τ_{sto} increases, the acoustic wave gets closer to the background thermal noise, increasing the fluctuations in the retrieved data field during the read-process. This effect is more clearly illustrated in Fig. 6.5, where the constellation points spread out in both radial and angular directions, indicating an increase in both amplitude and phase noise in the retrieved data field. In Fig. 6.6 we see that the rate of increase in the variance of the phase and amplitude of each encoding scheme is the same for the first 40 nanoseconds. However, in Fig. 6.4(f) we see that the PER in the phase storage case

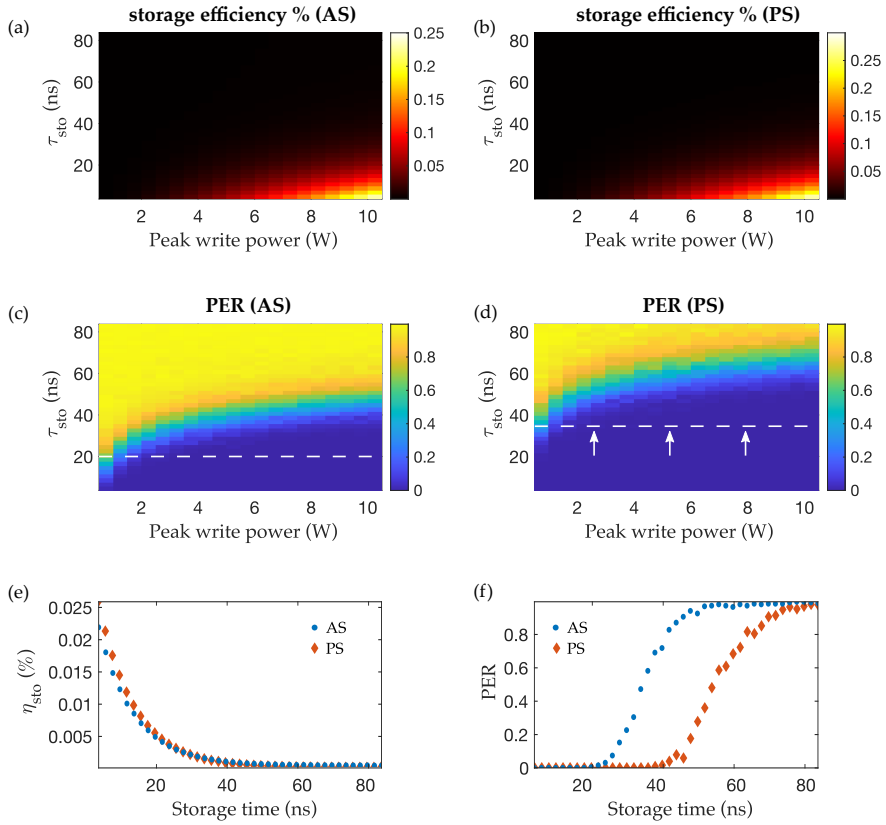

FIGURE 6.4: Simulations of Brillouin storage with thermal noise only, for varying read-/write pulse peak power and different storage times in amplitude storage and phase storage. Panels (a) and (b) show the storage efficiency of the two schemes, (c) and (d) the packet error rates, (e) and (f) illustrate the storage efficiency and PER at 3 W peak write power. The dashed horizontal line in (c) and (d) indicates the τ_{sto} at which data packet errors begin to occur, and the arrows in (d) show that this threshold is pushed further back in time.

begins to increase at longer τ_{sto} compared to the amplitude storage case, suggesting that phase-encoded data is more robust to thermal noise and hence allows for longer storage times. This occurs because the phase variations are primarily constrained to a single quadrant on the constellation plots (as shown in Fig. 6.5), whereas the amplitude variations reach the noise floor more rapidly. Consequently, the probability of detecting the wrong bit of information in the amplitude is higher compared to the phase. This is the same observation that would be expected from the additive white Gaussian noise (AWGN) model in discrete communication theory, where the probability of bit error for phase-shift-keying (PSK) is lower than for amplitude-shift-keying (ASK) [172, 173]. In addition, phase encoding allows the transfer of more bits per symbol, and this means that the pulse-size constraints imposed by the SVEA and RWA can be further relaxed.

6.4.2 Effect of laser phase noise

We now investigate the effect of adding input laser phase noise, at a linewidth of 100 kHz, with the same pulse and thermal noise parameters as before. We generate the phase noise in the data pulses and read/write pulses independently so they are statistically uncorrelated, but have the same mean and variance properties. Fig. 6.7 shows the results for storage efficiency and PER for both encoding schemes. The plots in

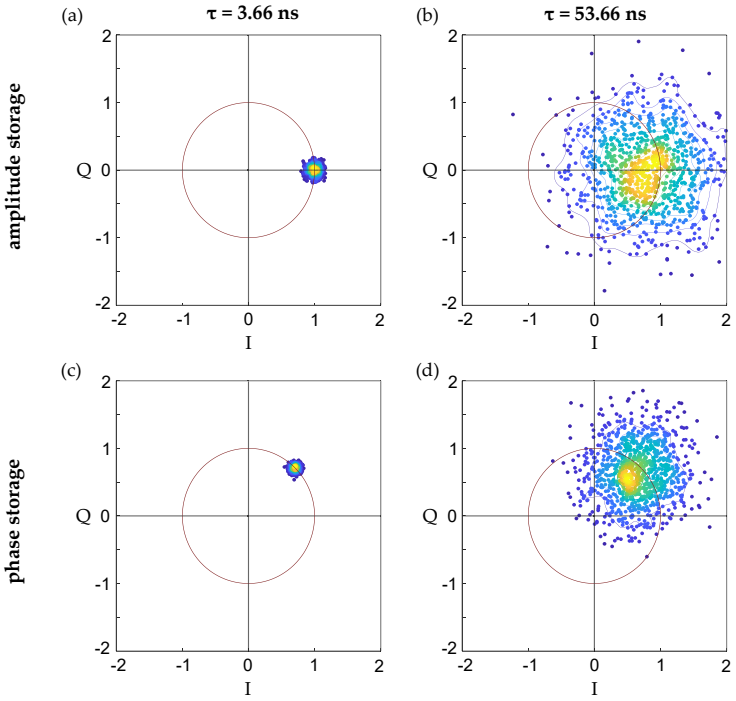

FIGURE 6.5: Constellation diagrams for the thermal noise only case, at 3 W peak write power. (a) and (b) show the amplitude storage plots at two storage times (3.66 ns is the minimum storage time achievable in this configuration) for a binary bit 1, while (c) and (d) show the phase storage plots for a binary bit pair 11.

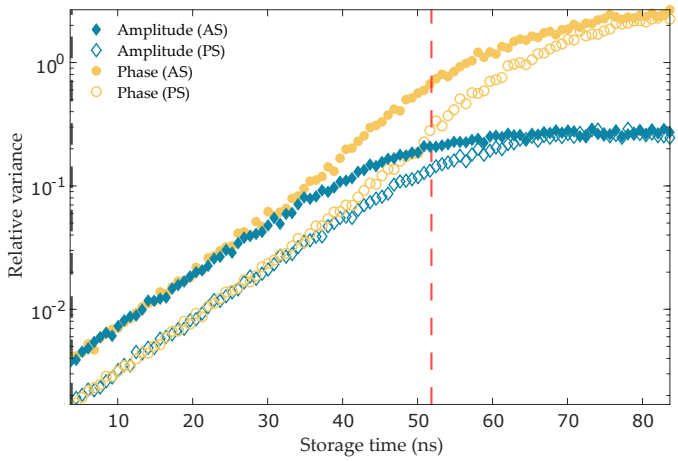

FIGURE 6.6: Relative variance in the amplitude and phase of the constellation data in Fig. 6.5 as a function of storage time. The dashed lines mark the storage times corresponding to the constellation diagrams in Fig. 6.5.

Fig. 6.7(a)−(d) look very similar to Fig. 6.4(a)−(d), indicating that laser phase noise does not have a significant impact on the storage efficiency or PER. This is consistent with previous work on SBS noise in short pulses [131], where it was found that laser phase noise only has a significant impact on the SBS process when the laser coherence time ($\tau_{coh} = 1/\pi\Delta\nu_L$) is comparable in magnitude to the SBS interaction time. Next, the constellation diagram results in Fig. 6.8 reveal that the input laser phase noise broadens the variance in the phase of the retrieved data field, making the distribution of constellation points slightly more elliptical compared to the thermal noise only case. This is

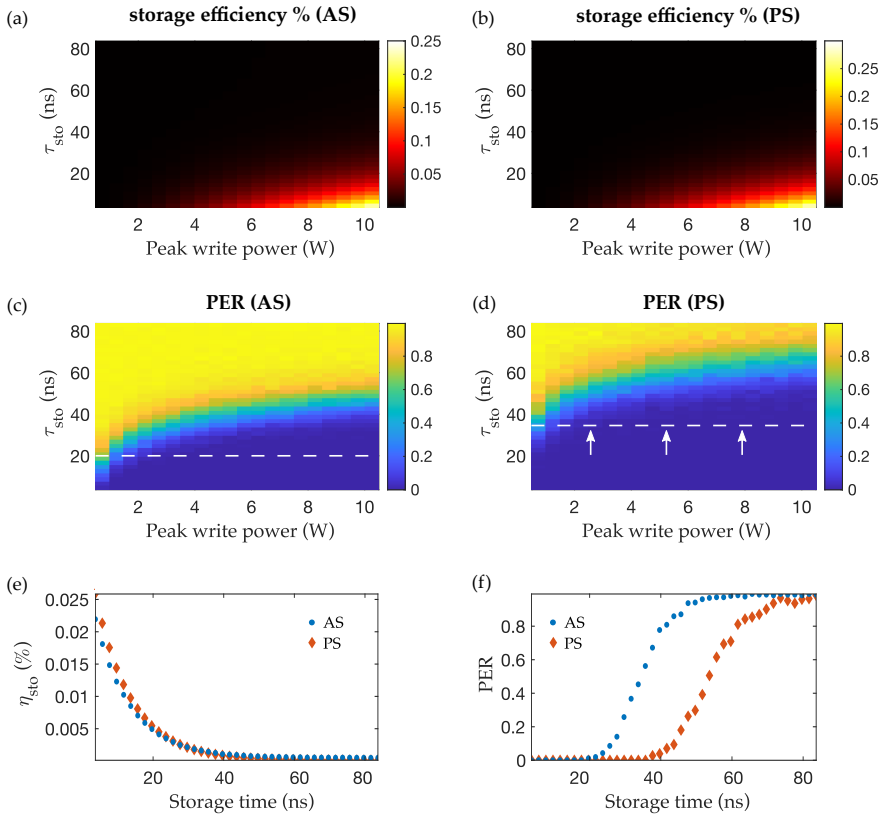

FIGURE 6.7: Simulations of Brillouin storage with both thermal and laser phase noise, for varying read/write pulse peak power and different storage times in amplitude storage and phase storage. Panels (a) and (b) show the storage efficiency of the two schemes, (c) and (d) the packet error rates, (e) and (f) illustrate the storage efficiency and PER at 3 W peak write power. The dashed horizontal line in (c) and (d) indicates the τ_{sto} at which data packet errors begin to occur, and the arrows in (d) show that this threshold is pushed further back in time.

also shown in Fig. 6.9, where the rates of increase for the amplitude and phase variances still remain approximately the same for the first 40 nanoseconds of storage time. This occurs because at this regime of powers for the data pulses, the SBS process acts as a linear amplifier, hence the total noise in the retrieved data is a linear combination of the waveguide thermal noise and the laser phase noise from the inputs.

6.5 Conclusion

We have numerically simulated the Brillouin storage of different data packets with thermal and laser noise, using amplitude storage and phase storage techniques in a photonic waveguide. Through these computer simulations, we have shown that phase encoded storage allows for longer storage times than amplitude encoded storage. This is because phase encoding is more robust to noise than amplitude encoding, in accordance with the additive-white-Gaussian-noise model of discrete communications theory [172]. It is therefore possible to increase Brillouin storage time by encoding information into the phase of the data field, without having to change the waveguide or laser properties. Furthermore, because phase storage techniques can encode more bits per symbol than amplitude storage [169, 172], one can use longer optical pulses without loss of data capacity.

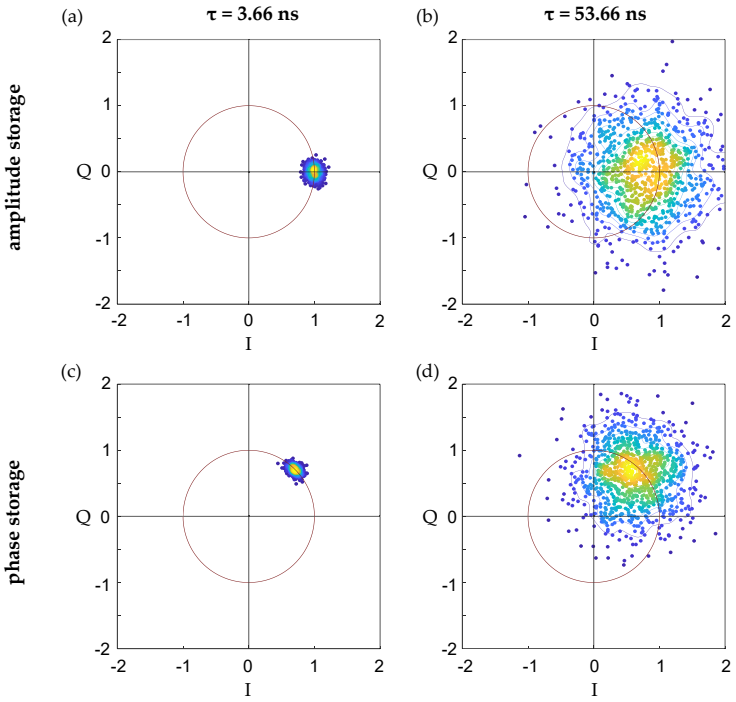

FIGURE 6.8: Constellation diagrams for the thermal noise and laser phase noise case, at 3 W peak write power. (a) and (b) show the amplitude storage plots at two storage times (3.66 ns is the minimum storage time achievable in this configuration) for a binary bit 1, while (c) and (d) show the phase storage plots for a binary bit pair 11.

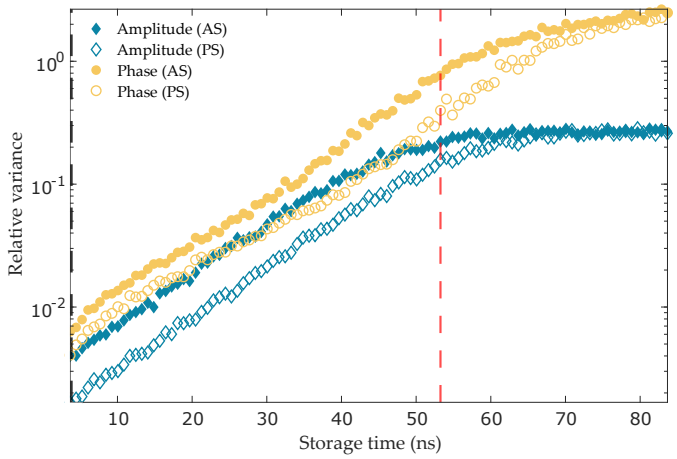

FIGURE 6.9: Relative variance in the amplitude and phase of the constellation data in Fig. 6.8 as a function of storage time. The dashed lines mark the storage times corresponding to the constellation diagrams in Fig. 6.8.

Chapter 7

Summary and Outlook

7.1 Summary

In this Thesis, we have developed a general mathematical framework for simulating the stochastic dynamics in backward SBS, with special emphasis on pulses. By building on previous work done in the context of steady-state or continuous-wave (CW) operation, we have extended our analysis to short pulses, and investigated the noise properties in the undepleted pump regime, which is outlined in [82]. In this research, we showed that in the case of a constant energy pump field and lossy media, the optical signal-to-noise ratio (OSNR) has a minimum in the region where the interaction time of the pulses matches their transit time in the waveguide. It was found that as the spontaneous Stokes noise increases towards a maximum value, the OSNR decreases, resulting from longer pump pulses compensating for the linear optical losses in the medium. Additionally, it was found that once the pump pulse becomes longer than the waveguide, the loss dominates due to less pump energy fitting inside the propagation medium. Therefore, we concluded that the OSNR is mediated by the pump energy, pump shape, waveguide length and optical loss, making it important to choose the right parameter combination to maximize the OSNR in a specific device.

The theoretical framework [82] for thermal noise was also extended to include laser phase noise, and a numerical solver for the coupled stochastic SBS equations was developed [131]. Using a splitting method in which the drift of the optical fields and the nonlinear interaction are solved separately during each time iteration, the method demonstrated linear convergence in both the ensemble averaged power and variance in the power of the envelope fields. We then used this method to investigate the role of pulse properties on the noise levels in a chalcogenide waveguide. We found that the noise properties of the fields rely on the length of the optical pulses involved as well as on the net SBS gain in the waveguide. For short-pump, low gain regimes, the spontaneous Stokes field is found to be incoherently amplified, thus exhibiting large spatial and temporal fluctuations, whereas for the long-pump, high gain regime the field is amplified coherently, resulting in a smooth field but with large variations in peak power between independent realizations. Similar observations were made for the stimulated scattering case using a Stokes seed. In addition, we found that laser phase noise does not play a significant role in the SBS interaction unless the laser coherence time is comparable to the characteristic time-scales of the SBS interaction.

The numerical method developed in this Thesis was more recently implemented in the simulation of Brillouin storage under different modulation schemes, namely amplitude storage (AS) and phase storage (PS), under the presence of thermal noise. Using a data sequence of 8-bits in a 30 cm chalcogenide waveguide using picosecond pulses, we investigated the effect of pulse properties on the retrieval efficiency after different storage times. Additionally, we investigated the accuracy of the retrieved data with respect to the input data stream by looking at the packet error rate (PER) of

8-bit sequences in each scheme (AS and PS). Through these simulations, we found that phase storage offers longer storage times than amplitude storage, as a result of phase encoding being more robust to noise than amplitude encoding, in accordance with the additive-white-Gaussian-noise (AWGN) model of discrete communication theory.

7.2 Outlook and future directions

The present Thesis has introduced a new mathematical framework for modelling thermal noise in SBS for short pulses, as well as a numerical method by which the SBS coupled equations (4.1a)−(4.1c) can be solved, and an analysis of how phase and amplitude storage schemes are impacted by SBS noise in Brillouin-based storage. Despite these models being quite general, there remain some aspects of these noise dynamics which could be expanded upon. In this Section, we outline some possible extensions to the theory which may be of use in future research.

7.2.1 Higher accuracy numerical methods

In this Thesis, we developed a numerical method for solving the SBS coupled equations with thermal and laser phase noise. The method uses a split-approach in which the optical fields are shifted in space during each time iteration, and then the nonlinear interaction is solved using the time-evolution equations. The method uses an Euler-Mayurama scheme for the time-evolution step involving thermal and laser noise. As a result, the method offers linear convergence in both the ensemble averaged power and the variance in the power of the fields.

One important challenge in these simulations is that higher order methods for stochastic partial differential equations (SPDEs) are still an active area of research [165]. Although Runge-Kutta methods exist for ordinary stochastic differential equations, it is unlikely that these methods will work on SPDEs given that the noise properties are different in space and in time. As research in this area progresses, new methods may arise, in which case new numerical schemes for solving the SBS equations with noise might become possible.

Another challenge in the computational realm is that Monte Carlo simulations are quite computationally expensive, and from several years of doing these computations on the large UTS high-performance computing cluster (iHPC) we found that more than 100 independent realizations of the envelope fields must be solved in order to obtain good estimates for the statistics of the fields, namely ensemble averages and variance. Depending on the scale of the problem and the numerical resolution required, such computations can take several days, or even weeks, to complete, especially when using very fine step-sizes. And this is all using parallel-computing on multi-core machines. It is possible that GPU-computing may offer an accelerated way of performing all these Monte Carlo runs simultaneously, thereby shortening the computation time needed [174, 175, 176]. However, we have so far not tested such methods, and their application may require the use of lower-level programming languages like C++ for optimum performance.

7.2.2 Multi-modal noise dynamics

One area for further investigation is, quite naturally, the extension of the mathematical theory to other types of SBS, such as forward SBS, cascaded SBS and inter-modal SBS. So far, our mathematical methods have focused on single-mode operation, based on the fact that we can select a certain Brillouin frequency by tuning the input laser fields.

However, it would be interesting to see how the noise properties may differ when more than one acoustic mode is involved in the interaction. A possible way to model this is to include additional envelope equations into the coupled SBS equations. For instance, if we wanted to include 2 acoustic modes with respective envelope fields $b_{1,2}(z,t)$ then one could potentially write

$$\frac{\partial a_1}{\partial z} + \frac{1}{v}\frac{\partial a_1}{\partial t} + \frac{1}{2}\alpha a_1 = i\omega_1 Q_1 a_2 b^*, \tag{7.1}$$

$$\frac{\partial a_2}{\partial z} - \frac{1}{v}\frac{\partial a_2}{\partial t} - \frac{1}{2}\alpha a_2 = i\omega_2 Q_2 a_1 b, \tag{7.2}$$

$$\frac{\partial b_1}{\partial z} + \frac{1}{v_{a,1}}\frac{\partial b_1}{\partial t} + \frac{1}{2}\alpha_{\mathrm{ac},1} b_1 = i\Omega_1 Q_{a,1} a_1^* a_2 + \sqrt{\sigma_1} R_1(z,t), \tag{7.3}$$

$$\frac{\partial b_2}{\partial z} + \frac{1}{v_{a,2}}\frac{\partial b_2}{\partial t} + \frac{1}{2}\alpha_{\mathrm{ac},2} b_2 = i\Omega_2 Q_{a,2} a_1^* a_2 + \sqrt{\sigma_2} R_2(z,t), \tag{7.4}$$

each with their own coupling constants $Q_{a,j}$, group speeds $v_{a,j}$, frequencies Ω_j and so on. Additionally, one could assign different noise properties σ_j to each mode. In this sense, it is also possible that the noises from different modes may be correlated to one another, by which we establish

$$\left\langle R_i(z,t) R_j^*(z,t) \right\rangle = \kappa_{ij}\delta(z-z')\delta(t-t'), \tag{7.5}$$

for some constant κ_{ij}. Similarly, one could explore the effect of three or more acoustic modes, but this would potentially pose further computational challenges. Investigations on mode division and cross-correlated noises are potentially useful for future applications of SBS in optical signal processing, particularly in applications such as multi-plexing.

7.2.3 Extensions on noise and ultra-short pulses

In the work done in this Thesis, we assumed that the optical pulses introduced into the waveguide are long enough so that the slowly-varying envelope-approximation (SVEA) remains valid (i.e. the width of the field's envelope is a few orders of magnitude longer than the carrier frequencies). However, as has been suggested in recent theoretical works [168], the SVEA breaks down once the temporal width of the pulses gets close to period of oscillations associated with the Brillouin shift in the waveguide, which means that modified versions of Eq. (4.1a)−(4.1c) are required. Additionally, they found that short pulses in SBS can excite other nonlinearities, like the Kerr nonlinearity via self-phase modulation (SPM) and cross-phase modulation (XPM), which is dependent upon the peak power used and the waveguide material, and this could potentially change the noise properties being modelled.

Another possible extension to the theory of SBS noise could be to include the effect of heating on the waveguide as a result of the interacting optical fields. For instance, what happens when we use ultra-short pulses with very higher peak power in an SBS interaction? Does the thermal noise behave any differently from our equilibrium temperature model?. One approach for this would be to make the thermal noise parameter σ dependent upon the temperature T, and make the temperature itself dependent on space and time such as $T(z,t)$. In this sense, if one can find a relation between $T(z,t)$ and the optical envelope fields, this would change the behaviour of the thermal noise field in the waveguide, with regions of higher noise corresponding to regions of higher temperature.

Appendix A

Probability and Random Processes

In this Appendix we present the central mathematical tools that are used throughout this Thesis.

A.1 Random variables

A random variable X is characterized by a set of random outcomes $\omega \in \Omega$, where Ω is the set of all possible outcomes. It can be discrete or continuous. In the discrete case, it is sampled from a probability mass function obeying the property

$$\sum_{k=1}^{N} p_k = 1, \tag{A.1}$$

and in the continuous case it obeys

$$\int_{-\infty}^{\infty} p(x)\mathrm{d}x = 1. \tag{A.2}$$

Probability distributions $p(x)$ must therefore be continuous and bounded. To derive specific statistical properties of X, one can use the formula for the moments of X

$$\langle X^n \rangle = \begin{cases} \sum_{k=1}^{N} x_k^n p_k & \text{(discrete)}, \\ \int_{-\infty}^{\infty} x^n p(x)\mathrm{d}x & \text{(continuous)}, \end{cases} \tag{A.3}$$

where $\langle \cdot \rangle$ denotes the expectation operator. For a general random function $f(X)$ with probability density function $p(x)$, the expectation value is

$$\langle f(X) \rangle = \int_{-\infty}^{\infty} f(x)p(x)\mathrm{d}x. \tag{A.4}$$

We will also use $\langle X(t) \rangle$ to denote the ensemble average of a stochastic process $X(t)$, namely the average of the function at each point in t across N independent realizations of $X(t)$. Lastly, it is important to point out that the expectation operator is linear and has the property:

$$\langle [af + bg](x) \rangle = a \langle f(x) \rangle + b \langle g(x) \rangle, \tag{A.5}$$

for arbitrary constants a and b.

A.1.1 Variance and standard deviation

Variance is another concept that allows us to establish bounds on how much a random variable X deviates from its mean. If the deviation from the mean is very large, then

we say X is very unpredictable, or highly volatile. If the deviation is very small, then we would expect any arbitrary sample of X to be close to its mean value. Standard deviation is the squared root of the variance. Mathematically, the variance of a random variable X is defined by the formula

$$\mathrm{Var}\left[X\right] = \left\langle (X - \langle X \rangle)^2 \right\rangle . \tag{A.6}$$

However, it is often more useful to use the form

$$\mathrm{Var}\left[X\right] = \left\langle X^2 \right\rangle - \langle X \rangle^2 , \tag{A.7}$$

For a discrete random variable, this is equivalent to

$$\mathrm{Var}\left[X\right] = \sum_{n=1}^{N} x_n^2 p_n - \left(\sum_{n=1}^{N} x_n p_n \right)^2 , \tag{A.8}$$

and for a continuous random variable

$$\mathrm{Var}\left[X\right] = \int_{-\infty}^{\infty} x^2 f(x) \mathrm{d}x - \left(\int_{-\infty}^{\infty} x f(x) \mathrm{d}x \right)^2 , \tag{A.9}$$

from which we can calculate the standard deviation $\sqrt{\mathrm{Var}[X]}$. The variance as a mathematical operator has the following properties:

1. $\mathrm{Var}\left[c\right] = 0$ where c is a constant. The reason is that c has only a single value, so there are no deviations from this value, it is definite and unique.
2. $\mathrm{Var}\left[cX\right] = c^2 \mathrm{Var}\left[X\right]$, often referred to as the scaling property.
3. $\mathrm{Var}\left[aX + bY\right] = a^2 \mathrm{Var}\left[X\right] + b^2 \mathrm{Var}\left[Y\right] + 2\,\mathrm{cov}\left[X, Y\right]$, where $\mathrm{cov}\left[X, Y\right]$ is the covariance between X and Y.

A.1.2 Covariance

The covariance of two random variables X and Y is a measure of their joint variability. When normalized in a certain way, it can be used as a measure of the linear relation between the two variables, with higher values representing a stronger relationship. The covariance is given by

$$\mathrm{cov}\left[X, Y\right] = \left\langle \left(X - \langle X \rangle\right) \left(Y - \langle Y \rangle\right) \right\rangle . \tag{A.10}$$

Alternatively, it may be expressed as

$$\mathrm{cov}\left[X, Y\right] = \left\langle XY \right\rangle - \left\langle X \right\rangle \left\langle Y \right\rangle , \tag{A.11}$$

which is also applicable to random vectors $\mathbf{X}$ and $\mathbf{Y}$

$$\mathrm{cov}[\mathbf{X}, \mathbf{Y}] = \left\langle \mathbf{X}\mathbf{Y}^T \right\rangle - \left\langle \mathbf{X} \right\rangle \left\langle \mathbf{Y} \right\rangle^T . \tag{A.12}$$

In the special case where the covariance is 0, we can write

$$\left\langle XY \right\rangle = \left\langle X \right\rangle \left\langle Y \right\rangle . \tag{A.13}$$

This means that the two variables are statistically independent.

A.1.3 Correlation

The correlation of two random variables, also known as the correlation coefficient, is a measure of how strong the linear relationship between them is. It takes on a value between -1 and 1, with -1 representing perfect decreasing linear dependence, and 1 perfect increasing linear dependence. It can be calculated using

$$\text{corr}(X, Y) = \frac{\text{cov}\left[X, Y\right]}{\sqrt{\text{Var}[X]\text{Var}[Y]}}. \tag{A.14}$$

A.1.4 Combinations of random variables

Consider a random variable Z which is a linear combination of two random variables X and Y, such that

$$Z = aX + bY, \tag{A.15}$$

for some constants a and b. The mean of Z is given by

$$\langle Z \rangle = a \langle X \rangle + b \langle Y \rangle . \tag{A.16}$$

The variance of Z depends on the covariance between X and Y. If X and Y are statistically independent, then variance is

$$\text{Var}[Z] = a^2\text{Var}[Z] + b^2\text{Var}[Y]. \tag{A.17}$$

This last result can be extended to a sum of multiple independent random variables, namely

$$\text{Var}\left[\sum_{k=1}^{N} c_k X_k\right] = \sum_{k=1}^{N} c_k^2 \text{Var}[X_k]. \tag{A.18}$$

A.2 Normal random variables

Normal random variables are used in many fields of statistics and science. A normal random variable is defined by the probability density function

$$p(x) = \frac{1}{\sqrt{2\pi\sigma^2}} \exp\left\{-\frac{(x-\mu)^2}{2\sigma^2}\right\}, \tag{A.19}$$

and a random variable sampled from this distribution is denoted as $X \sim \mathcal{N}(\mu, \sigma^2)$. Basically, this is a Gaussian function which is completely symmetric about the mean value μ, and whose width depends on the variance σ^2. Normal random variables have some important properties. One of these is the scaling property, which states that

$$\mathcal{N}(\mu, \sigma^2) = \mu + \sigma\mathcal{N}(0, 1), \tag{A.20}$$

where $\mathcal{N}(0, 1)$ is a standard normal random variable of mean zero and variance 1.

A.3 Moment-generating functions

A moment-generating function corresponding to a random variable X is defined as follows

$$M_X(t) = \left\langle e^{tX} \right\rangle = \begin{cases} \sum_{k=1}^{\infty} e^{tx_k} p_k & \text{if } X \text{ is discrete} \\ \int_{-\infty}^{\infty} e^{tx} p(x) \mathrm{d}x & \text{if } X \text{ is continuous} \end{cases} \tag{A.21}$$

Thus, for continuous probability distributions, one can show that the nth moment centred around 0 is given by

$$\langle X^n \rangle = \int_{-\infty}^{\infty} x^n p(x) \mathrm{d}x = \lim_{t \to 0} \int_{-\infty}^{\infty} p(x) \left(\frac{d}{dt} \right)^n e^{tx} \mathrm{d}x = \lim_{t \to 0} \left(\frac{d}{dt} \right)^n M_X(t), \tag{A.22}$$

so by knowing the moment-generating function $M_X(t)$, we can easily find expressions for the nth moments using differentiation.

A.3.1 MGF of normal random variables

For the normally distributed random variable $X \sim \mathcal{N}(\mu, \sigma^2)$ with probability density function

$$\rho(x) = \frac{1}{\sqrt{2\pi\sigma^2}} \exp\left\{ -\frac{(x-\mu)^2}{2\sigma^2} \right\},$$

the moment-generating function (MGF) is given by

$$M_{\mathcal{N}}(t) = \frac{1}{\sqrt{2\pi\sigma^2}} \int_{-\infty}^{\infty} \exp\left\{ tx - \frac{(x-\mu)^2}{2\sigma^2} \right\} \mathrm{d}x.$$

Integrating the function using the Gaussian integral result $\int_{-\infty}^{\infty} e^{-ax^2} \mathrm{d}x = \sqrt{\pi/2}$ we obtain

$$M_{\mathcal{N}}(t) = \exp\left\{ \mu t + \frac{\sigma^2 t^2}{2} \right\} \tag{A.23}$$

From this, we can find the mean and variance by taking the first and second moments and using the fact that $\lim_{t \to 0} M_{\mathcal{N}}(t) = 1$

$$\langle X \rangle = \lim_{t \to 0} \frac{dM_{\mathcal{N}}(t)}{dt} = \lim_{t \to 0} \left[\left(\mu + \sigma^2 t \right) M_{\mathcal{N}}(t) \right] = \mu,$$

$$\left\langle X^2 \right\rangle = \lim_{t \to 0} \frac{d^2 M_{\mathcal{N}}(t)}{dt^2} = \lim_{t \to 0} \left[\sigma^2 M_{\mathcal{N}}(t) + \left(\mu + \sigma^2 t \right)^2 M_{\mathcal{N}}(t) \right] = \sigma^2 + \mu^2,$$

which leads to the result

$$\mathrm{Var}[X] = \left\langle X^2 \right\rangle - \langle X \rangle^2 = \sigma^2. \tag{A.24}$$

A.4 Stochastic processes

A stochastic process $x(t)$ is a discrete or continuous sequence of random variables which obey a specific function with respect to well-defined probability distributions. For each point in time t, the value $x(t)$ is sampled from a known probability distribution. A simple example of a discrete stochastic process is the random walk process: consider a particle whose position in n-dimensional space is denoted by $\mathbf{x}$. At each discrete time increment Δt, the position of the particle at time $t + \Delta t$ is computed

by adding a random space increment $\Delta\mathbf{r}$ (e.g. arising from a random external force). Mathematically this is expressed as:

$$\mathbf{x}_{n+1} = \mathbf{x}_n + \Delta\mathbf{r}_n, \tag{A.25}$$

where $\Delta\mathbf{r}_n$ is sampled from a specific distribution at each point in time t_n. Let us now consider a one-dimensional random walk in which some external normal force of variance $\sigma^2\Delta t$ (implying the variance increases linearly with time)

$$x_{n+1} = x_n + \sigma\sqrt{\Delta t}\mathcal{N}(0,1). \tag{A.26}$$

This is an example of Brownian motion, due to the random increment being normally distributed. As $\Delta t \to 0$, the discrete process $x(t)$ approaches a continuous stochastic process. Fig. A.1 shows multiple independent realizations of this random walk.

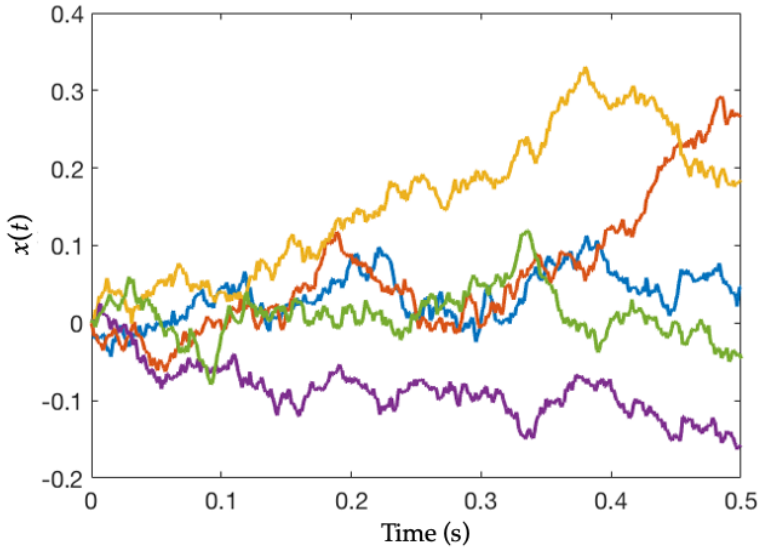

FIGURE A.1: Five independent realizations of the random walk $x_{n+1} = x_n + \sigma\sqrt{\Delta t}\mathrm{N}(0,1)$ for $\sigma = 0.2$ and initial condition $x_0 = 0$.

A.4.1 Wiener processes

A Brownian motion, sometimes called a Wiener process $W(t)$, is a normally distributed random process described as the cumulative sum of multiple independent random increments $\mathrm{d}W(s)$ over a time interval $s \in [0,t]$, namely [177]

$$W(t) = \int_0^t \mathrm{d}W(s). \tag{A.27}$$

The infinitesimal element $\mathrm{d}W(s)$ has properties

$$\langle \mathrm{d}W(t) \rangle = 0; \quad \langle \mathrm{d}W^2(t) \rangle = \mathrm{d}t, \tag{A.28}$$

In a discrete sense, we may also define this as

$$\Delta W(t) = W(t_{k+1}) - W(t_k) = \sqrt{\Delta t}\,\mathcal{N}(0,1), \tag{A.29}$$

where $\Delta t = t_{k+1} - t_k$. This means that the Wiener process $W(t)$ can be sampled from a normal distribution in the context of the difference at two times s and t

$$W(t) - W(s) = \sqrt{|t-s|}\,\mathcal{N}(0,1). \tag{A.30}$$

A.4.2 Auto-correlation functions

The auto-correlation function (ACF) of a stochastic process $x(t)$ gives the relation of the value of the process at some time t with respect to another time t', generally expressed through the lag-time τ as $\tau = t - t'$. In general, this gives a measure of how well we can predict the behaviour of x at t' provided we know the behaviour of x at t, and is found mathematically as

$$r_x(t,t') = \left\langle x(t)x^*(t')\right\rangle. \tag{A.31}$$

A.4.3 Stationarity and the Wiener-Khinchin theorem

A process $x(t)$ is said to be stationary if its statistical properties do not vary with time. Analytically, we can test if a process is stationary by looking at its ACF $r_x(t,t')$: if it is reducible to a function of the time difference $\tau = t - t'$, such that $r_x(t,t') = r_x(\tau)$, then $x(t)$ is stationary. In this sense, the ACF is symmetric about τ such that $r_x(\tau) = r_x(-\tau)$. One of the most important implications of this property is that the power-spectral density (PSD) of $x(t)$ is given by the Wiener-Khinchin theorem [143, 142]

$$S(\omega) = \left\langle |X(\omega)|^2\right\rangle = \frac{1}{2\pi}\int_{-\infty}^{\infty} r_x(\tau)e^{i\omega\tau}\mathrm{d}\tau. \tag{A.32}$$

A.4.4 Non-stationary processes

Most random processes found in nature are non-stationary. This means that the statistical properties of the process $x(t)$ change with time. Analytically, if the ACF is not reducible to a single variable of the time difference $r_x(t,t') \neq r_x(\tau)$, then $x(t)$ is non-stationary. This has several important implications when it comes to analysing the spectral density of $x(t)$ in frequency-space: for any non-stationary process, the spectral density is time-varying. This means that taking the Fourier transform of $r_x(t,t')$ does not explicitly give the PSD of $x(t)$, but rather a function of t and ω

$$S(t,\omega) = \frac{1}{2\pi}\int_{-\infty}^{\infty} r_x(t,t')e^{i\omega t'}\mathrm{d}t'. \tag{A.33}$$

One may then compute the PSD of $x(t)$ by integrating $S(t,\omega)$ in time, namely

$$\left\langle |X(\omega)|^2\right\rangle = \int_{-\infty}^{\infty} S(t,\omega)\mathrm{d}t. \tag{A.34}$$

Special care must be taken with this expression, as for stationary processes it may lead to infinite values. In that case it is necessary to apply a band-pass filter on $S(t,\omega)$. For this reason, with non-stationary processes it is often more appropriate to use the following definition of the PSD

$$S(\omega) = \left\langle |X(\omega)|^2\right\rangle = \frac{1}{2\pi}\left\langle \left|\int_{-\infty}^{\infty} x(t)e^{i\omega t}\mathrm{d}t\right|^2\right\rangle, \tag{A.35}$$

which is also more straight-forward to calculate numerically.

Appendix B

Elasticity Theory

Elasticity theory studies the relationship between the forces applied to an object and the resulting deformations. In this Appendix we provide a brief overview of the theory of elasticity, focusing on the fundamental concepts which are required to follow the derivations in this Thesis, especially the content in Chapter 2.

We begin our discussion by describing the deformations in an object due to applied forces. The deformations in an object can be quantified in terms of a displacement field $\mathbf{u}(\mathbf{X}, t)$ (in units of meters) which is a function both space $\mathbf{X}$ (noting here that $\mathbf{X}$ refers to the position vector of a specific point in space in any coordinate system) and time t. For instance, if you imagine a lattice of atoms in a solid, then the displacement field $\mathbf{u}$ tells you by how much each atom in the lattice moves from its equilibrium position when an external force is applied to the object. Displacements in the atomic lattice can also be induced by periodic excitations in the lattice, namely travelling elastic (or acoustic) waves. This same description of atomic displacements applies to a continuum picture of infinitesimally small particles, which is the basis of our treatment in this Thesis.

Displacements in a continuous medium (which can be a solid or a fluid) also lead to what is called strain, a dimensionless property that quantifies how much the particles in the medium are displaced from their original positions. When external forces are applied to a continuous medium, particles exert internal forces unto one another, creating something called stress in the medium. Stress is a physical quantity similar to pressure, and is also measured in Pascals (or force per unit area). Stresses and strains can be further classified into two types: normal and shear. A normal stress refers to the reaction of a continuous medium to a force applied perpendicular to some cross-sectional area, while a shear stress refers to the reaction of the medium to a force component that runs parallel to some cross-sectional area. The same definition applies to shear and normal strains. For further explanations on stresses and strains, see [178].

We now turn our attention to a displacement field $\mathbf{u}(\mathbf{X}, t)$ of a set of particles in a solid medium, at the generalized coordinates $\mathbf{X}$ and time t. This displacement field is also exrpessible as $\mathbf{u}(\mathbf{X}, t) = \mathbf{L}(\mathbf{X}, t) - \mathbf{X}$, where $\mathbf{L}$ is the displaced position vector. We can also write this in differential form as $\mathrm{d}\mathbf{u}(\mathbf{X}, t) = \mathrm{d}\mathbf{L}(\mathbf{X}, t) - \mathrm{d}\mathbf{X}$. Via the chain rule of partial derivatives, we also write

$$\mathrm{d}\mathbf{u}(\mathbf{X}, t) = \frac{\partial \mathbf{u}(\mathbf{X}, t)}{\partial X_1}\mathrm{d}X_1 + \frac{\partial \mathbf{u}(\mathbf{X}, t)}{\partial X_2}\mathrm{d}X_2 + \frac{\partial \mathbf{u}(\mathbf{X}, t)}{\partial X_3}\mathrm{d}X_3, \tag{B.1}$$

where $\partial_t \mathbf{u}(\mathbf{X}, t)\mathrm{d}t = 0$ under the assumption that the displacements are defined at

constant time [179]. In Cartesian coordinates, we write the displacements in three dimensions in matrix form

$$\begin{bmatrix} \mathrm{d}u_x(\mathrm{d}\mathbf{X},t) \\ \mathrm{d}u_y(\mathrm{d}\mathbf{X},t) \\ \mathrm{d}u_z(\mathrm{d}\mathbf{X},t) \end{bmatrix} = \begin{bmatrix} \frac{\partial u_x}{\partial x} & \frac{\partial u_x}{\partial y} & \frac{\partial u_x}{\partial z} \\ \frac{\partial u_y}{\partial y} & \frac{\partial u_y}{\partial y} & \frac{\partial u_y}{\partial z} \\ \frac{\partial u_z}{\partial x} & \frac{\partial u_z}{\partial y} & \frac{\partial u_z}{\partial z} \end{bmatrix} \begin{bmatrix} \mathrm{d}x \\ \mathrm{d}y \\ \mathrm{d}z \end{bmatrix} = \nabla \mathbf{u}\, \mathrm{d}\mathbf{X}, \tag{B.2}$$

where $\nabla \mathbf{u}$ denotes the displacement gradient. The strain field ϵ is defined as

$$\epsilon_{ij}(\mathbf{X},t) = \frac{1}{2}\left(\frac{\partial u_i}{\partial X_j} + \frac{\partial u_j}{\partial X_i} + \frac{\partial u_k}{\partial X_i}\frac{\partial u_k}{\partial X_j}\right), \tag{B.3}$$

where $i,j,k = x,y,z$ (for Cartesian coordinates), and we have assumed the Einstein summation convention of repeated indices:

$$\frac{\partial u_k}{\partial X_i}\frac{\partial u_k}{\partial X_j} = \sum_k^n \frac{\partial u_k}{\partial X_i}\frac{\partial u_k}{\partial X_j}. \tag{B.4}$$

In the case of very rigid materials, the displacement gradient is generally very small, such that the quadratic terms in (B.3) are negligible. This leads to the linearized strain-displacement relation [179]

$$\epsilon_{ij}(\mathbf{X},t) = \frac{1}{2}\left(\frac{\partial u_i}{\partial X_j} + \frac{\partial u_j}{\partial X_i}\right). \tag{B.5}$$

The strain-displacement relation can also be written in vector form

$$\boldsymbol{\epsilon} = \nabla_s \mathbf{u}, \tag{B.6}$$

where $\boldsymbol{\epsilon}$ is a rank-2 tensor with Cartesian components

$$\boldsymbol{\epsilon} = \begin{bmatrix} \epsilon_{xx} & \epsilon_{xy} & \epsilon_{xz} \\ \epsilon_{yx} & \epsilon_{yy} & \epsilon_{yz} \\ \epsilon_{zx} & \epsilon_{zy} & \epsilon_{zz} \end{bmatrix}, \tag{B.7}$$

where the main diagonal components ϵ_{xx}, ϵ_{yy} and ϵ_{zz} are the normal strains, and the rest are shear strains. Due to the symmetry properties of the strain tensor ($\epsilon_{ij} = \epsilon_{ji}$, as implied by (B.5)), it is customary to express the strain using Voigt-notation [179] as

$$\boldsymbol{\epsilon}^V = \begin{bmatrix} \epsilon_1 \\ \epsilon_2 \\ \epsilon_3 \\ \epsilon_4 \\ \epsilon_5 \\ \epsilon_6 \end{bmatrix} = \begin{bmatrix} \epsilon_{xx} \\ \epsilon_{yy} \\ \epsilon_{zz} \\ 2\epsilon_{yz} \\ 2\epsilon_{xz} \\ 2\epsilon_{xy} \end{bmatrix}. \tag{B.8}$$

In this notation, (B.6) is written in matrix form as

$$\begin{bmatrix} \epsilon_1 \\ \epsilon_2 \\ \epsilon_3 \\ \epsilon_4 \\ \epsilon_5 \\ \epsilon_6 \end{bmatrix} = \begin{bmatrix} \partial_x & 0 & 0 \\ 0 & \partial_y & 0 \\ 0 & 0 & \partial_z \\ 0 & \partial_z & \partial_y \\ \partial_z & 0 & \partial_x \\ \partial_y & \partial_x & 0 \end{bmatrix} \begin{bmatrix} u_x \\ u_y \\ u_z \end{bmatrix}. \tag{B.9}$$

Therefore, we can write the Nabla operator in Voigt notation as

$$\nabla_s^V = \begin{bmatrix} \partial_x & 0 & 0 \\ 0 & \partial_y & 0 \\ 0 & 0 & \partial_z \\ 0 & \partial_z & \partial_y \\ \partial_z & 0 & \partial_x \\ \partial_y & \partial_x & 0 \end{bmatrix}. \tag{B.10}$$

In a similar manner to the strain tensor, the stress tensor $\mathbf{T}$ is defined as

$$\mathbf{T} = \begin{bmatrix} \mathrm{T}_{xx} & \mathrm{T}_{xy} & \mathrm{T}_{xz} \\ \mathrm{T}_{yx} & \mathrm{T}_{yy} & \mathrm{T}_{yz} \\ \mathrm{T}_{zx} & \mathrm{T}_{zy} & \mathrm{T}_{zz} \end{bmatrix}. \tag{B.11}$$

The diagonal components T_{xx}, T_{yy} and T_{zz} represent the normal stresses, while the rest are shear stresses. From this tensor, we can calculate the traction force $\mathbf{f}_{\text{traction}}$ (defined as the external force applied to some cross-sectional area) acting on a surface normal to some unit vector $\hat{\mathbf{n}}$ as $\mathbf{T} \cdot \hat{\mathbf{n}}$. It is therefore of interest to derive a translational dynamic equation for elastic waves in a solid medium, by incorporating the effect of these stresses. First, we consider a vibrating particle of arbitrary shape in the material, with infinitesimal volume δV and surface area δs. The total traction force across the surface is then

$$\mathbf{f}_{\text{traction}} = \int_{\delta s} \mathbf{T} \cdot \hat{\mathbf{n}} \, \mathrm{d}s = \int_{\delta V} \nabla \cdot \mathbf{T} \, \mathrm{d}V, \tag{B.12}$$

which is obtained via the divergence theorem. Next, consider a set of external forces acting on the particle, denoted as $\int_{\delta V} \mathbf{f} \mathrm{d}V$. Finally, the inertial force of the particle is given by Newton's 2nd law, namely $\int_{\delta V} \rho \partial_t \mathbf{v} \mathrm{d}V$ where ρ is the density and $\mathbf{v}$ is the particle's velocity. The balanced force equation across the particle's surface is

$$\int_{\delta V} \rho \frac{\partial \mathbf{v}}{\partial t} \, \mathrm{d}V = \int_{\delta V} \nabla \cdot \mathbf{T} \, \mathrm{d}V + \int_{\delta V} \mathbf{f} \mathrm{d}V. \tag{B.13}$$

Taking the limit as $\delta V \to 0$ yields the so-called elastodynamic equation [180]

$$\rho \frac{\partial \mathbf{v}}{\partial t} = \nabla \cdot \mathbf{T} + \mathbf{f}. \tag{B.14}$$

The stress tensor must also obey the constitutive relation

$$\mathbf{S} : \frac{\partial \mathbf{T}}{\partial t} = \nabla_s \mathbf{v}, \tag{B.15}$$

where $\mathbf{S}$ is the rank-4 compliance tensor (which is inversely proportional to the stiffness tensor $\mathbf{C}$, measuring the material's resistance to deformation), and : is the double dot

product defined as

$$\mathbf{A} : \mathbf{B} = \sum_{i,j} A_{ij} B_{ji}. \tag{B.16}$$

The stress tensor can also be described in terms of the rank-4 stiffness tensor $\mathbf{C}$ [181]

$$\mathbf{T} = \mathbf{C} : \boldsymbol{\epsilon}. \tag{B.17}$$

If we want to include medium damping into the equation, which is related to the 4-rank viscosity tensor $\boldsymbol{\eta}$, we may write [182]

$$\mathbf{T} = \mathbf{C} : \boldsymbol{\epsilon} + \boldsymbol{\eta} : \frac{\partial \boldsymbol{\epsilon}}{\partial t}, \tag{B.18}$$

and using the relation $\boldsymbol{\epsilon} = \nabla_s \mathbf{u}$ we obtain

$$\mathbf{S} : \frac{\partial \mathbf{T}}{\partial t} = \mathbf{S} : \frac{\partial}{\partial t} \left[\mathbf{C} : \boldsymbol{\epsilon} + \boldsymbol{\eta} : \nabla_s \frac{\partial}{\partial t} \mathbf{v} \right] = (\mathbf{S} : \mathbf{C}) : \frac{\partial \boldsymbol{\epsilon}}{\partial t} + \mathbf{S} : \boldsymbol{\eta} : \frac{\partial}{\partial t} \nabla_s \mathbf{v},$$

and using the identity $\mathbf{S} : \mathbf{C} = 1$ leads to the constitutive relation

$$\mathbf{S} : \frac{\partial \mathbf{T}}{\partial t} = \nabla_s \mathbf{v} + \mathbf{S} : \boldsymbol{\eta} : \frac{\partial}{\partial t} \nabla_s \mathbf{v}. \tag{B.19}$$

The elastodynamic equation in (B.14) admits certain types of wave solutions, depending on the boundary conditions imposed, and these include: longitudinal waves (compression and elongation), shear waves and torsional waves [180].

Appendix C

Brownian Motion

To develop an understanding for how thermal noise and other noise mechanisms play a role in Brillouin scattering, we need to first understand the basics of how noise arises in physical contexts. In this section, we present a general theory of Brownian motion, starting with Albert Einstein's original derivation from 1906, and extending it to the theory of stochastic calculus and Langevin equations.

C.1 Brownian motion as diffusion of particles

The theory of Brownian motion was first investigated by Albert Einstein in 1905 in his paper "Investigations on the theory of the Brownian movement" [183], which explained the experimental observations made by botanist Robert Brown with regards to the random movement of pollen particles immersed in a liquid. In this paper, Einstein noted the following approach: first we assume that there is an ensemble of n particles suspended in a liquid. In an interval of time τ, suppose that the x coordinates of each of these particles changes by Δ, where Δ is a real random variable that is different for each particle. Using the laws of probability, we postulate that the number of particles $\mathrm{d}n$ which experience a displacement between Δ and $\Delta + \mathrm{d}\Delta$ during the interval τ obeys the equation

$$\mathrm{d}n = n\phi(\Delta)\mathrm{d}\Delta, \tag{C.1}$$

where $\phi(\Delta)$ is a probability distribution obeying $\int_{-\infty}^{+\infty} \phi(\Delta)\mathrm{d}\Delta = 1$. Because the particles should have equal probability of moving left or right, the distribution must be symmetric $\phi(\Delta) = \phi(-\Delta)$. Then, let's assume that the number of particles per unit volume is given by $f(x,t)$. We would like to calculate the distribution of particles at time $t+\tau$ from the distribution at t. For this, we assume the time evolution of the particle displacement is Markovian, that is: the value of the process at $t+\tau$ only depends on the value at t and not on the entire past history. We can also think of this as follows: $f(x,t+\tau)$ must result from all possible sample paths $f(x+\Delta,t)$ for some random variable Δ, such that we know for certain that $f(x,t+\tau)$ is equal to the ensemble average of all such paths taken at t. Mathematically, we can write this in the form

$$f(x,t+\tau) = \langle f(x+\Delta,t)\rangle_\Delta = \int_{-\infty}^{+\infty} f(x+\Delta,t)\phi(\Delta)\mathrm{d}\Delta, \tag{C.2}$$

where $\langle\cdot\rangle_\Delta$ is the ensemble average or expectation operator with respect to the variable Δ. Now, for small τ, we can write

$$f(x,t+\tau) = f(x,t) + \tau\frac{\partial f}{\partial t}. \tag{C.3}$$

Similarly, we can expand $f(x+\Delta,t)$ as a Taylor series in Δ as

$$f(x+\Delta,t) = f(x,t) + \Delta\frac{\partial f(x,t)}{\partial x} + \frac{\Delta^2}{2!}\frac{\partial^2 f(x,t)}{\partial x^2} + \cdots . \tag{C.4}$$

Substituting (C.3) and (C.4) into (C.2) yields

$$f(x,t) + \tau\frac{\partial f}{\partial t} = \int_{-\infty}^{+\infty} f(x,t)\phi(\Delta)\mathrm{d}\Delta + \int_{-\infty}^{+\infty} \Delta\frac{\partial f(x,t)}{\partial x}\phi(\Delta)\mathrm{d}\Delta + \int_{-\infty}^{+\infty} \frac{\Delta^2}{2!}\frac{\partial^2 f(x,t)}{\partial x^2}\phi(\Delta)\mathrm{d}\Delta + \cdots . \tag{C.5}$$

It is important to note that we can extract all the derivatives of f on the right-hand side from the integrals, such that

$$f(x,t) + \tau\frac{\partial f}{\partial t} = f(x,t)\int_{-\infty}^{+\infty} \phi(\Delta)\mathrm{d}\Delta + \frac{\partial f(x,t)}{\partial x}\int_{-\infty}^{+\infty} \Delta\phi(\Delta)\mathrm{d}\Delta + \frac{\partial^2 f(x,t)}{\partial x^2}\int_{-\infty}^{+\infty} \frac{\Delta^2}{2!}\phi(\Delta)\mathrm{d}\Delta + \cdots . \tag{C.6}$$

Because we defined $\phi(\Delta) = \phi(-\Delta)$, all odd moments of Δ will vanish. Furthermore, using the property $\int_{-\infty}^{+\infty}\phi(\Delta)\mathrm{d}\Delta = 1$, letting $D = \frac{1}{\tau}\int_{-\infty}^{+\infty}\frac{\Delta^2}{2}\phi(\Delta)\mathrm{d}\Delta$ and truncating the series up to 2nd order, we end up with the equation

$$\frac{\partial f}{\partial t} = D\frac{\partial^2 f}{\partial x^2}. \tag{C.7}$$

As it turns out, this is just a diffusion equation, with the diffusion constant D. It should be noted that we have assumed here that all the particles have the same displacement x, but as Einstein pointed out this is not a necessary condition, since the displacements of individual particles should be mutually independent [183].

The solution to this equation gives the probability distribution of the particle displacement x as a function of time. Multiple approaches can be employed, but here we will focus on the Fourier transform method [184]. First, we assume that the initial distribution of some particle at $t = 0$ is deterministic, such that $x(0) = x_0$ and thus it can be represented as a shifted Dirac-delta function as $f(x,0) = \delta(x - x_0)$. First, let us define the solution in terms of the Fourier-transform pairs

$$f(x,t) = \frac{1}{\sqrt{2\pi}}\int_{-\infty}^{\infty}\hat{f}(k,t)e^{ikx}\mathrm{d}k,$$
$$\hat{f}(k,t) = \frac{1}{\sqrt{2\pi}}\int_{-\infty}^{\infty} f(x,t)e^{-ikx}\mathrm{d}x,$$

We will also make use of the properties

$$\frac{1}{\sqrt{2\pi}}\int_{-\infty}^{\infty}\frac{\partial f(x,t)}{\partial x}e^{-ikx}\mathrm{d}x = ik\hat{f}(k,t), \tag{C.8a}$$
$$\frac{1}{\sqrt{2\pi}}\int_{-\infty}^{\infty}\frac{\partial^2 f(x,t)}{\partial x^2}e^{-ikx}\mathrm{d}x = -k^2\hat{f}(k,t), \tag{C.8b}$$
$$\frac{1}{\sqrt{2\pi}}\int_{-\infty}^{\infty}\frac{\partial f(x,t)}{\partial t}e^{-ikx}\mathrm{d}x = \frac{\partial\hat{f}(k,t)}{\partial t}. \tag{C.8c}$$

Applying the Fourier transform in k to both sides of (C.7) yields

$$\frac{\partial \hat{f}(k,t)}{\partial t} = -k^2 D \hat{f}(k,t).$$

Using separation of variables with respect to t, this equation has solution

$$\hat{f}(k,t) = Ae^{-k^2 Dt}, \tag{C.9}$$

for an arbitrary constant A. Now, to recover the original solution, we apply the Fourier transform to the initial condition $f(x,0) = \delta(x - x_0)$

$$\hat{f}(k,0) = \frac{1}{\sqrt{2\pi}} \int_{-\infty}^{\infty} f(x,0) e^{-ikx} \mathrm{d}x = \frac{1}{\sqrt{2\pi}} \int_{-\infty}^{\infty} \delta(x - x_0) e^{-ikx} \mathrm{d}x = \frac{e^{-ikx_0}}{\sqrt{2\pi}},$$

which leads to

$$\hat{f}(k,t) = \frac{e^{-ikx_0}}{\sqrt{2\pi}} e^{-k^2 Dt} = \frac{1}{\sqrt{2\pi}} e^{-(Dtk^2 + ix_0 k)}.$$

Finally, we apply the inverse Fourier transform to $\hat{f}(k,t)$ to recover the original solution

$$f(x,t) = \frac{1}{\sqrt{2\pi}} \int_{-\infty}^{\infty} \hat{f}(k,t) e^{ikx} \mathrm{d}k = \frac{1}{\sqrt{4\pi^2}} \int_{\infty}^{\infty} e^{-Dtk^2 + i(x - x_0)k} \mathrm{d}k.$$

Completing the square on the right-hand side exponent leads to

$$f(x,t) = \frac{1}{\sqrt{4\pi^2}} \exp\left\{ -\frac{(x - x_0)^2}{4Dt} \right\} \int_{-\infty}^{\infty} \exp\left\{ -Dt \left(k - \frac{i(x - x_0)}{2Dt} \right)^2 \right\} \mathrm{d}k.$$

Finally, we use the change of variable $\eta = k - \frac{i(x - x_0)}{2Dt}$ and the well-known result $\int_{-\infty}^{\infty} e^{-ax^2} \mathrm{d}x = \sqrt{\pi / a}$, we obtain

$$f(x,t) = \frac{1}{\sqrt{4\pi Dt}} \exp\left\{ -\frac{(x - x_0)^2}{4Dt} \right\}. \tag{C.10}$$

This is just a normal probability density function with mean x_0 and variance $\sigma^2 = 2Dt$. In fact, as Einstein pointed out in his derivation, the mean-squared displacement for a particle with $x_0 = 0$ is given by $\langle x^2(t) \rangle = 2Dt$, and the arithmetic mean (or root-mean-square displacement) is

$$\lambda_x(t) = \sqrt{\langle x^2(t) \rangle} = \sqrt{2Dt}. \tag{C.11}$$

The main implication of this result is that the mean displacement of the particle is proportional to $\sqrt{t}$. This is what is known as Brownian motion, and it forms the basis of the more general theory of stochastic calculus by which we can model physical systems with noise. An example of how the probability distribution in (C.10) evolves in time is given in Fig. C.1(a).

C.1.1 Brownian motion and stochastic differential equations

Now that we understand Brownian motion as a zero-mean normally distributed process with variance proportional to t, we can discuss the differential equations used to

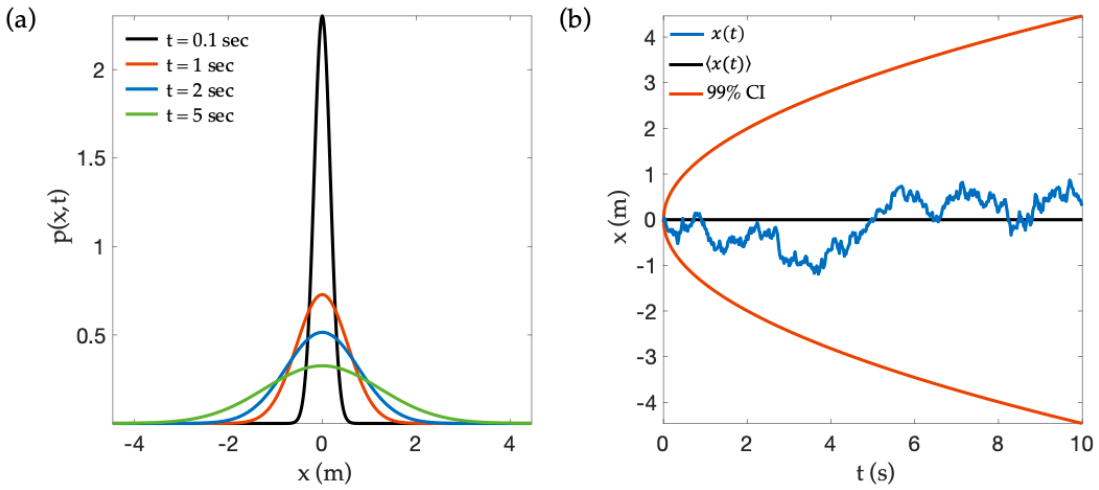

FIGURE C.1: (a) Evolution of the probability density function $p(x,t)$ of a Brownian particle in (C.10) using $x_0 = 0$ and $D = 0.15$. (b) Single trajectory of a Brownian particle by solving (C.14) numerically with step-size $\Delta t = 0.02$ s, showing the 99% confidence intervals with standard deviation $\sqrt{2Dt}$.

model this random movement. We assume the reader is familiar with the theory of random variables, which is covered in Appendix A.

Let us define $W(t)$ as a stochastic process with statistical properties $\langle W(t)\rangle = 0$ and $\langle W^2(t)\rangle = t$, as well as the auto-correlation function $\langle W(t)W(s)\rangle = \min(s,t)$. This is known as a standard Wiener process in the stochastic calculus literature [138, 177]. In this same spirit, we can define an infinitesimal increment $\mathrm{d}W(t) = W(t+\mathrm{d}t) - W(t)$ with properties $\langle \mathrm{d}W(t)\rangle = 0$ and $\langle \mathrm{d}W^2(t)\rangle = \mathrm{d}t$, since the process is uncorrelated at different times. Following the Itô calculus [152], we can model a stochastic differential equation as

$$\mathrm{d}x(t) = \mu(x,t)\mathrm{d}t + \sigma(x,t)\mathrm{d}W(t), \tag{C.12}$$

where $\mu(x,t)$ and $\sigma(x,t)$ are the drift and volatility components, respectively. Here we can give this equation a simple physical interpretation: In the absence of noise (e.g. neglecting the σ term), this reduces to an ordinary differential equation where $x(t)$ is a deterministic trajectory of the particle. However, introducing a noise term $\sigma(x,t)\mathrm{d}W(t)$ now makes that trajectory random, given that at every time step $\mathrm{d}t$ the particle may be nudged by a random force proportional to $\sqrt{\mathrm{d}t}$, just as one might expect from Einstein's original analysis. This Itô equation is also connected to the Fokker-Planck equation (FPE) [185, 186, 187]

$$\frac{\partial \rho(x,t)}{\partial t} = -\frac{\partial}{\partial x}\left[\mu(x,t)\rho(x,t)\right] + \frac{1}{2}\frac{\partial^2}{\partial x^2}\left[\sigma^2(x,t)\rho(x,t)\right], \tag{C.13}$$

where $\rho(x,t)$ is the probability density function of $x(t)$. We can thus model a Brownian motion as in (C.10) via the stochastic differential equation

$$\mathrm{d}x(t) = \sqrt{2D}\mathrm{d}W(t), \tag{C.14}$$

subject to $x(0) = x_0$. Using $\mu(x,t) = 0$ and $\sigma(x,t) = \sqrt{2D}$, we find through (C.13) that the probability density function of $x(t)$ in this case is given by (C.10). A numerical simulation of (C.14) is shown in Fig. C.1(b), using finite time increments Δt.

C.1.2 Langevin equations

In real physical systems, we often deal with Langevin-type equations such as

$$\frac{\mathrm{d}x}{\mathrm{d}t} = \mu(x,t) + \sigma(x,t)\xi(t), \tag{C.15}$$

where $\xi(t)$ is a random force term. It is therefore necessary to establish a link between (C.12) and (C.15). Assuming $\xi(t)$ is itself normally distributed, which corresponds to the case of white noise, then this implies that $\xi(t) = \mathrm{d}W(t)/\mathrm{d}t$. However, the Wiener process $W(t)$ is nowhere differentiable, so this definition must be used with caution. The key is to establish the statistical properties of $\xi(t)$. It is easy to demonstrate that $\langle \xi(t) \rangle = 0$ given that both the expectation operator and the differential operator are linear. Another useful statistical measure is the two-time auto-correlation function $\langle \xi(t)\xi(s) \rangle$. To derive an expression for this, we resort to the theory of generalized functions: let $T_\varphi[f] = \int f(t)\varphi(t)\mathrm{d}t$ be a generalized function acting on $f(t)$, with kernel $\varphi(t)$. It follows that such a functional possesses the following derivative property [188, 189]:

$$T'_\varphi[f] = -T_\varphi\left[f'\right], \tag{C.16}$$

in other words, we can write

$$\int f(t)\frac{\mathrm{d}\varphi(t)}{\mathrm{d}t}\mathrm{d}t = -\int \varphi(t)\frac{\mathrm{d}f(t)}{\mathrm{d}t}\mathrm{d}t. \tag{C.17}$$

Let us now define a functional with Wiener process kernel $W(t)$ as

$$T_W[f] = \int_0^\infty f(t)W(t)\mathrm{d}t. \tag{C.18}$$

Here we also make the assumption that $\lim_{t\to\infty} f(t) = 0$. Then by the linearity property of the expectation operator $\langle \cdot \rangle$ [177], we obtain

$$\langle T_W[f] \rangle = \left\langle \int_0^\infty f(t)W(t)\mathrm{d}t \right\rangle = \int_0^\infty f(t)\langle W(t) \rangle \mathrm{d}t = 0. \tag{C.19}$$

From this result, as well as using the stochastic Fubini theorem [140], we obtain the expectation value of a product of these generalized functions, namely

$$\begin{aligned}
\langle T_W[f]\, T_W[g] \rangle &= \left\langle \int_0^\infty f(t)W(t)\mathrm{d}t \int_0^\infty g(s)W(s)\mathrm{d}s \right\rangle \\
&= \left\langle \int_0^\infty \int_0^\infty f(t)g(s)W(t)W(s)\mathrm{d}s\mathrm{d}t \right\rangle \\
&= \int_0^\infty \int_0^\infty f(t)g(s)\langle W(t)W(s) \rangle \mathrm{d}s\mathrm{d}t \\
&= \int_0^\infty \int_0^\infty f(t)g(s)\min(s,t)\mathrm{d}s\mathrm{d}t.
\end{aligned}$$

Now, using the property in (C.16), we write

$$\begin{aligned}
\left\langle T'_W\left[f\right] T'_W\left[g\right]\right\rangle &= \left\langle T_W\left[f'\right] T_W\left[g'\right]\right\rangle \\
&= \left\langle \int_0^\infty \frac{\mathrm{d}f(t)}{\mathrm{d}t} W(t)\mathrm{d}t \int_0^\infty \frac{\mathrm{d}g(s)}{\mathrm{d}s} W(s)\mathrm{d}s \right\rangle \\
&= \left\langle \int_0^\infty \int_0^\infty \frac{\mathrm{d}f(t)}{\mathrm{d}t}\frac{\mathrm{d}g(s)}{\mathrm{d}s} W(t)W(s)\mathrm{d}s\mathrm{d}t \right\rangle \\
&= \int_0^\infty \int_0^\infty \frac{\mathrm{d}f(t)}{\mathrm{d}t}\frac{\mathrm{d}g(s)}{\mathrm{d}s} \langle W(t)W(s)\rangle \mathrm{d}s\mathrm{d}t \\
&= \int_0^\infty \int_0^\infty \frac{\mathrm{d}f(t)}{\mathrm{d}t}\frac{\mathrm{d}g(s)}{\mathrm{d}s} \min(s,t)\mathrm{d}s\mathrm{d}t \\
&= \int_0^\infty \frac{\mathrm{d}f(t)}{\mathrm{d}t} \int_0^t s\frac{\mathrm{d}g(s)}{\mathrm{d}s}\mathrm{d}s\mathrm{d}t + \int_0^\infty t\frac{\mathrm{d}f(t)}{\mathrm{d}t} \int_t^\infty \frac{\mathrm{d}g(s)}{\mathrm{d}s}\mathrm{d}s\mathrm{d}t \\
&= \int_0^\infty \frac{\mathrm{d}f(t)}{\mathrm{d}t}\left[tg(t) - \int_0^t g(s)\mathrm{d}s\right]\mathrm{d}t + \int_0^\infty t\frac{\mathrm{d}f(t)}{\mathrm{d}t}\left[\lim_{s\to\infty} g(s) - g(t)\right]\mathrm{d}t \\
&= -\int_0^\infty \frac{\mathrm{d}f(t)}{\mathrm{d}t}\int_0^t g(s)\mathrm{d}s\mathrm{d}t \\
&= -\left[\lim_{t\to\infty}\left[f(t)\int_0^t g(s)\mathrm{d}s\right] - \int_0^\infty f(t)\frac{\mathrm{d}}{\mathrm{d}t}\int_0^t g(s)\mathrm{d}s\right] \\
&= \int_0^\infty f(t)g(t)\mathrm{d}t.
\end{aligned}$$

This last expression can also be written as

$$\int_0^\infty f(t)g(t)\mathrm{d}t = \int_0^\infty \int_0^\infty f(t)g(s)\delta(t-s)\mathrm{d}s\mathrm{d}t.$$

By the same property in (C.16), we write

$$\begin{aligned}
\left\langle T'_W\left[f\right] T'_W\left[g\right]\right\rangle &= \left\langle \int_0^\infty f(t)\frac{\mathrm{d}W(t)}{\mathrm{d}t}\mathrm{d}t \int_0^\infty g(s)\frac{\mathrm{d}W(s)}{\mathrm{d}s}\mathrm{d}s \right\rangle \\
&= \left\langle \int_0^\infty \int_0^\infty f(t)g(s)\frac{\mathrm{d}W(t)}{\mathrm{d}t}\frac{\mathrm{d}W(s)}{\mathrm{d}s}\mathrm{d}s\mathrm{d}t \right\rangle \\
&= \int_0^\infty \int_0^\infty f(t)g(s)\left\langle \frac{\mathrm{d}W(t)}{\mathrm{d}t}\frac{\mathrm{d}W(s)}{\mathrm{d}s} \right\rangle \mathrm{d}s\mathrm{d}t,
\end{aligned}$$

from which we obtain the relation

$$\left\langle \frac{\mathrm{d}W(t)}{\mathrm{d}t}\frac{\mathrm{d}W(s)}{\mathrm{d}s} \right\rangle = \delta(t-s). \tag{C.20}$$

Henceforth, the white noise term $\xi(t)$ has auto-correlation function

$$\langle \xi(t)\xi(s)\rangle = \left\langle \frac{\mathrm{d}W(t)}{\mathrm{d}t}\frac{\mathrm{d}W(s)}{\mathrm{d}s} \right\rangle = \delta(t-s). \tag{C.21}$$

This result has very important implications in the theory of stochastic dynamics. It tells us that $\xi(t)$ is statistically uncorrelated at any two different times, and this is what is defined as white noise.

Appendix D

MATLAB Numerical Solver

In this Appendix, we show how to implement the SBS solver for the backward SBS coupled equations presented in Chapter 3 are solved, namely

$$\frac{\partial a_1}{\partial z} + \frac{1}{v}\frac{\partial a_1}{\partial t} + \frac{1}{2}\alpha a_1 = i\omega_1 Q_1 a_2 b^*, \tag{D.1}$$

$$\frac{\partial a_2}{\partial z} - \frac{1}{v}\frac{\partial a_2}{\partial t} - \frac{1}{2}\alpha a_2 = i\omega_2 Q_2 a_1 b, \tag{D.2}$$

$$\frac{\partial b}{\partial z} + \frac{1}{v_a}\frac{\partial b}{\partial t} + \frac{1}{2}\alpha_{\text{ac}} b = i\Omega Q_a a_1^* a_2 + \sqrt{\sigma} R(z,t). \tag{D.3}$$

We use the numerical algorithm outlined in Chapter 5, which is also explained in detail the paper [131]. The code is available on:

`https://github.com/oscarnieves100/MATLAB-Simulations/`

in the MATLAB script `SBS_solver.m`, along with documentation inside the script. Here we will briefly discuss what the input parameters are, namely:

```
function [a1,a2,b,zv,tv] = SBS_solver(phase_noise,thermal_noise,L,fwhm_p,...
    fwhm_s,va,n,Nz,Pp0,Ps0,tau_a,nu_laser,lambda,f_ph,chirp1,chirp2,...
    alpha_dBpcm,T,g0,Q2)
```

The first parameters `phase_noise` and `thermal_noise` correspond to either 1 or 0 each (true or false), indicating whether the user desires to include laser phase noise in the boundary conditions and thermal noise in the waveguide, respectively. The next argument `L` is the length of the waveguide in meters. `fwhm_p` and `fwhm_s` are the temporal full-width at half-maximums of the pump and signal (Stokes seed) respectively (assuming Gaussian pulses) in seconds. `va` is the acoustic group velocity of the medium in m/s, `n` is the optical refractive index (e.g. approximately 2.44 for chacogenide), and `Nz` is the grid-size in space. The peak powers for the pump and signal (Stokes seed) are `Pp0` and `Ps0` respectively in Watts. `tau_a` is the acoustic lifetime of the medium (in seconds), `nu_laser` is the laser's intrinsic linewidth in Hertz, `lambda` is the wavelength of the laser source in meters, `f_ph` is the acoustic phonon frequency in Hertz (which should correspond to the Brillouin frequency shift typically between $1-10$ GHz). The parameters `chirp1` and `chirp2` are the constant chirp of pump and seed Stokes pulses respectively in GHz/ns. `alpha_dBpcm` is the optical attenuation in dB/cm (typically for materials like chalcogenide, this will be in the range of $0.1-0.5$ dB/cm). `T` is the temperature of the medium in Kelvin, `g0` is the SBS gain parameter in $\text{m}^{-1}\text{W}^{-1}$ (and is waveguide dependent, also changes with the acoustic loss or acoustic lifetime), and `Q2` is the Stokes overlap integral in $\text{s}\cdot\text{m}^{-1}\text{W}^{-1/2}$.

Out of all these parameters, `Q2` is not necessary, as it can be estimated from the value of `g0` and the other parameters entered. Similarly, the other overlap integral coupling constants (namely `Q1` and `Qa`) are calculated from `Q2`.

The outputs here are the envelope fields for the pump, Stokes and acoustic field (`a1`, `a2` and `b` respectively), which are given as arrays in space z and time t. The other two outputs are the vector `zv` which contains the spatial grid points starting at 0 and going up to L, while `tv` is the vector of points in time for the simulation (the function implicitly makes the simulation long

enough so that the input optical pulses have exited the waveguide in the end). An example of how to implement this function and produce some waterfall plots and animations is given in `SBS_solver_example.m` on:

`https://github.com/oscarnieves100/MATLAB-Simulations/`

Bibliography

[1] National Research Council et al. *Optics and photonics: Essential technologies for our nation*. National Academies Press, 2013.

[2] Sergey V Gaponenko. *Introduction to nanophotonics*. Cambridge University Press, 2010.

[3] Heinrich Hertz. Über einen einfluß des ultravioletten lichtes auf die electrische entladung. *Annalen der Physik*, 267(8):983–1000, 1887.

[4] Joseph John Thomson. XL. Cathode rays. *The London, Edinburgh, and Dublin Philosophical Magazine and Journal of Science*, 44(269):293–316, 1897.

[5] Philipp Lenard. On cathode rays (Nobel lecture). https://www.nobelprize.org/prizes/physics/1905/lenard/lecture/. Accessed: 2021-09-10.

[6] Albert Einstein. On a heuristic viewpoint concerning the production and transformation of light. *Annalen der Physik*, 17:132–148, 1905.

[7] Vincent Laude and Jean-Charles Beugnot. Lagrangian description of Brillouin scattering and electrostriction in nanoscale optical waveguides. *New Journal of Physics*, 17(12):125003, 2015.

[8] J. E. Sipe and M. J. Steel. A Hamiltonian treatment of stimulated Brillouin scattering in nanoscale integrated waveguides. *New J. Phys.*, 18(4):045004, 2016.

[9] Peter Brüesch. *Phonons: Theory and experiments I: Lattice dynamics and models of interatomic forces*, volume 34. Springer Science & Business Media, 2012.

[10] Regine Celia Da Silva Barros Allil, Marcelo Martins Werneck, and Fábio Vieira Batista de Nazaré. *FiberBragg gratings: theory, fabrication, and applications*. SPIE Press, 2017.

[11] Léon Brillouin. Diffusion de la lumière et des rayons x par un corps transparent homogène. In *Annales de physique*, volume 9, pages 88–122, 1922.

[12] CV Raman. Optical observation of the thermal agitation of the atoms in crystals. *Nature*, 109(2724):42–42, 1922.

[13] LI Mandelstam. Light scattering by inhomogeneous media. *Zh. Russ. Fiz-Khim. Ova*, 58:381, 1926.

[14] William Henry Bragg and William Lawrence Bragg. The reflection of x-rays by crystals. *Proceedings of the Royal Society of London. Series A, Containing Papers of a Mathematical and Physical Character*, 88(605):428–438, 1913.

[15] E Gross. Change of wave-length of light due to elastic heat waves at scattering in liquids. *Nature*, 126(3171):201–202, 1930.

[16] P Debye and FW Sears. On the scattering of light by supersonic waves. *Proceedings of the National Academy of Sciences of the United States of America*, 18(6):409, 1932.

[17] CV Raman and NS Nagendra Nathe. The diffraction of light by high frequency sound waves: Part i. In *Proceedings of the Indian Academy of Sciences-Section A*, volume 2, pages 406–412. Springer, 1935.

[18] BV Raghavendra Rao. The Doppler effect in light scattered by liquids. In *Proceedings of the Indian Academy of Sciences-Section A*, volume 1, pages 765–767. Springer, 1935.

[19] CV Raman and CS Venkateswaran. Optical observation of the Debye heat waves in crystals. *Nature*, 142(3588):250–250, 1938.

[20] V Chandrasekharan. Thermal scattering of light in crystals. In *Proceedings of the Indian Academy of Sciences-Section A*, volume 32, pages 379–385. Springer India, 1950.

[21] TH Maiman. Stimulated optical radiation in ruby. *SPIE milestone series*, (173):61–61, 2002.

[22] RY Chiao, CH Townes, and BP Stoicheff. Stimulated Brillouin scattering and coherent generation of intense hypersonic waves. *Physical Review Letters*, 12(21):592, 1964.

[23] Norman M Kroll. Excitation of hypersonic vibrations by means of photoelastic coupling of high-intensity light waves to elastic waves. *Journal of Applied Physics*, 36(1):34–43, 1965.

[24] Yo R Shen and N Bloembergen. Theory of stimulated Brillouin and Raman scattering. *Physical Review*, 137(6A):A1787, 1965.

[25] CL Tang. Saturation and spectral characteristics of the Stokes emission in the stimulated Brillouin process. *Journal of Applied Physics*, 37(8):2945–2955, 1966.

[26] D Pohl, M Maier, and W Kaiser. Phonon lifetimes measured in amplifiers for Brillouin radiation. *Physical Review Letters*, 20(8):366, 1968.

[27] EP Ippen and RH Stolen. Stimulated Brillouin scattering in optical fibers. *Applied Physics Letters*, 21(11):539–541, 1972.

[28] KO Hill, BS Kawasaki, and DC Johnson. CW Brillouin laser. *Applied Physics Letters*, 28(10):608–609, 1976.

[29] KO Hill, DC Johnson, and BS Kawasaki. CW generation of multiple Stokes and anti-Stokes Brillouin-shifted frequencies. *Applied Physics Letters*, 29(3):185–187, 1976.

[30] JR Sandercock. Structure in the Brillouin spectra of thin films. *Physical Review Letters*, 29(26):1735, 1972.

[31] Rodney Loudon. Theory of surface-ripple Brillouin scattering by solids. *Physical Review Letters*, 40(9):581, 1978.

[32] R Normandin, V CY So, N Rowell, and GI Stegeman. Scattering of guided optical beams by surface acoustic waves in thin films. *JOSA*, 69(8):1153–1165, 1979.

[33] Ravi Pant, Christopher G Poulton, Duk-Yong Choi, Hannah Mcfarlane, Samuel Hile, Enbang Li, Luc Thevenaz, Barry Luther-Davies, Stephen J Madden, and Benjamin J Eggleton. On-chip stimulated Brillouin scattering. *Opt. Express*, 19(9):8285–8290, 2011.

[34] Peter T Rakich, Charles Reinke, Ryan Camacho, Paul Davids, and Zheng Wang. Giant enhancement of stimulated Brillouin scattering in the subwavelength limit. *Physical Review X*, 2(1):011008, 2012.

[35] Eric A Kittlaus, Heedeuk Shin, and Peter T Rakich. Large Brillouin amplification in silicon. *Nature Photonics*, 10(7):463–467, 2016.

[36] Eric A Kittlaus, Nils T Otterstrom, and Peter T Rakich. On-chip inter-modal Brillouin scattering. *Nature communications*, 8(1):1–9, 2017.

[37] Gustavo S Wiederhecker, Paulo Dainese, and Thiago P Mayer Alegre. Brillouin optomechanics in nanophotonic structures. *APL photonics*, 4(7):071101, 2019.

[38] Amol Choudhary, Yang Liu, David Marpaung, and Benjamin J Eggleton. On-chip Brillouin filtering of RF and optical signals. *IEEE J. Sel. Top. Quantum Electron.*, 24(6):1–11, 2018.

[39] Hengyun Jiang, Lianshan Yan, Wei Pan, Bing Luo, and Xihua Zou. Ultra-high speed RF filtering switch based on stimulated Brillouin scattering. *Opt. Lett.*, 43(2):279–282, 2018.

[40] PT Rakich, E Kittlaus, N Otterstrom, RO Behunin, and Z Wang. Silicon-based Brillouin photonics and signal processing. In *Optical Fiber Communication Conference*, pages M1H–3. Optical Society of America, 2018.

[41] Eric A Kittlaus, Prashanta Kharel, Nils T Otterstrom, Zheng Wang, and Peter T Rakich. Rf-photonic filters via on-chip photonic–phononic emit–receive operations. *Journal of Lightwave Technology*, 36(13):2803–2809, 2018.

[42] Adrien Godet, Abdoulaye Ndao, Thibaut Sylvestre, Vincent Pecheur, Sylvie Lebrun, Gilles Pauliat, Jean-Charles Beugnot, and Kien Phan Huy. Brillouin spectroscopy of optical microfibers and nanofibers. *Optica*, 4(10):1232–1238, 2017.

[43] Atiyeh Zarifi, Birgit Stiller, Moritz Merklein, Yang Liu, Blair Morrison, Alvaro Casas-Bedoya, Guanghui Ren, Thach G Nguyen, Khu Vu, Duk-Yong Choi, et al. Brillouin spectroscopy of a hybrid silicon-chalcogenide waveguide with geometrical variations. *Optics Letters*, 43(15):3493–3496, 2018.

[44] Benjamin J Eggleton, Christopher G Poulton, Peter T Rakich, Michael J Steel, and Gaurav Bahl. Brillouin integrated photonics. *Nature Photonics*, 13(10):664–677, 2019.

[45] Adrien Godet, Jacques Chrétien, Kien Phan Huy, and Jean-Charles Beugnot. Ultrasensitive Brillouin nanofiber force sensor. In *Optical Sensors*, pages SW1F–2. Optical Society of America, 2020.

[46] Bastien Steinhausser, Arnaud Brignon, Eric Lallier, Jean-Pierre Huignard, and Patrick Georges. High energy, single-mode, narrow-linewidth fiber laser source using stimulated Brillouin scattering beam cleanup. *Opt. Express*, 15(10):6464–6469, 2007.

[47] William Loh, Adam AS Green, Fred N Baynes, Daniel C Cole, Franklyn J Quinlan, Hansuek Lee, Kerry J Vahala, Scott B Papp, and Scott A Diddams. Dual-microcavity narrow-linewidth Brillouin laser. *Optica*, 2(3):225–232, 2015.

[48] G Lin, S Diallo, K Saleh, R Martinenghi, JC Beugnot, T Sylvestre, and YK Chembo. Brillouin lasing in barium fluoride whispering-gallery-mode resonators. In *The European Conference on Lasers and Electro-Optics*, page CD_10_1. Optical Society of America, 2015.

[49] Ryan O. Behunin, Nils T. Otterstrom, Peter T. Rakich, Sarat Gundavarapu, and Daniel J. Blumenthal. Fundamental noise dynamics in cascaded-order Brillouin lasers. *Phys. Rev. A*, 98:023832, Aug 2018.

[50] Nils T Otterstrom, Ryan O Behunin, Eric A Kittlaus, Zheng Wang, and Peter T Rakich. A silicon Brillouin laser. *Science*, 360(6393):1113–1116, 2018.

[51] Irina V Kabakova, YuChen Xiang, Carl Paterson, and Peter Török. Fiber-integrated Brillouin microspectroscopy: towards Brillouin endoscopy. *Journal of Innovative Optical Health Sciences*, 10(06):1742002, 2017.

[52] Irina V Kabakova, Yuchen Xiang, Carin Basirun, Joshua Chou, Majid Warkiani, Peter Török, Yingying Wang, and Shoufei Gao. Background-free Brillouin fibre probe for remote mapping of micromechanics. In *Optical Elastography and Tissue Biomechanics VIII*, volume 11645, page 116450N. International Society for Optics and Photonics, 2021.

[53] David T Hon. Pulse compression by stimulated Brillouin scattering. *Opt. Lett.*, 5(12):516–518, 1980.

[54] Gilad Marcus, Shaul Pearl, and Guerman Pasmanik. Stimulated Brillouin scattering pulse compression to 175 ps in a fused quartz at 1064 nm. *Journal of Applied Physics*, 103(10):103105, 2008.

[55] Iavor Tzvetanov Veltchev. *Stimulated Brillouin scattering pulse compression and harmonic generation: applications to precision XUV laser spectroscopy*. PhD thesis, Amsterdam: Vrije Universiteit, 2001.

[56] Paulo F Jarschel, Erick Lamilla, Yovanny AV Espinel, Ivan Aldaya, Julian L Pita, Andres Gil-Molina, Gustavo S Wiederhecker, and Paulo Dainese. Intermodal Brillouin scattering in solid-core photonic crystal fibers. *APL Photonics*, 6(3):036108, 2021.

[57] Joël Cabrel Tchahame, Jean-Charles Beugnot, Kien Phan Huy, Vincent Laude, Alexandre Kudlinski, and Thibaut Sylvestre. Surface Brillouin scattering in photonic crystal fibers. *Optics letters*, 41(14):3269–3272, 2016.

[58] WH Renninger, H Shin, RO Behunin, P Kharel, EA Kittlaus, and PT Rakich. Forward Brillouin scattering in hollow-core photonic bandgap fibers. *New Journal of Physics*, 18(2):025008, 2016.

[59] Zhaoming Zhu, Daniel J Gauthier, and Robert W Boyd. Stored light in an optical fiber via stimulated Brillouin scattering. *Science*, 318(5857):1748–1750, 2007.

[60] Herbert G Winful. Chirped Brillouin dynamic gratings for storing and compressing light. *Optics Express*, 21(8):10039–10047, 2013.

[61] Mark Dong and Herbert G Winful. Area dependence of chirped-pulse stimulated Brillouin scattering: implications for stored light and dynamic gratings. *JOSA B*, 32(12):2514–2519, 2015.

[62] Moritz Merklein, Birgit Stiller, Khu Vu, Stephen J Madden, and Benjamin J Eggleton. A chip-integrated coherent photonic-phononic memory. *Nat. Commun.*, 8(1):1–7, 2017.

[63] Birgit Stiller, Moritz Merklein, Christian Wolff, Khu Vu, Pan Ma, Stephen J Madden, and Benjamin J Eggleton. Coherently refreshing hypersonic phonons for light storage. *Optica*, 7(5):492–497, 2020.

[64] Robert W Boyd, Kazimierz Rzazewski, and Paul Narum. Noise initiation of stimulated Brillouin scattering. *Phys. Rev. A*, 42(9):5514, 1990.

[65] Alexander L Gaeta and Robert W Boyd. Stochastic dynamics of stimulated Brillouin scattering in an optical fiber. *Phys. Rev. A*, 44(5):3205, 1991.

[66] MF Ferreira, JF Rocha, and JL Pinto. Analysis of the gain and noise characteristics of fiber Brillouin amplifiers. *Opt. Quantum Electron.*, 26(1):35–44, 1994.

[67] Prashanta Kharel, RO Behunin, WH Renninger, and PT Rakich. Noise and dynamics in forward Brillouin interactions. *Phys. Rev. A*, 93(6):063806, 2016.

[68] Robert W Boyd. *Nonlinear optics*. Elsevier, 2003.

[69] Christian Wolff, MJA Smith, Birgit Stiller, and CG Poulton. Brillouin scattering—theory and experiment: tutorial. *JOSA B*, 38(4):1243–1269, 2021.

[70] Andrey Kobyakov, Michael Sauer, and Dipak Chowdhury. Stimulated Brillouin scattering in optical fibers. *Adv. Opt. Photonics*, 2(1):1–59, 2010.

[71] Yan Pennec, Vincent Laude, Nikos Papanikolaou, Bahram Djafari-Rouhani, Mourad Oudich, Said El Jallal, Jean Charles Beugnot, Jose M Escalante, and Alejandro Martínez. Modeling light-sound interaction in nanoscale cavities and waveguides. *Nanophotonics*, 3(6):413–440, 2014.

[72] Michael J Smith, C Martijn de Sterke, Boris Kuhlmey, Christian Wolff, Mikhail Lapine, and Chris Poulton. Elastic modelling of electrostriction in dielectric composite materials. In *Bragg Gratings, Photosensitivity, and Poling in Glass Waveguides*, pages JM6A–21. Optical Society of America, 2016.

[73] Hans Mueller. The theory of photoelasticity. *Journal of the American Ceramic Society*, 21(1):27–33, 1938.

[74] Pericles S Theocaris and Emmanuel E Gdoutos. *Matrix theory of photoelasticity*, volume 11. Springer, 2013.

[75] V Sundar and RE Newnham. Electrostriction and polarization. *Ferroelectrics*, 135(1):431–446, 1992.

[76] Christian Wolff, Michael J Steel, Benjamin J Eggleton, and Christopher G Poulton. Stimulated Brillouin scattering in integrated photonic waveguides: Forces, scattering mechanisms, and coupled-mode analysis. *Phys. Rev. A*, 92(1):013836, 2015.

[77] Donald F Nelson and R Bruce Lindsay. Electric, optic, and acoustic interactions in dielectrics by donald f. nelson, 1984.

[78] Richard G Brewer and Klaus E Rieckhoff. Stimulated Brillouin scattering in liquids. *Physical Review Letters*, 13(11):334, 1964.

[79] MJ Damzen, V Vlad, Anca Mocofanescu, and V Babin. *Stimulated Brillouin scattering: fundamentals and applications*. CRC press, 2003.

[80] Robert J Williams, Zhenxu Bai, Soumya Sarang, Ondrej Kitzler, David J Spence, and Richard P Mildren. Diamond Brillouin lasers. *arXiv preprint arXiv:1807.00240*, 2018.

[81] Benjamin J Eggleton, Christopher G Poulton, and Ravi Pant. Inducing and harnessing stimulated Brillouin scattering in photonic integrated circuits. *Advances in Optics and Photonics*, 5(4):536–587, 2013.

[82] Oscar A Nieves, Matthew D Arnold, MJ Steel, Mikołaj K Schmidt, and Christopher G Poulton. Noise and pulse dynamics in backward stimulated Brillouin scattering. *Optics Express*, 29(3):3132–3146, 2021.

[83] Moritz Merklein, Alvaro Casas-Bedoya, David Marpaung, Thomas FS Büttner, Mattia Pagani, Blair Morrison, Irina V Kabakova, and Benjamin J Eggleton. Stimulated Brillouin scattering in photonic integrated circuits: novel applications and devices. *IEEE Journal of Selected Topics in Quantum Electronics*, 22(2):336–346, 2016.

[84] Raphaël Van Laer, Alexandre Bazin, Bart Kuyken, Roel Baets, and Dries Van Thourhout. Net on-chip Brillouin gain based on suspended silicon nanowires. *New Journal of Physics*, 17(11):115005, 2015.

[85] Kwang Yong Song, Kazi S Abedin, Kazuo Hotate, Miguel González Herráez, and Luc Thévenaz. Highly efficient Brillouin slow and fast light using as_2se_3 chalcogenide fiber. *Optics Express*, 14(13):5860–5865, 2006.

[86] Heedeuk Shin, Wenjun Qiu, Robert Jarecki, Jonathan A Cox, Roy H Olsson, Andrew Starbuck, Zheng Wang, and Peter T Rakich. Tailorable stimulated Brillouin scattering in nanoscale silicon waveguides. *Nature Communications*, 4(1):1–10, 2013.

[87] Raphaël Van Laer, Bart Kuyken, Dries Van Thourhout, and Roel Baets. Analysis of enhanced stimulated Brillouin scattering in silicon slot waveguides. *Optics Letters*, 39(5):1242–1245, 2014.

[88] Raphaël Van Laer, Christopher J Sarabalis, Roel Baets, Dries Van Thourhout, and Amir H Safavi-Naeini. Thermal Brillouin noise observed in silicon optomechanical waveguide. *Journal of Optics*, 19(4):044002, 2017.

[89] David Marpaung, Blair Morrison, Mattia Pagani, Ravi Pant, Duk-Yong Choi, Barry Luther-Davies, Steve J Madden, and Benjamin J Eggleton. Low-power, chip-based stimulated Brillouin scattering microwave photonic filter with ultrahigh selectivity. *Optica*, 2(2):76–83, 2015.

[90] Heedeuk Shin, Jonathan A Cox, Robert Jarecki, Andrew Starbuck, Zheng Wang, and Peter T Rakich. Control of coherent information via on-chip photonic–phononic emitter–receivers. *Nature Communications*, 6(1):1–8, 2015.

[91] Shmuel Sternklar and Er'el Granot. Narrow spectral response of a Brillouin amplifier. *Optics Letters*, 28(12):977–979, 2003.

[92] Nils T Otterstrom, Eric A Kittlaus, Shai Gertler, Ryan O Behunin, Anthony L Lentine, and Peter T Rakich. Resonantly enhanced nonreciprocal silicon Brillouin amplifier. *Optica*, 6(9):1117–1123, 2019.

[93] Irina V Kabakova, Ravi Pant, Duk-Yong Choi, Sukhanta Debbarma, Barry Luther-Davies, Stephen J Madden, and Benjamin J Eggleton. Narrow linewidth Brillouin laser based on chalcogenide photonic chip. *Optics Letters*, 38(17):3208–3211, 2013.

[94] Sarat Gundavarapu, Grant M Brodnik, Matthew Puckett, Taran Huffman, Debapam Bose, Ryan Behunin, Jianfeng Wu, Tiequn Qiu, Cátia Pinho, Nitesh Chauhan, et al. Sub-hertz fundamental linewidth photonic integrated Brillouin laser. *Nature Photonics*, 13(1):60–67, 2019.

[95] A Fellay, Luc Thévenaz, M Facchini, M Nikles, and P Robert. Distributed sensing using stimulated Brillouin scattering: towards ultimate resolution. In *Optical Fiber Sensors*, page OWD3. Optical Society of America, 1997.

[96] D Culverhouse, F Farahi, CN Pannell, and DA Jackson. Potential of stimulated Brillouin scattering as sensing mechanism for distributed temperature sensors. *Electronics Letters*, 25(14):913–915, 1989.

[97] Toshio Kurashima, Tsuneo Horiguchi, Hisashi Izumita, Shin-ichi Furukawa, and Yahei Koyamada. Brillouin optical-fiber time domain reflectometry. *IEICE transactions on communications*, 76(4):382–390, 1993.

[98] Xiaoyi Bao, David J Webb, and David A Jackson. 22-km distributed temperature sensor using Brillouin gain in an optical fiber. *Optics Letters*, 18(7):552–554, 1993.

[99] Xiaoyi Bao, David J Webb, and David A Jackson. 32-km distributed temperature sensor based on Brillouin loss in an optical fiber. *Optics Letters*, 18(18):1561–1563, 1993.

[100] Marc Nikles, Luc Thévenaz, and Philippe A Robert. Simple distributed fiber sensor based on Brillouin gain spectrum analysis. *Optics Letters*, 21(10):758–760, 1996.

[101] D Garcus, Torsten Gogolla, Katerina Krebber, and Frank Schliep. Brillouin optical-fiber frequency-domain analysis for distributed temperature and strain measurements. *Journal of Lightwave Technology*, 15(4):654–662, 1997.

[102] Stella M Foaleng, Moshe Tur, Jean-Charles Beugnot, and Luc Thévenaz. High spatial and spectral resolution long-range sensing using Brillouin echoes. *Journal of Lightwave Technology*, 28(20):2993–3003, 2010.

[103] Atiyeh Zarifi, Birgit Stiller, Moritz Merklein, Neuton Li, Khu Vu, Duk-Yong Choi, Pan Ma, Stephen J Madden, and Benjamin J Eggleton. Highly localized distributed Brillouin scattering response in a photonic integrated circuit. *APL Photonics*, 3(3):036101, 2018.

[104] Atiyeh Zarifi, Birgit Stiller, Moritz Merklein, Yang Liu, Blair Morrison, Alvaro Casas-Bedoya, Guanghui Ren, Thach G Nguyen, Khu Vu, Duk-Yong Choi, et al. On-chip correlation-based Brillouin sensing: design, experiment, and simulation. *JOSA B*, 36(1):146–152, 2019.

[105] Irina V Kabakova, YuChen Xiang, Carl Paterson, and Peter Török. Fiber-integrated Brillouin microspectroscopy: towards Brillouin endoscopy. *Journal of Innovative Optical Health Sciences*, 10(06):1742002, 2017.

[106] Robert Prevedel, Alba Diz-Muñoz, Giancarlo Ruocco, and Giuseppe Antonacci. Brillouin microscopy: an emerging tool for mechanobiology. *Nature methods*, 16(10):969–977, 2019.

[107] Giuliano Scarcelli and Seok Hyun Yun. In vivo Brillouin optical microscopy of the human eye. *Optics Express*, 20(8):9197–9202, 2012.

[108] Kristie J Koski, Paul Akhenblit, Keri McKiernan, and Jeffery L Yarger. Non-invasive determination of the complete elastic moduli of spider silks. *Nature materials*, 12(3):262–267, 2013.

[109] VP Kalosha, Wenhai Li, Feng Wang, Liang Chen, and Xiaoyi Bao. Frequency-shifted light storage via stimulated Brillouin scattering in optical fibers. *Optics Letters*, 33(23):2848–2850, 2008.

[110] Moritz Merklein, Birgit Stiller, Khu Vu, Pan Ma, Stephen J Madden, and Benjamin J Eggleton. On-chip broadband nonreciprocal light storage. *Nanophotonics*, 1(ahead-of-print), 2020.

[111] Victor Fiore, Yong Yang, Mark C Kuzyk, Russell Barbour, Lin Tian, and Hailin Wang. Storing optical information as a mechanical excitation in a silica optomechanical resonator. *Physical Review Letters*, 107(13):133601, 2011.

[112] Victor Fiore, Chunhua Dong, Mark C Kuzyk, and Hailin Wang. Optomechanical light storage in a silica microresonator. *Physical Review A*, 87(2):023812, 2013.

[113] Chun-Hua Dong, Zhen Shen, Chang-Ling Zou, Yan-Lei Zhang, Wei Fu, and Guang-Can Guo. Brillouin-scattering-induced transparency and non-reciprocal light storage. *Nature Communications*, 6(1):1–6, 2015.

[114] M Horowitz, AR Chraplyvy, RW Tkach, and JL Zyskind. Broad-band transmitted intensity noise induced by Stokes and anti-Stokes Brillouin scattering in single-mode fibers. *IEEE Photonics Technology Letters*, 9(1):124–126, 1997.

[115] Wei Chen and Zhou Meng. Forward and backward intensity noises induced by stimulated Brillouin scattering in optical fiber. *Chinese Opt. Lett.*, 10(2):020603, 2012.

[116] A Kobyakov, SA Darmanyan, and DQ Chowdhury. Exact analytical treatment of noise initiation of SBS in the presence of loss. *Opt. Commun.*, 260(1):46–49, 2006.

[117] William Loh, Scott B Papp, and Scott A Diddams. Noise and dynamics of stimulated Brillouin scattering microresonator lasers. *Phys. Rev. A*, 91(5):053843, 2015.

[118] Weiwei Zhang and Robert A Minasian. Widely tunable single-passband microwave photonic filter based on stimulated Brillouin scattering. *IEEE Photonics Technology Letters*, 23(21):1775, 2011.

[119] Ravi Pant, David Marpaung, Irina V Kabakova, Blair Morrison, Christopher G Poulton, and Benjamin J Eggleton. On-chip stimulated Brillouin scattering for microwave signal processing and generation. *Laser Photonics Rev.*, 8(5):653–666, 2014.

[120] Xinpeng Huang and Shanhui Fan. Complete all-optical silica fiber isolator via stimulated Brillouin scattering. *Journal of Lightwave Technology*, 29(15):2267–2275, 2011.

[121] John David Jackson. *Classical electrodynamics*, pages 8–21. Wiley New York, 1998.

[122] Lev Davidovich Landau, JS Bell, MJ Kearsley, LP Pitaevskii, EM Lifshitz, and JB Sykes. *Electrodynamics of continuous media*, volume 8. Elsevier, 2013.

[123] Bahaa EA Saleh and Malvin Carl Teich. *Fundamentals of photonics*. john Wiley & sons, 2019.

[124] Cavour Yeh and Fred I Shimabukuro. *The essence of dielectric waveguides*. Springer, 2008.

[125] Elias Snitzer. Cylindrical dielectric waveguide modes. *JOSA*, 51(5):491–498, 1961.

[126] Weng Cho Chew, Mei Song Tong, and Bin Hu. *Integral equation methods for electromagnetic and elastic waves*, volume 3. Morgan & Claypool Publishers, 2008.

[127] Daniel A Fleisch. *A Student's Guide to the Schrödinger Equation*. Cambridge University Press, 2020.

[128] Paul N Butcher and David Cotter. *The elements of nonlinear optics*, pages 216–220. Cambridge university press, 1990.

[129] Chris Fleming, NI Cummings, Charis Anastopoulos, and BL Hu. The rotating-wave approximation: consistency and applicability from an open quantum system analysis. *Journal of Physics A: Mathematical and Theoretical*, 43(40):405304, 2010.

[130] Christian Wolff, Philipp Gutsche, Michael J Steel, Benjamin J Eggleton, and Christopher G Poulton. Impact of nonlinear loss on stimulated Brillouin scattering. *JOSA B*, 32(9):1968–1978, 2015.

[131] Oscar A. Nieves, Matthew D. Arnold, Michael J. Steel, Mikołaj K. Schmidt, and Christopher G. Poulton. Numerical simulation of noise in pulsed Brillouin scattering. *JOSA B*, 38(8):2343–2352, Aug 2021.

[132] Arman B Fallahkhair, Kai S Li, and Thomas E Murphy. Vector finite difference modesolver for anisotropic dielectric waveguides. *J. Light. Technol.*, 26(11):1423–1431, 2008.

[133] Nathan Dostart, Yangyang Liu, and Miloš A Popović. Acoustic waveguide eigenmode solver based on a staggered-grid finite-difference method. *Scientific reports*, 7(1):1–11, 2017.

[134] Björn CP Sturmberg, Kokou Bertin Dossou, Michael JA Smith, Blair Morrison, Christopher G Poulton, and Michael J Steel. Finite element analysis of stimulated Brillouin scattering in integrated photonic waveguides. *J. Light. Technol.*, 37(15):3791–3804, 2019.

[135] B. Sturmberg and M. J. Steel. Numbat. https://github.com/bjornsturmberg/NumBAT, 2019.

[136] JAS Lima and AR Plastino. On the classical energy equipartition theorem. *Brazilian Journal of Physics*, 30(1):176–180, 2000.

[137] Rep Kubo. The fluctuation-dissipation theorem. *Rep. Prog. Phys.*, 29(1):255, 1966.

[138] Werner Horsthemke. Noise induced transitions. In *Non-equilibrium dynamics in chemical systems*, pages 44–49. Springer, 1984.

[139] Jan Van Neerven and Mark C Veraar. On the stochastic fubini theorem in infinite dimensions. In *Stochastic Partial Differential Equations and Applications VII, Levico Terme, 2004, in: Lecture Notes Pure Appl. Math.*, page 323–336. CRC Press, 2005.

[140] Mark Veraar. The stochastic Fubini theorem revisited. *Stochastics*, 84(4):543–551, 2012.

[141] C Gardiner and P Zoller. Cold atoms: Volume 2 the quantum world of ultra-cold atoms and light book i: Foundations of quantum optics, 2014.

[142] N Leibovich and E Barkai. Aging Wiener-Khinchin theorem. *Phys. Rev. Lett.*, 115(8):080602, 2015.

[143] Andreas Dechant and Eric Lutz. Wiener-Khinchin theorem for nonstationary scale-invariant processes. *Physical Review Letters*, 115(8):080603, 2015.

[144] Behzad Moslehi. Analysis of optical phase noise in fiber-optic systems employing a laser source with arbitrary coherence time. *Journal of Lightwave Technology*, 4(9):1334–1351, 1986.

[145] Alexis Debut, Stéphane Randoux, and Jaouad Zemmouri. Linewidth narrowing in Brillouin lasers: Theoretical analysis. *Physical Review A*, 62(2):023803, 2000.

[146] Chen Wei, Meng Zhou, Zhou Hui-Juan, and Luo Hong. Stimulated Brillouin scattering-induced phase noise in an interferometric fiber sensing system. *Chinese Physics B*, 21(3):034212, 2012.

[147] Yuval Atzmon and Moshe Nazarathy. Laser phase noise in coherent and differential optical transmission revisited in the polar domain. *Journal of Lightwave Technology*, 27(1):19–29, 2009.

[148] P.E. Kloeden and E. Platen. *Numerical Solution of Stochastic Differential Equations*. Springer-Verlag Berlin Heidelberg, 1st edition, 1992.

[149] Mark Pelusi, Takashi Inoue, and Shu Namiki. Noise characterization of Brillouin amplified narrowband carriers for coherent communications. In *2018 European Conference on Optical Communication (ECOC)*, pages 1–3. IEEE, 2018.

[150] Atiyeh Zarifi, Moritz Merklein, Yang Liu, Amol Choudhary, Benjamin J Eggleton, and Bill Corcoran. Broadband SBS filter for optical carrier recovery applications in telecommunication systems. In *2020 Conference on Lasers and Electro-Optics (CLEO)*, pages 1–2. IEEE, 2020.

[151] Pavel Drábek and Gabriela Holubová. *Elements of partial differential equations*. Walter de Gruyter GmbH & Co KG, 2014.

[152] Kiyosi Itô. On a formula concerning stochastic differentials. *Nagoya Mathematical Journal*, 3:55–65, 1951.

[153] Govind P Agrawal. *Fiber-optic communication systems*. John Wiley & Sons, 4th edition, 2012.

[154] Yiwei Xie, Amol Choudhary, Yang Liu, David Marpaung, Khu Vu, Pan Ma, Duk-Yong Choi, Stephen Madden, and Benjamin J Eggleton. System-level performance of chip-based Brillouin microwave photonic bandpass filters. *J. Light. Technol.*, 37(20):5246–5258, 2019.

[155] Andrei A Fotiadi, Roman Kiyan, Olivier Deparis, Patrice Mégret, and Michel Blondel. Statistical properties of stimulated Brillouin scattering in single-mode optical fibers above threshold. *Opt. Lett.*, 27(2):83–85, 2002.

[156] Mark S Bowers and Nicholas M Luzod. Stimulated Brillouin scattering in optical fibers with end reflections excited by broadband pump waves. *Optical Engineering*, 58(10):102702, 2019.

[157] George E Uhlenbeck and Leonard S Ornstein. On the theory of the Brownian motion. *Physical Review*, 36(5):823, 1930.

[158] Nicolaas G Van Kampen. Stochastic differential equations. *Physics reports*, 24(3):171–228, 1976.

[159] Bernt Øksendal. Stochastic differential equations. In *Stochastic differential equations*, pages 29–33. Springer, 2003.

[160] Xiaojie Wang and Siqing Gan. The tamed Milstein method for commutative stochastic differential equations with non-globally Lipschitz continuous coefficients. *Journal of Difference Equations and Applications*, 19(3):466–490, 2013.

[161] Alexander L Gaeta and Robert W Boyd. Stochastic dynamics of stimulated Brillouin scattering in an optical fiber. *Physical Review A*, 44(5):3205, 1991.

[162] Rebecca L Honeycutt. Stochastic Runge-Kutta algorithms. i. white noise. *Physical Review A*, 45(2):600, 1992.

[163] Rebecca L Honeycutt. Stochastic Runge-Kutta algorithms. ii. colored noise. *Physical Review A*, 45(2):604, 1992.

[164] A Tocino and R Ardanuy. Runge–kutta methods for numerical solution of stochastic differential equations. *Journal of Computational and Applied Mathematics*, 138(2):219–241, 2002.

[165] Zhongqiang Zhang and George Karniadakis. *Numerical methods for stochastic partial differential equations with white noise*. Springer-Verlag, 1st edition, 2017.

[166] Moritz Merklein, Birgit Stiller, and Benjamin J Eggleton. Brillouin-based light storage and delay techniques. *Journal of Optics*, 20(8):083003, 2018.

[167] Leslie Allen and Joseph H Eberly. *Optical resonance and two-level atoms*, volume 28. John Wiley & Sons., 1975.

[168] Johannes Piotrowski, Mikołaj K Schmidt, Birgit Stiller, Christopher G Poulton, and Michael J Steel. Picosecond acoustic dynamics in stimulated Brillouin scattering. *Optics Letters*, 46(12):2972–2975, 2021.

[169] Saleh Faruque. *Radio frequency modulation made easy*, pages 69–83. Springer, 2017.

[170] Douglas Walsh, David Moodie, Iain Mauchline, Steve Conner, Walter Johnstone, and Brian Culshaw. Practical bit error rate measurements on fibre optic communications links in student teaching laboratories. In *9th International Conference on Education and Training in Optics and Photonics (ETOP), Marseille, France, Paper ETOP021*, 2005.

[171] Er'el Granot. Propagation of chirped rectangular pulses in dispersive media: analytical analysis. *Optics Letters*, 44(19):4745–4748, 2019.

[172] David R Smith. *Digital transmission systems*, pages 370–381. Springer science & business media, 2012.

[173] Diponkor Bala. Analysis the probability of bit error performance on different digital modulation techniques over AWGN channel using MATLAB. *Journal of Electrical Engineering, Electronics, Control and Computer Science*, 7(3):9–18, 2021.

[174] Paul Martinsen, Johannes Blaschke, Rainer Künnemeyer, and Robert Jordan. Accelerating Monte Carlo simulations with an NVIDIA® graphics processor. *Computer Physics Communications*, 180(10):1983–1989, 2009.

[175] Tobias Preis, Peter Virnau, Wolfgang Paul, and Johannes J Schneider. Gpu accelerated Monte Carlo simulation of the 2D and 3D Ising model. *Journal of Computational Physics*, 228(12):4468–4477, 2009.

[176] Jason Mick, Eyad Hailat, Vincent Russo, Kamel Rushaidat, Loren Schwiebert, and Jeffrey Potoff. Gpu-accelerated gibbs ensemble Monte Carlo simulations of Lennard-Jonesium. *Computer Physics Communications*, 184(12):2662–2669, 2013.

[177] Ovidiu Calin. *An informal introduction to stochastic calculus with applications*. World Scientific, 2015.

[178] Winthrop Dickinson Means. *Stress and strain: basic concepts of continuum mechanics for geologists*. Springer Science & Business Media, 2012.

[179] Bertram Alexander Auld. *Acoustic fields and waves in solids*. Wiley, 1973.

[180] Kip S Thorne and Roger D Blandford. *Modern Classical Physics: Optics, Fluids, Plasmas, Elasticity, Relativity, and Statistical Physics*. Princeton University Press, 2017.

[181] Anthony James Merrill Spencer. *Continuum mechanics*. Courier Corporation, 2004.

[182] Bertram Alexander Auld. *Acoustic fields and waves in solids*. Wiley, 1973.

[183] Albert Einstein. On the theory of the brownian movement. *Ann. Phys*, 19(4):371–381, 1906.

[184] Harumi Hattori. *Partial differential equations: methods, applications and theories*. World Scientific, 2019.

[185] Marshall N Rosenbluth, William M MacDonald, and David L Judd. Fokker-Planck equation for an inverse-square force. *Physical Review*, 107(1):1, 1957.

[186] RF Pawula. Approximation of the linear boltzmann equation by the Fokker-Planck equation. *Physical Review*, 162(1):186, 1967.

[187] GW Wei. A unified approach for the solution of the Fokker-Planck equation. *Journal of Physics A: Mathematical and General*, 33(27):4935, 2000.

[188] Michael J Lighthill. *An introduction to Fourier analysis and generalised functions*. Cambridge University Press, 1958.

[189] Sergey Nikolaevich Gurbatov, Oleg Vladimirovich Rudenko, and Aleksandr I Saichev. *Waves and structures in nonlinear nondispersive media: general theory and applications to nonlinear acoustics*, pages 441–455. Springer Science & Business Media, 2012.